

Mineralised Pegmatites of the Damara Belt,
Namibia: Fluid inclusion and geochemical
characteristics with implications for post-
collisional mineralisation

Luisa Ashworth

A dissertation submitted to the Faculty of Science, University of the Witwatersrand,
Johannesburg, in fulfilment of the requirements for the degree of Doctor of Philosophy.

Johannesburg, 2014

DECLARATION

I declare that this thesis is my own, unaided work. It is being submitted for the degree of Doctor of Philosophy at the University of the Witwatersrand, Johannesburg. It has not been submitted before for any degree or examination in any other university.

Luisa Ashworth

20 of March 2014

ABSTRACT

Namibia is renowned for its abundant mineral resources, a large proportion of which are hosted in the metasedimentary lithologies of the Damara Belt, the northeast-trending inland branch of the Neoproterozoic Pan-African Damara Orogen. Deposit types include late- to post-tectonic (~ 523 – 506 Ma) LCT (Li-Be, Sn-, and miarolitic gem-tourmaline-bearing) pegmatites, and uraniferous pegmatitic sheeted leucogranites (SLGs), which have an NYF affinity.

Fluid inclusion studies reveal that although mineralization differs between the different types of pegmatites located at different geographic locations, and by extension, different stratigraphic levels, the fluid inclusion assemblages present in these pegmatites are similar; thus different types of pegmatites are indistinguishable from each other based on their fluid inclusion assemblages. Thorough fluid inclusion petrography indicated that although fluid inclusions are abundant in the pegmatites, no primary fluid inclusions could be identified, and rather those studied are pseudosecondary and secondary. Fluid inclusions are aqueo-carbonic (\pm NaCl), carbonic, and aqueous. It is proposed that all of the pegmatites studied share a similar late-stage evolution, with fluids becoming less carbonic and less saline with the progression of crystallisation.

Oxygen isotope ratios allow the discrimination of different pegmatites into two groups, Group A (Sn-, Li-Sn-, and gem-tourmaline-bearing LCT pegmatites), and Group B (Li-Be-bearing LCT, and U-bearing NYF pegmatites). Group A pegmatites have O-isotope ratios ranging from 11 to 13 ‰ suggesting that they have an I-type affinity. These values are, however, elevated above those of typical I-type granites (7 - 9 ‰), indicating either a post-emplacement low-temperature exchange with meteoric fluid, high-temperature hydrothermal exchange with $\delta^{18}\text{O}$ country rocks during emplacement, or the derivation of these pegmatites from a non-pelitic/S-type metagneous source. Group B pegmatites have higher $\delta^{18}\text{O}$ ratios ($\delta^{18}\text{O} = 15 - 16$ ‰), indicative of their S-type affinity, and their derivation from metapelitic source rocks. δD values of all the pegmatites range from -40

‰ to -90 ‰ indicating that the pegmatitic fluids are primary magmatic with a metamorphic fluid component.

Trends in the trace element concentrations of both Group A and Group B pegmatites are very similar to each other, making the two groups indistinguishable from each other on this basis. The Damaran pegmatites also share similar geochemical trends with their country rocks. There is, however, no direct field evidence to suggest that the pegmatites were derived from the *in situ* anatexis of the country rocks. It is more likely that anatexis occurred some distance away from where the pegmatites were ultimately emplaced, and that the melts migrated and were finally emplaced in pre-existing structures, possibly formed during Damaran deformation.

O-isotope and Ti-in-quartz geothermometry indicate that Damaran pegmatites can be subdivided into two groups based on their crystallisation temperatures. LCT pegmatites crystallised at temperatures ranging from ~ 450 - 550 °C, while the NYF pegmatites crystallised at higher temperatures, ranging from 630 - 670 °C. It is important to note that the subdivision of pegmatites in Groups A and B based on their O-isotope systematics does not correspond with their subdivision into the LCT and NYF pegmatite families according to their crystallisation temperatures.

In addition to clarifying aspects of the emplacement and evolution of the Damaran pegmatites, this study points out that there are several discrepancies in the current classification schemes of pegmatites. It shows that in addition to the problems encountered when trying to distinguish between LCT and NYF pegmatites based on their mineralogy, they also cannot truly be distinguished from each other using their geochemical and isotopic characteristics, or their tectonic settings. It is tentatively proposed that crystallisation temperature be considered as an alternative or additional characteristic in the classification of pegmatites, and that it be considered on a regional scale rather than only in the evaluation of the highly evolved end-members of a pegmatite swarm.

ACKNOWLEDGEMENTS

I would like to thank my supervisors, Prof. J.A. Kinnaird and Dr P.A.M. Nex for giving me such an interesting and challenging project to work on, for their guidance, supervision, pearls of wisdom along the way, and for taking me to some beautiful places in the world.

None of this research would have been possible without the financial assistance of the University of the Witwatersrand, the National Research Foundation, the Geological Society of South Africa, and the Society of Economic Geologists. In addition to this, I would like to thank the Geological Survey of Namibia for letting me look at, and take, their rocks, Eddie for allowing me short-notice access to the Omapyu pegmatite, and John Stewart of Licore Mining cc for allowing me access to the Rubicon pegmatite.

Many thanks to Jan-Marten Huizenga and Lynette Greyling for guidance and assistance pertaining to all bubble-related matters, and to Rudolph Erasmus (School of Physics, University of the Witwatersrand), Wojciech Przybylowicz (iThemba LABS, Somerset West), and Chris Harris (Department of Geological Sciences, University of Cape Town), for allowing me the use of their laboratory facilities. Thank you also to all of the pegmatologists who I was fortunate to meet at the PEG 2011 and PEG 2013 meetings, who are abundantly generous with their knowledge, and who make pegmatites fun. Special thanks to Axel Müller at the Geological Survey of Norway for running my Ti-in-quartz samples at such short notice.

I would also like to thank all technical staff at the School of Geosciences (University of the Witwatersrand) and the Department of Geological Sciences (University of Cape Town) for all the sample preparation that they did for me, especially since some of the preparation was quite challenging, and a special thanks goes to Ryan McIntosh and Michael Donze for the many, many hours they spent helping me to crush, mill, and separate minerals. Also, a special thanks to Fayrooza Rawoot at the University of Cape Town, for teaching me how not to be afraid of the silicate line.

Many friends have helped me keep it together over the last few years, especially Natasha Barbolini and Nicole Burri, and several great listeners, including Grant Bybee, Trishya Owen-Smith, Sara Turnbull, Debra Colarossi, Traiana Naydenova, Louise Coney, my running buddy, Mary-Rose Howe-Watson, and the rest of the church gang. Thank you also to Luke Longridge and Guy Freemantle, who were so generous with their knowledge of Namibia, and with their samples. Special thanks go to Kalin Naydenov, Lorenzo Milani, and Jeremie Lehmann, William Rankin and Russell Johnson for taking such great care of me on our field trip together, and for many hours of support and good coffee. To my dance teachers and the ladies in my dance classes, thank you for helping me to keep a clear mind, and to my band mates, thanks for all the mid-thesis rock-and-roll.

To the staff of GeoSpectral Imaging, thank you for your patience, and for encouraging me to see this through.

I would like to thank my family for their love, support, and encouragement; mom and dad, thank you for believing in me and for thinking that what I do is interesting even though it doesn't make a lot of sense.

Lastly, and most importantly, thank you to my husband, Jason, for his unending understanding, empathy through the tough times, and several kick-starts.

TABLE OF CONTENTS

DECLARATION	I
ABSTRACT	II
ACKNOWLEDGEMENTS	IV
TABLE OF CONTENTS	VI
LIST OF FIGURES	XII
LIST OF TABLES	XVII
CHAPTER 1	1
OVERVIEW OF THE GEOLOGY OF THE DAMARA BELT, NAMIBIA	1
1.1 INTRODUCTION	1
1.2 REGIONAL GEOLOGY: THE DAMARA BELT	1
1.2.1 Stratigraphy and depositional history of the Damara Belt	5
1.2.2 Structural evolution of the Damara Belt	8
1.2.3 Metamorphism in the Damara Belt	9
1.2.4 Magmatism in the Damara Belt	11
1.2.4.1 Goas intrusive suite	15
1.2.4.2 Salem granites	15
1.2.4.3 Red granites	15
1.2.4.4 Homogeneous syn-tectonic granites	16
1.2.4.5 Post-tectonic leucogranites	16
1.2.4.6 Post-tectonic pegmatites	16
1.3. PROJECT AIMS	17
CHAPTER 2	19
REGIONAL GEOLOGY OF THE STUDY AREAS	19
2.1 INTRODUCTION	19
2.2 REGIONAL STRATIGRAPHY	22
2.2.1 Pre-Damaran Geology: Abbabis Complex	22
2.2.2 The Damara Supergroup: Nosib Group	23
2.2.2.1 Etusis Formation	23
2.2.2.2 Khan Formation	24
2.2.3 The Damara Supergroup: Swakop Group	25
2.2.3.1 Rössing Formation (Ugab Subgroup)	25
2.2.3.2 Chuos Formation (Usakos Subgroup)	25
2.2.3.3 Arandis Formation (Usakos Subgroup)	26
2.2.3.4 Ghaub Formation (Navachab Subgroup)	26
2.2.3.5 Karibib Formation (Navachab Subgroup)	27
2.2.3.6 Kuiseb Formation (Navachab Subgroup)	27
2.2.4 The Damara Supergroup: Zerrissenne Group (Southern Kaoko Zone)	27
2.2.4.1 Zebrapütz Formation	28

2.2.4.2 Brandberg West Formation	28
2.2.4.3 Brak River Formation	29
2.2.4.4 Ghaub Formation	29
2.2.4.5 Gembok River Formation	29
2.2.4.6 Amis River Formation	30
2.3 METAMORPHISM AND DEFORMATION IN THE STUDY AREAS	30
2.3.1 <i>Metamorphism in the southern Central Zone</i>	31
2.3.2 <i>Deformation in the southern Central Zone</i>	32
2.3.3 <i>Metamorphism in the Northern Zone/Southern Kaoko Zone</i>	33
2.3.4 <i>Deformation in the Northern Zone/Southern Kaoko Zone</i>	34
CHAPTER 3	36
AN INTRODUCTION TO PEGMATITES	36
3.1 INTRODUCTION	36
3.2 REGIONAL AND GLOBAL DISTRIBUTION OF PEGMATITES	37
3.3 PEGMATITE CLASSIFICATION	38
3.3.1 <i>Pegmatite classes</i>	39
3.3.2 <i>Pegmatite families</i>	40
3.3.2.1 LCT Pegmatites	40
3.3.2.2 NYF Pegmatites.....	41
3.3.2.3 Mixed LCT-NYF Pegmatites.....	42
3.3.3 <i>Controversies regarding pegmatite classification</i>	42
3.4 INTERNAL ANATOMY OF PEGMATITES	43
3.4.1 <i>Unzoned pegmatites</i>	44
3.4.2 <i>Zoned pegmatites</i>	44
3.4.2.1 Border zone.....	45
3.4.2.2 Wall zone.....	46
3.4.2.3 Intermediate zone	46
3.4.2.4 Core	46
3.5 GENERATION AND CONSOLIDATION OF PEGMATITE MELTS	46
3.5.1 <i>Models for the formation of pegmatites</i>	46
3.5.2 <i>The importance of volatiles in pegmatites</i>	47
3.6 RATES OF PEGMATITE CRYSTALLISATION AND CONSTITUTIONAL ZONE REFINING	49
CHAPTER 4	52
PEGMATITES OF THE DAMARA OROGEN	52
4.1 INTRODUCTION	52
4.2 LI-BE-BEARING PEGMATITES OF THE DAMARA BELT: RUBICON AND HELICON PEGMATITES	54
4.2.1 <i>Introduction</i>	54
4.2.2 <i>The Rubicon Pegmatite</i>	55
4.2.2.1 Structural setting of the Rubicon pegmatite	55
4.2.2.2 Internal zonation and mineralogy of the Rubicon pegmatite	56
4.2.2.2.1 Wall Zone:	57
4.2.2.2.2 Perthite Zone	58

4.2.2.2.3 Beryl Zone	58
4.2.2.2.4 Lithium Ore Zones	59
4.2.2.2.5 Core Zone.....	62
4.2.3 <i>The Helicon Pegmatites</i>	62
4.2.3.1 Structural setting of the Helicon pegmatites	62
4.2.3.2 Internal zonation and mineralogy of the Helicon II pegmatite.....	63
4.2.3.2.1 Albite-quartz-muscovite (perthite) Zone (Wall Zone)	64
4.2.3.2.2 Albite-quartz-petalite Zone (Intermediate Zones)	65
4.2.3.2.3 Lepidolite Zone (Lithium Ore Zone)	66
4.2.3.2.4 Core Zone.....	67
4.3 SN-BEARING PEGMATITES OF THE DAMARA BELT: UIS AND KARLOWA PEGMATITES.....	67
4.3.1 <i>Introduction</i>	67
4.3.2 <i>The Uis Pegmatite Swarm</i>	69
4.3.2.1 Structural setting of the Uis pegmatites	69
4.3.2.2 Mineralogy of the Uis pegmatites	71
4.3.3 <i>Karlowa Pegmatite Swarm</i>	72
4.3.3.1 Structural setting of the Karlowa pegmatites	72
4.3.3.2 Internal zonation and mineralogy of the Karlowa pegmatites	74
4.3.3.2.1 Border Zone	75
4.3.3.2.2 Intermediate Zone	75
4.3.3.2.3 Core Zone.....	76
4.4 TOURMALINE-BEARING PEGMATITES OF THE DAMARA BELT: USAKOS AND OMAPYU PEGMATITES.....	77
4.4.1 <i>Introduction</i>	77
4.4.2 <i>The Usakos Pegmatite</i>	78
4.4.2.1 Structural setting of the Usakos pegmatite.....	78
4.4.2.2 Internal zonation and mineralogy of the Usakos pegmatite.....	80
4.4.2.2.1 Border Zone	80
4.4.2.2.2 Wall Zone	82
4.4.2.2.3 Intermediate Zone	82
4.4.2.2.4 Core Zone.....	83
4.4.3 <i>The Omapyu Pegmatites</i>	83
4.4.3.1 Structural setting of the Omapyu pegmatites.....	83
4.4.3.2 Mineralogy of the Omapyu pegmatites.....	85
4.5 PEGMATITIC SHEETED LEUCOGRANITES OF THE DAMARA BELT: VALENCIA AREA	87
4.5.1 <i>Introduction</i>	87
4.5.2 <i>The Valencia (SLGs) pegmatites</i>	88
4.5.2.1 Structural setting of the Valencia (SLGs) pegmatites	88
4.5.2.2 Mineralogy of the Valencia (SLGs) pegmatites	90
4.5.2.2.1 Type A (SLGs) pegmatites	90
4.5.2.2.2 Type B (SLGs) pegmatites	90
4.5.2.2.3 Type C (SLGs) pegmatites	91
4.5.2.2.4 Type D (SLGs) pegmatites	93
4.5.2.2.5 Type E (SLGs) pegmatites	93
4.5.2.2.6 Type F (SLGs) pegmatites.....	93
4.6 SAMPLING	94
4.7 SUMMARY	95

CHAPTER 5	96
GEOCHEMISTRY AND GENERAL CHARACTERISTICS OF FLUID INCLUSIONS FROM MINERALISED PEGMATITES	96
5.1 INTRODUCTION.....	96
5.2 METHODOLOGY.....	97
5.2.1 Sampling.....	97
5.2.2 Sample preparation.....	97
5.2.3 Analytical techniques.....	98
5.2.3.1 Fluid inclusion petrography.....	98
5.2.3.2 Fluid inclusion microthermometry.....	98
5.2.3.3 Raman microspectroscopy.....	101
5.2.3.4 Particle-induced X-ray emission (PIXE).....	103
5.3 RESULTS.....	105
5.3.1 Cathodoluminescence and petrography.....	105
5.3.1.1 Type 1 fluid inclusions.....	105
5.3.1.2 Type 2 fluid inclusions.....	106
5.3.1.3 Type 3 fluid inclusions.....	108
5.3.1.4 Type 4 fluid inclusions.....	108
5.3.1.5 Type 5 fluid inclusions.....	108
5.3.2 Geochemical characteristics of fluid inclusions: microthermometry, Raman microspectroscopy and Particle-Induced X-ray Emission	108
5.3.2.1 Li-Be-bearing pegmatites: Rubicon pegmatite.....	109
5.3.2.1.1 Type 1 fluid inclusions.....	109
5.3.2.1.2 Type 2 fluid inclusions.....	110
5.3.2.1.3 Type 3 fluid inclusions.....	111
5.3.2.1.4 Type 5 fluid inclusions.....	113
5.3.2.2 Sn-bearing pegmatites: Uis pegmatite	114
5.3.2.2.1 Type 1 fluid inclusions.....	114
5.3.2.2.2 Type 5 fluid inclusions.....	117
5.3.2.3 Li-Sn-bearing pegmatites: Karlowa pegmatite	118
5.3.2.3.1 Type 1 fluid inclusions.....	119
5.3.2.3.2 Type 5 fluid inclusions.....	120
5.3.2.4 Gem tourmaline-bearing pegmatites: Omapyu pegmatite.....	122
5.3.2.4.1 Type 1 fluid inclusions.....	122
5.3.2.4.2 Type 4 fluid inclusions.....	125
5.3.2.4.3 Type 5 fluid inclusions.....	126
5.3.2.5 U-bearing pegmatites: Valencia pegmatites (SLGs).....	127
5.3.2.5.1 Type 1 fluid inclusions.....	127
5.3.2.5.2 Type 4 fluid inclusions.....	127
5.3.2.5.3 Type 5 fluid inclusions.....	128
5.4 DISCUSSION OF RESULTS	130
5.5 INTERPRETATION OF RESULTS.....	133
5.5.1 Fluid evolution of LCT and NYF pegmatites from the Damara Belt	135
5.5.2: Implications for mineralisation.....	137
5.6 SUMMARY	139

CHAPTER 6	140
GEOCHEMICAL CHARACTERISTICS OF MINERALISED PEGMATITES AND THEIR COUNTRY ROCKS	140
6.1 INTRODUCTION.....	140
6.2 METHODOLOGY.....	141
6.2.1 <i>Sample preparation</i>	141
6.2.2 <i>XRF analyses</i>	141
6.2.3 <i>ICP-MS analyses</i>	142
6.2.3.1 Whole-rock trace element analyses.....	142
6.2.3.2 Trace element analyses in quartz.....	142
6.3 RESULTS.....	143
6.3.1 <i>Li-Be-bearing pegmatites</i>	143
6.3.1.1 Rubicon and Helicon pegmatites.....	143
6.3.1.2 Rubicon and Helicon country rocks.....	156
6.3.2 <i>Sn-bearing pegmatites</i>	157
6.3.2.1 Uis pegmatites.....	157
6.3.2.2 Uis country rocks.....	157
6.3.3 <i>Li-Sn-bearing pegmatites</i>	158
6.3.3.1 Karlowa pegmatites.....	158
6.3.3.2 Karlowa country rocks.....	159
6.3.4 <i>Gem tourmaline-bearing pegmatites: Usakos and Omapyu pegmatites</i>	159
6.3.4.1 Usakos and Omapyu pegmatites.....	159
6.3.4.2 Usakos and Omapyu country rocks.....	160
6.3.5 <i>U-bearing pegmatites: Valencia pegmatites (SLGs)</i>	161
6.3.5.1 Valencia pegmatites (SLGs).....	161
6.3.5.2 Valencia country rocks.....	161
6.4 DISCUSSION OF RESULTS.....	162
6.4.1 <i>Major element composition of mineralised pegmatites</i>	162
6.4.2 <i>Trace element composition of mineralised pegmatites</i>	164
6.4.3 <i>Major element composition of country rocks</i>	170
6.4.4 <i>Trace element composition of country rocks</i>	171
6.5 INTERPRETATION OF RESULTS.....	173
6.6. SUMMARY.....	182
CHAPTER 7	183
O- AND H-ISOTOPE CHARACTERISTICS OF MINERALISED PEGMATITES AND THEIR COUNTRY ROCKS	183
7.1 INTRODUCTION.....	183
7.2 METHODOLOGY.....	184
7.2.1 <i>Sampling</i>	184
7.2.2 <i>Sample preparation</i>	184
7.2.3 <i>Analytical techniques</i>	184
7.3 RESULTS.....	186
7.3.1 <i>Oxygen- and Hydrogen-isotope results</i>	186

7.3.1.1 Li-Be-bearing pegmatites: Rubicon and Helicon pegmatites	186
7.3.1.2 Sn-bearing pegmatites: Uis pegmatites.....	187
7.3.1.3 Li-Sn-bearing pegmatites: Karlowa pegmatites	188
7.3.1.4 Gem-tourmaline-bearing pegmatites: Usakos and Omapyu pegmatites.....	192
7.3.1.5 U-bearing pegmatites (SLGs): Valencia pegmatites (SLGs)	193
7.4 DISCUSSION OF RESULTS	193
7.5 INTERPRETATION OF RESULTS.....	200
7.6 SUMMARY	210
CHAPTER 8.....	213
DISCUSSION AND CONCLUSIONS.....	213
8.1 INTRODUCTION.....	213
8.2 CRYSTALLISATION TEMPERATURES OF THE DAMARAN PEGMATITES.....	213
8.3 LATE-STAGE EVOLUTION OF THE DAMARAN PEGMATITES: IMPLICATIONS FOR MINERALISATION	215
8.4 POTENTIAL SOURCES OF DAMARAN PEGMATITE MAGMAS	218
8.5 MELT GENERATION AND MAGMA TRANSPORT	223
8.6 DISCREPANCIES IN THE CLASSIFICATION OF LCT AND NYF PEGMATITES	225
8.6.1 <i>Complications in relating pegmatite geochemistry to tectonic processes.....</i>	225
8.6.1.1 Kibaran pegmatites in South Africa.....	226
8.6.1.2 Pan-African pegmatites Mozambique	227
8.6.2 <i>Factors to consider in interpreting the geochemical signatures of pegmatites</i>	227
8.6.3 <i>Suggestions for future work and revisions of pegmatite classification schemes.....</i>	228
REFERENCES.....	230
APPENDIX 1: SAMPLE INVENTORY.....	267
APPENDIX 2: MICROTHERMOMETRY DATA.....	274
APPENDIX 3: TRACE ELEMENT IN QUARTZ DATA.....	297

LIST OF FIGURES

Figure 1.1: Neoproterozoic fold belts and magmatic arcs between various cratonic blocks of southwestern Gondwana	3
Figure 1.2: Tectonostratigraphic zones of the Damara Orogen	4
Figure 1.3: Stratigraphy and lithostratigraphic correlations across the Damara Belt with approximate deposition ages	6
Figure 1.4: Simplified representation of peak metamorphism in the Damara Orogeny	11
Figure 2.1: Google Earth image showing the locations of sample localities in relation to the tectonostratigraphic zones of the Damara Belt	20
Figure 2.2: Summary of pegmatite emplacement in metasedimentary units of the Damara Supergroup.	35
Figure 3.1: The relationships between parent granite plutons and surrounding pegmatites	38
Figure 3.2: Pressure-temperature conditions for the formation of Ginsburg's (1984) and Černý's (1991a) abyssal (AB), muscovite (MS), rare-element (RE) and miarolitic (MI) pegmatites	39
Figure 3.3: Idealised block diagram of a zoned pegmatite, illustrating concentric zonation around a central core zone	45
Figure 3.4: Temperature-wt % H ₂ O paths for a generic granite, rhyolite and pegmatite illustrating the differences between them, in water retention and subsequent undercooling	49
Figure 3.5: Schematic diagram illustrating crystal growth, pile-up in the boundary layer, local saturation, and fluxed constitutional zone-refining	50
Figure 4.1: Geographic extent of five major pegmatite belts in the Damara Belt	53
Figure 4.2: Google Earth map with a 1:250 000 geological map overlay of the Karibib pegmatite district	55
Figure 4.3: Goas Suite granodiorite into which the Rubicon pegmatite has intruded	56
Figure 4.4: Zonation observed in the Rubicon pegmatite	57
Figure 4.5: Poikilitic quartz (Qz) and muscovite (Ms) from the Wall Zone	58
Figure 4.6: Perthite (Ksp) "rosette" from the Beryl Zone	59

Figure 4.7: Petalite from the Petalite Zone of Rubicon pegmatite	60
Figure 4.8: Relationship between albite and lepidolite in the Lepidolite Zone of the Rubicon pegmatite	61
Figure 4.9: Features of the Karibib Marble in the vicinity of the Helicon pegmatites	63
Figure 4.10: Mineralogical zonation in the footwall of Helicon II pegmatite	64
Figure 4.11: Tourmaline (Tur) and muscovite (Ms) nests in the Wall Zone of the Helicon II Pegmatite	65
Figure 4.12: Low grade lepidolite ore at the Helicon II pegmatite	66
Figure 4.13: Google Earth map with a 1:250 000 geological map overlay of the Uis-Karlowa pegmatite district	68
Figure 4.14: Unzoned Uis pegmatites intruding into the "knotted" schists of the Khomas Group	69
Figure 4.15: "Knottenschiefer"/"knotted" schist	70
Figure 4.16: Anhedral and zoned cassiterite (Cas) grains overprinting a groundmass of albite (Ab), quartz (Qz), muscovite (Ms) and lepidolite (Lpd)	72
Figure 4.17: The Karlowa pegmatite swarm	73
Figure 4.18: Photomicrograph of metapelites into which the Karlowa pegmatites have intruded, composed predominantly of quartz (Qz) with subordinate biotite (Bt) and magnetite (Mag)	74
Figure 4.19: Zonation observed in a pegmatite of the Karlowa swarm	75
Figure 4.20: Google Earth map with a 1:250 000 geological map overlay of the Usakos Pegmatite Field	79
Figure 4.21: Kuiseb schist adjacent to the contact with the Usakos pegmatite	80
Figure 4.22: Zonation observed in the Usakos pegmatite	81
Figure 4.23: Border Zones of the Usakos pegmatite	82
Figure 4.24: Schist xenolith in the Intermediate Zone of the Usakos pegmatite	83

Figure 4.25: Google Earth map with a 1:250 000 geological map overlay of the Omapyu pegmatites	84
Figure 4.26: Karibib marble adjacent to the largest pegmatite in the Omapyu pegmatite swarm	85
Figure 4.27: Line rock observed in the main Omapyu pegmatite	86
Figure 4.28: Giant black tourmalines (Tur) exposed by diggings in the largest of the Omapyu pegmatites	87
Figure 4.29: Google Earth map with a 1:250 000 geological map overlay over a portion of the Valencia area	89
Figure 4.30: Type Ct pegmatite	92
Figure 5.1: Fluid Inclusions Laboratory at the School of Geosciences, University of the Witwatersrand	99
Figure 5.2: OH stretching band of deionised water	102
Figure 5.3: Aluminium sample envelope containing a double-polished quartz wafer	104
Figure 5.4: Selected CL images of double-polished wafers used for fluid inclusion microthermometry	106
Figure 5.5: Type 1 fluid inclusion from the Rubicon pegmatite	110
Figure 5.6: Type 2 fluid inclusion from the Rubicon pegmatite	111
Figure 5.7: Type 3 fluid inclusion from the Rubicon pegmatite	112
Figure 5.8: Type 5 fluid inclusion from the Rubicon pegmatite	114
Figure 5.9: Type 1 fluid inclusion from an Uis pegmatite	116
Figure 5.10: PIXE elemental map of an individual Type 1A fluid inclusion from an Uis Sn-bearing pegmatite	117
Figure 5.11: Type 5 fluid inclusion from an Uis pegmatite	118
Figure 5.12: Type 1 fluid inclusion from a Karlowa pegmatite	119
Figure 5.13: Type 5 fluid inclusion from a Karlowa pegmatite	121

Figure 5.14: Type 1 fluid inclusion from the Omapyu pegmatite	123
Figure 5.15: PIXE elemental map of an two Type 1 fluid inclusions from the Omapyu gem tourmaline-bearing pegmatite	124
Figure 5.16: Type 4 fluid inclusion from the Omapyu pegmatite	125
Figure 5.17: Type 5 fluid inclusion from the Omapyu pegmatite	126
Figure 5.18: Type 4 fluid inclusion from a Valencia pegmatite	128
Figure 5.19: Type 5 fluid inclusion from a Valencia pegmatite	129
Figure 5.20: Homogenisation temperatures of all measured fluid inclusions	131
Figure 5.21: Homogenisation temperatures of all measured fluid inclusions, showing the relationship between the homogenization temperatures of pseudosecondary and secondary inclusions	132
Figure 5.22: Schematic diagram of the evolution of fluids in Namibian pegmatites	135
Figure 6.1: Major element plots for mineralised pegmatites and their country rocks	163
Figure 6.2: Selected trace element plots for mineralised pegmatites and their country rocks.	165
Figure 6.3: Chondrite normalised trace element concentrations in mineralised pegmatites	167
Figure 6.4: Chondrite normalised REE data from mineralised pegmatite samples	168
Figure 6.5: Chondrite normalised trace element concentrations of country rocks into which mineralised pegmatites have intruded	172
Figure 6.6: Chondrite normalized REE data for country rock samples	173
Figure 6.7: Aluminium Saturation Indices (molar Al/Na + K + Ca) of mineralised pegmatites	176
Figure 6.8: Geochemical granite discrimination diagrams for selected trace and major elements	179
Figure 6.9: Y + Nb vs. Rb tectonic discrimination diagram for mineralised pegmatites	181
Figure 7.1: Histograms showing the distribution of $\delta^{18}\text{O}$ values measured in quartz, feldspar, whole-rock, and country rock samples from mineralised pegmatites and SLGs in Namibia	195

Figure 7.2: Plot of $\delta^{18}\text{O}$ values of quartz (qz) plotted against $\delta^{18}\text{O}$ values of feldspar (fs), whole-rock (wr), and country rock (cr) samples	197
Figure 7.3: Histogram showing the distribution of δD values measured in micas from mineralised pegmatites and SLGs in Namibia	198
Figure 7.4: Histogram showing the water content measured in muscovites and biotites from mineralised pegmatites and SLGs in Namibia	199
Figure 7.5: Whole-rock $\delta^{18}\text{O}$ values vs. Alumina Saturation Index (A.S.I.) of pegmatites and their country rocks	203
Figure 7.6: $\delta^{18}\text{O}$ ranges for known geological reservoirs, including I- and S-type granites, clastic sedimentary rocks, carbonates, low $\delta^{18}\text{O}$ granites and Pan-African granites from the Damara Belt	205
Figure 7.7: δD ranges for known geological reservoirs, including sea water, juvenile water, igneous and metamorphic rocks, low $\delta^{18}\text{O}$ granites, and meteoric water	207
Figure 7.8: Plot of $\delta^{18}\text{O}$ and δD values obtained from silicate minerals in mineralised pegmatites from Namibia	208
Figure 7.9: Plot of δD values vs. the water content of micas	210
Figure 8.1: Tectonic model for sources of melt generation and emplacement of post-collisional (505 - 490 Ma) pegmatites in the Damara Belt	224

LIST OF TABLES

Table 1.1: Summary of published and unpublished ages for granitoids from the CZ and NZ.	13
Table 2.1: Correlated lithostratigraphy of the Central Zone of the Damara Belt and Southern Kaoko Zone	21
Table 3.1: Pegmatite classification scheme of Černý and Ercit (2005) modified to illustrate the correlation between pegmatite classes and families	40
Table 5.1: Summary of fluid inclusion populations observed and measured, their homogenisation temperatures and geochemical characteristics.	107
Table 6.1: Whole-rock major element concentrations (in wt %) of LCT and NYF pegmatites.	145
Table 6.2: Whole-rock trace element concentrations (in ppm) of LCT and NYF pegmatites	146
Table 6.3: Whole-rock major element concentrations (in wt %) of country rock samples	150
Table 6.4: Whole-rock trace element concentrations (in wt %) of country rock samples	151
Table 6.5: Ti-in-quartz data for quartz samples from mineralised Namibian pegmatites	155
Table 7.1: $\delta^{18}\text{O}$ values for quartz, feldspar, and whole-rock LCT and NYF pegmatite samples, as well as adjacent country rocks	189
Table 7.2: δD values for muscovite and biotite samples from LCT and NYF pegmatite samples.	191
Table 8.1: Summary of geochemical and structural characteristics of mineralised Namibian pegmatites	214



"They'd take me aboard their beautiful ship, and show me the world as I'd love to see it"

- *Radiohead, Subterranean Homesick Alien*

CHAPTER 1

OVERVIEW OF THE GEOLOGY OF THE DAMARA BELT, NAMIBIA

1.1 Introduction

In Namibia, a large variety of mineral deposits occur, and are distributed throughout the country; these include volcanogenic-exhalative-hosted base metals (Killick, 1986), vein-hosted tin and tungsten (Diehl, 1992a), rare-metal pegmatite-hosted cassiterite, lithium, beryllium, niobium-tantalum and semi-precious stones (e.g. Roering and Gevers, 1964; Richards, 1986; Wagener, 1989; Diehl, 1992a, b & c; Keller *et al.*, 1999; Schneider and Seeger, 1992; Diehl, 1993; Singh, 2007, 2008, 2009), and pegmatite-hosted uranium (Berning; 1986; Basson and Greenway, 2004), to name a few (Miller, 1992a). A large proportion of Namibia's mineralisation is hosted within the meta-sedimentary sequences and magmatic intrusive bodies of the Damara Belt, which represent the depositional and orogenic phases of the Pan-African Damara Orogen (Miller, 1992a).

This thesis examines aspects of mineralisation in post-collisional pegmatites of the Damara Belt in an effort to relate the differences in mineralisation between them to the activity of fluids during their emplacement.

1.2 Regional Geology: The Damara Belt

The Damara Belt is the northeast-trending arm of the Neoproterozoic Damara Orogen, which extends north into Angola and the Democratic Republic of Congo, east through central Namibia, and into Botswana (Kennedy, 1964; Martin and Porada, 1977; Unrug, 1996; Miller, 2008; Miller *et al.*, 2009a). It is part of a network of similar orogenic belts in Africa which represent the sutures between continental fragments which amalgamated during the Pan-African Orogeny to form Gondwana, and which partially surround and

cross-cut the African continent today (Figure 1.1; Kennedy, 1964; Cahen *et al.*, 1984; Unrug, 1996; Miller, 2008; Frimmel, 2009). The Belt meets the north-northwest-trending sinistral transpressional Kaoko Belt and the north-trending sinistral transpressional Gariiep Belt (Figure 1.1) at a triple junction centred near Swakopmund, Namibia (Davies and Coward, 1982; Goscombe, 2003a; Goscombe, 2004; Miller, 2008; Frimmel, 2009). These Pan-African Belts developed as a result of successive phases of rifting, spreading, subduction, and continental collision between the Kalahari, Congo and Rio de la Plata Cratons which occurred between approximately 900 Ma and 460 Ma (Martin and Porada, 1977; Porada, 1979; Porada *et al.*, 1983; Stanistreet *et al.*, 1991; Prave, 1996; Goscombe, 2003a; Gray *et al.*, 2008; Miller, 2008; Frimmel, 2009; Miller *et al.*, 2009a; Frimmel *et al.*, 2011).

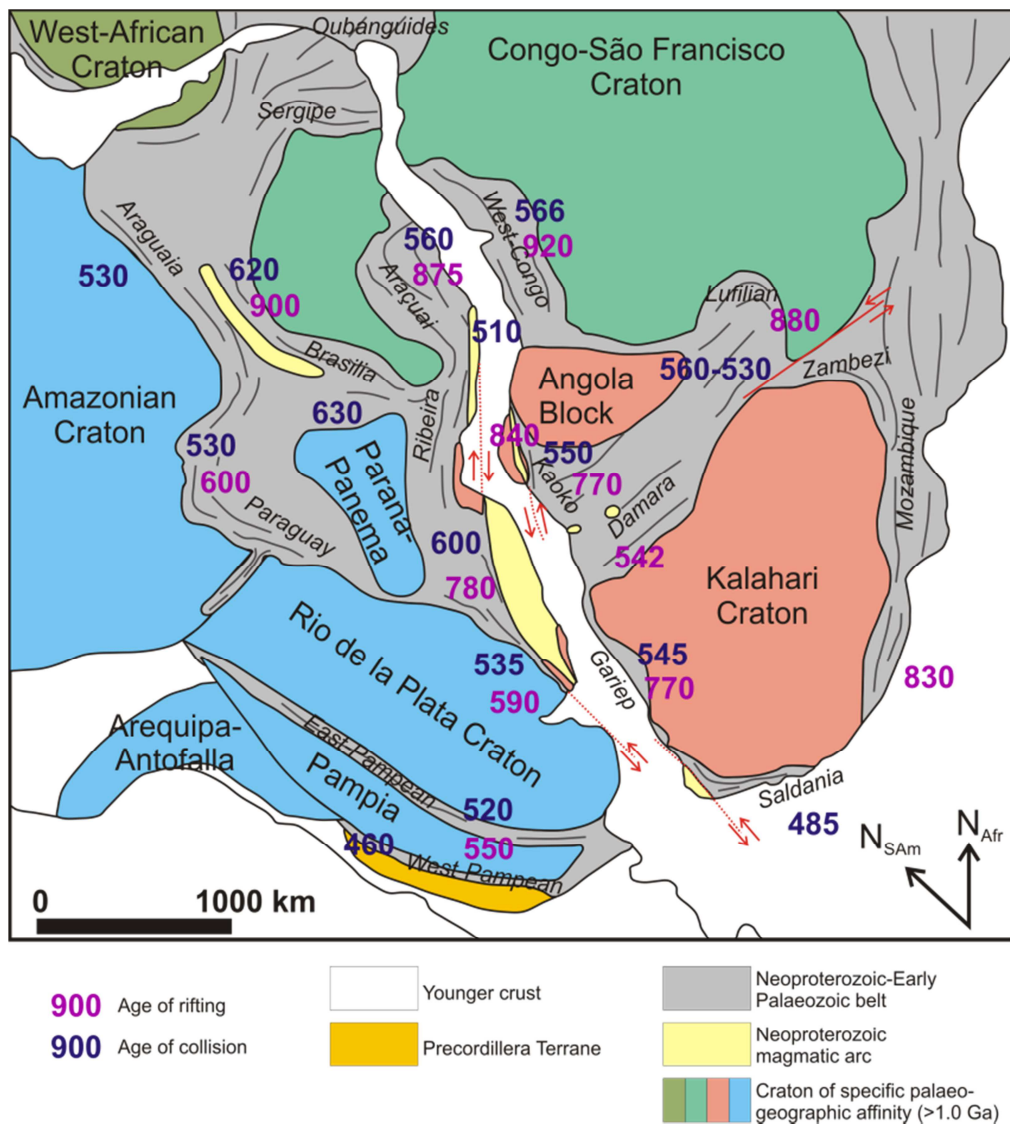


Figure 1.1: Neoproterozoic fold belts and magmatic arcs between various cratonic blocks of southwestern Gondwana with ages of rifting and continental collision indicated (modified after Gaucher *et al.*, 2009 and Frimmel *et al.*, 2011).

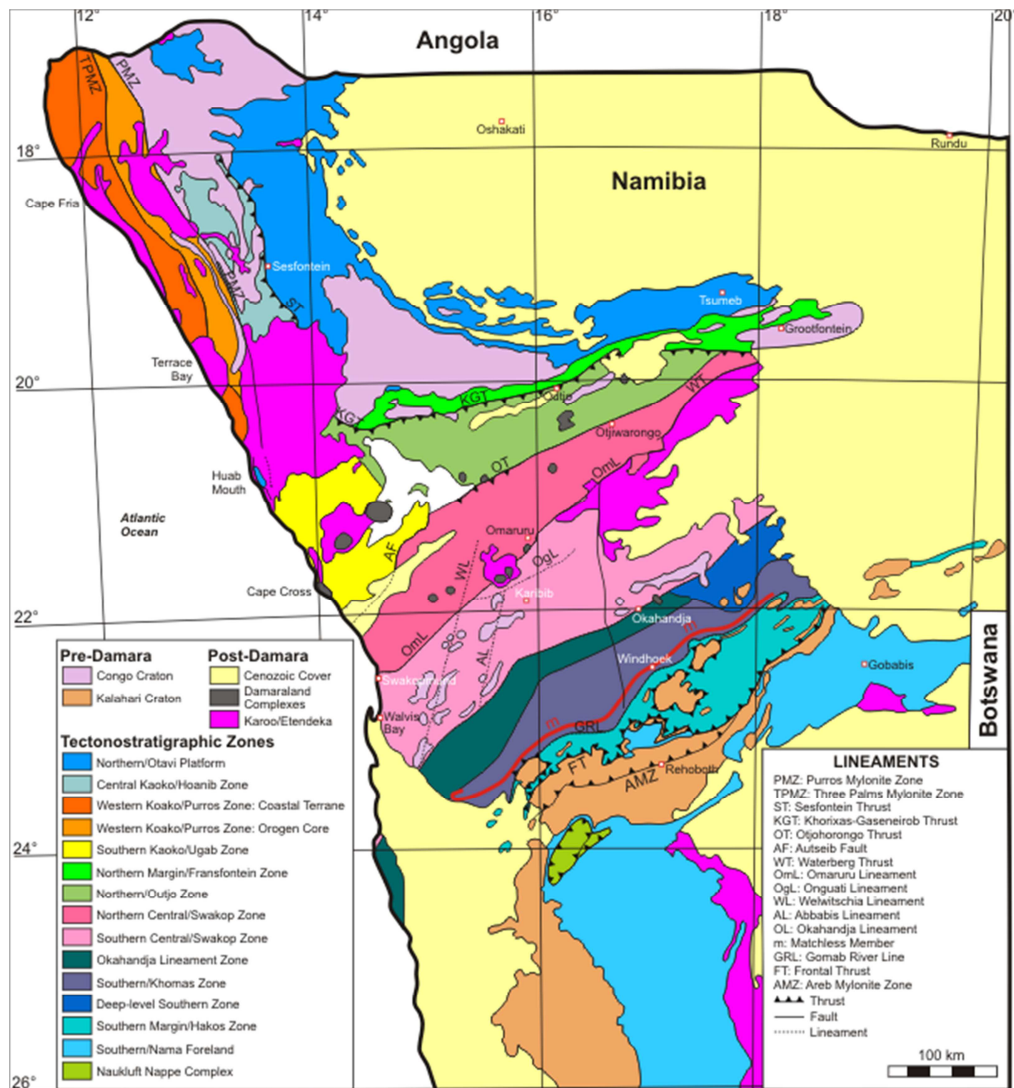


Figure 1.2: Tectonostratigraphic zones of the Damara Orogen (modified after Miller, 1983, 2008; Hoffmann, 1983, 1987, 1989; Goscombe *et al.*, 2003b).

Miller (1979, 1983, 2008) divided the Damara into tectono-stratigraphic zones (Figure 1.2) according to the variations in stratigraphic successions observed in them, as well as their tectono-metamorphic and magmatic histories. The boundaries of these zones are delineated by major linear structures which produce significant aeromagnetic anomalies, and which correspond with large-scale facies changes (see reviews in Miller, 2008; Frimmel *et al.*, 2011). The zones are, as they appear from north to south in the Damara

Belt, the Northern Platform (NP), Northern Margin Zone (NMZ), Northern Zone (NZ), Central Zone (CZ; further subdivided into the northern Central Zone, nCZ, and southern Central Zone, sCZ), Southern Zone (SZ), Southern Margin Zone (SMZ) and Southern Platform (SP) (Figure 1.2; Clifford, 1967; Hoffmann, 1987, 1989; Miller, 1983; Miller, 2008).

1.2.1 Stratigraphy and depositional history of the Damara Belt

The Damara Belt comprises meta-sedimentary lithologies of the Damara Supergroup, which were deposited unconformably upon the Pre-Damara Abbabis Complex gneisses (Miller, 2008). The Supergroup is composed of seven major stratigraphic units representing continental rift and shelf sediments. Figure 1.3 illustrates the stratigraphy of the Damara Supergroup and places the stratigraphic units in the context of the tectono-stratigraphic zones of Miller (1979, 1983, 2008)

The oldest stratigraphic unit is the Nosib Group (Figure 1.3), which is composed of feldspathic quartzites, subordinate metagreywackes, and conglomerates. Sedimentation was initiated by the breakup of the supercontinent Rodinia and the opening of the Adamaster Ocean, which began between approximately 800 and 900 Ma (Stanistreet *et al.*, 1991; Hoffman *et al.*, 1996; de Kock *et al.*, 2000; Gray *et al.* 2008; Miller, 2008). Although the exact timing of rifting has not been well constrained, Copperbelt-type chalcocite deposits in the shales at the top of the Nosib Group suggest similar ages in rift-sedimentation between the Katanga and Damara Supergroups (post-880 Ma; Frimmel and Miller, 2009), and rift-related magmatism in the Damara Belt has been dated at between 752 Ma and 759 Ma (Hoffman *et al.* 1996; Halverson *et al.* 2005; Jung *et al.* 2007; summarised in Frimmel and Miller 2009b). Rift sediments were deposited in two northeast-trending, parallel grabens, which later developed into the Outjo and Khomas Seas of the Damara Ocean (Porada, 1979; Stanistreet *et al.*, 1991; Miller, 1992b; Miller 2008; Frimmel *et al.*, 2011).

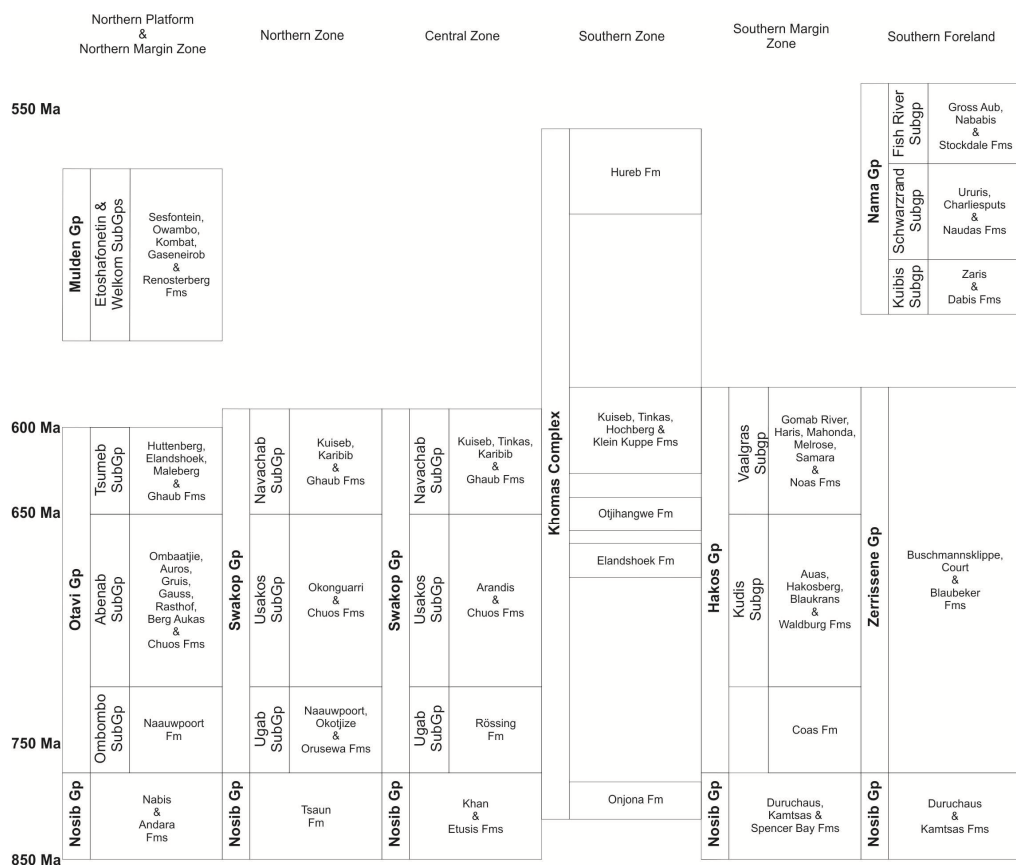


Figure 1.3: Stratigraphy and lithostratigraphic correlations across the Damara Belt with approximate deposition ages. Note the post-600 Ma ages of the Mulden and Nama Groups, which corresponds with the initiation of continental collision (thicknesses are not to scale; modified after SACS, 1980, De Kock, 2001 and Miller, 2008).

The deposition of the Nosib Group was followed by that of the laterally equivalent Groups (Figure 1.3) of the Otavi (carbonate-dominated), Swakop (lower carbonates and upper siliciclastics), Hakos (siliciclastics) and Witvlei (carbonates and siliciclastics) Groups. Glacio-marine sediments are preserved, intercalated banded-ironstone and quartzites, and manganese stones, in the Chuos Formation (Otavi and Swakop Groups); these have been dated at approximately 730 Ma and their formation has been attributed to the Neoproterozoic Sturtian “Snowball Earth” event (Killick, 1986; Bühn *et al.*, 1992; Stanistreet *et al.*, 1991; Miller, 1992b; Miller, 2008; Frimmel, 2009; Miller *et al.*, 2009a, b).

A second, younger glaciation occurred at 635.5 ± 1.2 Ma (Hoffmann *et al.*, 2004; Miller, 2008; Frimmel *et al.*, 2002; Miller *et al.*, 2009a, b) and this resulted in the deposition of the Ghaub Formation in the upper parts of the Swakop Group (Miller, 2008). Its formation, coupled with the deposition of siliciclastic successions and tholeiitic magmatic activity, was followed by large-scale subsidence of the entire region between the Northern and Southern Zones, and the subsequent accumulation of a thick succession of turbiditic greywackes (Kuseb Formation) in both the Outjo and Khomas Seas (Miller, 2008). These greywackes reach up to 10 km thickness in the Northern Zone and mark the end of the spreading phase (Frimmel *et al.*, 2011).

While there is no evidence of progressive deepening and subsequent continental rupture in the Outjo Sea (northern graben), evidence of these processes has been found in the rocks of the Khomas Sea (southern graben) in the form of Besshi-Type Matchless Amphibolite Member, a 350 km-long, narrow, linear belt of metabasic rocks with a MORB or plume-type geochemical affinity and Cu-Fe sulphide deposits (see Figure 1.2; Barnes and Sawyer, 1980; Breitkopf and Maiden, 1986; Killick, 2000; Miller *et al.*, 2009a, b; Frimmel *et al.*, 2011). This active mid-ocean ridge occurs at the base of, and was largely covered by, the greywackes of the Kuseb Formation, but the presence of pillow lavas and cupreous pyrite deposits in the Matchless Member indicate that submarine volcanism and volcanogenic exhalative processes were at work at the time (Barnes and Sawyer, 1980; Breitkopf and Maiden, 1986; Killick, 2000; Miller *et al.*, 2009a, b; Frimmel *et al.*, 2011).

A reversal of plate motion initiated the subduction of the Kalahari Craton beneath the Congo Craton (Miller, 2008; Miller *et al.*, 2009a, b; Frimmel *et al.*, 2011). Although the exact timing of this event remains unclear, it has been somewhat constrained by the dates of deposition of the Hartelust Rhyolite Member (Gomab River Formation, Hakos Group; Figure 1.3) 609 Ma (Nagel, 1999) and of the formation of the oldest syn-tectonic garnets formed during the first stages of transpressive continental collision in the Kaoko Belt (595 Ma; Goscombe *et al.*, 2005). With the uplift and erosion of the active continental margin, the arc-trench molasse successions (shales, greywackes, sandstones and carbonates) of

the Mulden Group (580 – 541 Ma; Gray *et al.*, 2006), and the foreland orogenic flysch and molasse successions (sandstones, shales and carbonates) of the Nama Group (Figure 1.3) were deposited into the closing Khomas Sea (Stanistreet *et al.*, 1991; Grotzinger and Miller, 2008; Miller, 2008; Germs *et al.*, 2009; Frimmel *et al.*, 2011).

1.2.2 Structural evolution of the Damara Belt

The closing of the Khomas Sea and eventual continent-continent collision, represented by the Kaoko, Damara and Gariep Belts, between 560 Ma and 542 Ma (Stanistreet *et al.*, 1991; Prave, 1996; Miller, 2008) was accompanied by the polyphase deformation of the psammitic and pelitic gneisses, marbles, and calc-silicate lithologies of the Damara sequence (Smith, 1965; Longridge *et al.*, 2008; Miller, 2008; Frimmel *et al.*, 2011). The SZ ocean floor and adjacent Kalahari Craton in the south were subducted during their northeasterly transpressive collision with the Congo Craton, thus the most intensely deformed zones of the Damara Belt are the southern Central Zone, SZ, and SMZ (Will *et al.*, 2009). Various authors have identified anything from two (Jacob *et al.*, 1983) to six (Sawyer, 1981) deformation events, however it is generally accepted that there were two major events, and that later events were only locally and weakly developed (Smith, 1965; Nash, 1971; Coward, 1983). These have been termed D₂ and D₃ (in acknowledgment of an early regional fabric-forming event, D₁, which has been identified by some workers e.g. Smith, 1965; Nash, 1971).

D₂ deformation is characterised by tight to isoclinal, gently north-dipping to recumbent folds, with associated S-verging thrusts and shear zones, as well as boudinage of stratigraphic layers and the formation of a penetrative fabric. This deformation event resulted from continental collision between the Congo and Kalahari Cratons and has been dated at ± 555 Ma (Smith, 1965; Nash, 1971, Blaine, 1977; Coward, 1983; Miller, 2008; Will *et al.*, 2009; Frimmel *et al.*, 2011).

D₃ represents the final stages of continent closure. It formed upright folds with NE-trending fold axes (Smith, 1965; Nash, 1971; Blaine, 1977; Barnes, 1981; Coward, 1981; Jacob *et al.*, 1983). This event is responsible for the regional northeasterly structural trend observed in satellite and aerial photography of the Damara Belt, and the tightening and refolding of earlier structures to form northeast-trending, elongate domal structures in the southern Central Zone (Smith, 1965; Nash, 1971; Oliver, 1995; Kisters, *et al.*, 2004; Kinnaird and Nex, 2007; Will *et al.*, 2009; Frimmel *et al.*, 2011). The domes are typically 2 - 5 km long, but may extend several tens of kilometres along strike (Smith, 1965), and their cores are predominantly, although not exclusively (e.g. Rössing Dome), composed of basement material from the Abbabis Complex (Smith, 1965; Kisters *et al.*, 2004; Kinnaird and Nex, 2007).

D₃ deformation is typically focused at the interface between basement and supracrustal rocks, leading Oliver (1995) to suggest that the interface marks a mid-crustal extensional detachment, and that the southern Central Zone represents a deep metamorphic core complex. The timing of D₃ deformation, continental closure, and doming in the southern Central Zone has been constrained at ± 542 Ma by the dating of syn-D₃ granites (Marlow, 1983; Tack *et al.*, 2002). Its importance is evident, as it has controlled the emplacement and formation of post-orogenic magmatism and mineralisation in the Damara Belt (e.g. Corner, 1982; Diehl, 1993; Kisters *et al.*, 2004; Kisters, 2005; Kinnaird and Nex, 2007).

1.2.3 Metamorphism in the Damara Belt

The metamorphic grade in the Damara Belt increases inward from the Northern Platform and Southern Margin Zone to the Central Zone, as well as from the interior of Namibia towards the coast (Figure 1.4; Kinnaird and Nex, 2007; Will *et al.*, 2009). Lithologies of the Southern Zone and Southern Margin Zone are dominated by a high pressure, low temperature (~ 600 °C at ~ 10 kbar; Kasch, 1983) kyanite facies mineral assemblages, while those of the Central Zone contain low pressure, high temperature (~ 750 °C at ~ 5.0-6.0 kbar; Kasch 1983; Jung *et al.*, 2000) cordierite-sillimanite facies minerals, and are

associated with syn- to post-tectonic intrusive bodies, predominantly of granitic composition, indicating that the Damara Belt is a paired metamorphic belt (Goscombe *et al.*, 2004; Miller, 2008).

Debate exists over whether the Damara Orogen experienced one or two metamorphic episodes (Nex *et al.*, 2001a). Numerous authors (e.g. Nash, 1971; Barnes, 1981; Horstmann *et al.*, 1990; Jung and Mezger, 2003; Gray *et al.*, 2008) are in favour of the latter, and have suggested that an initial high pressure metamorphic event, M_1 , (600 °C at 6- 7 kbar), occurred at 530 and 500 Ma, coinciding with the thrusting of the Congo Craton onto the Kalahari Craton. This was followed by the overprinting of the D_3 deformation event by a higher temperature granulite facies event, M_2 (700 °C at 4 kbar) caused by extensive and voluminous magmatism.

Longridge (2012), however, found no evidence for two separate events, and suggested instead that the Damara Belt experienced a single metamorphic event, following a clockwise P-T path, which reached peak temperatures of ~ 800 °C at 4.5 - 5.0 kbar, and which experienced slight decompression at the thermal peak. Contradictory age data were produced from the same study, however, therefore it was concluded that even given the absence of petrographic evidence of M_1 metamorphism, its occurrence could not be unequivocally discounted.

Metamorphism in the study areas will be discussed in greater detail in Chapter 2.

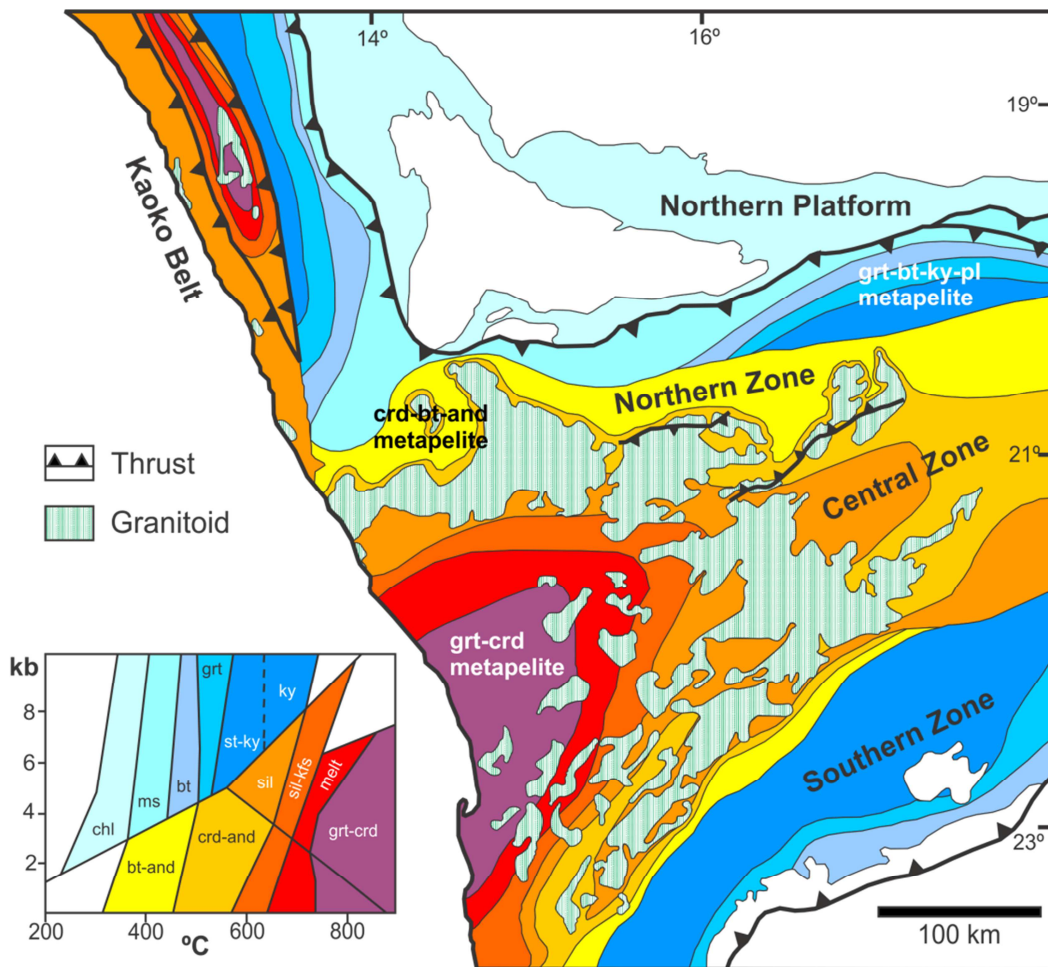


Figure 1.4: Simplified representation of peak metamorphism in the Damara Orogeny (modified after Goscombe *et al.*, 2004).

1.2.4 Magmatism in the Damara Belt

The intrusive suite of the Damara Belt comprises in excess of 200 plutons, plugs, stocks, and syn- to post-tectonic granites, as well as thousands of granite dykes and pegmatites, and it covers an area of approximately 74 000 km² (Figure 1.4; Miller, 2008; Miller and Frimmel, 2009). These plutonic rocks may be characterised by their composition and shape in relation to the timing of their emplacement.

The majority of granitic intrusions occur within the Central Zone (Miller and Frimmel, 2009), and their emplacements span the entire tectonic history of the Damara Belt (Wagener, 1989). Of these voluminous granitoid intrusions, 96% are granitic, with the remaining 4 % comprising rocks of minor calc-alkaline to granodioritic composition (Miller, 1983; Miller and Frimmel, 2009), and their emplacement is largely influenced by the northeasterly, D₃-related structural trend common to the entire Damara Belt (Roering and Gevers, 1964; Wagener, 1989; Richards, 1986; Kisters *et al.*, 2004; Kisters, 2005; Miller, 2008).

The majority of the intrusions are syn- to post-tectonic, and occur in a region overlying the shallow portion of the Damara subduction zone (Miller and Frimmel, 2009). In the southern Central Zone, where the highest metamorphic grade is observed, magmatism of different compositions occurred at different times in the development of the Damara Belt; these magmatic suites, from oldest to youngest, are summarised in Table 1.1 and briefly described in Table 1.1.

Post-Damaran anorogenic alkaline intrusions, such as the Brandberg and Erongo Complexes (190 – 120 Ma), also occur within the Damara Belt along an extension of oceanic transform faults which trend in a northeasterly direction (Marsh, 1973; Wagener, 1989). Magmatism in the Damara Belt is discussed more comprehensively in Section 1.3.2 of this chapter.

Table 1.1: Summary of published and unpublished ages for granitoids from the CZ and NZ.

Rock	Age (Ma)	Method	Reference
<i>Goas Suite and related rocks</i>			
Goas granite	580 ± 30	U-Pb discordia	Allsop <i>et al.</i> (1983)
Oamikaub diorite	566 ± 10	U-Pb single zircon	Milani (pers. comm. 2013)
Mon Repos quartz diorite	564 ± 5	U-Pb single zircon	Jacob <i>et al.</i> (2000)
Palmental diorite	564 ± 55	Rb-Sr whole-rock	McDermott (1986)
Palmental diorite	557 ± 0	U-Pb zircon	Milani (pers. comm. 2013)
Mon Repos diorite	558 ± 8	U-Pb zircon	Milani (pers. comm. 2013)
Okangava diorite	558 ± 8	U-Pb single zircon	De Kock <i>et al.</i> (2000)
Rotekuppe granite	543 ± 5	U-Pb single zircon	Jacob <i>et al.</i> (2000)
Okangava diorite	539 ± 10	U-Pb titanite	Jung <i>et al.</i> (2002)
Goas granite	535 ± 2	U-Pb discordia	Allsop <i>et al.</i> (1983)
<i>Salem Granites</i>			
Salem-type granite	601 ± 79	Rb-Sr whole-rock	Marlow (1983)
Salem-type granite	563 ± 63	Rb-Sr whole-rock	Hawkeworth <i>et al.</i> (1983)
Salem-type granite	554 ± 17	Rb-Sr whole-rock	Kröner (1982)
Sorris Sorris granite	542 ± 19	U-Pb discordia	Milani (pers. comm. 2013)
Omangambo granite	527 ± 7	U-Pb zircon	Milani (pers. comm. 2013)
<i>Red Granites</i>			
Red granite	539 ± 17	U-Pb zircon	Longridge (2012)
Red granite	536 ± 7.2	Concordant monazite	Longridge (2012)
Goanikontes red granite	534 ± 7	U-Pb discordia	Briqueu <i>et al.</i> (1980)
<i>Leucogranites and grey granites</i>			
Stinkbank leucogranite	549 ± 11	U-Pb zircon	Johnson <i>et al.</i> (2006)
Ida Dome grey granite	542 ± 6	U-Pb single zircon	Tack <i>et al.</i> (2002)
Baukwab leucogranite	525 ± 1	Pb-Pb zircon evaporation	Jung <i>et al.</i> (1998)

Table 1.1: continued

Leucogranites and grey granites cont.			
Oetmoed granite	526 ± 16	U-Pb monazite, titanite	Jung <i>et al.</i> (2000)
Grey granite	520 ± 4.2	U-Pb zircon	Longridge (2012)
Garnet-bearing leucogranite	520 ± 4.6	U-Pb zircon	Longridge (2012)
Pegmatites and mineralised veins			
Uraniferous leucogranite	514 ± 22	Discordant monazite	Longridge (2012)
Brandberg West Sn veins	509 ± 11	Rb-Sr	Jacob & Kruger (1994)
Goanikontes uraniferous alaskite	508 ± 2	Concordant monazite	Briqueu <i>et al.</i> (1980)
Rubicon pegmatite	505 ± 2.6	U-Pb columbite	Melcher <i>et al.</i> (2013)
Navachab Au veins	500 ± 10	U-Pb single titanite	Jacob <i>et al.</i> (2000)
Rubicon pegmatite	496 ± 30	Rb-Sr mineral age	Haack and Gohn (1988)
Uis pegmatite, K5 mine pit	496 ± 30	Rb-Sr whole-rock	Haack and Gohn (1988)
Navachab Au veins	494 ± 8	U-Pb single titanite	Jacob <i>et al.</i> (2000)
Sandamap Noord pegmatite	473 ± 23	Rb-Sr whole-rock	Steven <i>et al.</i> (1993)
Sandamap tin pegmatite	468 ± 14	Rb-Sr whole-rock	Steven <i>et al.</i> (1993)

1.2.4.1 Goas intrusive suite

The Goas Intrusive Suite is located in the area south of Karibib (see Figure 1.2) and comprises metagabbroic to dioritic rocks, which occur as a number of individual (the Okatuwo, Mon Repos, Oamikaub, Okongava, and Palmental) plutons (Miller, 2008). They display evidence of syn-tectonic deformation, and contain xenoliths of older meta-sedimentary lithologies. The Goas Intrusive Suite is the oldest magmatic suite, suggested to be the only record of subduction-related magmatism in the Damara Belt, with recent studies giving a range of ages from 558 - 573 Ma (Milani, pers. comm., 2013). The granodioritic plutons are thought to represent the active margin calc-alkaline component of the suite, while the mafic and ultramafic lithologies have been suggested to have formed in a volcanic arc setting (De Kock, 1991; Miller, 2008).

1.2.4.2 Salem granites

The Salem Granites are the most abundant and extensive of the Damaran intrusive rocks; they are generally monzogranitic in composition, however the term "Salem Granite" actually includes not only granites, but also granodiorites and adamellites (Blaxland *et al.*, 1979; Miller, 2008). The Suite has been subdivided into a non-porphyrific gneissic granite, a porphyritic biotite granite, and a leucogranite (Jacob, 1974), and of these, the biotite granites are the most abundant (Miller, 2008). They are thought to be the result of extensive melting in the lower crust during a period spanning from 511 - 539 Ma (Longridge, 2012; Milani, pers. comm., 2013). Longridge (2012) invoked slab break-off and subsequent asthenospheric upwelling, resulting from the collision between the Kalahari and Congo Cratons, as a heat source for early magmatism in the Damara Belt.

1.2.4.3 Red granites

Similar to the name, Salem Granite, the term "Red Granite" encompasses a variety of granite types, including red gneissic granites, red homogeneous granites, and buff leucocratic granites, which earlier workers considered to be coeval and consanguineous (e.g. Sawyer, 1976; 1981). The red gneissic granites occur in the southwestern parts of the Damara Belt, suggesting their emplacement at lower

stratigraphic levels, while the red homogeneous granites are pervasive throughout the Central Zone (Smith, 1965; Brandt, 1987). Some workers (see reviews in Miller, 2008) have suggested that the Red Granites are the oldest of the Damaran intrusive suites, however field relationships observed by Sawyer (1976) and a U-Pb zircon/monazite age of 534 ± 7 Ma obtained by Briquieu *et al.*, (1980) indicate that the Red Granites are younger than both the Goas and Salem intrusives. Longridge (2012) showed that they are the products of melting of a 1 Ga year-old metasedimentary protolith.

1.2.4.4 Homogeneous syn-tectonic granites

Homogeneous grey granites occur predominantly in the northern Central Zone. They are monzogranitic in composition. They have been dated at 517 Ma (Briquieu *et al.*, 1980; Nex *et al.*; 2001b) and show evidence of syn-D₂ emplacement, and as well as D₂ and D₃ deformation (Miller, 2008). Longridge (2012) obtained ages for grey granites ranging from 519 - 520 Ma, indicating that they are younger than the Red Granites of the Damara Belt.

1.2.4.5 Post-tectonic leucogranites

A number of small leucogranitic dykes and plugs (the Baukwab, Otjua, Kubas, Stinkbank and Elba granites), as well as two major plutons (Donkerhuk and Bloedkoppie granites) occurs throughout the Central Zone (see reviews in Miller, 2008). They contain abundant garnet and muscovite, and have been suggested to have formed as a result of the anatexis of metapelitic material, although some have suggested that they represent the residua of the Salem granite melts (Marlow, 1983).

1.2.4.6 Post-tectonic pegmatites

A vast number of pegmatites occur within the Central Zone and Northern Zone, as well as the Southern Kaoko Zone, where metamorphic conditions reached their peak during the Damara Orogeny. They include large, internally-zoned Li- and Be-rich bodies and unzoned to weakly-zoned Sn-rich bodies of the LCT family (Li-Cs-Ta-bearing, see Chapter 2; Černý, 1991a; Černý and Ercit, 2005) and rare-metal class, weakly- to strongly-zoned LCT miarolitic gem-bearing pegmatites, and unzoned NYF

(Nb-Y-F-bearing; Černý, 1991a; Černý and Ercit, 2005) and abyssal class characteristics (e.g. Roering, 1963; Roering and Gevers, 1964; Diehl, 1992a, b, c, 1993; Schneider and Seeger, 1992; Nex and Kinnaird, 1995; Nex *et al.*, 2001a; Basson and Greenway, 2004; Kinnaird and Nex, 2007; for details on the classification of pegmatites see Chapter 2). Mineralisation varies in the pegmatites according to their geographic locations, and thus stratigraphic levels, within the Belt. They have been dated by various workers, who obtained ages ranging from 509 - 492 Ma (Briqueu *et al.*, 1980; Steven; 1993; Melcher *et al.*, 2013; Longridge, 2012) More detail on the classification of pegmatites and the various types present in the Central Zone and Northern Zone/Southern Kaoko Zone will be presented in Chapter 2 and 3.

1.3. Project aims

In terms of mineralisation, the pegmatites of the Damara Belt appear to display a zonation from LCT pegmatites in the Southern Kaoko Zone (Uis area), northern Central Zone and the northwestern and central parts of the southern Central Zone (Karibib and Usakos areas) to uranium-bearing NYF pegmatites in the southwestern parts of the southern Central Zone (Swakopmund area). Although mineralisation varies amongst these pegmatites, they share a common late-syn-tectonic to post-tectonic age of emplacement, ranging between ~ 510 Ma and ~ 490 Ma (Kröner and Hawkesworth, 1977; Briqueu *et al.*, 1980; Haack and Gohn, 1988; Longridge, 2012).

The aim of this research was thus to characterise the fluids present as fluid inclusions in quartz from LCT and NYF pegmatites in an attempt to investigate what role they played during the crystallisation and mineralisation of, the pegmatites. In conjunction with this, oxygen- and hydrogen isotopes, as well as major and trace elements, were analysed in both the pegmatites and their host rocks in order better to understand the relationship between the two. Furthermore, the data obtained from this study were combined with previously published age data for the pegmatites, in order to determine the timing of pegmatite emplacement relative to the regional evolution of the Damara Belt.

The pegmatites of the Damara Belt, as well as those found in other Pan-African and older mobile belts (e.g. Hugo, 1969; Pezzotta, 1999; Dewaele *et al.*, 2011) also provide excellent examples of the pitfalls associated with pegmatite classification, which will be discussed in greater detail in Chapter 2. In so doing, they may provide insight into plausible models for the derivation of pegmatitic melts and their emplacement during, or towards the end of, large-scale collisional events.

In order to understand the processes involved in the regional evolution of the Damaran pegmatites, it is necessary to understand their emplacement in terms of a regional context, as well as the processes responsible for the internal evolution of pegmatites. The following chapter thus provides a synthesis of the regional geology of the study areas, while Chapter 3 presents current research pertaining to the classification and evolution of pegmatites.

CHAPTER 2

REGIONAL GEOLOGY OF THE STUDY AREAS

2.1 Introduction

The mineralised pegmatites under investigation in this study occur in the southern Central Zone of the Damara Belt and the junction between the Northern Zone and the Southern Kaoko Zone of the coeval Kaoko Belt (also referred to as the Ugab Zone and western Northern Zone by Goscombe *et al.*, 2004). They are located in three areas situated near the towns of Karibib/Usakos, Uis, and Swakopmund (Figure 2.1).

These pegmatites have been emplaced into the metasedimentary lithologies of the Damara Supergroup, as well as earlier Pan-African intrusive lithologies. The stratigraphy of the Damara Belt has been extensively documented by numerous workers (e.g. Nash, 1971; De Kock, 2001; Kisters *et al.*, 2004; Paciullo *et al.*, 2007; see reviews in Miller, 2008) who have constrained deformations, metamorphism and magmatism in various parts of the Damara Belt, and shown that in these regions the stratigraphy is spatially very variable.

The geology in the Central Zone and Northern Zone/Southern Kaoko Zone comprises pre-Damara basement gneisses of the Abbabis Metamorphic Complex, has been overlain unconformably by (meta)sedimentary rocks of the Damara Belt. These metasediments have been subdivided into the Nosib and Swakop Groups in the Damara Belt, and the Zerrissene Group in the Kaoko Belt, which were deposited during a period of extension, rifting between, and subsequent collision of the Congo and Kalahari Cratons (Miller, 2008). The lithologies that comprise the Damara Sequence in the Central and Southern Kaoko Zones are extremely variable, and include quartzites, marbles, metapelites, diamictites and diopside-plagioclase gneisses.

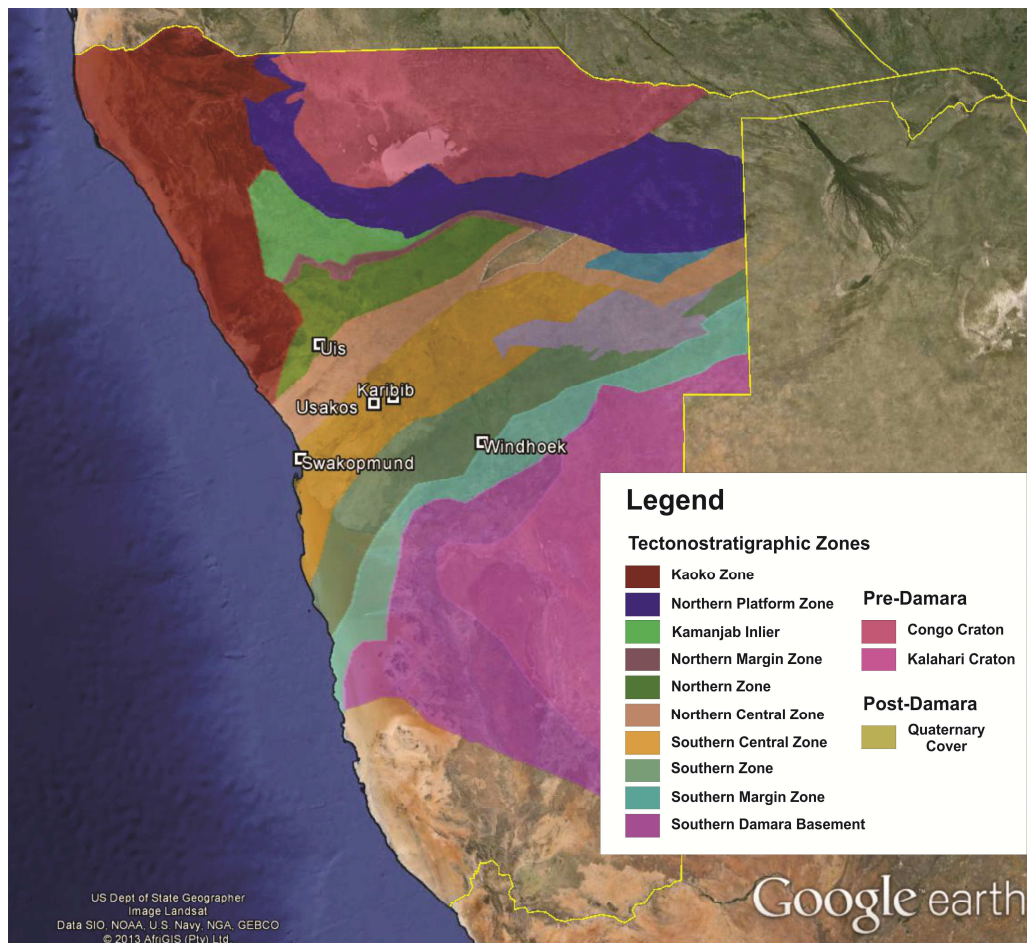


Figure 2.1: Google Earth image showing the locations of towns near the sample localities in relation to the tectonostratigraphic zones of the Damara Belt (Google, 2012).

Table 2.1: Correlated lithostratigraphy of the Central Zone of the Damara Belt and Southern Kaoko Zone (modified after Nash, 1971; Badenhorst, 1992; Nex, 1997; De Kock, 2001; Hofmann *et al.*, 2004; Paciullo *et al.*, 2007; Miller, 2008; Owen, 2011).

	Central Zone				Southern Kaoko Zone			
	Group	Subgroup	Formation	Lithology	Group	Formation	Lithology	
Damara Supergroup	Swakop	Navachab	Kuiseb	Quartz-biotite-cordierite schist and turbiditic psammites	Zerrissene	Amis River	Interbedded sandstone-shale couplets, laterally continuous sandstones and thinly-bedded shales	
			Karibib	Grey and white calcitic and dolomitic marbles with intermittent calc-silicate felses and marble breccias		Gemsbok River	Calcarenites, schists, blue marbles locally interbedded with breccias, calcarenites and shales	
			Ghaub	<i>Daheim Member:</i> Amphibolites locally within a carbonate matrix		Ghaub	Interbedded sandstone-shale couplets, calcarenite and blue marble, greywakes with glaciogenic clasts	
		<i>Kachab Member:</i> Glaciomarine pelites and dropstone units						
		Usakos	Arandis	<i>Oberwasser Member:</i> Grey quartz-biotite-tremolite-cordierite schist and calc-silicate felses		Zerrissene	Brak River	Interbedded sandstone-shale couplets, calcarenite and blue marble, greywakes
				<i>Okawayo Member:</i> Blue-grey dolomitic and calcitic marbles and calc-silicate felses, intercalated calc-silicates			Brandberg West	Interbedded white, yellow to brown calcarenite with siliceous lamination, shales and light blue marbles
				<i>Spes Bona Member:</i> Quartz-biotite schists and meta-psammites			Zebraapütz	Distal greywakes and distal, fine-grained, thinly laminated shales
		Ugab	Rössing	Interbedded marbles, calc-silicates and siliciclastics		Zerrissene	No exposure	
		Nosib		Khan		Greyish green, clino-pyroxene-hornblende quartz arenites	Zerrissene	No exposure
Etusis	Pinkish-brown to pale grey quartz arenites, with rare arkose and orthoquartzite layers							
Abbabis Complex			Pink and grey quartzo-feldspathic augen gneisses, schists, amphibolites and pegmatites					

2.2 Regional Stratigraphy

2.2.1 Pre-Damaran Geology: Abbabis Complex

The Abbabis Complex, or Abbabis Metamorphic Complex, comprises feldspathic augen gneisses, schists, amphibolites and pegmatites, which occur in three units, the Tsawisis and Noab Formations, and the Narubis Granitoid Complex (Brandt, 1987). Although these three units have been identified, particularly the Tsawisis and Noab Formations have not been extensively described, and the work of Brandt (1987) provides the most detailed information on them.

The Tsawisis Formation comprises feldspathic quartzite, biotite and biotite-sillimanite schists, locally containing muscovite, garnet and tourmaline, as well as minor amphibole schists, marbles and calc-silicates (Brandt, 1987).

The Noab Formation is composed of similar lithologies, including a lower biotite schist containing subordinate calc-silicates, a middle quartzite, marble and calc-silicate member, and an upper meta-volcanic member (Brandt, 1987).

The Narubis Granitoid Complex comprises a number of granitic intrusions which have been deformed into the characteristic augen gneisses of the Abbabis Complex. The augen gneisses are cross-cut by numerous amphibolite dykes, which, due to the fact that they generally do not cross cut any Damaran metasediments, have been interpreted as representing the youngest event in the formation of the Abbabis Complex (Steven, 1994; Barnes, 1981; Longridge, 2012). Owing to this relationship, the presence of amphibolites has been used a parameter for distinguishing pre-Damaran from Damaran units (Barnes, 1981), however they have been observed cross-cutting Damaran metasediments at Rössing Mine (Nex, pers. comm., 2009).

Numerous studies have indicated an age of *ca.* 2 Ga for the Abbabis Complex gneisses as well as inherited cores of Damaran magmatic zircons (e.g. Jacob *et al.*, 2000; De Kock *et al.*, 2000; Tack *et al.*, 2002; Longridge, 2012). This is older than ages obtained by the earlier work of Kröner *et al.* (1991), which range between 1.10 and 1.04 Ga. It

has been suggested that the discrepancy between these ages may either be attributed to a 1 Ga Kibaran overprint on older 2 Ga Eburnian basement material from the Congo Craton (Rumvegeri, 1991; Rainaud *et al.*, 2005; Longridge, 2012), or to the presence of an extension of the younger Rehoboth terrane of the Kalahari Craton in the area (Kröner *et al.*, 1991).

Deformation in the Abbabis Complex has not been documented or described, although Smith (1965) and Blaine (1977) noted that the fabrics in the pre-Damaran basement material and those in the overlying Damaran metasediments are oblique to each other. In addition to this, Poli (1997) proposed that the metamorphic grade of the Abbabis Complex is higher than that observed in the overlying Damaran cover, however, due to the fact that the fabrics in the basement material have been strongly overprinted by those of Damaran age, the suggestion of Poli (1997) has not been explored by other workers, thus the deformation history of the Abbabis Complex remains largely unexplored.

2.2.2 The Damara Supergroup: Nosib Group

The Nosib Group overlies the Abbabis Complex unconformably and has been subdivided into two formations, the older Etusis Formation, and the younger Khan Formation (Table 2.1 Smith, 1965; Nash, 1971; Lehtonen *et al.*, 1995; 1996). Both the Etusis and Khan Formations have given model ages of *ca.* 2 Ga, an age identical to that of their source material, the underlying Abbabis Complex (Hawkesworth and Marlow, 1983; Miller, 2008), however ages obtained from volcanic units of the Nosib Group indicate that sedimentation began at *ca.* 750 Ma (Hoffman *et al.*, 1996; De Kock *et al.* (2000).

2.2.2.1 Etusis Formation

The Etusis Formation comprises quartzites, conglomerates and quartzo-feldspathic gneisses (arkoses), which were originally suggested by De Kock and Botha (1988) to have been deposited in an alluvial fan environment, but which Henry (1992) later proposed were deposited in an extensive sandy, braided fluvial system. Many of the

outcrops of the Etusis Formation are wedge-shaped, suggesting that deposition occurred in half grabens (Miller, 2008).

The quartzites show cross-bedding enhanced by the presence of ilmenite and magnetite on the foresets of the sedimentary structures, a distinctive characteristic of these particular units in the Etusis Formation (Sawyer, 1981). Conglomerates are more abundant in the lower parts of the Etusis succession, and the remaining part of it is composed of alkali feldspar-rich arkoses, indicating that a large proportion of the Etusis Formation is in fact composed of recrystallised peralkaline felsic volcanic rocks (Miller, 1983; 2008).

The Etusis Formation is laterally variable, apparently not present in some areas while reaching thicknesses of in excess of 3000 m in others, suggesting that there was differential subsidence during the deposition of the Formation in an extensional environment (Henry, 1992; Miller, 2008).

2.2.2.2 Khan Formation

The Khan Formation is composed of very fine-grained to medium-grained, thinly- to very thickly-bedded and massive clinopyroxene and hornblende-bearing gneisses and calc-silicates (Sawyer, 1981; Miller, 2008). Cyclical sedimentary units have been identified in the Khan Formation, and sedimentary structures formed by current action suggest that the rocks were deposited in a low energy, distal fluvial system characterised by floodplains and ephemeral lakes (Henry, 1992).

The metasedimentary lithologies of the Khan Formation show evidence of extensive metamorphism and metasomatism/hydrothermal alteration (Henry, 1992; Miller, 2008). Locally *in situ* migmatites have resulted from partial melting of Khan Formation rocks, and in some areas e.g. Khan Mine, local anatexis has produced concordant copper-bearing pegmatites which have been emplaced in boudin-like constrictions (Miller, 2008).

2.2.3 The Damara Supergroup: Swakop Group

The Swakop Group overlies the older Nosib group conformably. It has been subdivided into the Ugab, Usakos, and Navachab Subgroups (Table 2.1; SACS, 1980). De Kock (2001) revised the stratigraphy of the Swakop Group in the region of the current study, subdividing the Swakop Group into the Adler, Quelle, Okomis, Omusema, Karibib, Tinkas, and Fahlwater Formations, however this reappraisal has not been widely cited, and the more commonly recognised stratigraphic are described below.

2.2.3.1 Rössing Formation (Ugab Subgroup)

The Rössing Formation (Table 2.1) is the lowermost stratigraphic unit of the Swakop Group, and its base marks the first appearance of carbonate in the Damara Supergroup (SACS, 1980). It is composed of a variety of different rock types, including quartz-biotite and quartz-feldspar gneisses, quartzites, quartz-feldspar-biotite-calc-silicates, quartz-biotite and pelitic schists, and marbles (Miller, 2008), which were originally deposited in a shallow marine environment such as an epicontinental marine platform (Henry, 1992). Stanistreet *et al.* (1991) suggested that during the deposition of the Swakop Group, subsidence caused a marine transgression and the subsequent deposition of the Rössing Formation carbonates and siliciclastic rocks. This Formation shows high variability laterally, and its upper limit is bounded by an unconformity (Henry, 1992; Nex, 1997).

2.2.3.2 Chuos Formation (Usakos Subgroup)

The Chuos Formation (Table 2.1) unconformably overlies the Rössing Formation. It is a distinctive unit, composed predominantly of unsorted, matrix-supported glacial diamictites with subordinate banded ironstones, quartzites, minor marbles and pelitic units (Miller, 2008). It has been correlated with the world-wide Sturtian glaciation, which occurred at ± 710 Ma (Hoffman (2005).

2.2.3.3 Arandis Formation (Usakos Subgroup)

The Arandis Formation (Table 2.1) comprises calc-silicates, metagreywackes, schists, and carbonates, which constitute the cap carbonate to the Chuos Formation diamictite (Lehtonen *et al.*, 1995; Miller, 2008). It has been further subdivided into the Spes Bona (intercalated biotite schists and calc-silicate felses), Okawayo (turbidites, interbedded marbles, marble breccias, biotite schists and calc-silicate horizons), and Oberwasser Members (feldspathic biotite schists and quartz-biotite schists with lesser calc-silicate units; Badenhorst, 1992; Miller, 2008).

The various units of the Arandis Formation were deposited at a time of large-scale marine transgression and basin deepening (Stanistreet *et al.*, 1991), and the extent of the Okawayo Member in particular indicates that sedimentation occurred during a period of crustal stability in warm, shallow water (Badenhorst, 1992).

The upper limit of sedimentation has been constrained at 635 ± 1 Ma, a date obtained from a felsic volcanic unit by Hoffmann *et al.* (2004).

2.2.3.4 Ghaub Formation (Navachab Subgroup)

The Ghaub Formation conformably overlies the Oberwasser Member of the Arandis Formation. It comprises a series of diamictites, and graded siltstones and shales which contain dropstones (Sawyer, 1981; Miller, 2008). It has been subdivided into the Kachab (dropstone-bearing siliciclastic rocks; Badenhorst, 1992) and Daheim Members (metamorphosed alkaline, basic pillow lavas and pyroclastic rocks; Miller, 1983; Badenhorst, 1992).

The glacial event preserved in the Ghaub Formation has been correlated with the world-wide Marinoan glaciation, which occurred at *ca.* 635 Ma (Hoffmann, *et al.*, 2004). U-Pb ages obtained from zircons in the volcanic horizons have been used to constrain the timing of deposition at 635 ± 1 Ma (Hoffmann *et al.*, 2004), and the alkali composition of these metavolcanics suggests that they were deposited on the margins of a deep, submerged basin close to the southern passive continental margin of the Congo Craton (Miller, 1983; 2008).

2.2.3.5 Karibib Formation (Navachab Subgroup)

The Karibib Formation is composed almost entirely of carbonate marbles and dolomites (De Kock, 2001; Miller, 2008), which were deposited in a shallow marine environment during an extended period of marine transgressions between 625 Ma and 600 Ma (Miller, 2008). It is substantially thicker (up to 1000 m; Sawyer, 1981; Badenhorst, 1992), than the earlier Okawayo Member of the Arandis Formation, and is likely to record the submergence of the rift edges (grabens), resulting in the development of a larger platform upon which deposit carbonates, which may or may not have been coupled with a decrease in ocean floor spreading (Miller, 2008). The turbidites of the Tinkas Formation (Jacob, 1974) in the southwestern parts of the southern Central Zone have been correlated with the Karibib Formation in the Karibib area.

2.2.3.6 Kuiseb Formation (Navachab Subgroup)

The Kuiseb Formation is the highest stratigraphic unit in the Swakop Group, and it overlies the Karibib Formation conformably. It comprises a very thick metaturbiditic sequence, reaching thicknesses of up to 10 000m in the Khomas Trough (Miller, 1983). The dominant lithologies in the Formation are fine- to coarse-grained biotite-rich quartzo-feldspathic schists which contain cordierite, amphibole, or sillimanite porphyroblasts (Richards, 1986; Diehl, 1993; Miller, 2008). The schists become more migmatitic closer to Swakopmund, where the highest regional metamorphic conditions were attained.

The transition from carbonate deposition in the Karibib Formation to the deposition of turbidites in the Kuiseb Formation suggests an increase in basin subsidence at the time of sedimentation (Miller, 2008).

2.2.4 The Damara Supergroup: Zerrissenne Group (Southern Kaoko Zone)

The Zerrissenne Group is found at the junction between the Southern Kaoko Zone and Northern Zone (see Chapter 1, Figure 1.2), which is adjoined to the western portion of the Northern Zone (Miller, 2008), and which can be correlated with the Swakop Group

in the Central Zone. The unit is composed almost entirely of turbidites with some minor carbonates, which have been tightly folded by gently plunging, westerly verging N-S folds, resulting in a regular east-west repetition of the stratigraphy (Miller, 1983, 2008; Macey and Harris, 2006).

2.2.4.1 Zebrapütz Formation

The Zebrapütz formation is the lowest exposed unit of the Zerrissene Group. It is composed of thinly-bedded distal greywackes which are intercalated with siliciclastic pelites containing minor amounts of calcite, and has been correlated with the Spes Bona Member of the Arandis Formation in the Central Zone (Table 2.1; Swart, 1992; Miller, 2008).

Swart (1992) suggested that the Zebrapütz sequences were deposited in a very low energy, lobe fringe to basin plain environment by pelagic settling. During extended periods of progradation, medium- to thick-bedded sandstones were deposited; their deposition has been attributed to high density liquified flows down the low-angled lobe slopes (Swart, 1992; Miller, 2008).

2.2.4.2 Brandberg West Formation

The Brandberg West Formation conformably overlies the Zebrapütz Formation, and although it only attains a maximum thickness of 20 m, it is laterally extensive, and individual layers show a high degree of lateral continuity (Swart, 1992; Miller, 2008). This unit has been correlated with the Okawayo Member of the Arandis Formation in the Central Zone (Table 2.1; Miller, 2008).

It comprises interbedded sandstones, calc-arenites, commonly containing siliceous laminations, shales, which were deposited by turbidity currents adjacent to a carbonate margin, and blue marbles, which may represent hemipelagic, per-platform oozes (Swart, 1992; Miller, 2008). Swart (1992) attributed the deposition of the Brandberg West Formation to a rise in sea level and a simultaneous decrease in the volume of terrigenous material available to the basin during sedimentation.

2.2.4.3 Brak River Formation

The Brak River Formation conformably overlies the Brandberg West Formation, and in some regions its base is interfingered with the upper strata of the latter. It correlates with the Oberwasser Member of the Arandis Formation in the Central Zone (Table 2.1; Miller, 2008).

This unit is composed of interbedded sandstone-shale couplets, calcarenite and blue marble, greywakes, which Swart (1992) interpreted as representing classic fan fringe deposits.

2.2.4.4 Ghaub Formation

The Ghaub Formation is conformable to the underlying Brak River Formation, and, with the exception of the presence of glaciogenic clasts within it, it is virtually indistinguishable from the latter (Miller, 2008). The unit correlates with the similarly named Ghaub Formation in the Central Zone (Table 2.1; Miller, 2008).

Like the Brak River Formation, it is composed of interbedded sandstone-shale couplets, calcarenite and blue marble, greywakes. The glacial clasts in the Formation occur either as isolated dropstones or as clusters of clasts, with individual clasts reaching up to 30 cm in size (Miller, 2008).

The sediments of the Ghaub Formation were deposited in fan fringe or distal lobe environments during the Marinoan glacial event, with the uppermost shales having been deposited during a period of glacial retreat succeeded by a post-glacial increase in sea level (Swart, 1992).

2.2.4.5 Gemsbok River Formation

The Gemsbok River Formation is again very similar in composition to the Brandberg West Formation, however it correlates with the Karibib Formation of the Swakop Group in the Central Zone (Miller, 2008).

It comprises calcarenites, schists, blue marbles locally interbedded with breccias, calcarenites and shales. These sediments represent debris derived from a shelf environment, which were deposited as aprons on the slopes of drowned continental margins (Swart, 1992; Miller, 2008).

2.2.4.6 Amis River Formation

The Amis River Formation is the uppermost unit of the Zerrissene Group. It conformably overlies the Gemsbok River Formation, and its basal strata are intercalated with the uppermost strata of the latter (Miller, 2008). This Formation has been correlated with the Kuiseb Formation in the Central Zone (Miller, 2008).

It comprises interbedded sandstone-shale couplets, laterally continuous sandstones and thinly-bedded shales, and is generally dominated by sandstone sequences in its western parts and shales in its eastern reaches (Miller, 2008).

The Amis River Formation is a classic distal outer-fan lobe or fan fringe deposit (Swart, 1992). The sequences to the west were probably deposited in more proximal, variable environments (Swart, 1992), whereas, according to Swart (1992), the entire succession between Cape Cross and Uis was deposited in a distal basin plain environment.

2.3 Metamorphism and deformation in the study areas

Both basement lithologies of the Abbabis Complex and the supracrustal sequence of the Damara Supergroup have been exposed to metamorphic and deformation events associated with various stages of collision between the Congo and Kalahari Cratons. While these events have been documented to some degree in the Southern Kaoko Zone/Northern Zone (e.g. Goscombe *et al.*, 2004; Macey and Harris, 2006), the most extensive studies have been conducted in the southern Central Zone (e.g. Kisters *et al.*, 2004; Longridge *et al.*, 2009; Longridge, 2012). The metamorphic and structural characteristics of the two major regions of study i.e. the Southern Kaoko

Zone/Northern Zone and southern Central Zone are briefly discussed in the following sections.

2.3.1 Metamorphism in the southern Central Zone

The Central Zone is the part of the Damara Belt that experienced high temperature, low pressure metamorphic conditions during the process of orogenesis. It represents the southern leading edge of the active continental margin of the Congo Craton, and the root zone of the Damara Belt (Prave, 1996; Miller and Frimmel, 2009).

Metamorphic conditions in the Central Zone have been well documented and constrained by various authors (e.g. Nex *et al.*, 2001a; Jung and Mezger, 2003; Longridge, 2012). They reached upper amphibolite facies (~ 750 - 850 °C at ~ 4.5 - 6.0 kbar; Kasch 1983; Jung *et al.*, 2000; Longridge, 2012), although Masberg *et al.* (1992) suggested that it reached lower granulite facies, with an increase in metamorphic grade from the northeastern to the southwestern parts of the zone (Puhan, 1983; Goscombe *et al.*, 2004; Miller, 2008).

Although some debate exists over how many metamorphic events occurred in the Central Zone, there is agreement that its thermal evolution advanced as a result of isothermal decompression, where peak pressures were syn-tectonic and peak temperatures were post-tectonic (Miller, 1983, 2008). Nex *et al.* (2001a), based on observations made in the Goanikontes area near Swakopmund, proposed that post-tectonic isobaric heating, caused by the intrusion of massive volumes of granitic magma, succeeded a syn-tectonic decrease in pressure conditions. This hypothesis is similar to that of Bühn *et al.* (1995), based on the interpretation of data obtained from the Otjosondou area northeast of Windhoek, suggesting that the traditionally held view that metamorphic grade increases towards the western parts of the Central Zone may be an oversimplification of the metamorphic characteristics of the zone (Nex *et al.*, 2001a; Goscombe *et al.*, 2004; Miller, 2008).

The upwelling of asthenospheric material following slab break-off has been proposed as a heat source for M₁ metamorphism (Longridge, 2012). M₂, however, occurred at

lower pressures, indicating that extensive crustal thickening is unlikely to have been responsible for metamorphic conditions reaching upper amphibolite to granulite facies in the Central Zone, thus an additional heat source must have been responsible for the high grades of metamorphism attained during M₂ (Longridge, 2012).

A number of hypotheses have been proposed in order to account for this heat source e.g. Nex *et al.* (2001b), who proposed that the voluminous granitoids in the Central Zone were the heat source for M₂, however the absence of any contact aureoles around the granitoid bodies of the Central Zone and Northern Zone indicates that they were not transported particularly far from the site of melt generation, thus they appear to be a product of M₂ rather than its cause (Chamberlain and Sonder, 1990; Longridge, 2012).

Another suggestion is that the crust that was thickened during the Damara Orogeny was highly radioactive, and as such radioactive decay may have been the source of M₂ heat. Modelling by Longridge (2012) showed, however, that the basement rocks were not particularly enriched in heat producing elements, therefore they must have been emplaced in the crust with the granitoids.

The P-T evolution of the Damara Belt remains a debated issue; nonetheless, low pressure and high temperature metamorphism (M₂) cannot be accounted for through a "simple" mechanism of crustal thickening and thermal relaxation, and an additional heat source must have been responsible for M₂.

2.3.2 Deformation in the southern Central Zone

The southern Central Zone is characterised by kilometre-scale, elongate, northeast-trending dome structures (Oliver, 1995; Kisters *et al.*, 2004; Longridge *et al.*, 2009; Longridge, 2012). The domes usually comprise cores of basement material, generally ortho- and para-gneissic in composition, which are enveloped by and a host of tightly-folded metapelitic lithologies of the Damara Supergroup, including quartzites, schists, marbles, amphibolites, and calc-silicates (Oliver, 1995; Nex, *et al.*, 2002; Kisters *et al.*,

2004; Longridge *et al.*, 2009). A number of mechanisms of dome formation have been proposed over the last few decades, and some are briefly discussed here.

Earlier workers such as Sawyer (1981) and Steven (1993) proposed buoyancy-driven e.g. solid-state diapirism of basement material, or extension-related e.g. ballooning of granitic intrusives, vertical tectonics as a mechanism for dome formation. In contrast to this, other workers (e.g. Coward, 1983; Oliver, 1995) suggested rather that the domes represent sheath folds caused by crustal-scale shearing, leading Oliver (1995) to suggest a metamorphic core complex origin for them. Detailed mapping of the southwestern portion of the southern Central Zone by Longridge *et al.* (2009), however, did not produce any evidence for a crustal-scale shear zone. A further hypothesis is that doming resulted from mid-crustal constrictional folding coupled with top-to-the-west transport of rocks of the Damara sequence over basement gneisses (Poli and Oliver, 2001).

According to Kisters *et al.* (2004), however, the kilometre-scale doming observed in the Karibib area (see Figure 2.1) represents large-scale tip-folding or fault-propagation folding located at the ends of underlying blind thrusts. This is contradictory to the findings of Longridge (2012), who suggested that domes in the southwestern parts of the southern Central Zone may represent Type 2 interference structures which resulted from the folding of earlier D_2 folds during D_3 .

While each of these mechanisms is intended as a regional-scale model, it is most likely that none is mutually exclusive, and that multiple mechanisms acted together to a greater or lesser degree to cause doming (Barnes, 1981).

2.3.3 Metamorphism in the Northern Zone/Southern Kaoko Zone

Lithologies of the Zerrissene Group located at the junction between the Northern Zone and Southern Kaoko Zone have been regionally metamorphosed to greenschist facies, and thermally metamorphosed to mid-amphibolite facies by the intrusion of Salem Type granites (Macey, 2003; Macey and Harris, 2006; Miller, 2008).

The thermal metamorphism of the metaturbidites has caused the development of a biotite-cordierite aureole in the turbiditic schists of the Amis River Formation, resulting in the formation of cordierite porphyroblasts (Miller, 2008). Studies by Macey (2003) and Goscombe *et al.* (2004) indicated that heat derived from the intrusive suite added to the regional thermal budget, and therefore may be responsible for the regional metamorphism. Evidence for this lies in the fact that regional metamorphic isograds in the area are oriented almost parallel to the contacts of the granites, and the lowest metamorphic grades in the surrounding country rocks are found in metapelites furthest from the intrusions (Macey and Harris, 2006).

Peak metamorphic conditions in the area reached ~ 350 °C at a distance from granitic intrusions and 550 - 600 °C near their contacts at pressure ranging from 1.0 - 3.2 kbar (Macey, 2003; Goscombe *et al.*, 2004).

2.3.4 Deformation in the Northern Zone/Southern Kaoko Zone

The metapelites of the Northern Zone/Southern Kaoko Zone were deformed during the D₁ and D₂ deformation events (see Chapter 1). Deformation is characterised by relatively tight north-south-striking folds with moderately- to steeply-inclined fold axial planes which dip to the east (Goscombe *et al.*, 2004; Macey and Harris, 2006; Miller, 2008).

The structural evolution of the Southern Kaoko Zone/Northern Zone involved only the sedimentary lithologies of the Damara Supergroup i.e. there is no basement exposure in the area. Deformation has been attributed to the convergent and shortening phases of the Damara Orogen (Goscombe *et al.*, 2003a).

Figure 2.2 summarises the stratigraphic location of pegmatites from this study in the units of the Damara Supergroup and Southern Kaoko Zone, relative to deformation observed in these units, and metamorphic grades recorded.

Formation	Deformation	Metamorphic Grade	Pegmatite Occurrence				
Kuiseb/Amis River	D ₃ doming/D ₂ tight N-S folds	Upper greenschist facies (540 - 570 °C at 2 - 3 kbar)					
Karibib	D ₃ doming	Lower amphibolite facies (560 - 650 °C at 3 ± 1 kbar)					
Chuoss	D ₃ doming						
Rössing	D ₃ doming	Granulite facies (750 - 850 °C at 5.0-6.0 kbar)					
Khan	D ₃ doming						
Etusis	D ₃ doming						
Abbabis Complex							
	Rubicon		Uis		Usakos		Valencia (Type B)
	Helicon		Karlowa		Omapyu		Valencia (Type C)

Figure 2.2: Summary of pegmatite emplacement in metasedimentary units of the Damara Supergroup. Refer to Chapter 4 for pegmatite names and localities. Structural and metamorphic conditions cited from Puhan (1983), Steven (1993), Goscombe *et al.* (2004), Kisters *et al.* (2004), Freemantle (2012), and Longridge (2012).

CHAPTER 3

AN INTRODUCTION TO PEGMATITES

3.1 Introduction

The term “pegmatite” is traditionally used to describe igneous rocks containing extremely coarse-grained minerals (Simmons, 2007; London, 2008; London and Kontak, 2012). Pegmatites themselves, though, are usually described based not only on their coarse grain size, but on other textural characteristics as well, such as skeletal and granophyric textures, and unidirectional crystal growth structures (Simmons, 2007; London, 2008; London and Kontak, 2012). All granitic pegmatites are similar in their mineralogy (quartz + feldspar \pm tourmaline, muscovite, garnet), however they may display variations in texture, structure and mineralogy (Cameron *et al.*, 1949). Pegmatites have also been described to some degree on their geochemical characteristics, such as their overall granitic composition (though carbonatitic, mafic, ultramafic and alkaline pegmatites do exist) and their enrichment in rare elements e.g. Li, Rb, Cs, Be, Ga, Sc, Y, REE, Sn, Nb, Ta, U, Th, Zr and Hf which are the constituents of a number of exotic minerals, and which have a variety of technological applications (Černý, 1991a, b; Ercit, 2005; London, 2008; Glover *et al.*, 2012; London and Kontak, 2012). They are also exploited for industrial minerals such as feldspar, quartz, fluorite, spodumene and petalite, not only because of the concentration of mineralisation in large, very pure crystals, but also because they accommodate the concurrent extraction of several ores (Černý, 1991a; Linnen *et al.*, 2012; London and Kontak, 2012). Although the paragenesis, geochemical characteristics and structural features of granitic pegmatites differ greatly, they share the common genetic feature of their crystallisation from volatile-rich melts containing varying enrichments of lithophile rare elements (Černý, 1991b; London, 2008).

3.2 Regional and global distribution of pegmatites

Most pegmatites occur in groups or swarms which consist of cogenetic bodies occupying an area of a few to hundreds of square kilometres which may be associated with a particular granitic source pluton, and which are distributed systematically around it, from the less fractionated granite to the most highly evolved pegmatitic bodies occurring at the greatest distance from the pluton (Figure 2.1; Černý *et al.*, 1981; Černý, 1991b; Ercit, 2005; Simmons, 2007; London, 2008).

In syn- to late-orogenic suites the emplacement of a group of pegmatites is commonly restricted by the metamorphic grade of the host rocks into which they have intruded (Černý, 1991b). The pegmatites of a given swarm share a common geological/structural environment, such as a deep fault lineament or mobilised cratonic margin, which may cover a large aerial extent ($< 10\,000\text{ km}^2$; Černý, 1991a, b), thus its formation may be attributed to a single tectono-magmatic event, with all pegmatite bodies within it being consanguineous and sharing a similar age (Černý, 1991b; Simmons, 2007; London, 2008).

By extension, a pegmatite belt refers to all fields/swarms related to a particular geological structure; a belt may contain different classes of pegmatites which formed under different tectono-magmatic conditions, but all of these are related to the history of the said structure (Černý, 1991b; London, 2008). Finally, a pegmatite province encompasses all swarms and belts in a particular region, and thus consists of various classes of pegmatite that formed at different stages of crustal evolution (Černý, 1991b; London, 2008).

Černý (1991a, b) identified three groups of pegmatite based on their proximity to a granitic pluton, interior, marginal and exterior (Figure 3.1). Interior pegmatites (Figure 3.1C) lie within a granitic body, and are the least fractionated, and mineralogically and structurally the least complex of all pegmatites. Marginal pegmatites (Figure 3.1B) occur within or at the margin of a granitic pluton and are relatively more complex than interior pegmatites. Lastly, exterior pegmatites (Figure 3.1A) are hosted in

metamorphic lithologies outside of the granitic body. The regional zonation around a given pluton is influenced by the composition and structure of the host rock as well as the vertical level of exposure, and in general, as the degree of fractionation and mineralogical complexity increases away from the pluton, the number of associated exterior pegmatites decreases. It is generally accepted that the reason for this regional zonation is that more fractionated melts contain greater amounts of volatiles and are therefore less viscous. Fluid-rich melts are able to remain fluid at lower temperatures and so are able to travel greater distances from their source pluton (Černý, 1991a, b).

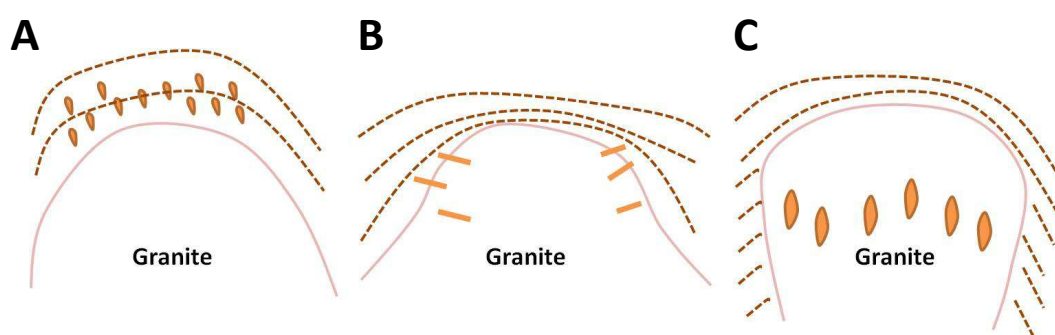


Figure 3.1: The relationships between parent granite plutons and surrounding pegmatites showing A) Exterior pegmatites occurring in a pegmatite aureole surrounding a granitic pluton; B) Marginal pegmatites; C) Interior pegmatites (modified after Varlamoff, 1972; Černý, 1991a, b).

3.3 Pegmatite classification

The classification of pegmatites is rather complicated. The first attempt at it was made by Landes (1933) who distinguished between chemically simple and chemically complex pegmatites based on their mineralogical similarities with, or differences from, common plutonic rocks (London, 2008). The terms “simple” and “complex” were coupled with the modifiers acid, intermediate or basic denoting the predominant igneous composition of the rock (Landes, 1933).

The major factor influencing the modern classification of granitic pegmatites is the depth-zone classification of granitic rocks (Buddington, 1959; Ginsburg *et al.*, 1979).

According to this method pegmatites are categorised according to their depth of emplacement and their relationship to metamorphic grade, as well as their relationship to granitic plutons (Ercit, 2005; Simmons, 2007).

3.3.1 Pegmatite classes

The current classification of pegmatites is based on a fourfold subdivision of pegmatites by Ginsburg *et al.* (1979) into abyssal, muscovite, rare-element and miarolitic classes, based predominantly on mineralogical and textural characteristics, the pressure and temperature conditions of pegmatite formation, and to a limited degree, the metamorphic grade of their host rocks (Figure 3.2; Černý *et al.*, 2012). Černý (1990; 1991a), and later Černý and Ercit (2005), expanded upon the classification scheme of Ginsburg *et al.* (1979) to produce the most recent and most commonly used granitic pegmatite classification scheme. This system further subdivides the four pegmatite classes into subclasses, types and subtypes based on the trace element signatures of pegmatites as determined from their mineral assemblages and mineral chemistry (Table 3.1; Černý and Ercit, 2005; Černý *et al.*, 2012).

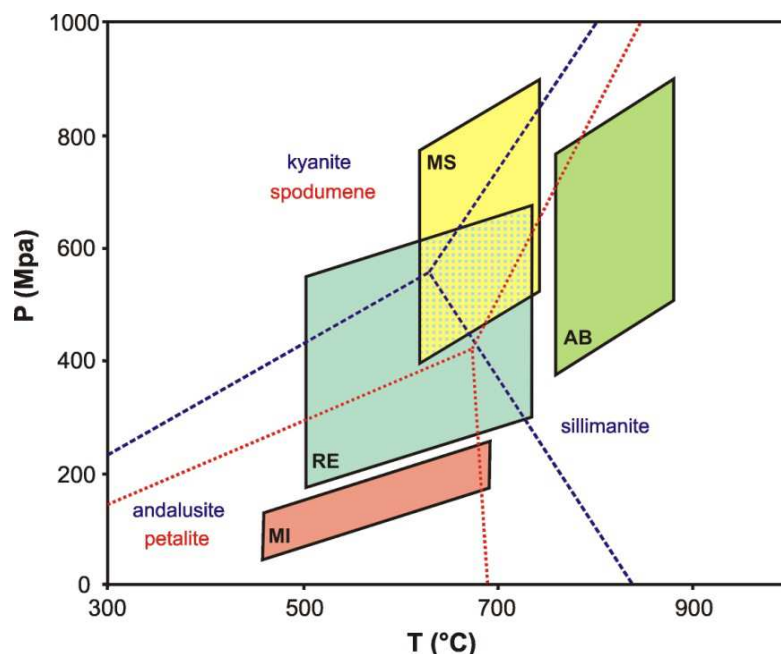


Figure 3.2: Pressure-temperature conditions for the formation of Ginsburg's (1984) and Černý's (1991a) abyssal (AB), muscovite (MS), rare-element (RE) and miarolitic (MI) pegmatite classes in relation to aluminosilicate and lithium-aluminosilicate stability fields.

Table 3.1: Pegmatite classification scheme of Černý and Ercit (2005) modified to illustrate the correlation between pegmatite classes and families (LCT = Lithium-Caesium-Tantalum; NYF = Niobium-Yttrium-Fluorine; see text for explanation).

Class	Subclass	Type	Subtype	Family
Abyssal	HREE			NYF
	LREE			
	U			NYF
	BBe			LCT
Muscovite				
Muscovite-rare element	REE			NYF
	Li			LCT
Rare element	REE	allanite-monazite		NYF
		euxenite		
		gadolinite		
	Li	beryl	beryl-columbite beryl-columbite-phosphate spodumene petalite lepidolite elbaite amblygonite	LCT
		complex		
		albite-spodumene albite		
Mirolitic	REE	topaz-beryl gadolinite-fergusonite		NYF
	Li	beryl-topaz spodumene petalite lepidolite		LCT

3.3.2 Pegmatite families

Expanding upon the work of Ginsburg *et al.* (1979) , Černý (1990; 1991a;1992) proposed the **Lithium-Caesium-Tantalum (LCT)**, **Niobium-Yttrium-Fluorine (NYF)** and mixed LCT – NYF families by relating pegmatite classes to other petrological, paragenetic and geochemical data.

3.3.2.1 LCT Pegmatites

LCT pegmatites are enriched in the elements Li, Rb, Cs, Be, Ga, Sn, Nb, Ta, B, F, P, Mn and Hf, elements which become progressively enriched in the residual magma as they behave incompatibly with the crystallisation of quartz and feldspars (Černý, 1991b;

Černý, 1992; Černý and Ercit, 2005; Simmons, 2007; Martin and De Vito, 2005; Martin *et al.*, 2009). In terms of bulk geochemistry, they share a compositional affinity with S-type granites; they are typically per- to sub-aluminous, a characteristic manifested in the presence of minerals such as muscovite, tourmaline, spessartine garnet and rarely gahnite, topaz or andalusite (London, 2008). These pegmatites crystallise from hydrous magmas, they usually display an S- and rarely I-type geochemical signature, and their source lithologies are undepleted upper- to middle-crustal rocks (S-type) and basement gneisses (I-type; Černý, 1991b; Chappell and White, 1992, 2001; London, 2008; London and Kontak, 2012).

The Li enrichment in LCT pegmatites results from the melting of mica-rich metamorphic rocks at the pegmatite source, and causes the crystallisation of the Li-Al-silicates, spodumene and petalite, and somewhat less frequently in lepidolite, amblygonite-montebrazite, or elbaite (London, 1995; 2005; 2008; Černý *et al.*, 2012). Cs enrichment is evident in rare-element pegmatites containing pollucite that also results from the melting of micas, predominantly biotite and muscovite, at the pegmatite source (London, 1995, 2005). The source of Ta enrichment in LCT pegmatites is poorly understood, however London (2008) suggests that micas or minor quantities of ilmenite in mica schists may act as a possible source for Ta in LCT pegmatites.

3.3.2.2 NYF Pegmatites

NYF pegmatites are enriched in Ti, Nb, Y, HREE, Zr, U, Th, F and Sc (Černý, 1991b; Černý, 1992; London, 2008; Černý *et al.*, 2012). Their bulk composition is sub- to metaluminous, and in contrast to LCT pegmatites they crystallise from relatively dry magmas (Černý, 1991b). Although NYF magmas are believed to be H₂O-poor, Skjerlie and Johnston (1992) suggested that they accumulate F during the growth of pyroxene from amphiboles and mica. NYF pegmatites typically display an A-type (anorogenic) geochemical signature, their sources including depleted middle to lower crust granulites or juvenile granitoid rocks, and they usually contain some chemical constituents from the mantle (Lenharo *et al.*, 2003; Černý and Ercit, 2005; Martin and De Vito, 2005; Černý *et al.*, 2012).

In terms of mineralogy, NYF pegmatites commonly contain amazonitic K-feldspar and sodic pyroxenes and amphiboles (London, 2008). Unlike LCT pegmatites, the origins of the NYF trace element signature are relatively poorly understood (London, 2008; Černý *et al.*, 2012).

3.3.2.3 Mixed LCT-NYF Pegmatites

Mixed LCT-NYF pegmatite suites are predominantly NYF bodies that show strong LCT overtones resulting from contamination from local sources (Černý, 1991b; Martin and De Vito, 2005; Černý *et al.*, 2012). In these systems, late-stage orthomagmatic fluids from the formation of the NYF pegmatites cause hydrothermal reactions in the sedimentary host rocks, releasing Li and B and thus overprinting the NYF intrusion with a LCT signature (Martin and De Vito, 2005; Černý *et al.*, 2012).

3.3.3 Controversies regarding pegmatite classification

Recently authors have noted the limitations imposed by the classification of pegmatites based on their depth of emplacement, and have pointed out the need for a classification scheme that relates pegmatite melt generation to tectonic processes (e.g. Martin and De Vito, 2005; Martin, 2007; Martin *et al.*, 2009).

Martin and De Vito (2005) have proposed two main types of pegmatite, those generated by anatexis, and those derived from the fractional crystallisation of more primitive felsic intrusions. They have also suggested that the geochemical nature of a pegmatite melt is determined by the tectonic environment in which a given pegmatite occurs, such that LCT melts are orogenic i.e. generated in compressional environments, and NYF melts are anorogenic i.e. generated in extensional environments (Martin and De Vito, 2005; Tkachev, 2011; Černý *et al.*, 2012).

Thus, in the case of LCT pegmatites, the parent magma is derived from partial melting of the mantle wedge during subduction processes, and, strictly speaking, at the post-tectonic phase of continent collision (Martin and De Vito, 2005; Tkachev, 2011; Černý

et al., 2012). The magma rises into the lower crust and undergoes assimilation-fractional crystallisation. At the same time a regional increase in the geothermal gradient, caused by the hydrothermal plume rising from the subducting plate, contributes towards the melting of mica-bearing metasedimentary lithologies in the crust. Magma mixing and mingling result in the increasing enrichment of H₂O, B, P, F and Li in the melt, and the ultimately per- to metaluminous nature of the LCT pegmatite melt (Martin and De Vito, 2005; Martin, 2007).

In contrast, NYF melt generation is related to the focusing of volatiles ahead of a rising mantle plume of fertile asthenospheric material (Woolley, 1987; Martin and De Vito, 2005; Martin, 2007). The fluids are typically alkaline, H₂O – CO₂ bearing, and rich in trace elements, particularly high field strength elements and LREE (Martin and De Vito, 2005; Martin, 2007). They metasomatise the upper mantle and rise through the bulged crust, preparing for the commencement of anatexis; Abdel-Rahman and Martin (1990) refer to this process as metasomatic "ground preparation". Because of the highly selective nature of metasomatic "ground preparation", there is a greater influx of alkalis and silica relative to Al, resulting in the A-type geochemical signature of the pegmatite melt (Martin and De Vito, 2005; Martin, 2007).

There are many instances in Africa e.g. South Africa, Namibia, Mozambique, and Zambia (Von Knorring and Condliffe, 1987) where the model of Martin and De Vito (2005) does not seem plausible as an explanation for the differences between LCT and NYF pegmatites. Here coeval, typically post-collisional LCT and NYF pegmatites occur within the same tectonic setting. In these instances it may be necessary to consider the influences that bulk protolith composition and crustal contamination may have on a pegmatite melt composition. This will be further discussed in Chapter 7.

3.4 Internal anatomy of pegmatites

Cameron *et al.* (1949) compiled the key reference on the internal structure of pegmatites based on extensive field work in the early 1940s on behalf of the U.S. Geological Survey, and their terminology is still used today. The term "zone" is used in

the identification of areas in the pegmatite which are dominated by a particular mineral, and which form “successive shells around the innermost unit that reflect the shape and structure of the pegmatite” (Cameron *et al.*, 1949).

3.4.1 Unzoned pegmatites

The term "unzoned" does not imply that the composition of the pegmatite is primitive; rather it refers to the fact that texture and mineralogy are homogeneous in these bodies, although they may display a porphyritic texture and oriented mineral fabrics (Heinrich, 1958; Simmons, 2007; London, 2008).

Unzoned pegmatites are composed essentially of quartz and feldspar with subordinate amounts of mica, and may contain accessory tourmaline, garnet and some rarer phases (Simmons, 2007). They are commonly found in high grade metamorphic terranes which fall within the kyanite and spodumene stability fields (Figure 3.2; Simmons, 2007; London, 2008).

3.4.2 Zoned pegmatites

Zonation in pegmatites refers to the development of discreet, mapable "shells" within a pegmatite body, which differ in mineralogy, texture, grain size and crystal habit (Cameron, 1949; Ercit, 2005; Simmons, 2007; London, 2008). The zones reflect the structure of the pegmatite body, and ideally the shells are developed concentrically about an innermost core (Figure 3.3; Cameron *et al.*, 1949).

Zoned pegmatites are primary in nature having crystallised directly from a pegmatitic melt from the outside inward, with grain size increasing from the outer zones inward (Cameron *et al.*, 1949; Simmons, 2007). Coupled with these features are the tendencies to become mineralogically simpler and more silica-rich from the edges inwards (Cameron *et al.*, 1949; Simmons, 2007). Bulges in the pegmatite commonly host the most fractionated part of the body, whereas more primitive units are developed in pinched out parts of the body (Cameron *et al.*, 1949; Simmons, 2007).

Cameron *et al.* (1949) described the following zones which may or may not be present and/or continuous in a given pegmatite, and which are illustrated in Figure 3.3:

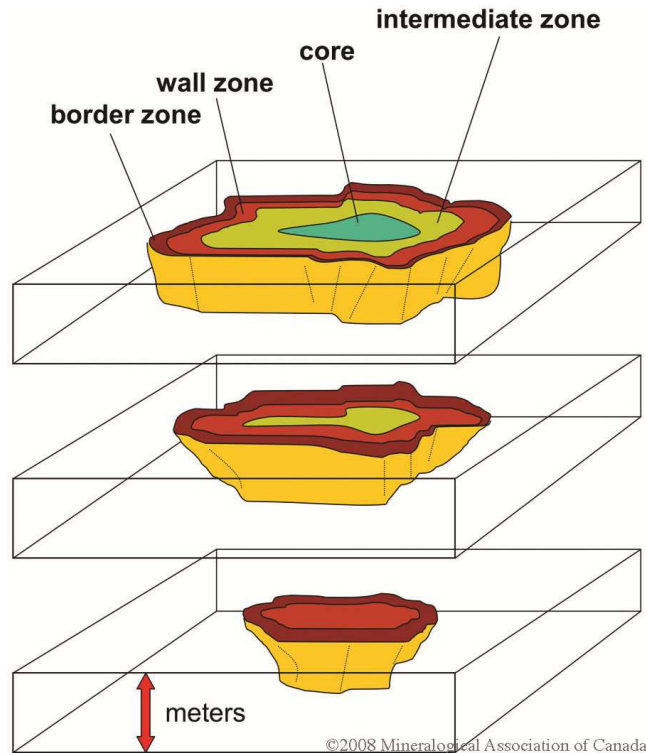


Figure 3.3: Idealised block diagram of a zoned pegmatite, illustrating concentric zonation around a central core zone (modified after Cameron *et al.*, 1949; London, 2008). Zonation may be developed to the scale of several meters. Note that some zones may or may not be (fully) developed in a given pegmatite.

3.4.2.1 Border zone

The border zone is typically a few centimetres thick and is similar to the chill margin of other intrusive bodies. It is commonly aplitic to fine-grained, but may have a bimodal texture. The contact between the border zone and the wall rock is abrupt. Mineralogically, the border zone is composed of feldspar, quartz and muscovite with accessory tourmaline, beryl, apatite and garnet, occasionally with minerals oriented parallel to the wall rock, but more commonly with one or more of the component minerals perpendicular or sub-perpendicular to the contact walls (also known as unidirectional crystal growth).

3.4.2.2 Wall zone

The wall zone is coarser-grained and thicker than the border zone, and it commonly grades into the adjacent border and intermediate zones. It is composed primarily of plagioclase, perthite, quartz, muscovite, tourmaline and beryl.

3.4.2.3 Intermediate zone

Intermediate zones are less commonly developed than other zones in a pegmatite. They vary both in thickness and mineralogy, and are most extensively developed in the thicker parts of the pegmatite, and pinch out where the body thins. Mineral assemblages in these zones usually include combinations of plagioclase, quartz, perthite, muscovite, biotite, Li-aluminosilicates, and amblygonite-montebrazite. Intermediate zones are commonly identifiable by a sudden increase in grain size and the dominance of a particular mineral.

3.4.2.4 Core

The core represents the innermost unit of a zoned pegmatite. Its size is usually determined by the overall size of the pegmatite, and the thickness of the wall and intermediate zones. It is normally composed of mono-mineralic quartz, however it may contain variable proportions of perthite, albite, Li-aluminosilicates and phosphates (e.g. montebrazite).

3.5 Generation and consolidation of pegmatite melts

3.5.1 Models for the formation of pegmatites

There are two dominant theories relating to the generation of pegmatitic melts which have prevailed since geoscientists began working on the subject in the early 1900s. The first of these is that they are formed by the fractional crystallisation of a flux-bearing magma of granitic composition and the second invokes the segregation of an aqueous fluid from a silicate fluid and the redistribution of geochemical components

in the system (Černý, 1991b; London, 2005; Simmons, 2007; Alfonso and Melgarejo, 2008; London and Morgan, 2012; Thomas *et al.*, 2012).

According to the first model, the first minerals to crystallise in a granitic system are alkali and sodic feldspars, quartz and minor muscovite/biotite into which Si, Al, K, Na, O and some H₂O are incorporated. As a result, incompatible elements become enriched in the residual melt or pegmatitic magma. The pegmatitic melt is enriched in volatiles and fluxes e.g. H₂O, CO₂, B, F, Li and P, which lower the viscosity and crystallisation temperature of the pegmatite system, relative to the initial granitic magma. Concurrently, the melt becomes enriched in rare elements e.g. Cs, Ta, Nb, Sn, REE, Zr and U (Cameron *et al.*, 1949; Simmons, 2007; London, 2008; London and Morgan, 2012).

The second model was developed by Jahns and Burnham (1969), who stated that "the appearance of an aqueous fluid can be regarded as the most decisive step in the genesis of pegmatites." According to their model, K partitions into the aqueous fluid while Na partitions into the silicate melt. The aqueous fluid is responsible for the removal of incompatible elements from the lower parts of the magma, and their upward transport and subsequent accumulation in giant, exotic crystals, while the silicate melt simply acts as a source of geochemical components.

The most recent model for pegmatite genesis draws from aspects of both of the former models. It is called Constitutional Zone Refining (CZR), and proposes the formation of flux-enriched boundary layer of silicate liquid adjacent at the crystal-melt interface (see reviews in London, 2008; London and Morgan, 2012). This model will be discussed in greater detail in section 3.6.

3.5.2 The importance of volatiles in pegmatites

Volatile enrichment in pegmatitic systems occurs as the result of the solubility of H₂O in felsic melts as well as the exclusion of volatiles from major rock-forming minerals during crystallisation (London, 2005; Simmons, 2007).

H₂O and other volatiles (e.g. F, Cl, B, Li and P) are the main components responsible for petrogenesis in a pegmatite system; they reduce the viscosity of the melt, enhancing transport of the melt in the crust, and they reduce the glass transition temperature allowing melts to crystallize well below the thermodynamic solidus (Nabalek *et al.*, 2010). In addition to this, as volatiles increase in abundance, they act to hinder the formation of crystal nuclei until the melt is sufficiently undercooled, and they increase the efficacy of diffusion to the nuclei that are able to form, thus resulting in the formation of fewer, larger crystals (Simmons, 2007; London, 2008; Nabalek *et al.*, 2010).

Once a mineral is able to nucleate, however, it may grow extremely quickly and its size will be determined by the distance between the site of nucleation and the point in the magma where its temperature is equal to that of the solidus of the crystallising mineral (London, 2008; Nabalek *et al.*, 2010). What distinguishes pegmatites from regular granites is, therefore, their ability to retain H₂O (Figure 3.4).

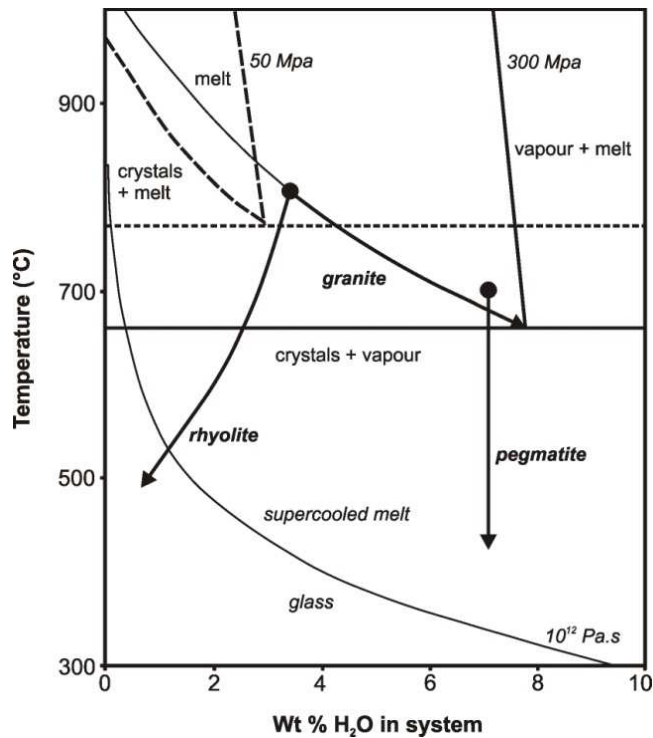


Figure 3.4: Temperature-wt % H₂O paths for a generic granite, rhyolite and pegmatite illustrating the differences between them, in water retention and subsequent undercooling. Water loss resulting from decompression and venting, results in a microcrystalline texture and possibly the development of glass. In a slow-cooling system water exsolves from the crystallising magma, equant crystals grow, and the magma finally solidifies at the thermodynamic solidus (from Nabalek *et al.*, 2010).

3.6 Rates of pegmatite crystallisation and Constitutional Zone Refining

It has traditionally been thought that giant crystals in a pegmatite are the result of slow cooling in the pegmatite system, however the results of several studies have shown that pegmatite dykes may have cooled to their solidus temperatures in as short a time as a few days to months, and that very large pegmatites may cool in decades to a few hundred years (Chakoumakos and Lumpkin, 1990; Webber *et al.*, 1997, 1999; Morgan and London, 1999; Černý, 2005; London, 2008).

Pegmatite melts may, in fact, be significantly undercooled (Nabalek *et al.*, 2010). The process of undercooling involves the removal of a particular flux as that flux becomes incorporated in a crystallising phase, which then initiates the rapid growth of crystals (Simmons, 2007; Nabalek *et al.*, 2010). Furthermore, because of the lag time (also

known as nucleation delay) between cooling and the onset of crystallisation, the melt becomes supersaturated in fluxes and incompatible elements. Once nuclei are able to form, rapid crystallisation from this undercooled melt generates a boundary layer (Figure 3.5) of excluded elements ahead of the growth front of crystallising phases, even where the amount of flux present in the melt is relatively low (~ 3 wt %; Webber *et al.*, 1997; Morgan and London, 1999; Simmons, 2007; London, 2008; Nabalek *et al.*, 2010).

With progressive crystallisation, the solidus of the boundary layer is reduced and it becomes further enriched in fluxes and trace elements in relation to the bulk melt composition (Figure 3.5; London 2005, 2008). Fluxes in the boundary layer form complexes with incompatible elements in the melt, resulting in the increased purity, homogeneity and size of crystallising phases. This process has been called Constitutional Zone-Refining (CZR; Morgan and London, 1999; London, 2005; London, 2008). Thus the outer zones of a pegmatite, containing anisotropic fabrics, graphic textures, and fine-grained minerals are dominated by the effects of undercooling, while the progressively coarse-grained and blocky inner zones result from the build-up of fluxes in the boundary layer (London, 2009; London and Morgan, 2012).

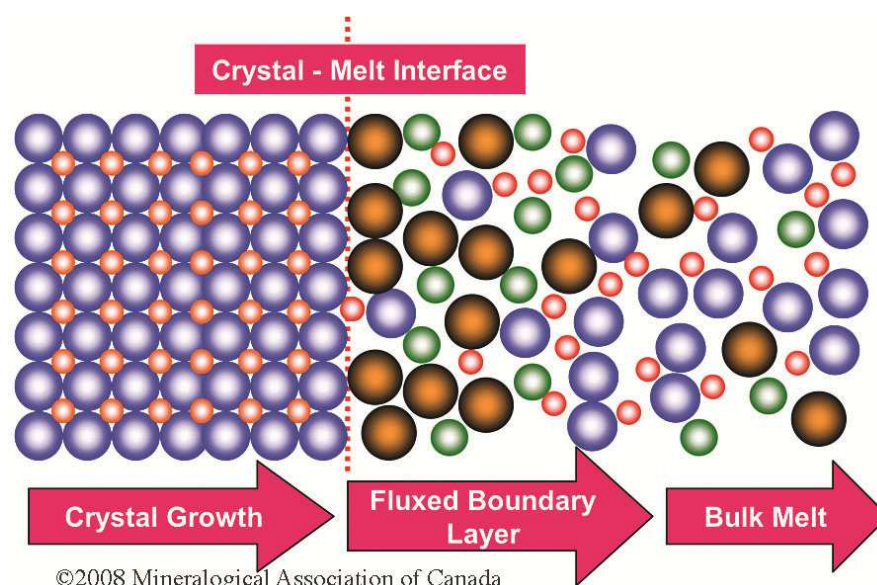


Figure 3.5: Schematic diagram illustrating crystal growth, pile-up in the boundary layer, local saturation, and fluxed constitutional zone-refining. The fluxing component (brown atoms) is incompatible with the main crystallising phase (blue and red atoms); it forms complexes or associated species with other incompatible elements (green atoms; from London, 2008).

Recent work by Thomas *et al.* (2006, 2009; 2011; 2012) and Thomas and Davidson (2012) has shown that pegmatite melts contain significantly greater proportion of "melt structure modifiers" such as OH^- , CO_2 , HCO_3^- , CO_3^{2-} , SO_4^{2-} , H_3BO_3 , and Cl, as well as the elements Li, Na, K, Rb, Cs, and Be, present in fluid inclusions, in addition to the traditionally recognised fluxes, H_2O , F, B and P, whose combined effect on pegmatitic melts could be responsible for the diversity observed in pegmatites around the world. In addition to this, the water content of pegmatites may vary from as little as 2 wt % to well over 50 wt % water (Thomas *et al.*, 2012). It has been suggested that the variability of water content in pegmatites may be attributed to processes of melt-melt immiscibility during crystallisation, which themselves may be attributed to the presence of, and interaction between, several melt structure modifiers in the melt (Thomas *et al.*, 2012). The conjugate melts, A and B (melt B preserved only as melt inclusions as a result of its reactivity throughout crystallisation), are peraluminous and peralkaline respectively, and the physical and chemical differences between the melts have a significant influence on element partitioning between them (Thomas and Davidson, 2012). Thomas *et al.* (2012) and Thomas and Davidson (2012) concluded that melt-melt immiscibility in pegmatites removes the necessity of a fluxed boundary layer CZR processes during the crystallisation of the melt and also suggested that the role of liquidus undercooling as a major process during pegmatite crystallisation may be greatly overestimated, and only really effective in melts containing high proportions of H_2O .

Due to their abundance, mineralogical variability and exposure pegmatites in the Damara Belt provide an excellent opportunity to examine the processes responsible for the regional variability of coeval pegmatites. A number of pegmatites displaying all of these attributes were selected for study, and an introduction to each is presented in Chapter 4.

CHAPTER 4

PEGMATITES OF THE DAMARA OROGEN

4.1 Introduction

Many of the economic ore deposits of the Damara Belt occur within the Central and Northern Zones. Among these deposits are Li-Be-, Sn- and tourmaline-bearing LCT pegmatites and U-bearing NYF pegmatitic leucogranites, which have been intruded into the tightly folded supracrustal rocks of the Damara Supergroup (Keller *et al.*, 1999). The main commodity extracted from each type of pegmatite varies according to its geographic location, and by extension, its position within the stratigraphy of the Damara Belt, even though all of these bodies are of similar, late tectonic age (~ 510 - 490 Ma). Figure 4.1 illustrates the geographic extent of the major pegmatite districts of the Damara Belt.

Ten pegmatites were sampled for the purpose of this investigation; their locations are varied, with two occurring within the Northern Tin Belt (1; Northern Zone/Southern Kaoko Zone), one within the Southern Tin Belt (3; southern Central Zone), three within the Karibib Pegmatite Belt (4), and four within the Rössing Pegmatite Belt (5; southern Central Zone; Figure 4.1).

Those occurring within the Southern Tin and Karibib Pegmatite Belts are large, zoned Li-Be- and gem-tourmaline-bearing pegmatites belonging to the LCT family (Černý and Ercit, 2005). Those located in the Northern Tin Belt are large, unzoned Sn-bearing bodies belonging also to the LCT family, while those occurring within the Rössing Pegmatite Belt are smaller, unzoned U-rich bodies which possess NYF characteristics (Černý and Ercit, 2005). They have been intruded into Damaran metasediments which were metamorphosed to upper amphibolite-granulite facies in the southern Central Zone, and to greenschist facies in the Northern Zone/Southern Kaoko Zone.

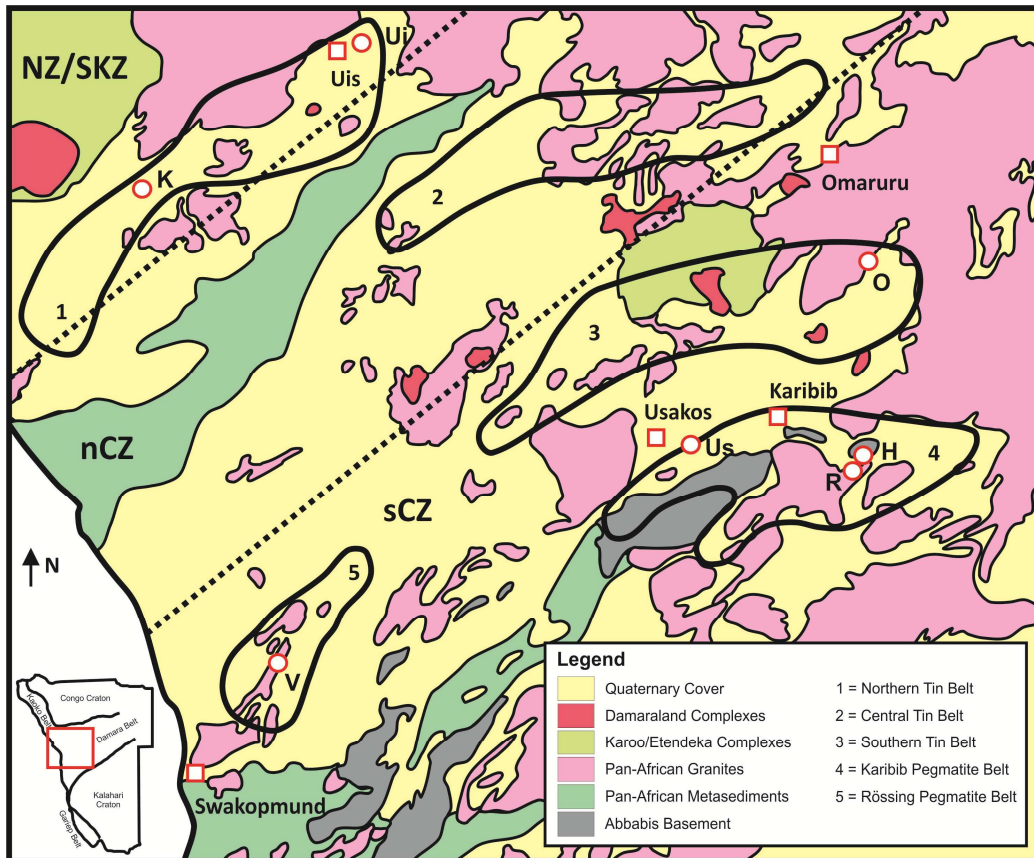


Figure 4.1: Geographic extent of five major pegmatite belts in the Damara Belt (modified after Keller *et al.*, 1999). Number 1 occurs in the Northern Zone (NZ)/Southern Kaoko Zone (SKZ), number 2 in the northern Central Zone (nCZ), and numbers 3, 4 and 5 in the southern Central Zone (sCZ). This study focuses on samples collected from 1, 3, 4, and 5. These localities are labelled R, H, O, Us, Ui, K, and V, where R = Rubicon, H = Helicon, Ui = Uis, K = Karlowa, Us = Usakos, O = Omapyu, and V = Valencia pegmatites. See text for details.

The pegmatites investigated were selected for a number of reasons. These include their diversity of mineralisation, their geographic, and therefore stratigraphic, distribution with respect to one another, as well as the ease with which they could be accessed. Furthermore, only pegmatites that have been mined at some point were selected for sampling.

4.2 Li-Be-bearing pegmatites of the Damara Belt: Rubicon and Helicon pegmatites

4.2.1 Introduction

The Li-Be-bearing pegmatites of this study are located in the Karibib Pegmatite Belt (see Figure 4.1). The two studied belong to a larger swarm of similar pegmatites which occur in the Karibib area. These include the Rubicon and Helicon pegmatites, sampled for this study, the Karlsbrunn, Becker's, Kaliombo, Brockmann's, Henckert's, and Van de Made's pegmatites, to name a few. The pegmatites of the Karibib area were extensively mapped, sampled and analysed for mineral chemistry by Roering (1963). Later studies by Diehl and Schneider (1990) elaborated upon the work of Roering (1963).

The Rubicon and Helicon pegmatites are large, internally- zoned LCT pegmatites. They are located on the farm, Onkangava Ost 72, approximately 30 km southeast of Karibib in the southern Central Zone, and occur within the Karibib Pegmatite Belt (Figures 4.1 and 4.2).

Exploration for beryl began in the 1930s in the Karibib district, however the Rubicon pegmatite in particular became Namibia's major source of lithium. From the 1950s it was selectively mined for petalite, amblygonite, lepidolite, beryl, quartz, pollucite, bismuth, and bismuth oxides (Diehl, 1992b). More recently it has been reworked for industrial minerals, particularly quartz. The Helicon pegmatites were mined for similar minerals, as well as niobium-tantalum oxides (Diehl, 1992b). By the early 1990s, the Rubicon and Helicon pegmatites collectively were the sources of approximately 90 % (approximately 250 t) of Namibia's total pollucite production (Diehl, 1992b).

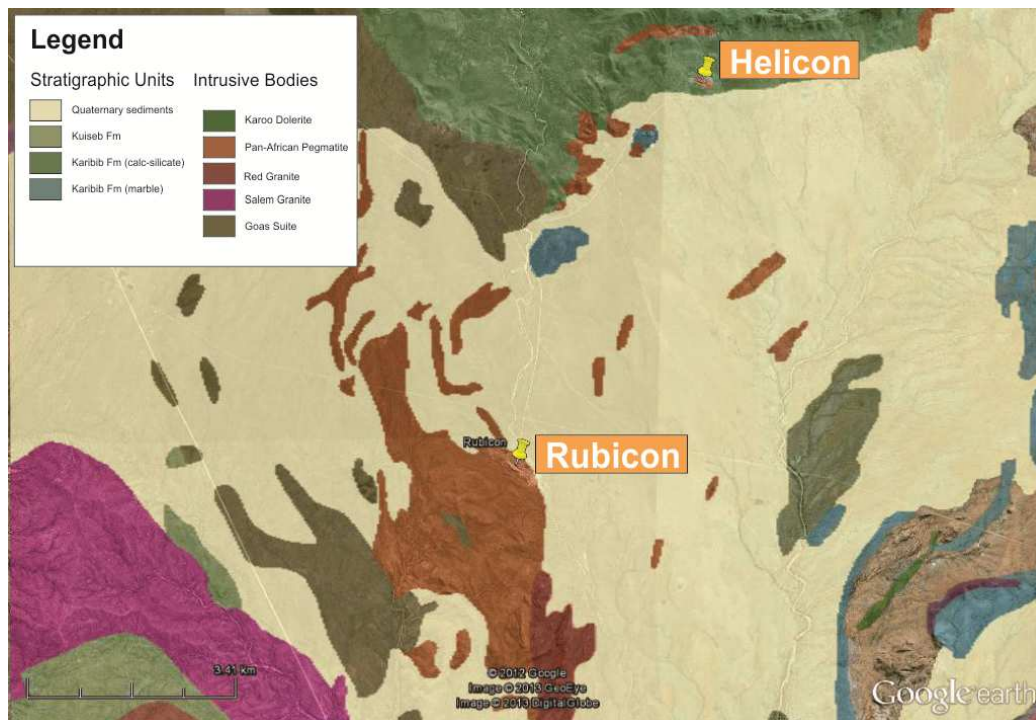


Figure 4.2: Google Earth map with a 1:250 000 geological map overlay of the Karibib pegmatite district indicating the locations of the Rubicon and Helicon pegmatites in relation to each other (Google, 2012).

Due to the extensive workings at the Rubicon and Helicon pegmatites, the bodies are relatively easily accessible by four-wheel drive. In addition to this, they provide excellent examples of three-dimensional exposure of the internal zoning of pegmatites. This allowed for sampling to be conducted across the strike, and therefore, zonation of the pegmatites.

4.2.2 The Rubicon Pegmatite

4.2.2.1 Structural setting of the Rubicon pegmatite

Because of the thick alluvial cover in the area, the exact orientation of the Rubicon pegmatite remains unclear, however the main ore body forms a prominent ridge which strikes northwest and dips between 20° and 65° north. It measures approximately 320 m in length and 25 - 35 m in width and according to Roering's (1963) mapping has an anticlinal structure which resulted from "the upward coalescence of Li-bearing zones occurring symmetrically about two quartzose core zones" (p. 27).

At its base it is in contact with granodiorite of the ~ 566 - 557 Ma Goas Suite (Milani, pers. comm., 2013; Figure 4.3A), however in the hanging wall the ore body grades into a pegmatitic granite whose grain size diminishes progressively (Roering, 1963; Roering and Gevers, 1964). Undeformed xenoliths of granodiorites are also present in the quartzo-feldspathic footwall of the pegmatite. The Rubicon pegmatite has been dated at 505.5 ± 2.6 Ma (U-Pb ratios obtained from columbite; Melcher *et al.* 2013).

The granodiorite is composed of abundant intergrown hornblende and plagioclase with minor fine-grained (0.3 - 0.5 mm) quartz, biotite, magnetite, and zircon. The hornblende grains are larger (~ 1.3 mm) than the other minerals and contain abundant and small (0.1 mm) inclusions of magnetite, plagioclase, quartz and biotite (Figure 4.3B). Individual plagioclase grains are also poikilitic, containing hornblende and magnetite.

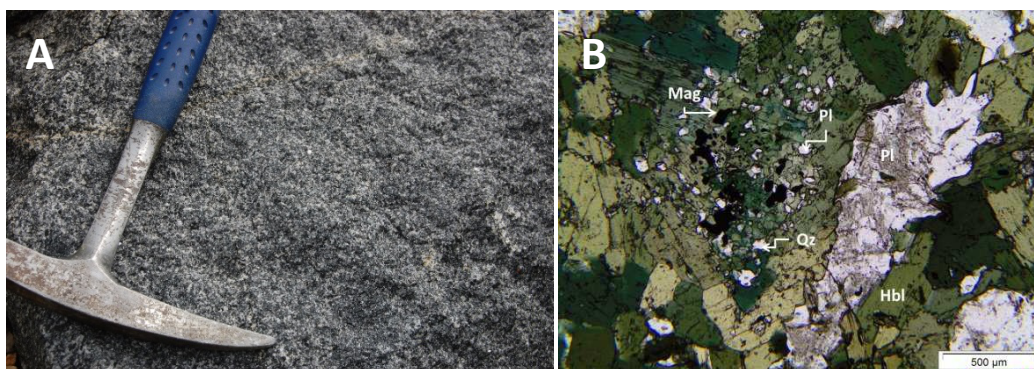


Figure 4.3: Goas Suite granodiorite into which the Rubicon pegmatite has intruded; A) Goas Suite xenolith hosted in the Wall Zone (see text) of the pegmatite. The xenolith measures approximately 2.5 m x 3 m and is situated in the footwall of the pegmatite; B) Poikilitic hornblende (Hbl) containing plagioclase (Pl), quartz (Qz) and magnetite (Mag) inclusions (ppl). Large hornblende grains are intergrown with plagioclase crystals of similar dimensions (GPS: UTM 33 K 597133 7557437).

4.2.2.2 Internal zonation and mineralogy of the Rubicon pegmatite

Roering (1963) used the generalised pegmatite zonation pattern of Cameron *et al.* (1949) (see Chapter 3) as a basis for the description of the zones identified in the Rubicon pegmatite, and using this model he identified border, wall, intermediate and core zones; a map showing the distribution of these zones is shown in Figure 4.4A and delineated in Figure 4.4B.

Legend

	albite - perthite - quartz - muscovite
	quartz - muscovite
	giant perthite
	beryl - bearing zone
	petalite - rich zone
	lepidolite - albite - petalite
	low - grade lepidolite ore
	high - grade lepidolite ore
	quartzose core zone

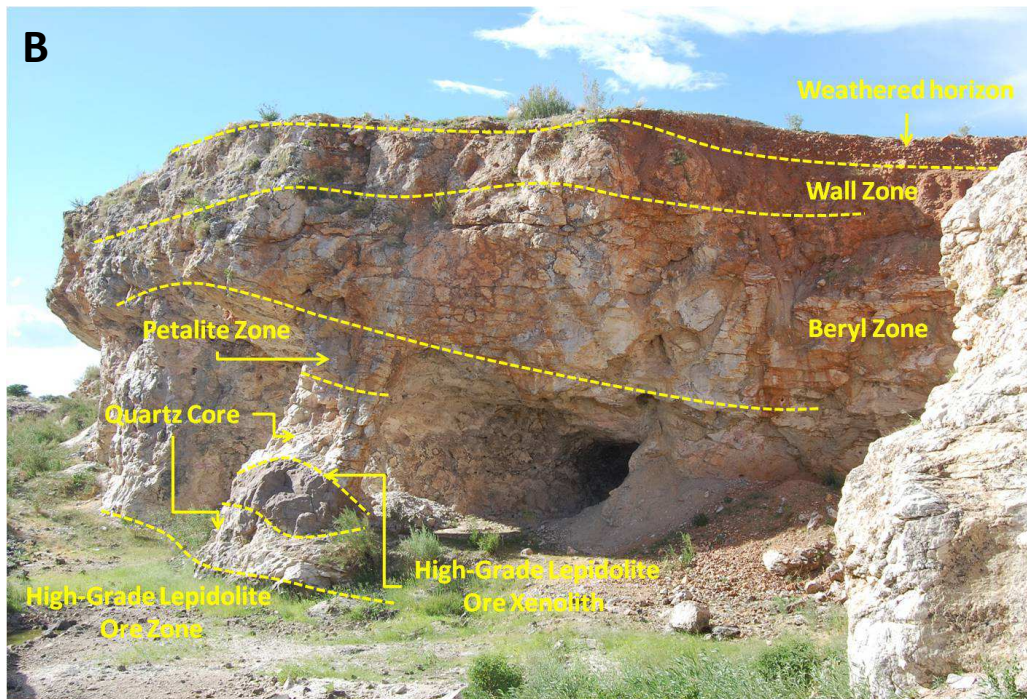
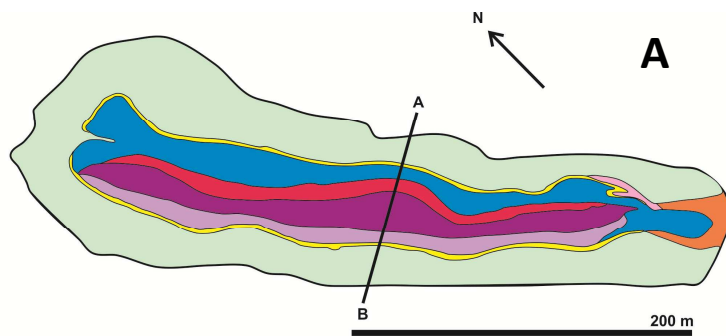


Figure 4.4: Zonation observed in the Rubicon pegmatite; A) schematic diagram of the zonation identified, with line A-B indicating the approximate location of the sampling transect; B) Mineralogical zonation in the hanging wall. Although Roering (1963) states that the Core Zone of the pegmatite is not composed of massive quartz, a small (~ 1 - 2 m) lens of massive quartz is present. Note that the Perthite Zone described in the text is situated in the footwall of the body, thus is not indicated in this figure (GPS: UTM 33K 602738 7555297).

4.2.2.2.1 Wall Zone:

This outer zone is variable in thickness but is generally a few metres thick. It contains albite, quartz, muscovite and garnet (spessartine). Quartz, muscovite and garnet tend to occur together in a more albite-rich matrix, and tourmaline (schörl) occurs as an accessory phase intergrown with albite, muscovite, and quartz. Large muscovite grains are poikilitic, containing small (up to 0.55 mm) grains of albite which are oriented along the long axis of the muscovite grains. Quartz grains show a similar

texture, enclosing grains of albite and minerals of the columbite-tantalite series (Figure 4.5). Veins up to 2 mm wide and containing albite, quartz and minor, fine-grained, altered muscovite sporadically cross-cut all minerals in this zone.

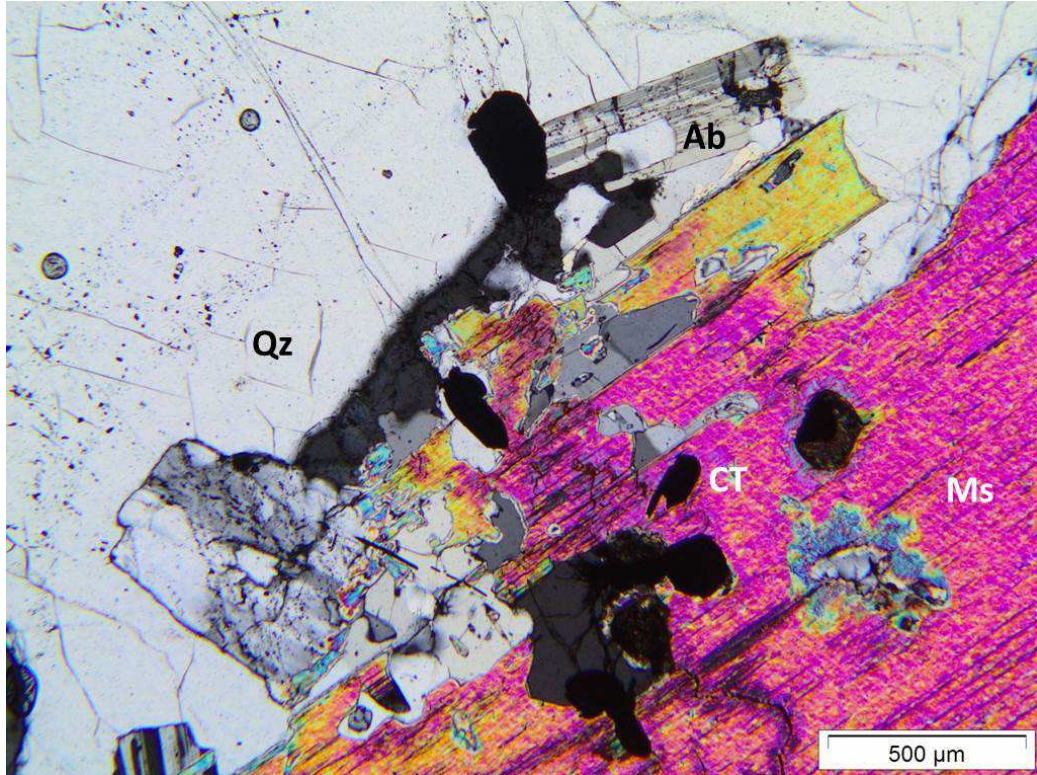


Figure 4.5: Poikilitic quartz (Qz) and muscovite (Ms) from the Wall Zone. Quartz and muscovite are intergrown and contain inclusions of euhedral albite (Ab) and columbite-tantalum oxides (CT; cross-polarised light). Note the reaction rim surrounding albite where it has been enclosed by muscovite

4.2.2.2.2 Perthite Zone

Like the Wall Zone, the thickness of the Perthite Zone is variable. Its mineralogy consists of quartz, Li-muscovite, lepidolite, microcline-perthite, cleavelandite, with accessory pale green to white beryl, apatite, and Li-phosphates (Diehl, 1992c). Locally individual perthite crystals reach dimensions of 1 x 3 m.

4.2.2.2.3 Beryl Zone

The Beryl Zone is 1 - 2 m thick. It contains cleavelandite and muscovite, quartz, lepidolite, perthite and accessory phosphates, with beryl as the primary economic mineral. Perthite crystals form nuclei which are enveloped by a rim of

albite/cleavelandite and subordinate quartz; albite displays a corrosive relationship with perthite, which is followed by a rim of muscovite and quartz to form "rosette" structures as large as 30 cm in diameter (Figure 4.6; Roering, 1963; Roering and Gevers, 1964). Albite in the Beryl Zone displays a poikilitic texture and contains small (0.02 - 0.2 mm) grains of lepidolite and albite.

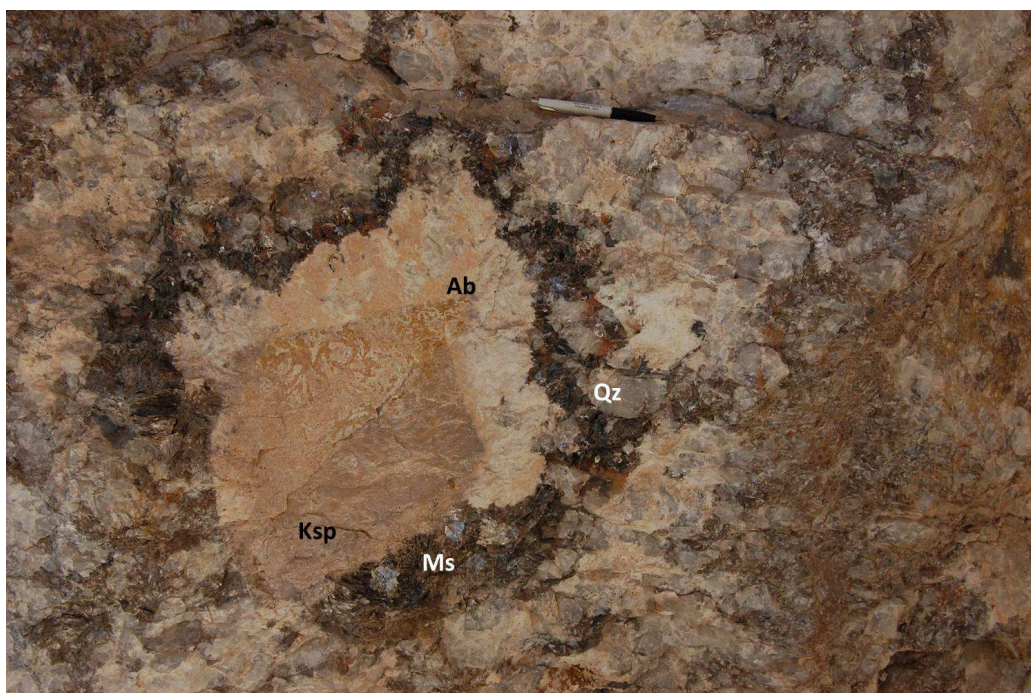


Figure 4.6: Perthite (Ksp) "rosette" from the Beryl Zone. A large perthite grain (Ksp) is enveloped by a cleavelandite (Ab) rim which is in turn enclosed by a rim of radiating muscovite and blocky quartz (GPS: UTM 33 K 602833 7555257; pencil for scale is 13 cm long).

4.2.2.2.4 Lithium Ore Zones

Two major lithium ore zones occur in the Rubicon pegmatite. These are the 1 - 6 m thick Petalite Zone, and the Lepidolite Zone which is in excess of 10 m thick. The mineralogy of the Petalite Zone is variable, ranging from pure petalite to an assemblage of petalite, albite, lepidolite, amblygonite, and subordinate quartz, with accessory columbite, apatite, fluorite, and Li-phosphates. Individual petalite crystals reach a length of 1.5 m (Figure 4.7A). At the micro-scale petalite grains are seen to be replaced by radiating nests of hectorite which also displays replacement textures where in contact with lepidolite (Figure 4.7B).

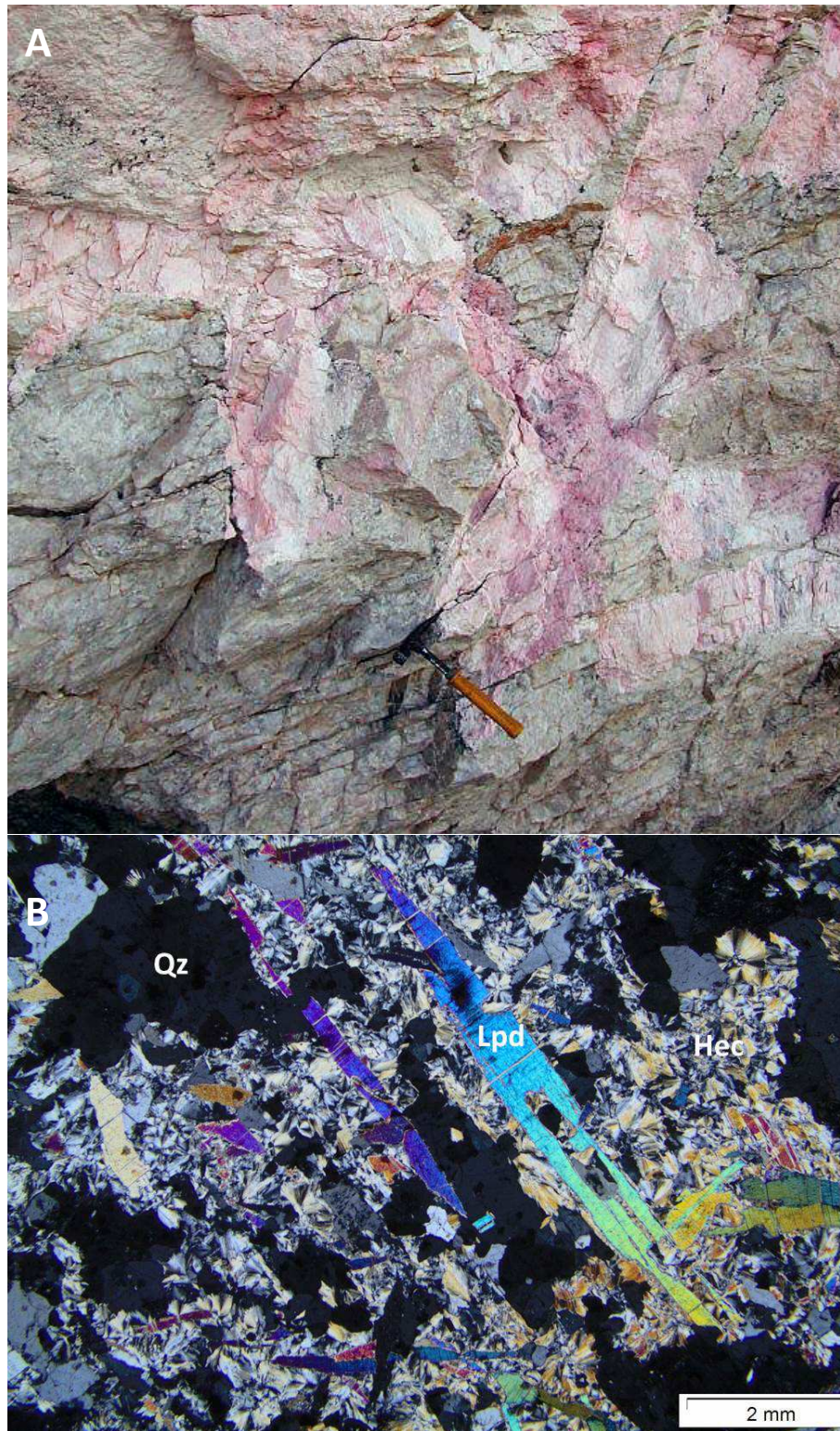


Figure 4.7: Petalite from the Petalite Zone of Rubicon pegmatite; A) Giant petalite crystals reach lengths as great as 1.5 m (photo courtesy of the Giant Crystal Project, <http://giantcrystals.strahlen.org/africa/rubicon.htm>); B) Large (up to 7 mm) lepidolite (Lpd) grains being replaced by hectorite (Hec; after petalite). Quartz and lepidolite are intergrown (xpl).

The Lepidolite Zone is slightly less complex in mineralogy than the Petalite Zone and includes lepidolite, albite, quartz, amblygonite, and petalite. It has been subdivided into low-grade ore and high-grade ore zones, distinguishable from each other by their percentage albite content. The intergrowth of lepidolite and albite shows vermicular textures, as shown in Figure 4.8A. At the microscopic scale, albite and lepidolite, in both the High and Low Grade Lepidolite Ore Zones, are fine-grained (0.2 mm). Locally large (up to 5 mm long) albite grains occur and these are poikilitic, containing small (0.02 mm) grains of lepidolite (Figure 4.8B).

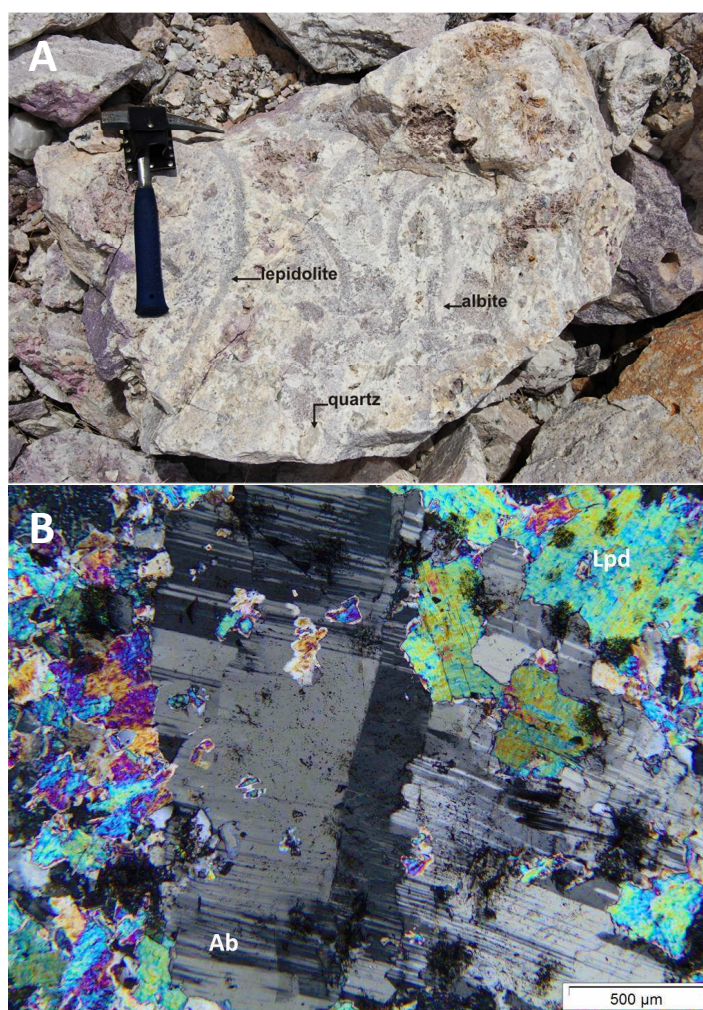


Figure 4.8: Relationship between albite and lepidolite in the Lepidolite Zone of the Rubicon pegmatite; A) Vermicular intergrowth of lepidolite and albite in the Low Grade Lepidolite Zone (GPS: UTM 33 K 602763 7555263); B) Fine-grained lepidolite intergrown with a larger grain of albite from the High Grade Lepidolite Ore Zone, The large albite is poikilitic, containing inclusions of lepidolite. Albite is a minor constituent of the mineralogy in this zone and is more commonly fine-grained with grains measuring 0.2 mm (xpl).

4.2.2.2.5 Core Zone

The Core Zone is only developed as pure massive quartz in the northern parts of the pegmatite where the zone reaches a thickness of 1.5 - 2 m. To the south lepidolite, albite, petalite, amblygonite and beryl are intergrown with quartz in this zone. Roering and Gevers (1964) attribute the mineralogical complexity of the Core Zone to the mixing of the final quartz-rich melt fraction with the adjacent lepidolite- and petalite-rich zones.

4.2.3 The Helicon Pegmatites

4.2.3.1 Structural setting of the Helicon pegmatites

The Helicon pegmatites include Helicon I and Helicon II., which are located approximately 7 km north-northeast of the Rubicon pegmatites. Helicon I is the larger of the two bodies; it is an elongate and lens-shaped body, measuring ~390 m in length and 65 m in width (Roering, 1963; Diehl, 1992b). Helicon II, south of the main pegmatite, is similarly shaped and measures approximately ~250 m in length and 50 m in width. For reasons pertaining to accessibility and sampling ease, Helicon II was sampled for the purposes of this study.

Helicon I and II are similarly orientated, striking east - west and dipping between 43° and 70° north. They have been emplaced into marbles of the Karibib Formation (Swakop Group) which also strike east - west, however dip 35° - 45° south. The marbles in this area are composed of alternating calcite-rich and actinolite-rich layers measuring 0.1 - 0.6 mm. They show extensive deformation in the form of a-symmetric boudinage and micro- to-centimetre-scale z-folds (Figure 4.9A and B).

Steeply-dipping fractures oriented sub-parallel to the strike of the pegmatite occur throughout the body. They are spaced at intervals of approximately 10 cm from each other and slicken sides on their surfaces indicate sinistral movement along the fracture planes.

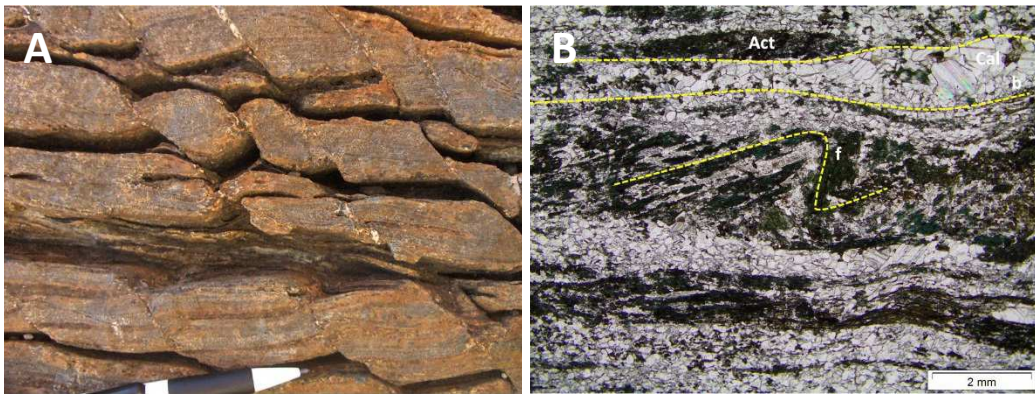


Figure 4.9: Features of the Karibib Marble in the vicinity of the Helicon pegmatites; A) A-symmetric boudinage observed in the marble (photo courtesy of K. Naydenov); B) Micro-folding (f) and boudinage (b) present in both calcite (Cal)- and actinolite (act)-rich layers (GPS: UTM 33 K 605773 7561642).

4.2.3.2 Internal zonation and mineralogy of the Helicon II pegmatite

Like the Rubicon pegmatite, the Helicon pegmatites are zoned bodies comprising outer quartzo-feldspathic zones with lithium and beryllium mineralisation occurring in the intermediate zones which are centred partially symmetrically around a massive quartz core. Roering (1963) did extensive mapping and compiled detailed descriptions of the zonation of Helicon I, however because of limited access Helicon II was sampled for the purpose of this study. The zones present in the Helicon II are described and illustrated (Figure 4.10) below based on field observation, the work of Roering (1963), and Cameron *et al.*'s (1949) models for mapping zoned pegmatites:

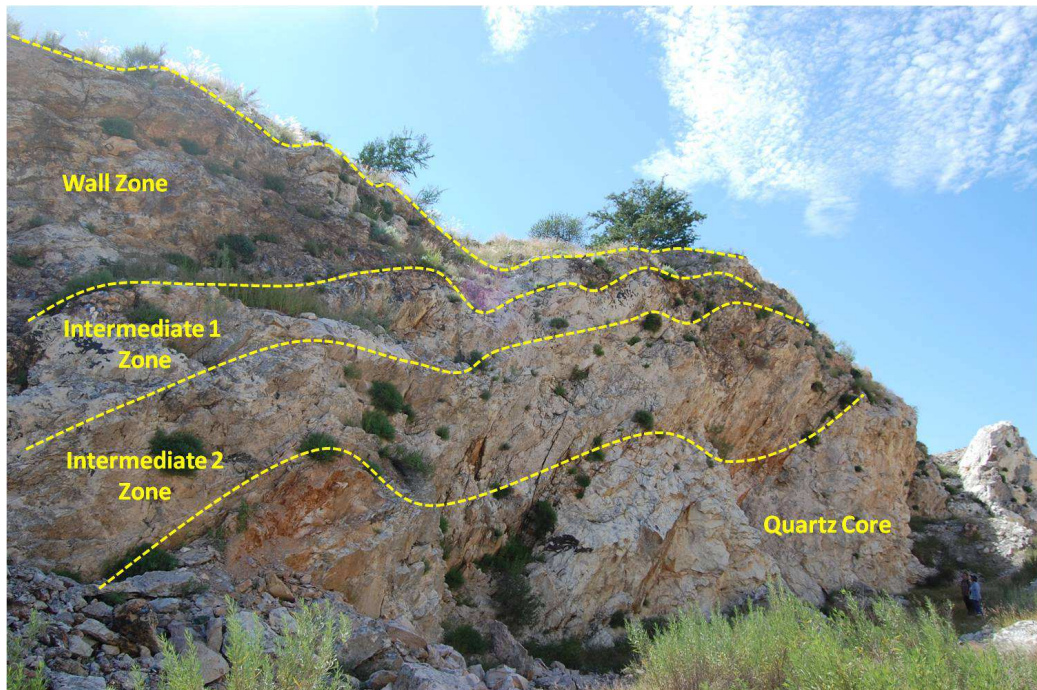


Figure 4.10: Mineralogical zonation in the footwall of Helicon II pegmatite. Note that the Lepidolite/Lithium Ore Zones described in the text occurs in the hanging wall of the pegmatite and is thus not indicated in this figure (GPS: UTM 33 K 605739 7561564).

4.2.3.2.1 Albite-quartz-muscovite (perthite) Zone (Wall Zone)

The outermost Wall Zone of Helicon II is approximately 4 m thick and is composed predominantly of albite (cleavelandite), quartz, and muscovite with accessory perthite, rare beryl, blue tourmaline, and columbite. The grain size of feldspar grains is variable, typically measuring between 0.5 and 3 cm in length. They occur as radiating/feathery nests showing undulatory extinction and bent twins. At the macro-scale quartz occurs as large, blocky crystals, however in thin section it can be seen also to occur as 0.2 - 0.5 mm annealed grains. Muscovite grains are large (> 3 cm) and form radiating nests (Figure 4.11). Locally, small (~ 50 μm) grains of muscovite and albite mark the interface between quartz and feldspar grains. Blue Tourmaline crystals have an acicular habit and, like muscovite, form nests, 15 - 20 cm long, of radiating blades (Figure 4.11). Tourmaline is poikilitic, containing inclusions of quartz whose orientation is largely, however not exclusively, crystallographically controlled.

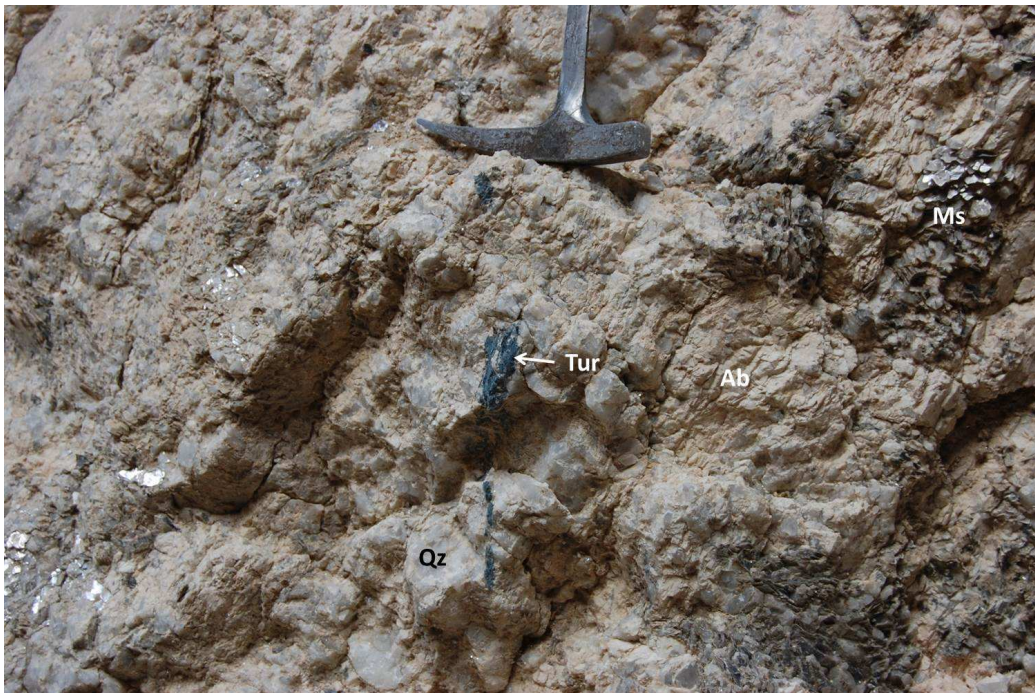


Figure 4.11: Tourmaline (Tur) and muscovite (Ms) nests in the Wall Zone of the Helicon II pegmatite. Tourmaline appears to overprint quartz and albite (Ab; GPS: UTM 33 K 605846 7561573).

4.2.3.2.2 Albite-quartz-petalite Zone (Intermediate Zones)

The Intermediate Zone is approximately 4.5 m wide and is composed of intergrown quartz and albite and large (up to 30 cm long) petalite crystals. Field observation suggests that it can be further subdivided into two zones, an outer petalite deficient zone (Intermediate 1 Zone; Figure 4.10), and an inner Intermediate 2 Zone (Figure 4.10) where petalite is more abundant. The petalite crystals are altered to hectorite and Mn-oxide dendrites are abundant on weathered surfaces of this zone. Phosphate dendrites are more abundant in the Intermediate 2 Zone where petalite mineralisation is more significant.

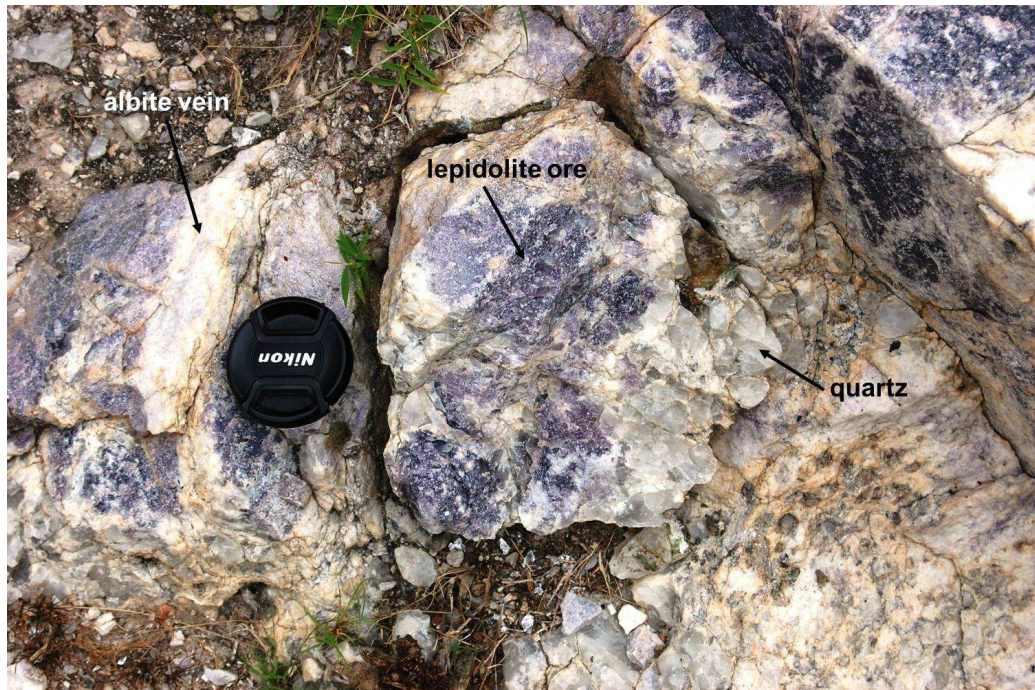


Figure 4.12: Low grade lepidolite ore at the Helicon II pegmatite. Lepidolite is intergrown with saccharoidal albite and blocky quartz (GPS: 33 K 605756 7561564).

4.2.3.2.3 Lepidolite Zone (Lithium Ore Zone)

The Lepidolite Zone is broad measuring over 10 m in width. The dominant minerals in the Zone are lepidolite, zinnwaldite, albite and quartz in varying proportions and accessory phases include minor muscovite, columbite-tantalite minerals, white beryl, amblygonite, and blue and pink tourmaline. Similar to the Lithium Ore Zone of the Rubicon pegmatite, the Lepidolite Zone at Helicon II has been subdivided into two zones, a high grade ore and a low grade ore zone based on albite content. The high grade ore zone is composed of fine-grained (0.2 - 0.5 mm) lepidolite and zinnwaldite whereas the low-grade ore zone contains abundant saccharoidal albite with minor blocky quartz (Figure 4.12). Lepidolite growth is patchy and locally forms worm-like structures measuring up to 30 cm in length, similar to those observed at the Rubicon pegmatites (see Figure 4.8A); the mineral also occurs as fine-grained (0.2 - 0.5 mm) grains intergrown with saccharoidal albite grains of similar dimensions.

4.2.3.2.4 Core Zone

The Core Zone is composed of massive quartz. It is developed as a thick (~ 3.5 m) pod in the central parts of Helicon II adjacent to which mineralised zones occur in both the foot and hanging walls. The quartz in this zone is milky due to the presence of abundant fluid inclusion trails. The trails appear to be oriented parallel to the strike of the pegmatite.

4.3 Sn-bearing pegmatites of the Damara Belt: Uis and Karlowa pegmatites

4.3.1 Introduction

Tin- and lithium-tin-niobium-tantalum-bearing pegmatites of the LCT variety are found in the Uis area (see Figures 4.1 and 4.13). They are located in the Cape Cross - Uis Pegmatite Belt, also known as the Northern Tin Belt, which is located in the Northern Zone, with its western-most extension located in the Southern Kaoko Zone (see Figure 4.1). The belt is 24 km wide and extends 120 km inland in a northeasterly direction from Cape Cross on the Namibian coast (Diehl, 1990; 1992a, 1993); it represents a half graben, bounded to the southeast by the Autseib Fault, which formed in a tensional environment and may have been active since Proterozoic times (Richards, 1986; Wagener, 1989; Diehl, 1992a; Diehl, 1993). Figure 4.13 shows the location of the Uis and Karlowa pegmatites in relation to each other, and to the town of Uis.

The pegmatites in this area were first discovered in 1911, and were mined on a small-scale for 40 years. Large-scale mining commenced in 1951 when the then newly-constituted Uis Tin Mine Company (SWA) acquired the property. For the following two decades Uis became established as the largest low-grade, hard rock tin-bearing pegmatite mine in the world (Richards, 1986; Diehl, 1992a), with production rates reaching 140 000 kg tin concentrate (67.5 % metallic tin) per month from 85 000 tons of ore in 1989 (Diehl, 1992a). Niobium and tantalum oxides were important by-products of the tin mining in the Uis area, however the recovery of these minerals proved difficult when they occurred as intergrowths with cassiterite, and they were

only recoverable from the slag after smelting at the time (Diehl, 1992c) Due to the low price of tin, and the low grade of the deposit, production ceased in 1990 (Diehl, 1992c).

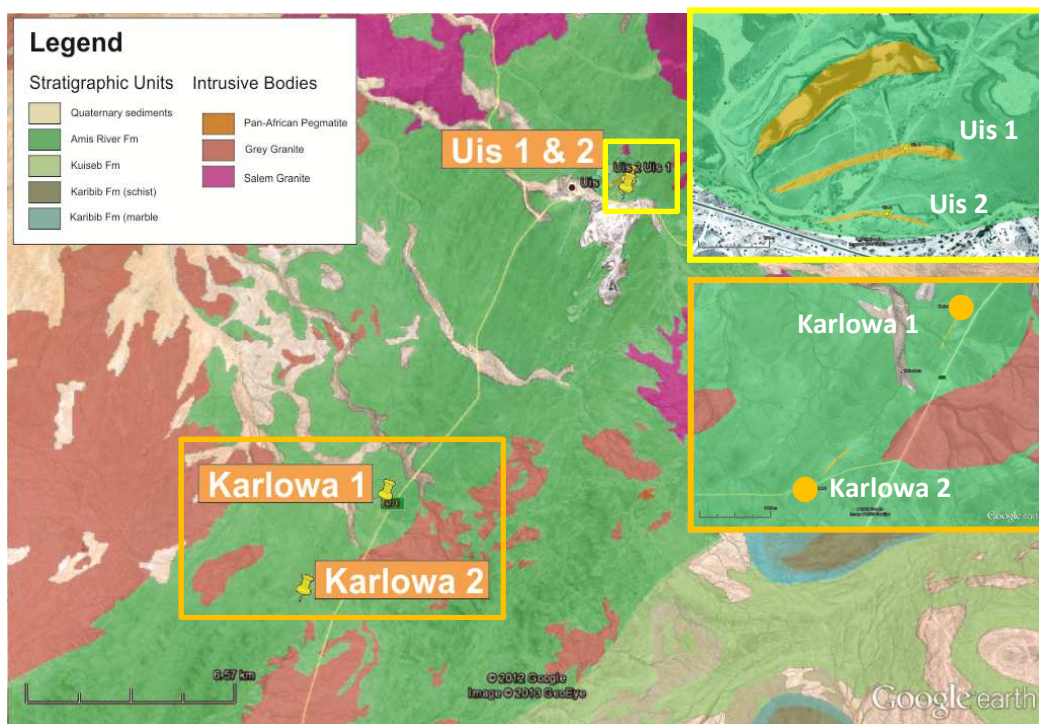


Figure 4.13: Google Earth map with a 1:250 000 geological map overlay of the Uis-Karlowa pegmatite district indicating the locations of pegmatites of the Uis and Karlowa swarms in relation to each other (Google, 2012). The yellow-bordered and orange-bordered insets show the individual Uis and Karlowa areas respectively at a larger scale.

Because of extensive flooding in the main pit at the Uis mine, the largest and most significant K5 pegmatite could not be sampled, however two of the eight main pegmatites mined were sampled due to the ease with which they could be accessed as well as their good exposure. Of the Karlowa pegmatites, again two bodies were sampled based on their exposure and ease of accessibility. Although these individual bodies do not appear to have been mined, in the strictest sense of the term, they have been extensively trenched, probably for the purposes of exploration or small-scale tin extraction.

4.3.2 The Uis Pegmatite Swarm

4.3.2.1 Structural setting of the Uis pegmatites

The Uis pegmatite swarm, also known as the central pegmatite swarm of the Cape Cross - Uis Pegmatite Belt, is 60 km long and 5 km wide; it comprises approximately 120 pegmatite bodies striking northeast, and dipping between 30° and 70° northwest (Richards, 1986; Wagener, 1989; Diehl, 1992a; Diehl, 1993; Singh, 2007). The sizes of pegmatites in the Belt are variable, usually attaining a few hundred metres in length and up to 10 m in width, however individual bodies are large, reaching dimensions of up to 1 km in length and 50 m in width (Figure 4.14; Richards, 1986; Diehl, 1992a; Diehl, 1993; Singh, 2007, 2009). Haack and Gohn (1988) and Diehl (1993) obtained ages between 486 ± 8 Ma (Diehl, 1993) and 496 ± 30 Ma (Haack and Gohn, 1988) for their emplacement.

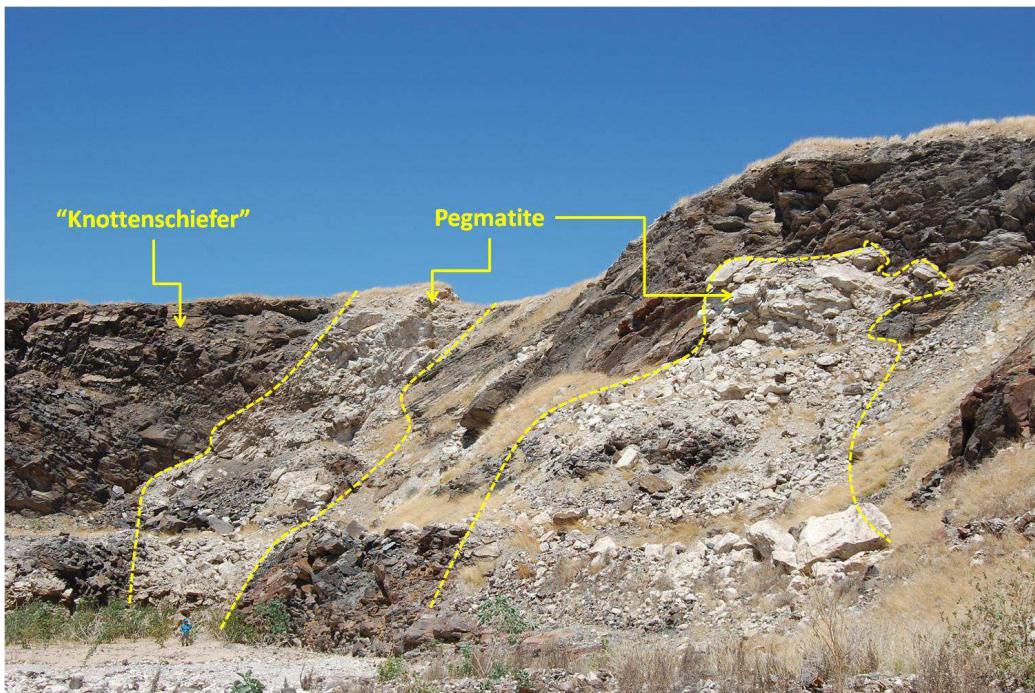


Figure 4.14: Unzoned Uis pegmatites intruding into the "knotted" schists of the Khomas Group (see text for details), exposed in a subsidiary pit at the abandoned Uis Tin Mine. (GPS: UTM 33 K 487930 7653565).

The pegmatites are hosted in the biotite-schists, "knotted schists" and quartzites of the Khomas Subgroup (Swakop Group, Amis River Formation). The diablatic schists, also known as "knotted schists" or "knottenschiefer" (Figure 4.15A), which are

composed of biotite and quartz, with minor plagioclase, muscovite and pyrite. The reason for their peculiar name is that they contain circular to lenticular "knots" measuring anything from a few millimetres to ~ 2 cm which are composed of a core of fine-grained (15 - 30 μm) quartz and biotite enclosed by a rim of larger (30 - 50 μm) biotite grains (Figure 4.15B).

The knotted schists act as a useful marker horizon since economic pegmatites show preferential emplacement within them (Richards, 1986) and where pegmatites have intruded into them the metasediments are bleached and/or fractured (Haack *et al.*, 1980; Diehl, 1993; Richards, 1986; Keller *et al.*, 1999; Singh, 2007, 2008). They are folded by metre-scale northwest verging open to tight folds whose axial planar cleavage strikes northeast and dip 30° east southeast. Pegmatite emplacement is parallel to the axes of the folds.

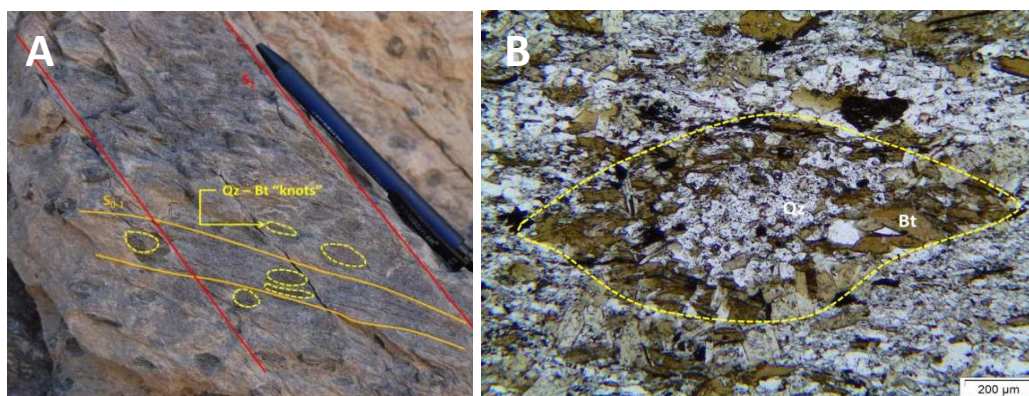


Figure 4.15: "Knottenschiefer"/"knotted" schist A) Exposure in a pit at the Uis Tin Mine (GPS: UTM 33 K 488085 7653561); B) Lenticular quartz (Qz)-biotite (Bt) "knot" in plane-polarised light. Individual "knots" locally appear to be randomly oriented however in other outcrops and in thin section they show elongation in the direction of S_{0-1} (indicated in orange), which is defined by the alignment of biotite grains. S_{0-1} strikes northeast-southwest, however it has been gently folded resulting in variable dip angles either to the northwest or southeast.

The "knotted schists" contain appreciable amounts of tin with concentrations ranging from 0.05 - 0.294 % Sn (Richards, 1986). Wagener (1989) identified a systematic distribution of tin among the Uis pegmatites, with the highest values occurring in bodies immediately adjacent to the stanniferous schists, particularly in the vicinity of boudin-like pinches in the country rock.

4.3.2.2 Mineralogy of the Uis pegmatites

The Uis pegmatites are large, pervasively albitised bodies, which do not display any conspicuous zoning such as that observed in the Li-Be-bearing bodies of the Karibib area (Richards, 1986; Diehl, 1992a; Diehl, 1993; Keller *et al.*, 1999; Singh, 2007, 2008, 2009), however their contacts with the country lithologies are marked by a highly micaceous rind where the direction of mica growth is perpendicular to the contact. They are typically coarse-grained, and their mineralogy is dominated by quartz, albite, muscovite and/or sericite (Richards, 1986; Diehl, 1992a; Diehl, 1993; Singh, 2007, 2008, 2009).

Accessory phases are abundant, and include cassiterite, minerals of the columbite - tantalite series, zircon, and Li-minerals such as amblygonite, lepidolite, and petalite, which occur in saccharoidal albite-rich replacement zones (Richards, 1986; Diehl, 1992a, b, c; Diehl, 1993; Singh, 2007, 2008). In addition to these, rare accessory phases such as spodumene, monazite, topaz, garnet, tourmaline, apatite and beryl, pyrite, galena, malachite, azurite, and calcite, to name a few, occur (Richards, 1986; Diehl, 1992a; Keller *et al.*, 1999).

Quartz typically occurs as large, blocky crystals measuring in excess of 2 cm, although fine-grained (1 - 2 mm) annealed quartz grains have been observed in thin section. Albite in the pegmatites is subhedral to euhedral and aplitic. Locally, fine-grained albite aggregates form radiating nests while larger individual grains are poikilitic, containing inclusions of muscovite, lepidolite and smaller euhedral albite grains. Myrmekitic textures are also observed at the boundaries between quartz and albite grains. Muscovite and lepidolite tend to be interstitial to quartz and albite grains, however they also occur as inclusions within poikilitic quartz, albite, and cassiterite grains. Cassiterite grains are anhedral to subhedral in shape and contain inclusions of muscovite and albite (Figure 4.16). The size of cassiterite grains is variable, typically measuring between 0.2 mm and 2 mm.

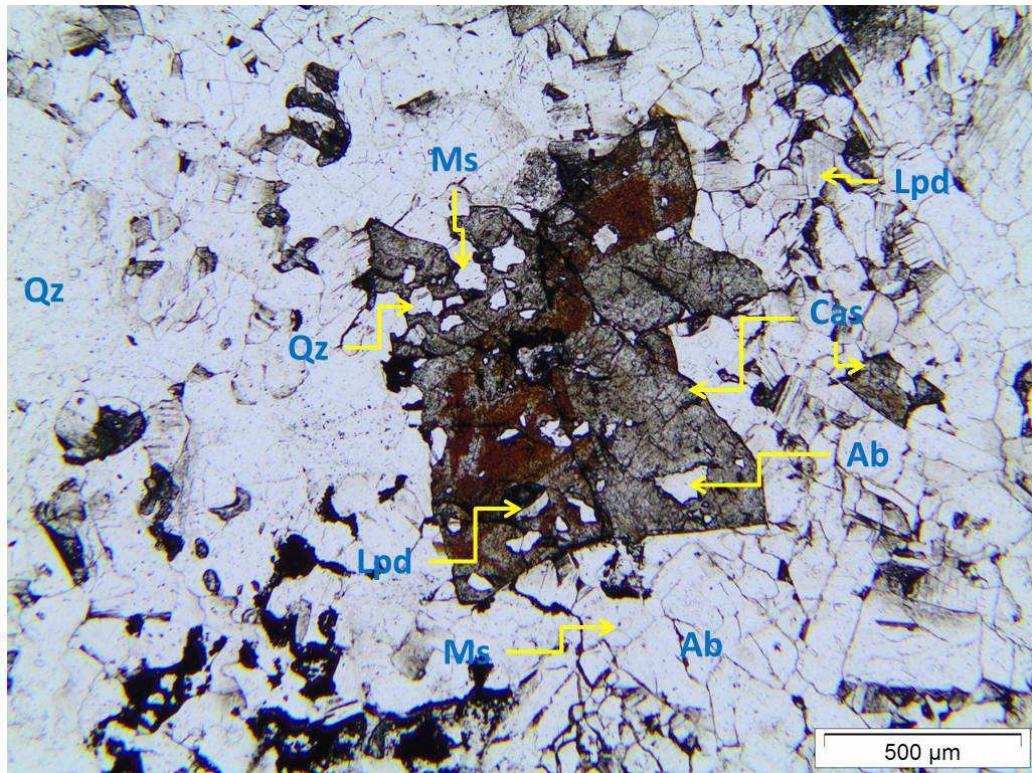


Figure 4.16: Anhedral and zoned cassiterite (Cas) grains overprinting a groundmass of albite (Ab), quartz (Qz), muscovite (Ms) and lepidolite (Lpd). The cassiterite grain contains abundant inclusions of the minerals present as groundmass (ppl).

4.3.3 Karlowa Pegmatite Swarm

4.3.3.1 Structural setting of the Karlowa pegmatites

The Karlowa pegmatite swarm has not been as extensively studied as the Uis and Karibib pegmatite swarms. Like the Uis pegmatite swarm, it constitutes part of the Cape Cross - Uis pegmatite belt (Northern Tin Belt, see Figure 4.1), and is located approximately 30 km south to southeast of the Brandberg Complex (Northern Zone/Southern Kaoko Zone; Diehl, 1993).

Karlowa pegmatites are relatively small in comparison to the dimensions of the Karibib and Uis pegmatites, measuring up to 120 m in length and 5 m in width; they strike northeast and dip approximately 35° to the north. Individual bodies have a sinuous shape, and Diehl (1993) suggested their passive emplacement of pegmatitic melt into an echelon Riedel fractures (Figure 4.17). Diehl (1993) proposed an age of 485 ± 6 Ma

for the emplacement of the Karlowa pegmatites, which is similar to the ages determined for the Uis pegmatites.

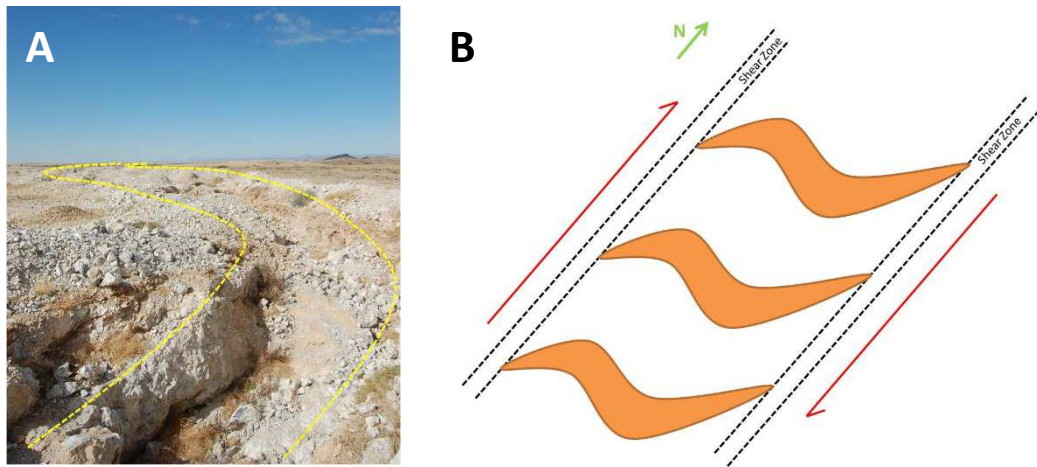


Figure 4.17: The Karlowa pegmatite swarm A) Sinuous unzoned pegmatite; B) schematic representation of the emplacement of pegmatites into en echelon sigmoidal tension gashes (modified after Richards, 1986; GSP: UTM 33 K 480212 7643761).

Like the pegmatites in the Uis area, the Karlowa pegmatites have intruded into stanniferous (~ 0.0 5 % Sn, this study) meta-sedimentary lithologies of the Khomas Subgroup (Swakop Group, Amis River Formation; Diehl, 1992a, 1993). The metasediments strike east - west and dip between 45° and 60° east southeast. The metapelites are composed of biotite, quartz and magnetite with minor tremolite. Biotite grains are relatively coarse-grained (80 - 150 µm) and define the foliation in the lithology (Figure 4.18). Quartz grains are a similar size (~ 100 µm) and are annealed; some grains contain small (15 µm) inclusions of biotite. Magnetite is much finer-grained (30 - 35 µm) than biotite and quartz and grains are typically euhedral. The Karlowa pegmatites do not appear to have intruded into the same "knotted" horizon of the Amis River Formation schists that the Uis pegmatites have.

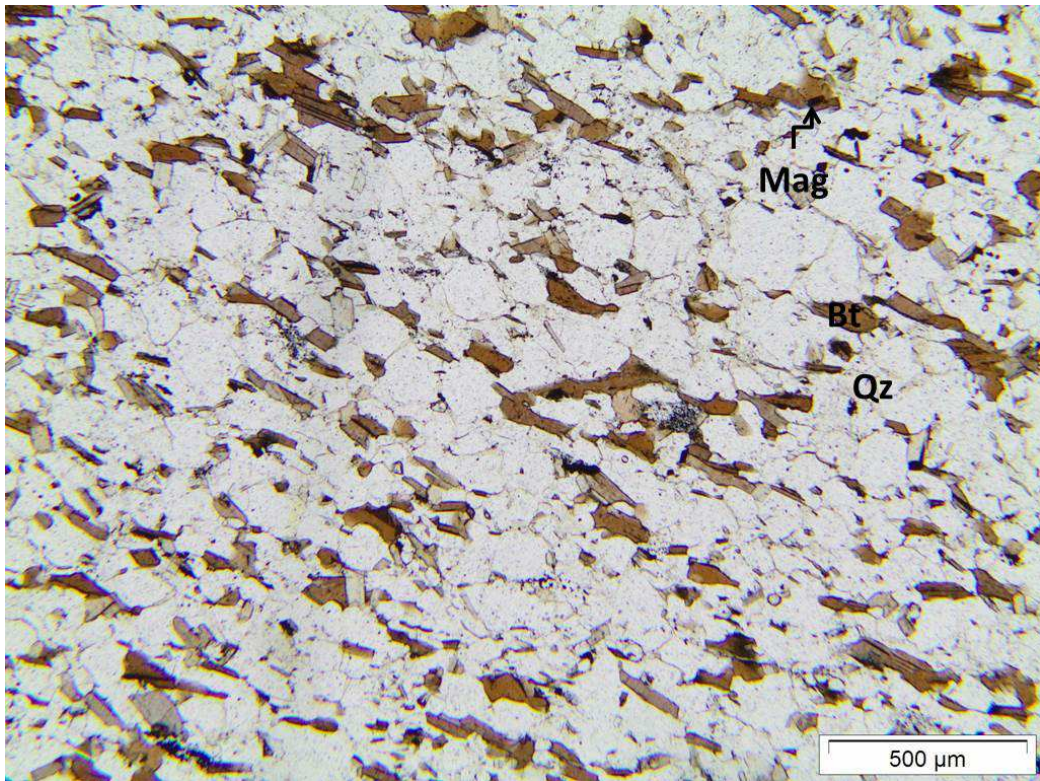


Figure 4.18: Photomicrograph of metapelites into which the Karlowa pegmatites have intruded, composed predominantly of quartz (Qz) with subordinate biotite (Bt) and magnetite (Mag). The foliation of the rock is defined by the alignment of biotite grains.

4.3.3.2 Internal zonation and mineralogy of the Karlowa pegmatites

Overall, the mineralogy of the Karlowa pegmatites, including those sampled, is dominated by quartz, albite and Li-rich muscovite with accessory phases including Li-alumino-silicates, particularly spodumene, minerals of the columbite - tantalite series, and cassiterite, the latter most prominently developed in greisens and associated with yellowish-red haematite halos and saccharoidal albite (Diehl, 1992a, c, 1993).

Although some of the Karlowa pegmatites are of the unzoned Uis-type, the majority of them show some vague zoning, however this may vary in prominence between different bodies (Diehl, 1993). The zoning in the Karlowa pegmatites, as observed in the bodies sampled, is described below:

4.3.3.2.1 Border Zone

This outermost zone is relatively narrow (~ 10 - 15 cm wide) and is composed of an extremely coarse-grained intergrowth of muscovite (up to 10 cm long) and blocky quartz, typically 5 - 10 cm in size. The mica shows unidirectional crystal growth perpendicular to the contact with the country rock (Figure 4.19).

4.3.3.2.2 Intermediate Zone

The Border Zone grades into a progressively coarser-grained intermediate zone (Figure 4.19) containing predominantly quartz, muscovite and albite, with some spodumene, cassiterite, and columbite - tantalite mineralisation, and accessory zircon.

Quartz is blocky and occurs as large (5 - 10 cm) blebs within fine-grained, saccharoidal albite. Individual crystals contain small (100 μm) inclusions of muscovite and albite. The saccharoidal texture of albite is defined by euhedral albite crystals of variable dimensions (100 μm - 1 mm). Individual grains are poikilitic, containing 40 - 350 μm inclusions of muscovite. Some of the albite grains show alteration to sericite along cleavage planes and mineral boundaries. Muscovite and spodumene are subordinate phases in this Zone; where muscovite crystals do occur they are relatively small, measuring approximately 1 cm. Spodumene crystals are significantly smaller (< 1 mm) and contain variably-sized (100 - 800 μm) inclusions of muscovite.

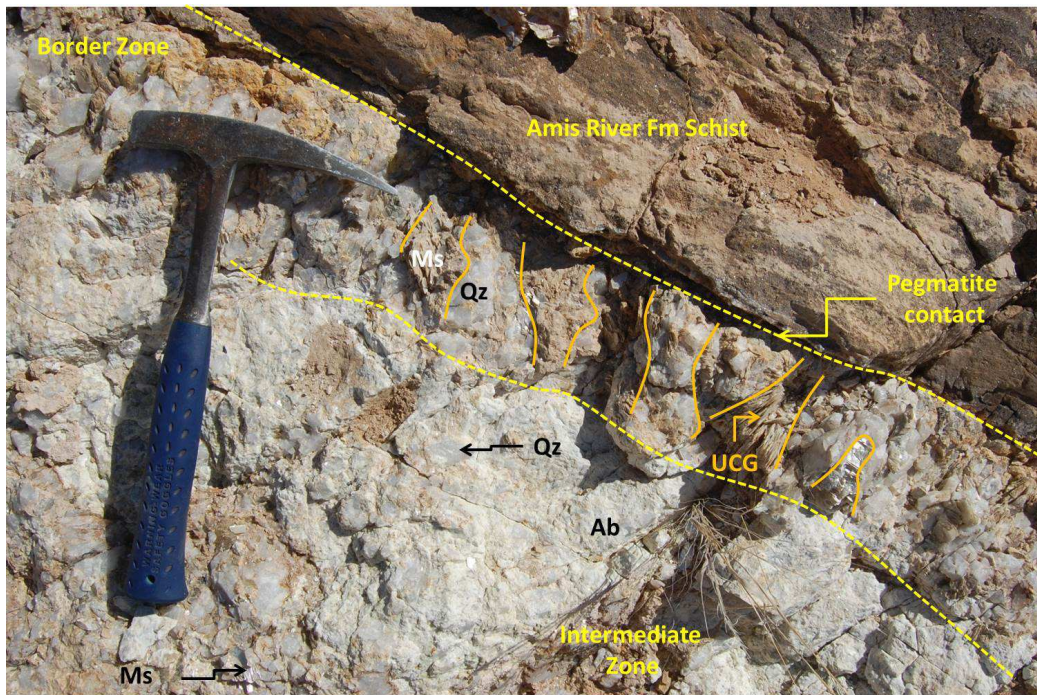


Figure 4.19: Zonation observed in a pegmatite of the Karlowa swarm. The contact with the Amis River Formation schists is sharp and zones are developed parallel to the contact. Unidirectional crystal growth (UCG indicated in orange) is present in large muscovites (Ms) intergrown with blocky quartz (Qz) in the Border Zone. The Intermediate Zone is composed of quartz (Qz), albite (Ab), and muscovite (Ms; GPS: UTM 33 K 477645 7640796).

4.3.3.2.3 Core Zone

Similar to the large, lithium-beryllium pegmatites of the southern Central Zone, this innermost zone of the Karlowa pegmatites is composed of massive quartz. The quartz is milky containing numerous, randomly orientated trails of fluid inclusions. The interface between the core and intermediate zones is extremely micaceous, with the growth of large (up to 3 cm) muscovite crystals oriented perpendicular to the edge of the core.

4.4 Tourmaline-bearing pegmatites of the Damara Belt: Usakos and Omapyu pegmatites

4.4.1 Introduction

Tourmaline is the most significant of Namibia's semi-precious stones and is found predominantly in Pan-African pegmatites of the Damara Belt (Schneider and Seeger, 1992 and references therein). The first significant discovery of tourmaline was made prior to World War I approximately 3 km east of Usakos (see Figure 4.1), in a pegmatite that was being worked for cassiterite (Schneider and Seeger, 1992). Since then a number of pegmatites, located predominantly in the Karibib District (Karibib Pegmatite Belt, Figure 4.1), have contributed towards Namibia's tourmaline production. These include the Usakos, Neu Schwaben, Becker's and Omapyu pegmatites, to name a few. In 1986, Namibia's tourmaline production values reached an all-time high, when its annual production value reached 2580 kg tourmaline (Schneider and Seeger, 1992).

The variety of colours of the Namibian tourmalines is extensive, and ranges from black, and blue, to green, pink, watermelon, and red. In addition to coloured tourmalines, the pegmatites of the Karibib District have produced spectacular specimens of quartz and beryl, many of which are housed at the Kristallgalerie in Swakopmund.

Two pegmatites from the Karibib Pegmatite Belt (Figure 4.1) - an approximately 100 km long and 50 km wide feature that extends northeast from Usakos, and which is located in the southern Central Zone - were selected and sampled for the purpose of this study. Both of the pegmatites have been mined in the past, and are currently still being worked to some degree for gem-quality tourmaline. Because of the extensive working, they are relatively easily accessible, however, as a result of it, the structural relationships between the pegmatites and their country rocks are not very clear.

4.4.2 The Usakos Pegmatite

4.4.2.1 Structural setting of the Usakos pegmatite

The Usakos pegmatite is a large (600 m long, ~ 350 m wide), zoned body that strikes northeast and has intruded obliquely into schists of the Kuiseb Formation (Swakop Group). Although tourmaline mineralisation occurs throughout the pegmatite, gem-quality tourmaline occurs specifically in 0.4 - 2 m wide kaolinised miarolitic cavities within the Intermediate Zone (feldspar-quartz zone, see descriptions of zonation below; Schneider and Seeger, 1992). The tourmaline crystals are green to blue in colour, with rare occurrences of red tourmaline (Reuning, 1923; Schneider and Seeger, 1992). At the time of this study, although mining operations were underway, no cavities were exposed, therefore descriptions are based purely on published references.

The Usakos pegmatite is located within the Usakos Pegmatite Field (Karibib Pegmatite Belt; Figures 4.1 and 4.20), whose emplacement is related to doming in the Usakos area and the development of the Usakos Dome and Kranzburg Syncline (Owen, 2011). Owen (2011) identified four pegmatite generations in the Usakos area based on the cross-cutting relationships that they exhibit with one another, deformation present in pegmatitic bodies, variations in their emplacement style, and their positions within the Damaran stratigraphy. According to this classification, the Usakos pegmatite is a fourth generation pegmatite, i.e. late syn-D₂ - post-D₂, which has been emplaced in the axial trace of the Kranzburg Syncline.

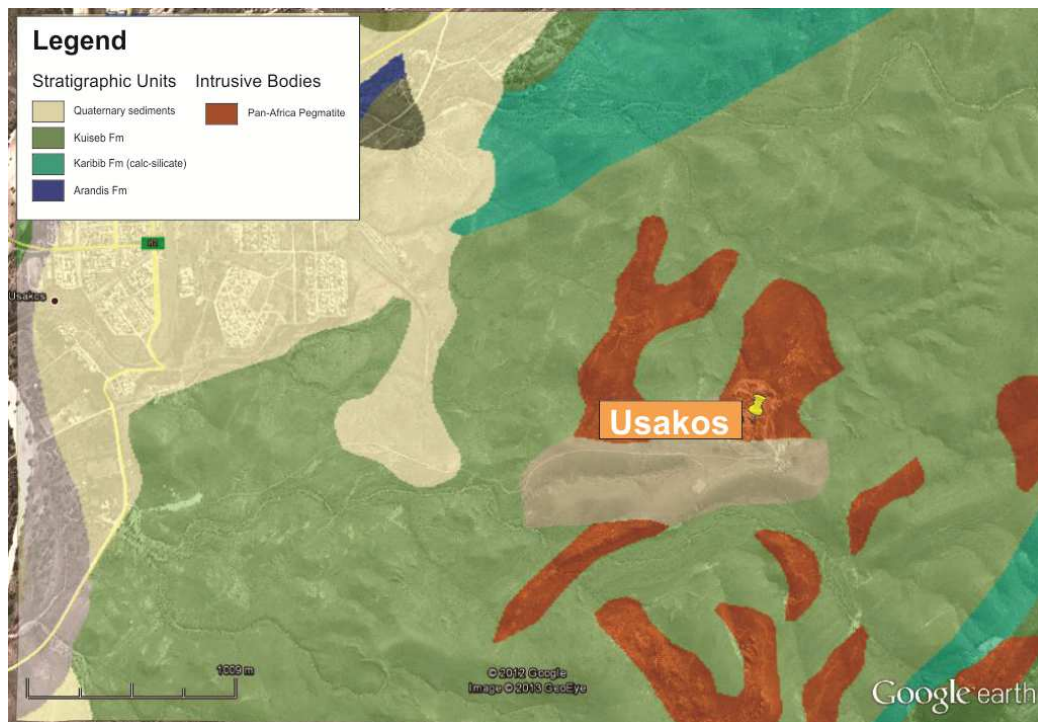


Figure 4.20: Google Earth map with a 1:250 000 geological map overlay of the Usakos Pegmatite Field indicating the location of the Usakos pegmatite east-southeast of the town of Usakos (Google, 2012).

The Kuiseb schists in the area are composed of fine-grained (200 - 300 μm) biotite, quartz, plagioclase, and magnetite, with accessory muscovite. Biotite grains are euhedral and aligned, defining the S_2 fabric in the rock (Figure 4.21A). Quartz and plagioclase grains are annealed, and magnetite occurs either as isolated subhedral to euhedral grains or as patchy disseminations. Locally, the metapelites in the vicinity of the pegmatite are "knotted" like those in the proximity of the Uis pegmatites. The "knots" are lenticular and measure anything from 2.5 mm to ~ 2 cm in length. They comprise an inner core of poikilitic quartz, plagioclase, and biotite, all containing inclusions of each other, enveloped by an outer core of similar composition, although containing less biotite, and finally a thin rind of biotite (Figure 4.21B). Quartz veins cross-cut the fine-grained quartz-plagioclase-magnetite-muscovite assemblage, however biotite growth overprints the veins.

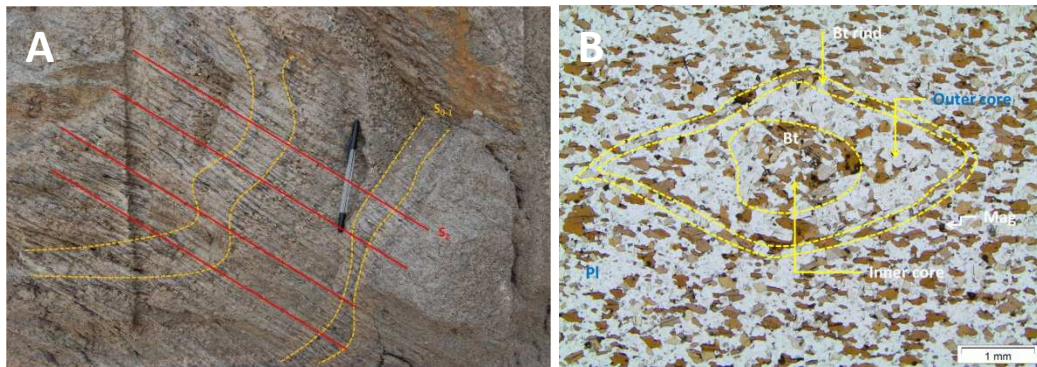


Figure 4.21: Kuseib schist adjacent to the contact with the Usakos pegmatite (GPS: UTM 33 K 563537 7566171); A) The bedding plane (S_{0-1} indicated in orange) dips steeply ($\sim 86^\circ$) to the north, while S_2 dips more shallowly ($\sim 35^\circ$) to the southeast; B) A lenticular "knot" in the Kuseib schist observed in plane-polarised light (plagioclase = Pl, biotite = Bt, magnetite = Mag).

4.4.2.2 Internal zonation and mineralogy of the Usakos pegmatite

Although the zonation in this pegmatite is not as complexly developed as in the Rubicon and Helicon pegmatites, individual zones can be identified and are shown (Figure 4.22A and B) and described briefly in the sections to follow.

4.4.2.2.1 Border Zone

This narrow zone, measuring approximately 30 cm or less, marks the contact between the Kuseib schists and the pegmatitic body. Its mineralogy comprises predominantly muscovite intergrown with tourmaline (schörl) and minor, blocky quartz ($\sim 5 - 8$ cm wide). Muscovite blades typically measure approximately 5 cm in length, and together with tourmaline crystals of 5 - 10 cm in length define a zone of unidirectional crystal growth (UCG) oriented perpendicular to the pegmatite contact (Figure 4.23).

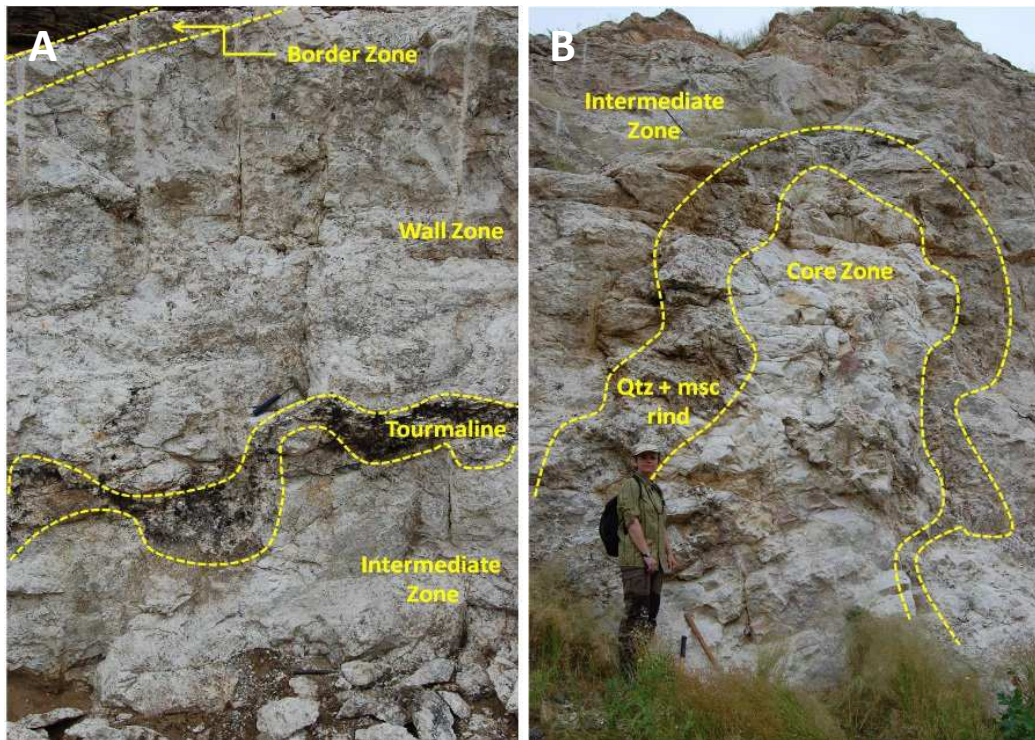


Figure 4.22: Zonation observed in the Usakos pegmatite A) Zonation in the footwall. The Wall and Intermediate Zones are separated by a thick, undulating band of tourmaline. In general, however, the zones of the pegmatite are developed parallel to sub-parallel to the contact between the pegmatite and country rock (GPS: UTM 33 K 563514 7566182); B) Zonation observed in the central parts of the pegmatite. Note that the zones are developed concentrically about the quartzose Core Zone (GPS: UTM 33 K 563511 7566132).

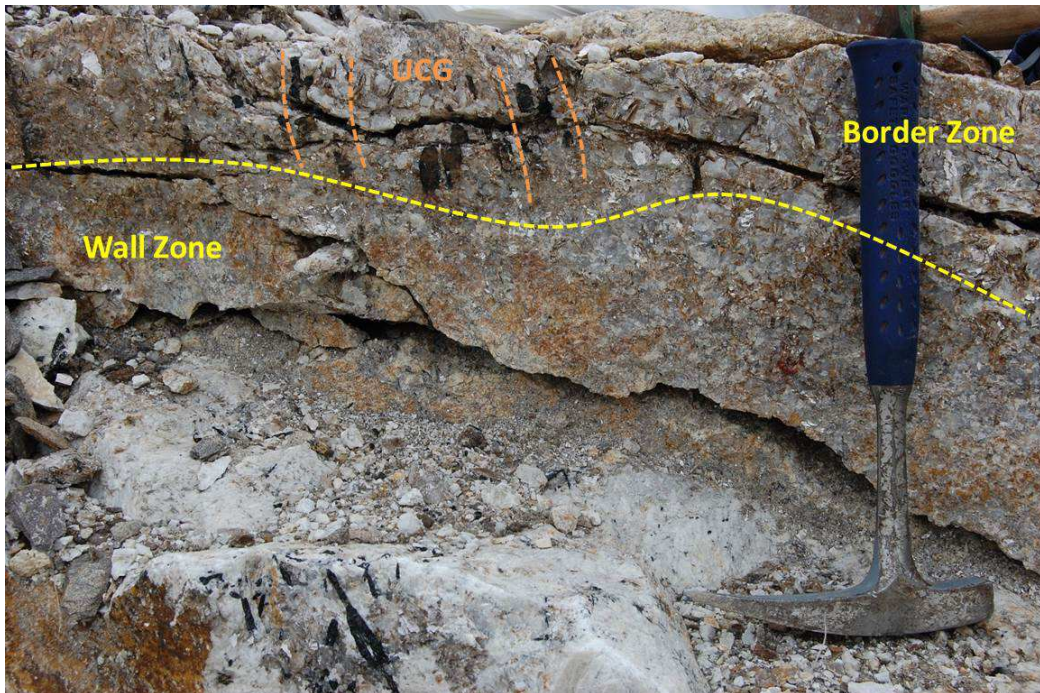


Figure 4.23: Border Zones of the Usakos pegmatite, showing UCG defined by the intergrowth of muscovite and black tourmaline (GPS: UTM 33 K 563516 7566178).

4.4.2.2.2 Wall Zone

The 2 m thick wall zone consists of equigranular quartz, albite, muscovite and schörl. Mineral grains are typically extremely coarse-grained, measuring a few centimetres. Individual muscovite and albite grains are poikilitic, with muscovite grains containing albite inclusions and vice versa. It is separated from the adjacent intermediate zone by a 10 - 15 cm wide band of tourmaline, again oriented with the long axis perpendicular to the contact of the pegmatite (see Figure 4.22A).

4.4.2.2.3 Intermediate Zone

The mineralogy in this zone is dominated by albite and quartz, with minor relatively fine-grained tourmaline and muscovite. Large (5 cm) lenses of quartz are intergrown with blocky albite; their orientation is crystallographically controlled, causing a graphic texture in the rock. Fine-grained (~ 2 mm) muscovite blades are also intergrown with the albite along crystallographic planes, however less so where the graphic texture is present. Tourmaline occurrence is sporadic. The Intermediate Zone contains large (20 cm - 1 m) xenoliths of deformed Kuiseb schist (Figure 4.24).

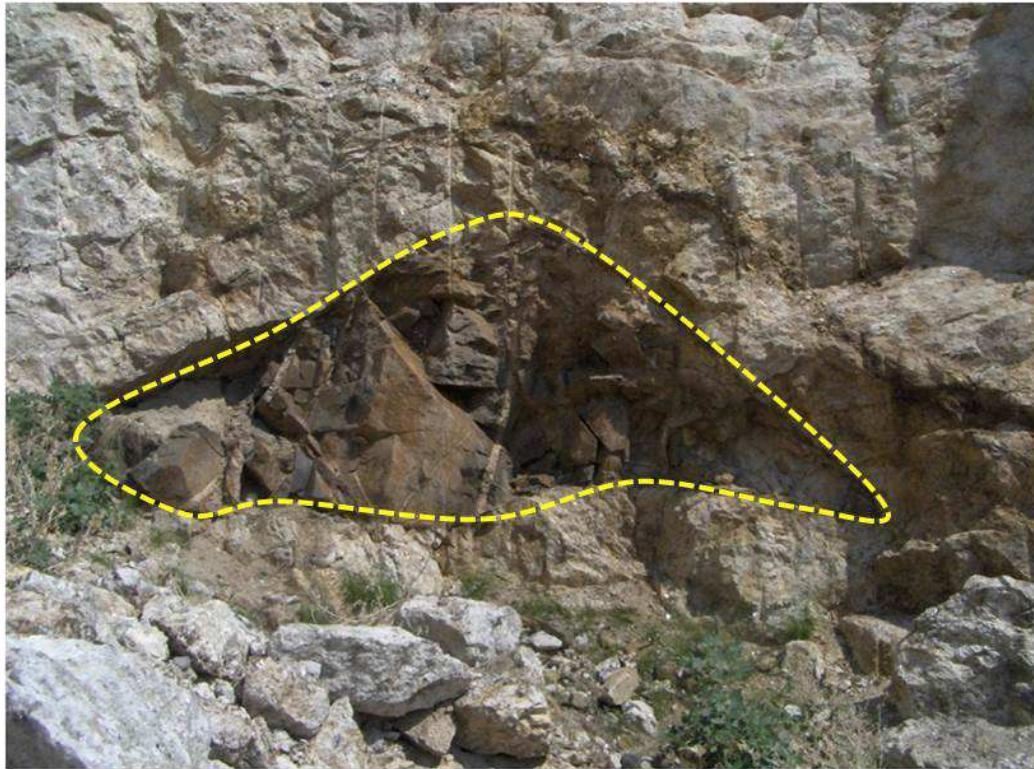


Figure 4.24: Schist xenolith (outlined in yellow) in the Intermediate Zone of the Usakos pegmatite (photograph courtesy of K. Naydenov).

4.4.2.2.4 Core Zone

The mineralogy of the Core Zone is dominated by massive milky quartz. Minor amounts of lepidolite, blue tourmaline and montebrasite are present however the mineralisation of these accessory phases is patchy. The Core Zone is surrounded by a thick (up to 50 cm), coarse-grained (in the order of a few centimetres) rind of intergrown muscovite and quartz (Figure 4.22B) whose growth is perpendicular to the interface between the Intermediate and Core Zones.

4.4.3 The Omapyu Pegmatites

4.4.3.1 Structural setting of the Omapyu pegmatites

Almost no work has previously been done on the Omapyu pegmatites, however records indicate that they were worked in the past for small quantities of gem-quality blue, green, and pink tourmaline (Schneider and Seeger, 1992). The majority of gem-quality tourmalines in the area have been extracted from the largest of the

pegmatites, which has been exposed diggings at least 50 m long, 20 m wide, and 6 m deep.

The Omapyu pegmatites occur in a swarm on the southern parts of the farms Omapyu Sud 77 and Omapyu Sud II 76 (Schneider and Seeger, 1992), approximately 44 km northeast of Karibib and 34.5 km southeast of Omaruru (Southern Tin Belt, southern Central Zone; Figures 4.1 and 4.25). On average individual bodies measure approximately 5 m in width and 10 - 20 m in length, although the largest of the pegmatites measures 70 m in length and 50 m in width. They strike northeast, dip 50° southeast, and they have intruded obliquely as a series of en echelon bodies into the marbles of the Karibib Formation (Swakop Group; Figure 4.25).

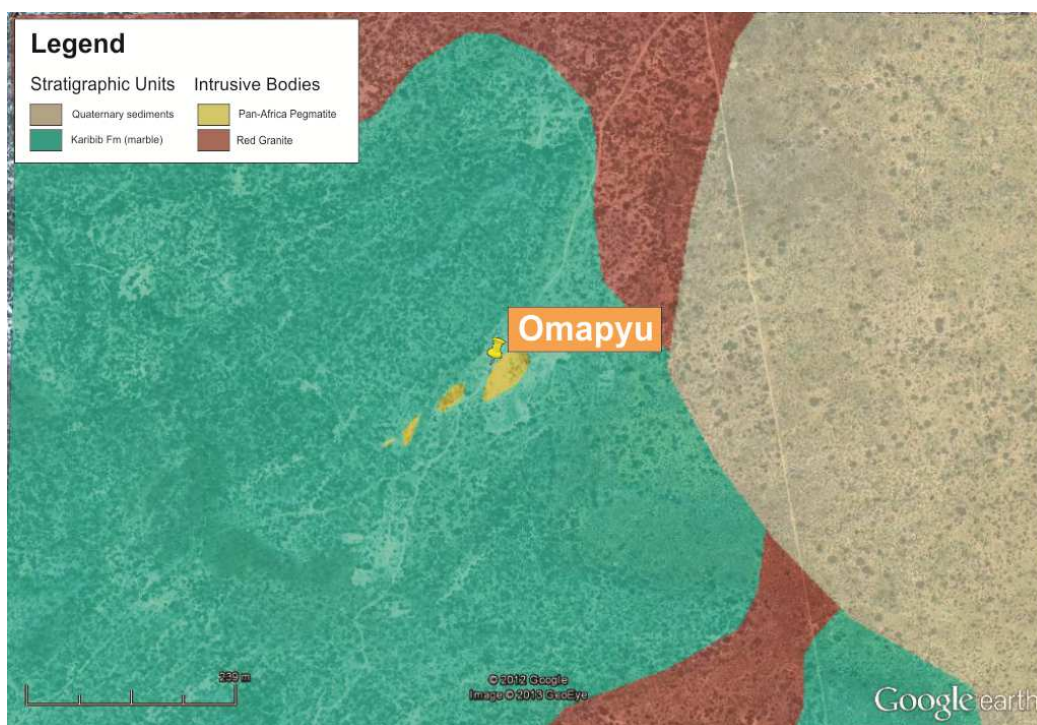


Figure 4.25: Google Earth map with a 1:250 000 geological map overlay of the Omapyu pegmatites (Google, 2012).

The marbles strike northeast - southwest and dip approximately 55° to the northwest. They are composed of large (0.5 - 1 mm), annealed calcite grains with minor amounts of muscovite and magnetite. At the macro-scale, large quartz lenses, measuring up to 5 cm are seen to occur sporadically along the bedding planes in the marble (Figure 4.26).



Figure 4.26: Karibib marble adjacent to the largest pegmatite in the Omapyu pegmatite swarm (GPS: UTM 33 K 619983 7601521).

4.4.3.2 Mineralogy of the Omapyu pegmatites

The mineralogy of the Omapyu pegmatites is dominated by quartz, albite and perthite, with varying amounts of schörl and muscovite. All the minerals are intergrown and although the pegmatites do not display any conspicuous zoning, a variety of mineral textures can be observed at the macro-scale, and grain size increases from the outer parts of the pegmatites inwards.

Quartz tends to occur as blocky, anhedral masses, ranging in size from 2 - 10 cm, while albite crystals are typically tabular, measuring in excess of 2.5 mm. Quartz and perthite are also intimately associated with each other, and are often characterised by a graphic texture. Tourmaline crystals occur as broad, acicular, hexagonal crystals (0.5

- 1.5 mm long). At the macro-scale, tourmaline occurs in nests and also defines a banded texture, known as line rock (Figure 4.27), which is oriented perpendicular to the strike of the pegmatites. In the largest of the bodies, however, line rock is developed parallel to the strike of the pegmatite. Individual tourmaline crystals reach very large dimensions, some over 30 cm in length (Figure 4.28). Muscovite occurs sporadically throughout the pegmatite. Other than its patchy occurrence as large (5 - 10 cm) books, it occurs along the boundaries of quartz, perthite and, albite, and in cross-cutting veinlets.



Figure 4.27: Line rock observed in the main Omapyu pegmatite. Banding is defined by large (1 -3 cm) tourmaline (Tur) grains whose growth direction is perpendicular to the direction of propagation of the band. The groundmass is composed of a perthite (Ksp) - quartz (Qz) – albite (Ab) assemblage (GPS: UTM 33 K 619980 7601519)..

Tourmaline mineralisation occurs in kaolinised miarolitic cavities which are associated with lepidolite, muscovite, giant smoky quartz crystals (> 30 cm long), and saccharoidal albite. The cavities appear to postdate the formation of the pegmatite, however, as they occur along a northeast trending fault which dips approximately 40° to the south.

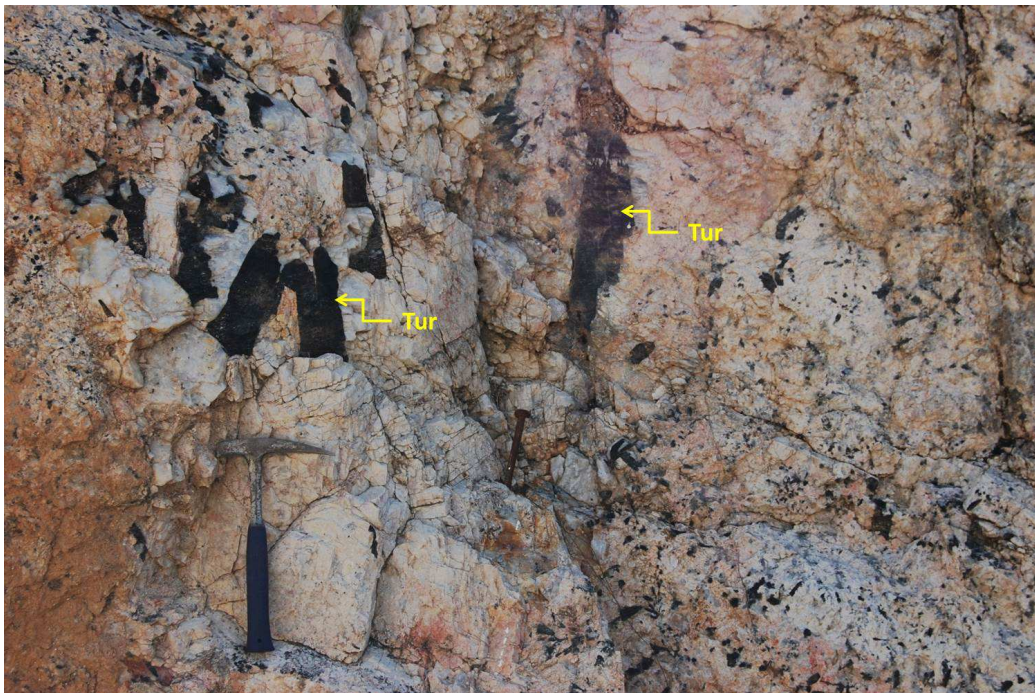


Figure 4.28: Giant black tourmalines (Tur) exposed by diggings in the largest of the Omapyu pegmatites (GPS: UTM 33 K 620103 7601613).

4.5 Pegmatitic sheeted leucogranites of the Damara Belt: Valencia Area

4.5.1 Introduction

Post-collisional uraniferous sheeted leucogranites occur in the southern Central Zone of the Damara within the Rössing Pegmatite Belt (see Figure 4.1), approximately 50 km east-northeast from Swakopmund (McDermott, 1986; Nex *et al.*, 2001b, 2002; Kinnaird and Nex, 2007). The sheeted leucogranites show a variety of textures, including graphic and pegmatitic textures, and a geochemical affinity with pegmatites of the NYF family. For the purposes of this study they shall be referred to as (uraniferous) NYF pegmatites.

Uranium mineralisation in this area was first discovered near Rössing Mountain in the early 1920s, and following continued exploration and prospecting, Rössing uranium deposit - now one of the world's leading uranium producers (containing approximately 6 % of the world's known uranium resources, and accounting for 7.5 % of the global uranium production) - was discovered (Abrahams, 2009; Freemantle *et al.*, pers.

comm., 2013; Freemantle, 2012). A rise in the uranium market in the 1970s led to extensive exploration for uranium, and with the aid of airborne surveys, a number of deposits were identified (Abrahams, 2009).

Uranium mineralisation in this area is hosted in what were termed by earlier workers as alaskites (Jacob, 1974), and later as sheeted leucogranites (e.g. Nex *et al.*, 2001b). The uranium deposits of the southern Central Zone have generated significant interest not only because of their extensive mineral wealth in terms of mineralisation, but also because they are the only producers of primary uranium-bearing ore from granitic rocks (Abrahams, 2009). Many studies have been conducted on the Rössing, Valencia, Ida Dome and Goanikontes areas, by workers such as Nex and Kinnaird (1995), Nex *et al.* (2001b), Abrahams (2009), Freemantle (2012), and Longridge (2012), to name a few, and have focused primarily on the timing of, and stratigraphic controls on, the emplacement of the pegmatites.

Four pegmatites from the Valencia area were sampled for this study. The samples were provided by G. Freemantle, who conducted extensive mapping of the Valencia area, as well as extensive mineralogical work on the pegmatites themselves. The purpose of sampling pegmatites from this area was for the purpose of conducting a more thorough comparison between the various pegmatites of the Damara Belt, without neglecting those not belonging to the LCT family.

4.5.2 The Valencia (SLGs) pegmatites

4.5.2.1 Structural setting of the Valencia (SLGs) pegmatites

The pegmatites of the Valencia area have intruded into a number of stratigraphic units in the area (Figure 4.29), including basement gneisses of the Abbabis Complex, lower Nosib Group metasedimentary units and gneisses (Etusis and Khan Formations), and the calcareous metapelitic units of the Upper Swakop Group (Rössing, Chuos, Karibib and Kuiseb Formations; Nex *et al.*, 2001b; 2002; Freemantle, 2012), which have been folded, and duplicated on a regional scale by the Kuiseb Syncline (Freemantle, 2012).

The majority of the SLGs has intruded obliquely into their host rocks, although locally they have been emplaced parallel to the regional foliation (Nex *et al.*, 2001b). In some instances their emplacement has truncated the metasedimentary packages (Freemantle, 2012). The occurrence of mineralised SLGs appears to be preferentially at, or near, the boundary between the Khan and Rössing Formations, or where the Rössing Formation is highly attenuated, and emplacement appears to be related to the transition from ductile to brittle deformation (Kinnaird and Nex, 2007).

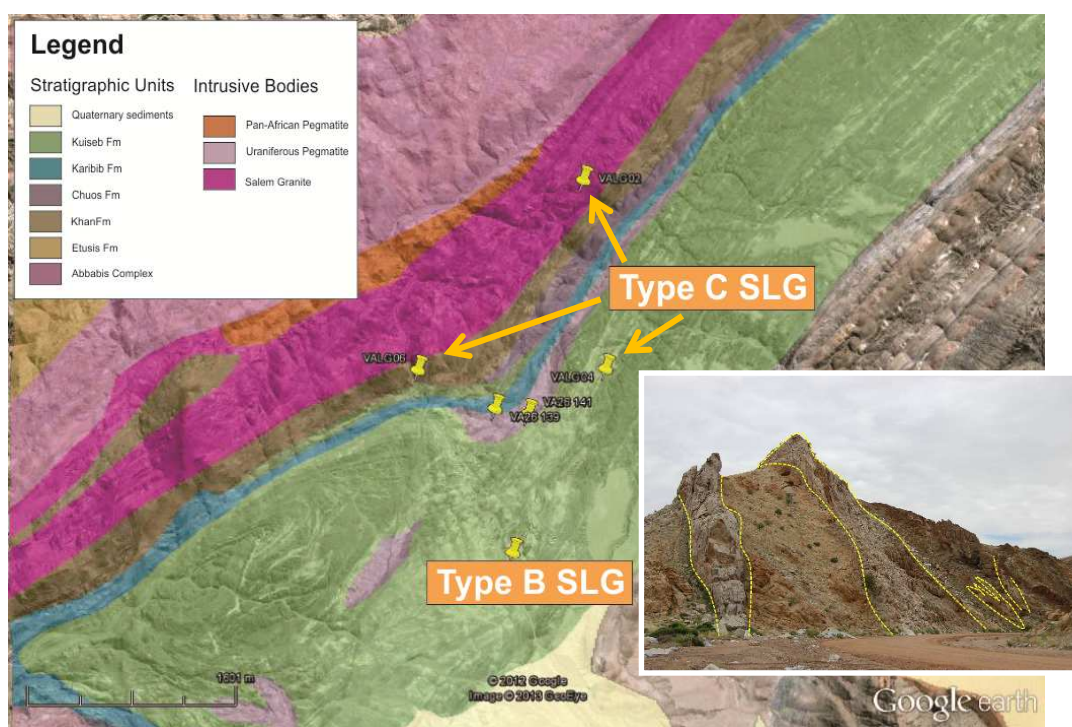


Figure 4.29: Google Earth map with a 1:250 000 geological map overlay over a portion of the Valencia area indicating the locations of surface and core samples taken by G. Freemantle (Google, 2012). Type B and C SLG are defined in section 4.5.2.2. The inset shows multiple cross-cutting generations (see text) of pegmatites as viewed from the Khan River.

While the regional model for the emplacement of mineralised NYF pegmatites in the southern Central Zone proposes that they were emplaced after the development of the D_3 extensional fabric and regional-scale doming at upper amphibolite metamorphic conditions (Kinnaird and Nex, 2007), Freemantle (2012) noted some characteristics of the Valencia deposit which make it incompatible with this model. Most notably, the emplacement of pegmatites at Valencia is not related to a regional doming event i.e. there is no competent dome-shaped structure at Valencia as there is at Rössing Uranium Mine, for example (Freemantle, 2012). Nonetheless, it is located

within the vicinity of a large basement-cored antiformal inlier (Miller, 2008), and the presence of a prominent shear zone sub-parallel to the contact between the basement-cored inlier and the overlying Damaran metasediments are indicative of similarities between Valencia and the High Strain Zone at Goanikontes (Nex *et al.*, 2001b); Freemantle, 2012).

4.5.2.2 Mineralogy of the Valencia (SLGs) pegmatites

Nex *et al.* (2001a) divided the (SLGs) NYF pegmatites of the southern Central Zone into six distinct categories, A - F (oldest to youngest) based on field observations and diagnostic structural and mineralogical characteristics (see list below). While the different types contain a similar mineral composition of quartz, alkali feldspar and feldspar, variations in their accessory assemblages appear to present a useful means in distinguishing them from one another (Freemantle, 2012). In addition to the six types of (SLG) pegmatite described, Nex *et al.* (2001b) observed that the earlier A,B, and C types were affected by the D₃ deformation event responsible for doming in the area, while Type D, E, and F pegmatites were not. In addition to this, the earlier pre-D₃ pegmatites are barren, while the post-D₃ granites are those containing appreciable amounts of uranium mineralisation (Kinnaird and Nex, 2007).

4.5.2.2.1 Type A (SLGs) pegmatites

Type A pegmatites are the oldest generation of the (SLGs) pegmatites. They are pink, fine-grained and display saccharoidal textures. Individual veins are typically fairly narrow, measuring less than 1.0 m and have been foliated by F₃ folds, a feature locally defined by the preferential alignment of biotite (Nex *et al.*, 2001b; Kinnaird and Nex, 2007; Freemantle, 2012). Freemantle (2012) noted that the Type A pegmatites in the Valencia area have been emplaced in the Khan and Kuiseb Formations.

4.5.2.2.2 Type B (SLGs) pegmatites

Type B pegmatites are more abundant than the Type A variety. They are pale cream to pink in colour and may range in texture from fine-grained to pegmatitic. These pegmatites are typically garnetiferous, with garnets occurring as disseminated grains

in the pegmatitic Type B variety, and as clusters in the finer-grained variety (Freemantle, 2012). These pegmatites may also contain tourmaline and biotite. They measure 1 - 4 m in width and the finer-grained pegmatites often show boudinaging and D₃ folds; the presence of sillimanite indicates that they were affected by a high-temperature, post-peak metamorphic thermal overprint (Nex *et al.*, 2001b; Kinnaird and Nex, 2007; Freemantle, 2012). Type B pegmatites in the Valencia area have intruded into the Kuiseb, and rarely the Chuos, Formations (Freemantle, 2012).

4.5.2.2.3 Type C (SLGs) pegmatites

Of all the pegmatites in the Valencia area, those of the Type C variety are the most abundant. They vary in colour from pink to white, and medium- to coarse-grained. These SLGs contain potassic feldspar, albite and interstitial quartz, as well as accessory tourmaline, zircon, magnetite and ilmenite. The width of the Type C SLGs is variable (0.5 - 10 m), their shape is irregular, and they typically occur in flexures associated with D₃ folding (Nex *et al.*, 2001b; Kinnaird and Nex, 2007; Freemantle, 2012).

Freemantle (2012) distinguished between tourmaline (Ct) and magnetite (Cm) Type C (SLGs) pegmatites based on variations observed in their accessory mineralogy. In the Type Ct pegmatites, tourmaline is the most prominent accessory phase. Tourmaline growth is typically massive (Figure 4.30A), however clusters composed of euhedral crystals (5 - 7 cm long) also occur. Tourmaline is intergrown with blocky, milky quartz (5 - 8 cm wide), and abundant potassic feldspar. At the microscopic scale, tourmaline and quartz are intergrown as finer-grained (~ 0.5 mm) symplectites (Figure 4.30B). Freemantle (2012) observed that these pegmatites often occur within the Kuiseb and Khan Formations.

As indicated by their name, Type Cm pegmatites are characterized by the fact that magnetite is their dominant accessory phase. They are typically medium- to coarse-grained, and are weakly foliated (Freemantle, 2012), and their emplacement is usually, although not exclusively, in magnetite- and diopside-bearing strata in the upper parts of the Khan Formation (Freemantle, 2012).

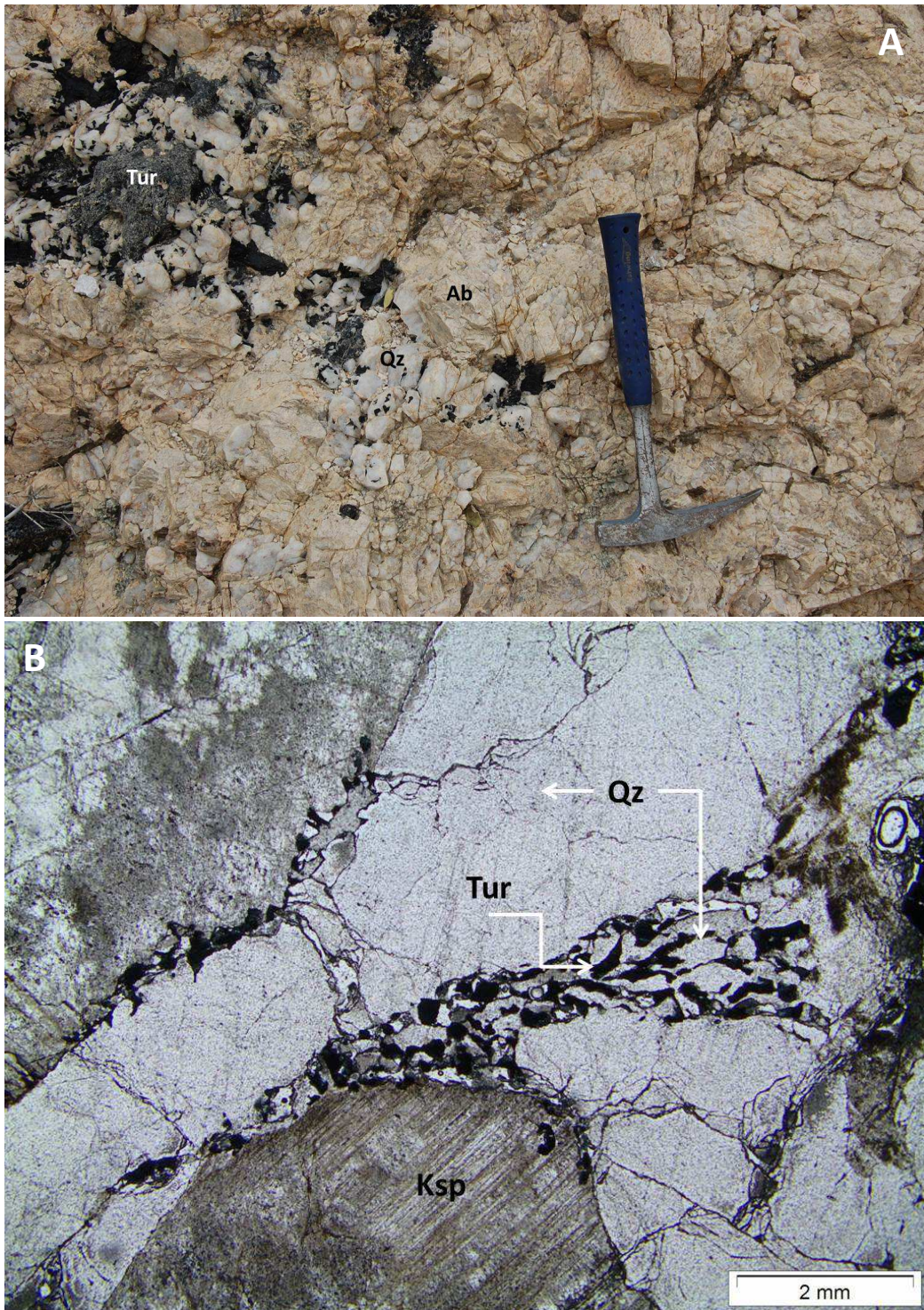


Figure 4.30: Type Ct pegmatite; A) Exposed in an outcrop along the Khan River Valley composed of extremely coarse-grained quartz (Qz), albite (Ab) and tourmaline (Tur; GPS: UTM 33 K 514839 7520085); B) Symplectic intergrowth of quartz and tourmaline in a Type Ct pegmatite.

4.5.2.2.4 Type D (SLGs) pegmatites

Type D SLGs are white in colour and constituent minerals are medium-grained and granular. They contain smoky quartz and accessory uraninite or/and betafite and topaz, and commonly have developed secondary beta-uranophane along joint surfaces. These pegmatites typically measure 1 - 7 m in width, and in terms of habit are irregular and anastomosing. Their occurrence is preferentially concentrated at the interface between the Khan-Rössing Formations (Kinnaird and Nex, 2007), where the Rössing and Chuos Formations are severely attenuated or missing.

4.5.2.2.5 Type E (SLGs) pegmatites

A diagnostic characteristic of Type E pegmatites is the presence of oxidation haloes enveloping red or grey cores, which were first observed in this type of pegmatite by Corner and Henthorn (1978). Modal mineralogy in these SLGs is variable, however in general red cores contain a high proportion of opaque minerals in relation to biotite while the opposite is true of the red cores, which also contain sericitised plagioclase with albite rims Nex *et al.*, 2001b). While Type E pegmatites do show some enrichment in uranium, Type D pegmatites are typically the most uraniferous (Kinnaird and Nex, 2007).

Recent work by Freemantle (2012), proposes that Type D and E pegmatites are not separate generations of granite, but rather represent Type D, and possibly Type Cm, pegmatites which have experienced metasomatism to varying degrees.

4.5.2.2.6 Type F (SLGs) pegmatites

Type F SLGs are typically a brick-red colour, containing feldspar, milky quartz and interstitial biotite. The feldspar is almost perthitic K-feldspar, which occurs as very large (30 cm) crystals. The Type F SLGs are typically narrow, tabular bodies, measuring 0.5 - 3 m, and they cross-cut all earlier generations of SLG (Kinnaird and Nex, 2007).

4.6 Sampling

Sampling was conducted on three field trips to the study areas in the period between April 2010 and March 2012. Sample localities were chosen based on the commodity for which a given pegmatite is being mined, or has been mined in the past.

In zoned pegmatites, sampling was directed using maps of the internal zonation of a given pegmatite (e.g. Roering, 1963), and sampling was conducted along a traverse intersecting each zone of the pegmatite. Where maps were not available, zones were identified in a pegmatite and sampling was directed accordingly. For the purposes of geochemical analyses, extra Wall Zone surface samples with as representative a mineral assemblage as possible were collected. The Wall Zone was sampled for the purposes of analytical continuity because in many cases the Border Zone could not be identified, and therefore sampled, in the field.

In unzoned pegmatites, surface samples were collected randomly across pegmatites in an effort to collect samples that contained an overall representative mineral assemblage for the entire body, again for the purposes of analytical continuity.

With respect to the SLG samples, the area was extensively mapped and sampled by G. Freemantle between 2007 and 2012, and so surface SLG samples were obtained from his voluminous collection of Valencia samples. These were selected based on their texture i.e. for the sake of sample continuity in the study, the coarsest-grained C-Type SLGs were selected with the exception of one B-Type sample.

It is important to note that sampling pegmatites for the purposes of whole rock geochemical analysis is complicated due to the inherently coarse texture of the rocks. The size of samples taken for this study varied according to the grain size of individual pegmatites, however whole rock samples were generally up to 30 cm in length and breadth, and at least 5 kg of sample was taken for each geochemical sample.

For the purposes of fluid inclusion studies, clear quartz samples were collected, again from each zone of zoned bodies, and randomly in unzoned bodies and pegmatitic SLGs.

Country rock samples were also obtained from each locality. These were sampled randomly, were as unweathered as possible, from areas directly adjacent to the contact between pegmatite and country rock. In the case of country rock samples from the Valencia area, core samples were taken that were known to be near to the contact of a SLG.

4.7 Summary

Zoned and unzoned mineralised pegmatites of Pan-African age are located throughout the southern Central and Northern/Southern Kaoko Zones of the Damara (Kaoko) Belt. The pegmatites belong both to the LCT and NYF families, and they have intruded into metapelitic sequences, of varying metamorphic grade, of the Damara Supergroup.

Mineralisation in these pegmatites shows a regional zonation, with Li-Be- and gem-tourmaline-bearing LCT pegmatites occurring in the central parts of the southern Central Zone, Sn-bearing LCT pegmatites occurring at the junction between the Northern and Southern Kaoko Zones in the northwestern parts of the Belt, and U-rich NYF pegmatites occurring in the southwestern parts of the southern Central Zone, where the highest metamorphic conditions were achieved.

Sampling was conducted in such a way as to facilitate the comparison of fluid inclusion and geochemical characteristics of the pegmatites described in this chapter in an effort to ascertain what geological factors might be responsible for the differences in mineralisation observed in the pegmatites, and the regional distribution of mineralisation, as well as to investigate what the possible sources of pegmatite magma may have been. The results of these analyses are presented in Chapters 5, 6, and 7.

CHAPTER 5

GEOCHEMISTRY AND GENERAL CHARACTERISTICS OF FLUID INCLUSIONS FROM MINERALISED PEGMATITES

5.1 Introduction

Fluid inclusions are small pockets of fluid trapped as imperfections in a crystal that grew in the presence of a fluid; they can also become trapped in fractures or along cleavage planes in a mineral during a much later ingress of fluid (Roedder, 1984; Shepherd, 1985; Bodnar, 2003a; Frezzotti, 2012). They remain fluid at ambient temperature, and may be composed of water, brines of varying salinity, gas, or gas-bearing liquid as a liquid, vapour, or supercritical fluid (Roedder, 1984; Shepherd *et al.*, 1985; Bodnar, 2003a). By studying fluid inclusions it is possible to constrain the P-T-X conditions of fluids in a variety of different geological settings.

Fluid inclusions can be classified as primary (those trapped during, and as a direct result of, crystal growth), secondary (those entrapped after a crystal has finished growing, usually along fractures), pseudosecondary (those trapped during crystal growth, but not directly as a result thereof), and indeterminate (those whose timing relative to crystal growth cannot be established; Roedder, 1984; Shepherd *et al.*, 1985; Bodnar, 2003a). The relative timing of a given fluid inclusion assemblage/population is crucial in compiling a reliable interpretation of the fluid history of the ore deposit under investigation. Assuming that no leaking or resetting has occurred during metamorphism, isolated inclusions, or those occurring along a poorly defined plane may be regarded as primary or pseudosecondary inclusions, respectively, while those occurring along well-defined fluid inclusion planes (FIPs) may be regarded as secondary (Roedder, 1984; Goldstein, 2003).

A key assumption made in any fluid inclusions study is that the inclusions represent an isoplethic and isochoric system i.e. their chemical composition and volume remain constant over geological time, thus the key to identify a representative fluid inclusion

population is to document a sufficient number of fluid inclusions of a given fluid inclusion assemblage (FIA; Roedder, 1984; Bodnar, 2003b; Goldstein, 2003).

Fluid inclusion microthermometry and Raman microspectroscopy respectively were undertaken at the School of Geosciences and School of Physics at the University of the Witwatersrand, while Cathodoluminescence (CL) was done at the University of Johannesburg, and Particle-Induced X-Ray Emission (PIXE) at iThemba LABS, Somerset West.

5.2 Methodology

5.2.1 Sampling

Quartz samples were taken from each pegmatite for the purposes of fluid inclusion analyses. In zoned bodies, samples were collected across all exposed zones, and in unzoned bodies, samples were taken from approximately 1 m from the contact of the pegmatites with their country rocks, and within the central parts of the bodies. Care was taken to sample the clearest quartz possible so as to ensure that not only late fluid inclusions were sampled, however in some of the pegmatites only milky quartz was present.

5.2.2 Sample preparation

Polished thin sections (30 μm thick) were cut from samples of each zone in zoned pegmatites, and from samples showing mineralisation in the unzoned pegmatites. Thin sections were also cut from pure quartz samples; these were thicker (50 μm) so as not to destroy any large fluid inclusions that there may have been in the samples. Once suitable fluid inclusions for measurement were identified, 150 - 200 μm thick double polished wafers were cut from the samples; these were prepared both at the School of Geosciences, University of the Witwatersrand and at the Department of Geological Sciences, University of Cape Town. A sample inventory can be found in Appendix 1 and all fluid inclusion microthermometry data in Appendix 2.

5.2.3 Analytical techniques

5.2.3.1 Fluid inclusion petrography

Optical transmitted light microscopy of fluid inclusion and thin sections was done on an Olympus BX51 petrographic microscope in the Fluid Inclusions Laboratory, School of Geosciences, University of the Witwatersrand. All samples and fluid inclusion populations were photographed using an Olympus SC30 camera and *Stream Essentials™* software. In conjunction with this, the samples were imaged using the cathodoluminescence detector on the VEGA3 Tescan scanning electron microscope, Spectrau, University of Johannesburg. Samples were attached to a glass slide using carbon tape and then carbon coated to reduce charging of the sample. Imaging was done at 20 kV acceleration potential.

Fluid inclusion populations were identified and their relative timing (primary vs. pseudosecondary vs. secondary) established using the classification of Roedder (1984). The degree of fill (D.F.) of each inclusion was estimated using the *Stream Essentials™* measuring tool and the following simple equation to calculate the vapour to liquid ratio:

$$D.F. = \text{bubble length } (\mu\text{m}) \div \text{fluid inclusion length } (\mu\text{m})$$

5.2.3.2 Fluid inclusion microthermometry

Microthermometry was done by heating and freezing double polished wafers on a Linkam MDSG600 motorised heating/freezing stage mounted on an Olympus BX51 transmitted light microscope in the Fluid Inclusions Laboratory, School of Geosciences, University of the Witwatersrand. The microscope is fitted with long working distance 10x, 20x, and 50x objectives, a short working distance 5x objective, and a 1.6x magnification changer that allows for magnification up to 80 times. The heating-freezing stage has a temperature range of - 196 - 600 °C and it is connected to a liquid nitrogen pump (LNP 2) and a programmable thermal control unit (TMS 94), allowing heating/cooling rates of 0.01 - 150 °C and stability of 0.001 °C (Figure 5.1). The stage

was calibrated using the triple point of CO₂ in aqueo-carbonic fluid inclusions containing pure CO₂ (composition confirmed using Raman microspectroscopy) from the Harare-Bindura greenstone belt, Zimbabwe, and synthetic aqueo-carbonic inclusions (SynFInc, supplied by FluidInc), and homogenisation temperatures of synthetic H₂O inclusions (SynFInc, supplied by FluidInc).



Figure 5.1: Fluid Inclusions Laboratory at the School of Geosciences, University of the Witwatersrand (see text for details).

The following temperatures were measured and recorded:

- Freezing temperatures of aqueous and gaseous phases ($T_{f_{H_2O}}$, $T_{f_{CO_2}}$).
- Final melting of CO₂ ($T_{m_{CO_2}}$).
- Initial melting of aqueous solutions (T_{m_i}/T_e).
- Final melting of aqueous solutions (T_m).
- Melting of clathrate ($T_{m_{cla}}$).
- Homogenisation of gaseous phases (T_{h_g}).
- Homogenisation of aqueous phases ($T_{h_{aq}}$).

Because of difficulties in observation when measuring Initial/eutectic melting (T_m/T_e), the error on these measurements may be as great as 5 - 6 °C. Furthermore, the fluid inclusions containing daughter minerals decrepitated before final homogenisation i.e. dissolution of solids could be observed, therefore Th_{aq} is taken as the final homogenisation temperature of these inclusions.

Bulk composition, density, and salinity were calculated using *Bulk version 01/03* (Bakker, 2003), and the equation of state of Bodnar (1993) and Archer (1992). Where T_m indicated metastability i.e. $T_m > 0$ °C), the chlorinity of the aqueous phase was calculated using Raman microspectroscopy as an alternative to equivalent wt % NaCl. In aqueo-carbonic fluid inclusions where the vapour phases was composed of components other than CO_2 , and the melting and homogenisation temperatures of the additional phases could not be measured, their relative proportions were calculated using Raman microspectroscopy.

Measured homogenisation temperatures indicate only the minimum temperature of trapping of a given fluid inclusion (Roedder, 1984; Shepherd *et al.*, 1985), thus in order to obtain a maximum temperature of trapping the P-T conditions of trapping must be constrained using the following (Shepherd, 1985):

- Temperatures of crystallisation calculated using independent geothermometers (e.g. stable isotope geothermometry).
- Vapour pressure at Th .
- Intersecting isochores of co-existing fluids.
- Daughter mineral dissolution temperatures.

In this study, stable isotope and Ti-in-quartz geothermometry were used to constrain the temperatures of pegmatite crystallisation and thus a maximum temperature for the trapping of fluid inclusions.

5.2.3.3 Raman microspectroscopy

Laser Raman spectroscopy is a non-destructive technique that can be used to identify and quantify molecular species in individual fluid inclusions (Burke, 2001; Burruss, 2003; Frezzotti *et al.*, 2012). It can also be used to calculate the chlorinity of a fluid as an alternative to Equivalent wt % NaCl where microthermometric measurements are impeded (Sun *et al.*, 2010) , and is thus a useful way to confirm the reliability of microthermometric data Raman microscopy was done at the Department of Physics, University of the Witwatersrand.

The basis for Raman spectroscopy is the inelastic scattering of light by the vibrations or molecular bonds (Burke, 2011; Burruss, 2003; Frezzotti *et al.*, 2012). To observe this phenomenon, an intense beam of monochromatic light, usually a visible wavelength laser, is directed at a sample, and the photons generated by the scattering of the laser light are measured. They appear as a Raman spectrum, a plot of light intensity expressed as arbitrary units versus Raman vibrational modes in wavenumbers (Burke, 2001; Frezzotti, 2012).

The same fluid inclusions that were measured for microthermometry were measured using Raman microspectroscopy, and no additional sample preparation was required. Raman spectra for liquid and vapour phases in fluid inclusions were acquired using a Jobin-Yvon LabRAM HR Raman spectrometer, and the 514.5 nm line of a Lexel argon ion laser as the excitation source. The incident laser beam was focussed onto the sample using a 100 x objective on an Olympus BX41 microscope attachment, giving a spot size of ~ 1 micron diameter. The backscattered light was dispersed via a 600 lines/mm grating onto a liquid nitrogen-cooled CCD detector. Spectra were acquired using LabSpec v5 software.

Raman microspectroscopy was done in order to corroborate microthermometric data as well as to calculate the amounts of a given substance where more than was present in the vapour phase of an inclusion. It was also done to obtain spectra for the OH stretching bands of aqueous inclusions (Figure1) so that the chlorinity of those inclusions could be calculated using the method of Sun (*et al.*, 2010). Deionised water

was used to calibrate the water spectra (Figure 5.2). The spectra were then plotted, and peaks fitted to them, using OriginLab *OriginPro 7.5*. Once the chlorinity (m) was determined, it was substituted into the following equation to calculate equivalent weight % NaCl:

$$\text{Equivalent wt \% NaCl} = \left(\frac{\text{mol NaCl}}{\text{mol NaCl} + 1000} \right) \times 100$$

where

$$\text{mol NaCl} = (m \times 22.99) + (m \times 35.45)$$

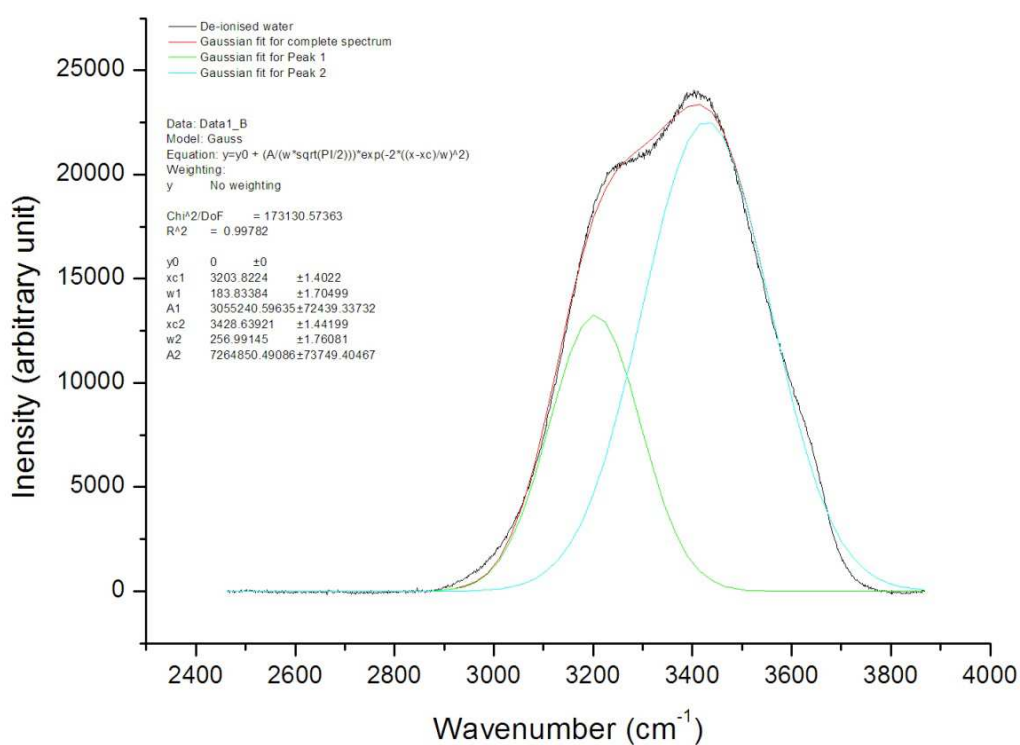


Figure 5.2: OH stretching band of deionised water. Note that there are some discrepancies between the spectrum and the Gaussian fit of the data, however this is in accordance with the method of Sun *et al.* (2010) who fit only two peaks to a given spectrum. The inset provides data on the positions of the fitted peaks (xc), their widths (w), and the areas below them (A).

Unfortunately, due to fluorescence caused by residual glue on the double-polished wafers, and weak spectra resulting from the depth of individual fluid inclusions, the majority of the spectra obtained were noisy, and the resultant salinities calculated were considerably higher than those calculated from the melting temperature of ice, and thus unreliable. Therefore the salinities determined using Raman spectroscopy could not be included in the geological interpretation of the fluid inclusion populations analysed.

5.2.3.4 Particle-induced X-ray emission (PIXE)

PIXE is a non-destructive analysis that allows one to create micro-elemental maps of, and determine element concentrations in, individual fluid inclusions. PIXE analyses of individual fluid inclusions was conducted on the nuclear microprobe belonging to the Materials Research Division of iThemba LABS, Somerset West.

The same double-polished wafers used for microthermometry were used for PIXE work. Prior to the analyses, appropriate fluid inclusions had to be selected from each sample based on their depth within the wafer and their size; large, near-surface fluid inclusions are ideal. Sample preparation for PIXE analyses involved the development of a new mounting technique with the help of Dr Y. Wang at iThemba LABS. Normally, samples for fluid inclusion PIXE analyses are glued to a glass slide and then carbon coated (Ryan, 1999), however, in this instance, the samples were required for further work and so could not be glued to a slide. Instead, they were mounted in 2 x 1 cm aluminium foil envelopes (Figure 5.3) which could then be fitted into the PIXE sample ladder. Samples that were prone to charging had additional aluminium sheets attached to counteract this effect.

Ideally a beam current of ~ 1 nA and a beam spot size of 3- 6 μm are the ideal settings for analysis of fluid inclusions, however because of complications with the microprobe and beam instability, measurements were taken using a 150 - 500 pA beam of 3 MeV protons at 5 μm spot size. Individual fluid inclusions were measured for varying lengths of time depending on the beam stability.

The raw data were processed using GeoPIXE software, and from them PIXE spectra and micro-elemental maps of the measured fluid inclusions were extracted. Although it is possible to analyse of fluid inclusions quantitatively using PIXE (Ryan, 1999), due to constraints imposed both by time and the equipment, only qualitative analyses were done for this study.



Figure 5.3: Aluminium sample envelope containing a double-polished quartz wafer. The tightly pressed envelope is mounted in a sample ladder that can hold eight samples vertically, which is inserted in to a sample chamber in the nuclear microprobe.

5.3 Results

5.3.1 Cathodoluminescence and petrography

In order to assist in the determination of fluid inclusion population chronology, CL images were taken of each sample. CL images show that the quartz sampled from the pegmatites for fluid inclusion analysis is bright, and areas of low luminescence occur along fractures and grain boundaries in the quartz. Since none of the samples showed any growth zonation (Figure 5.4) or any of the other criteria described by Roedder (1984) to identify primary fluid inclusions, it is impossible to classify any of the identified fluid inclusions in the pegmatites as unequivocally primary in origin, therefore they have been classified as pseudosecondary and secondary.

The five pseudosecondary and secondary fluid inclusion populations, ranging in composition from aqueo-carbonic to carbonic and aqueous, that were identified are shown in Table 5.1. This table also summarises their geochemical characteristics.

5.3.1.1 *Type 1 fluid inclusions*

Type 1 fluid inclusions are pseudosecondary, aqueo-carbonic inclusions. These fluid inclusions occur as clusters and are the earliest population observed in the LCT pegmatites; although this type of fluid inclusion was not observed in the uraniferous NYF pegmatite samples from this study, they were identified in pegmatites from the Goanikontes area by Nex (1993), who reported them as Type IC inclusions. They are relatively large, measuring from $\pm 15 \mu\text{m}$ to over $70 \mu\text{m}$, and they are typically sub- to anhedral in shape. These inclusions contain a halite crystal, indicating salinities in excess of 26.3 equivalent wt % NaCl, and a crystal of an unknown acicular opaque phase, possibly tantalum-niobium oxide.

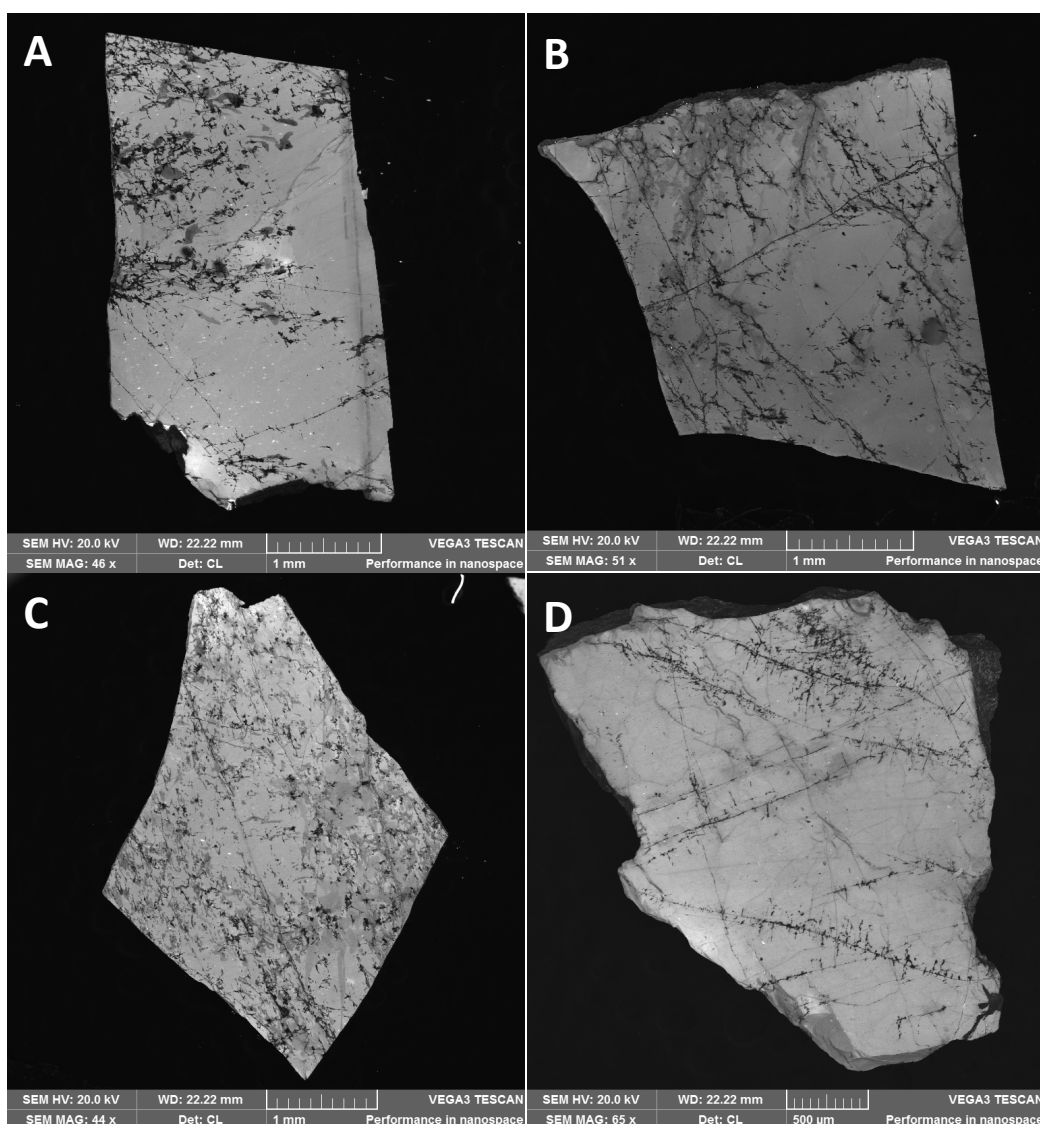
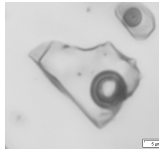
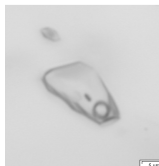
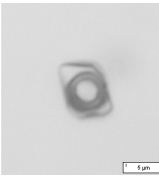
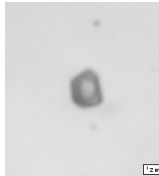
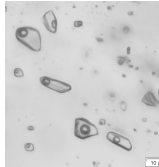


Figure 5.4: Selected CL images of double-polished wafers used for fluid inclusion microthermometry from A) Li-Be-bearing, B) Li-Sn-bearing, C) Sn-bearing pegmatites and D) U-bearing pegmatites (SLGs).

5.3.1.2 Type 2 fluid inclusions

Type 2 are aqueous fluid inclusions containing a halite crystal and an acicular opaque phase, and they are also pseudosecondary. They occur in clusters, and are typically subhedral in shape, measuring between 8 μm and 24 μm . They were observed only in the Li-Be-bearing LCT pegmatites, but not in the Sn-, Li-Sn-, gem tourmaline-bearing LCT pegmatites or the uraniferous NYF pegmatites, either in this study or in that of Nex (1993).

Table 5.1: Summary of fluid inclusions populations observed and measured, their homogenisation temperatures and geochemical characteristics.

Fluid inclusion type		Deposit type	Pegmatite family	Mineral	Relative timing	Phases	XH ₂ O	XCO ₂	Th (°C)	Bulk density (g/cc)	Salinity (eq. wt % NaCl)
Type 1		Li-Be Tourmaline Li-Sn Sn (U)	LCT NYF	quartz	PS	H ₂ O-CO ₂ ⁻ (CH ₄ -CO-N ₂) NaCl-opaque	0.7 - 0.8	0.2 - 0.3	~ 315 – 330	0.7 – 0.9	> 26.3
Type 2		Li-Be	LCT	quartz	PS	H ₂ O-(CO ₂ ⁻ CH ₄ -CO-N ₂) NaCl-opaque	1.0	-	~ 113.2	1.0	> 26.3
Type 3		Li-Be	LCT	quartz	S	H ₂ O-CO ₂ ⁻ NaCl	0.8	0.2	~ 325	0.8	~ 1.3
Type 4		Tourmaline U	LCT NYF	quartz	PS S	CO ₂	-	1.0	~ 11.9 ~ 23.5	0.8 0.7	NA
Type 5		Li-Be Tourmaline Li-Sn Sn U	LCT NYF	quartz	S	H ₂ O	1.0	-	~ 111.9 – 180.5	0.9 – 1.0	~ 2.2 – 6.8

5.3.1.3 Type 3 fluid inclusions

Type 3 fluid inclusions are secondary and aqueo-carbonic in composition. They are typically small, with an average length of 5.5 μm , and they are euhedral, showing negative crystal shapes. These inclusions are secondary, occurring in trails that cross-cut earlier fluid inclusion populations, and locally they cross-cut grain boundaries. They were observed in the LCT pegmatites, but again not in the NYF pegmatites, either in this study or in that of Nex (1993).

5.3.1.4 Type 4 fluid inclusions

Type 4 fluid inclusions are euhedral and occur in trails oriented along the surfaces of fracture planes. They are very small, usually measuring less than 5.5 μm . In LCT pegmatites they tend to be secondary, however in NYF pegmatites they show pseudosecondary characteristics. These fluid inclusions are composed of pure CO_2 .

5.3.1.5 Type 5 fluid inclusions

Type 5 fluid inclusions are the youngest inclusions observed. At the outcrop scale their orientation is parallel to the strike of a given pegmatite. They are commonly euhedral, and variable in size with individual inclusions measuring up to, and in excess of, 30 μm . Type 5 inclusions are secondary aqueous inclusions, occurring in trails which cross-cut massive quartz grains, and they also occur on the surfaces of fracture planes. They were observed in all LCT and NYF pegmatites studied.

5.3.2 Geochemical characteristics of fluid inclusions: microthermometry, Raman microspectroscopy and Particle-Induced X-ray Emission

Because no major differences were observed petrographically between the five fluid inclusion types across different types of pegmatites, a subset of samples was selected from one of each pegmatite for more detailed fluid inclusion analyses.

5.3.2.1 Li-Be-bearing pegmatites: Rubicon pegmatite

Four of the five fluid inclusion populations (Types 1, 2, 3, and 5) identified during petrography were identified in quartz samples from all of the zones of the Rubicon pegmatite. Samples from the Wall and Intermediate zones were used for microthermometric analyses and Raman microspectroscopy. Due to analytical difficulties, no PIXE data were obtained for fluid inclusions in the Rubicon pegmatite.

5.3.2.1.1 Type 1 fluid inclusions

Temperature data for the carbonic phase of Type 1 aqueo-carbonic inclusions from the Rubicon pegmatite (Figure 5.5A) show that this phase typically melts at temperatures ranging between $-56.6\text{ }^{\circ}\text{C}$ and $-56.2\text{ }^{\circ}\text{C}$, which, coupled with Raman microspectroscopy, indicate that the gaseous phase is composed of pure CO_2 (Figure 5.5B). Clathrate melting averages $7.0\text{ }^{\circ}\text{C}$, and homogenisation of the carbonic phase occurs to the liquid phase, very near to critical temperatures, with $T_{h\text{CO}_2}$ ranging between $29.8\text{ }^{\circ}\text{C}$ and $31.0\text{ }^{\circ}\text{C}$. The density of the CO_2 is moderate (0.5 g/cc), and although the degree of fill is also moderate, typically averaging 0.6, CO_2 only comprises approximately 30 % of the bulk composition of the fluid inclusions.

The aqueous phase of Type 1 fluid inclusions in the Rubicon pegmatite show T_{m_i} values ranging between $-22.3\text{ }^{\circ}\text{C}$ and $-18.5\text{ }^{\circ}\text{C}$ indicating that the dominant salt present in the inclusions is NaCl. The final melting of ice averages $-3.0\text{ }^{\circ}\text{C}$, giving salinities in the region 4.1 -6 equivalent wt % NaCl. The aqueous phase comprises up to 70 % of the bulk composition of these inclusions.

Final homogenisation of these inclusions is between $290.5\text{ }^{\circ}\text{C}$ and $348\text{ }^{\circ}\text{C}$, averaging $330.4\text{ }^{\circ}\text{C}$ (Figure 5.5C). Homogenisation is to the liquid phase, and the final melting temperature of daughter salts could not be determined since the inclusions tended to decrepitate before this could be measured. The bulk density of Type 1 fluid inclusions is quite high, ranging from $0.7 - 0.8\text{ g/cc}$.

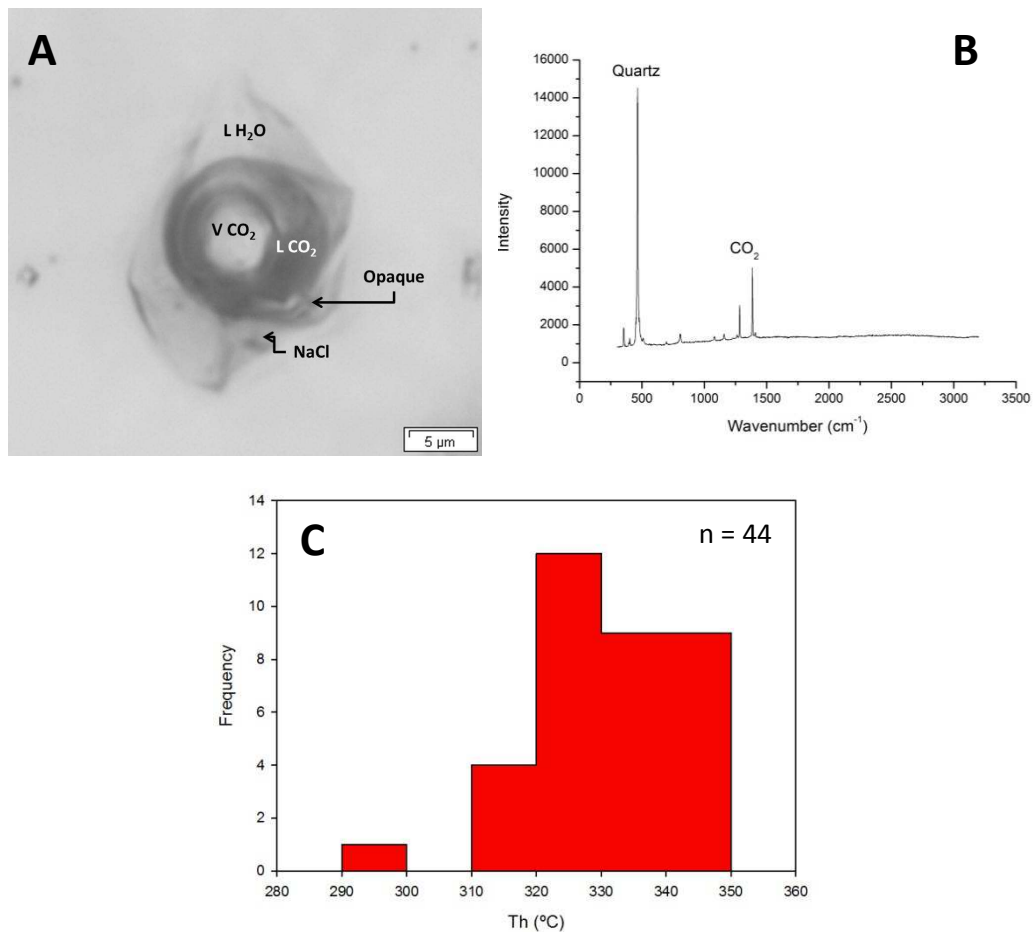


Figure 5.5: Type 1 fluid inclusion from the Rubicon pegmatite; A) Photomicrograph showing carbonic vapour, aqueous liquid and solid phases in the fluid inclusion; B) Spectrum of the vapour phase of the fluid inclusion obtained using Raman microspectroscopy, showing the composition of the vapour phase as pure CO₂; C) Histogram showing the distribution of Th values for Type 1 fluid inclusions.

5.3.2.1.2 Type2 fluid inclusions

Type 2 aqueous fluid inclusions (Figure 5.6A) were observed only in the Rubicon pegmatite. Raman microspectroscopy indicates that they are composed of NaCl-bearing water (Figure 5.6B), and the presence of halite daughter crystals in the inclusions indicates that the salinity of this generation of fluid inclusion is in excess of 26.3 equivalent wt % NaCl. In addition to this, the Tm_i values, ranging from -24.6 to -22.8 °C, indicate that the dominant salt in these inclusions is NaCl.

Like the Type 1 inclusions, the final melting temperatures of halite could not be measured because of the tendency of the inclusions to decrepitate at temperatures in

excess of their homogenisation temperatures, therefore their exact salinities could not be calculated. The density of Type 2 fluid inclusions is high, averaging 1.0 g/cc, and they homogenize to the liquid phase at low temperatures, averaging 113.2 °C (Figure 5.6C).

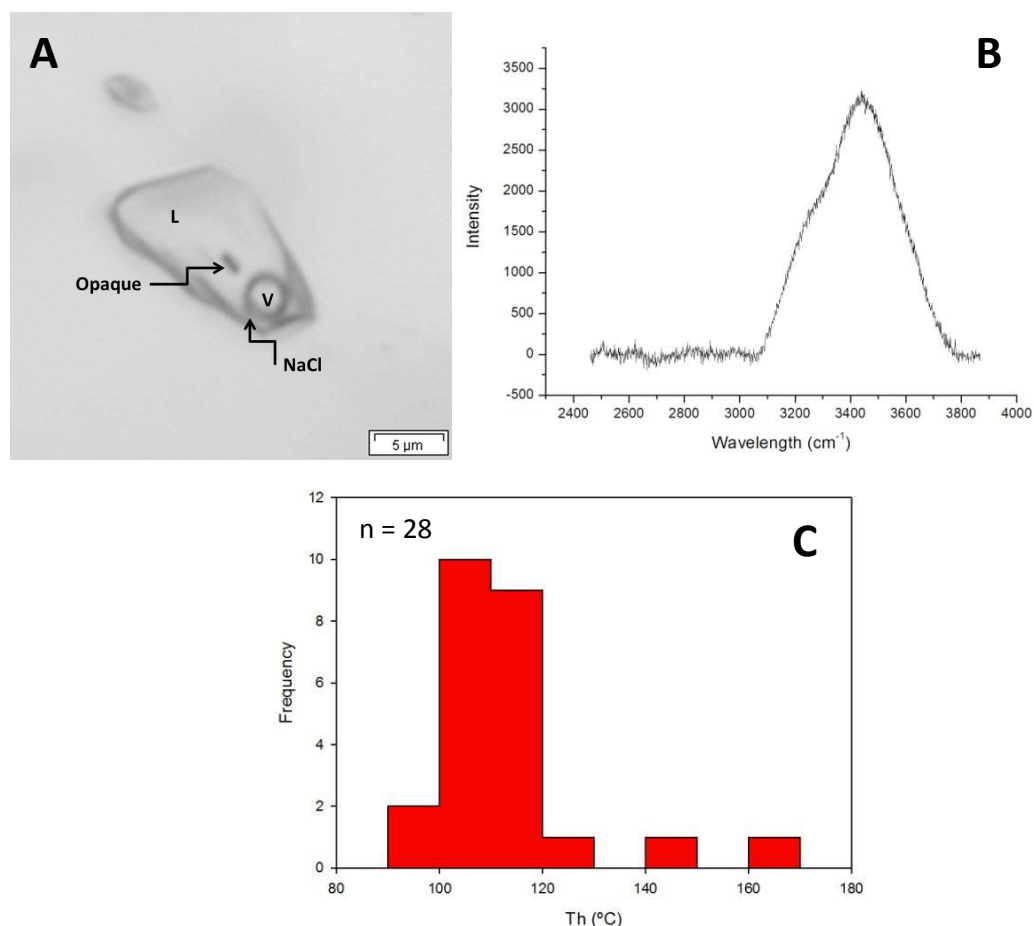


Figure 5.6: Type 2 fluid inclusion from the Rubicon pegmatite; A) Photomicrograph showing vapour, liquid and solid phases in the fluid inclusion; B) Normalised spectrum of the liquid phase of the fluid inclusion obtained using Raman microspectroscopy, showing the composition of the fluid inclusion as saline H₂O, expressed as a broad H₂O + NaCl feature from 3200 - 3800 cm⁻¹; C) Histogram showing the distribution of Th values for Type 2 fluid inclusions.

5.3.2.1.3 Type3 fluid inclusions

Similar to Type 1 fluid inclusions, the carbonic phase of Type 3 aqueo-carbonic inclusions (Figure 5.7A) typically melts at temperatures ranging between -56.8 °C and -54.2 °C. Although this range of homogenisation temperatures is not as tightly constrained as the values for the vapour phase of Type 1 inclusions, Raman microspectroscopy results show that this phase is composed of pure CO₂ (Figure 5.7B).

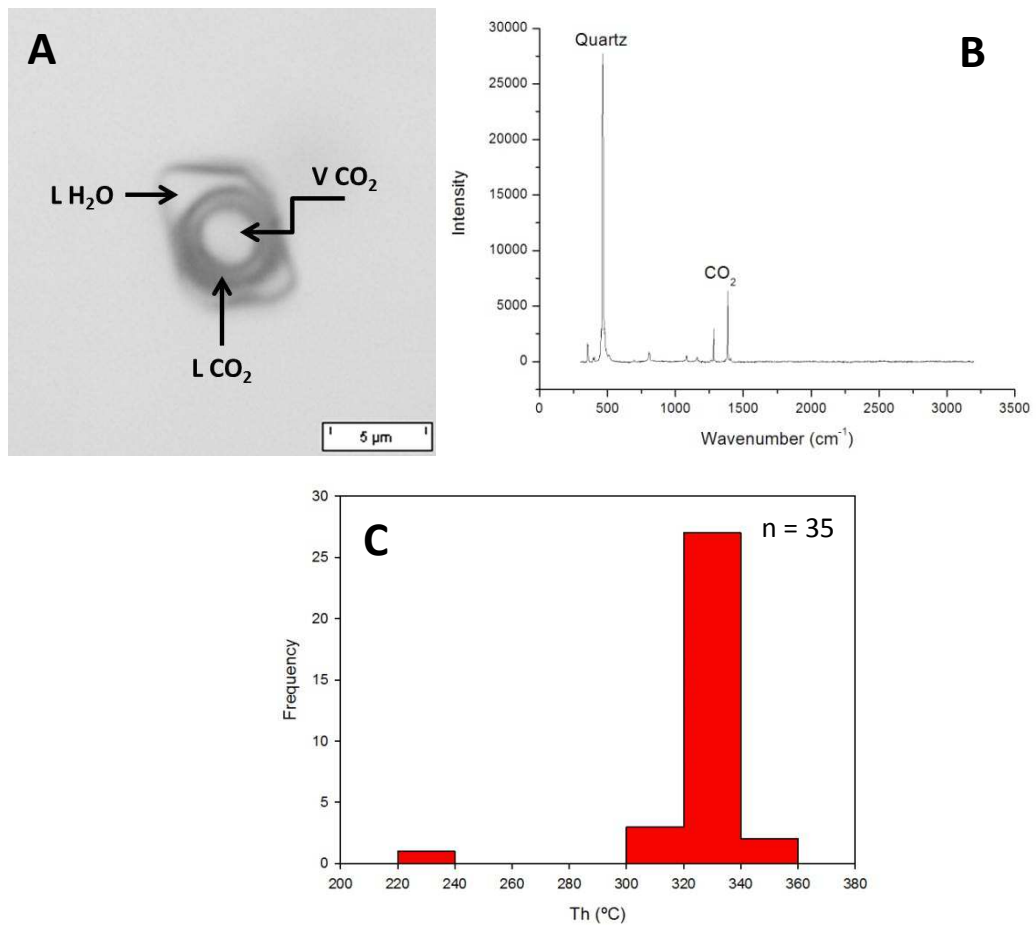


Figure 5.7: Type 3 fluid inclusion from the Rubicon pegmatite; A) Photomicrograph showing carbonic vapour and aqueous liquid phases in the fluid inclusion; B) Spectrum of the vapour phase of the fluid inclusion obtained using Raman microspectroscopy, showing the composition of the vapour phase as pure CO₂; C) Histogram showing the distribution of Th values for Type 3 fluid inclusions.

Clathrate melting typically averages 7.1 °C, similar to that of Type 1 inclusions, and CO₂ homogenises to the liquid phase at almost critical temperatures ranging from 30.5 - 30.9 °C. The density of the carbonic phase of Type 3 fluid inclusions ranges from 0.5 - 0.6 g/cc, and overall this phase constitutes only approximately 20 % of the bulk composition of the fluid inclusions.

The aqueous phase of Type 3 fluid inclusions constitutes up to 80 % of the inclusions. T_m_i values typically range from -20.0 to -25.0 °C indicating that the inclusions contain NaCl. Few ice melting temperatures could be obtained, but those measured range between -1.0 °C and -0.6 °C; such high melting temperatures show that the salinity of these inclusions is very low, typically between 1.1 and 1.8 equivalent wt % NaCl.

The final homogenisation of Type 3 fluid inclusions occurs between 316.1 °C and 346.6 °C; one measurement of 226.0 °C was obtained (Figure 5.7C). Homogenisation is to the liquid phase, and the bulk density of the inclusions is fairly high, ranging from 0.7 - 0.9 g/cc.

5.3.2.1.4 Type 5 fluid inclusions

The fourth type of fluid inclusions observed in the Rubicon pegmatite is of the Type 5 (Figure 5.8A) variety (see section 5.3.1.5). The aqueous inclusions are the most abundant in all the samples measured and are composed of moderately saline H₂O (Figure 5.8B). Initial melting occurs between -27.2 °C and -24.2 °C, and ice melting temperatures average -4.3 °C. The salinity of these inclusions ranges from 5.1 - 10.1 equivalent wt % NaCl. The inclusions homogenise to the liquid phase at relatively low temperatures (\pm 111.9 °C; Figure 5.8C), and the bulk density of the inclusions is high, ranging from 0.9 – 1.0 g/cc.

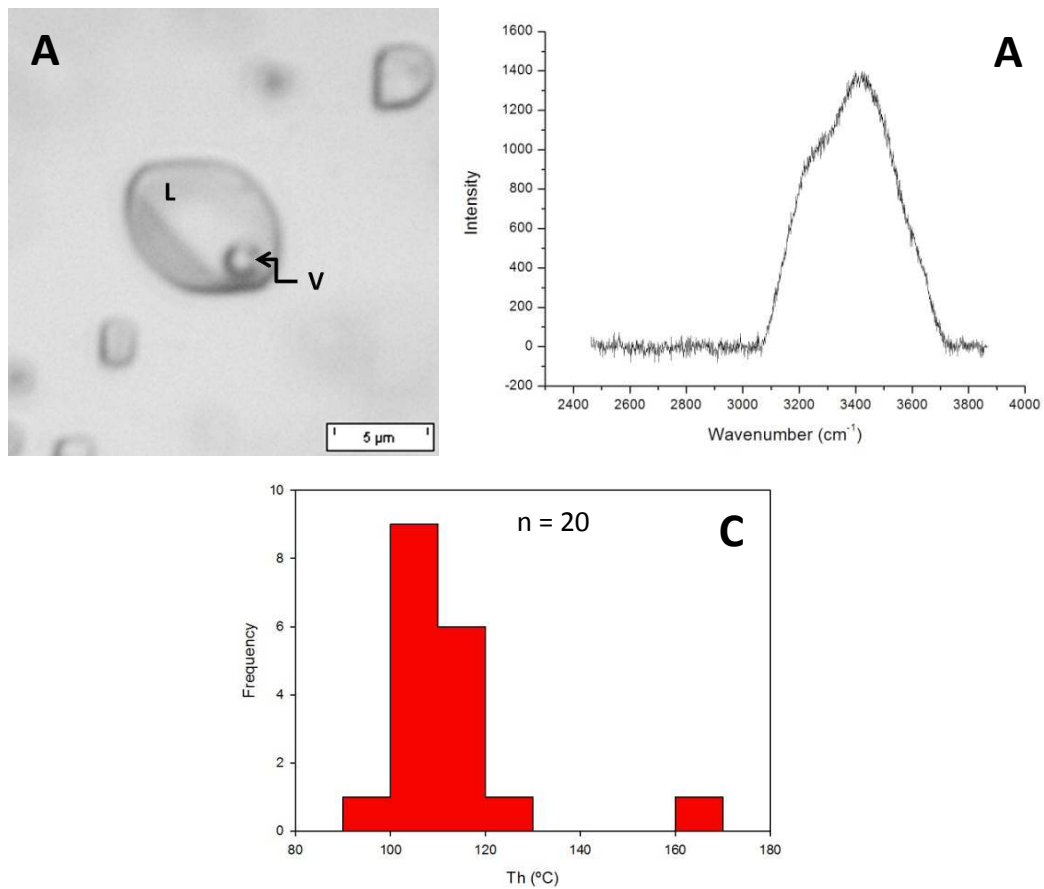


Figure 5.8: Type 5 fluid inclusion from the Rubicon pegmatite; A) Photomicrograph showing aqueous vapour, and liquid phases in the fluid inclusion; B) Normalised spectrum of the liquid phase of the fluid inclusion obtained using Raman microspectroscopy, showing the composition of the fluid inclusion as saline H₂O, expressed as a broad H₂O + NaCl feature from 3200 - 3800 cm⁻¹; C) Histogram showing the distribution of Th values for Type 5 fluid inclusions.

5.3.2.2 Sn-bearing pegmatites: Uis pegmatite

Two of the five fluid inclusion types (Type 1 and Type 5) were identified in quartz samples taken from an Uis pegmatite. The samples were taken both from near the contact and in the central parts of the pegmatite, and were used for microthermometric, Raman microspectroscopic and PIXE analyses.

5.3.2.2.1 Type 1 fluid inclusions

Type 1 fluid aqueo-carbonic fluid inclusions (Figures 5.9A and C) are generally large, with individual inclusions measuring up to 70 µm in length, and a relatively abundant in the samples studied.

The degree of fill of the carbonic phase of these inclusions appears to be variable, ranging from 0.5 - 0.9, however it typically constitutes on 20 - 30 % of the bulk composition of the inclusions. The carbonic phase typically melts at temperatures ranging from -58.2 - -56.9 °C, indicating that that they are not composed of pure CO₂ like Type 1 fluid inclusions in the Rubicon pegmatite. This observation is corroborated by Raman microspectroscopic data, which show that the vapour phase of these inclusions contains trace amounts of CH₄, CO, and N₂ (Figures 5.9B and D). Because of analytical constraints, the exact percentage of CH₄, CO, and N₂ could not be determined, however the melting temperatures of these inclusions indicate that only trace amounts of these components are present (Thiéry *et al.*, 1994). Clathrate melting in Type 1 fluid inclusions generally occurs between 8 °C and 9 °C. The homogenisation of the carbonic phase also shows that there are two subtypes of Type 1 fluid inclusions in the Sn-bearing pegmatites. In the first of these (Figure 5.10A), the carbonic phase homogenises to a liquid at approximately 24.4 °C ($\rho_{\text{CO}_2} = 0.7 \text{ g/cc}$), and in the second (Figure 5.10B), homogenisation is to the vapour phase at temperatures ranging from 25.7 - 28.5 °C ($\rho_{\text{CO}_2} = 0.3 \text{ g/cc}$).

The liquid aqueous phase of Type 1 fluid inclusions in the Uis pegmatites comprises 70 - 80 % of the bulk composition of the inclusions. Initial melting temperatures range from -27.6 - -21.5 °C, again showing that NaCl is the dominant salt in the fluid system. Because the inclusions decrepitated before salt melting temperatures could be recorded, the exact salinity of the inclusions could not be calculated, however the presence of the halite crystal in the inclusions indicates that the salinity of the fluid is in excess of 26.3 equivalent wt % NaCl. The bulk density of Type 1 fluid inclusions ranges from 0.5 - 0.8 g/cc. and they homogenise to the vapour phase at temperatures in the range of 320 °C (Figure 5.9E).

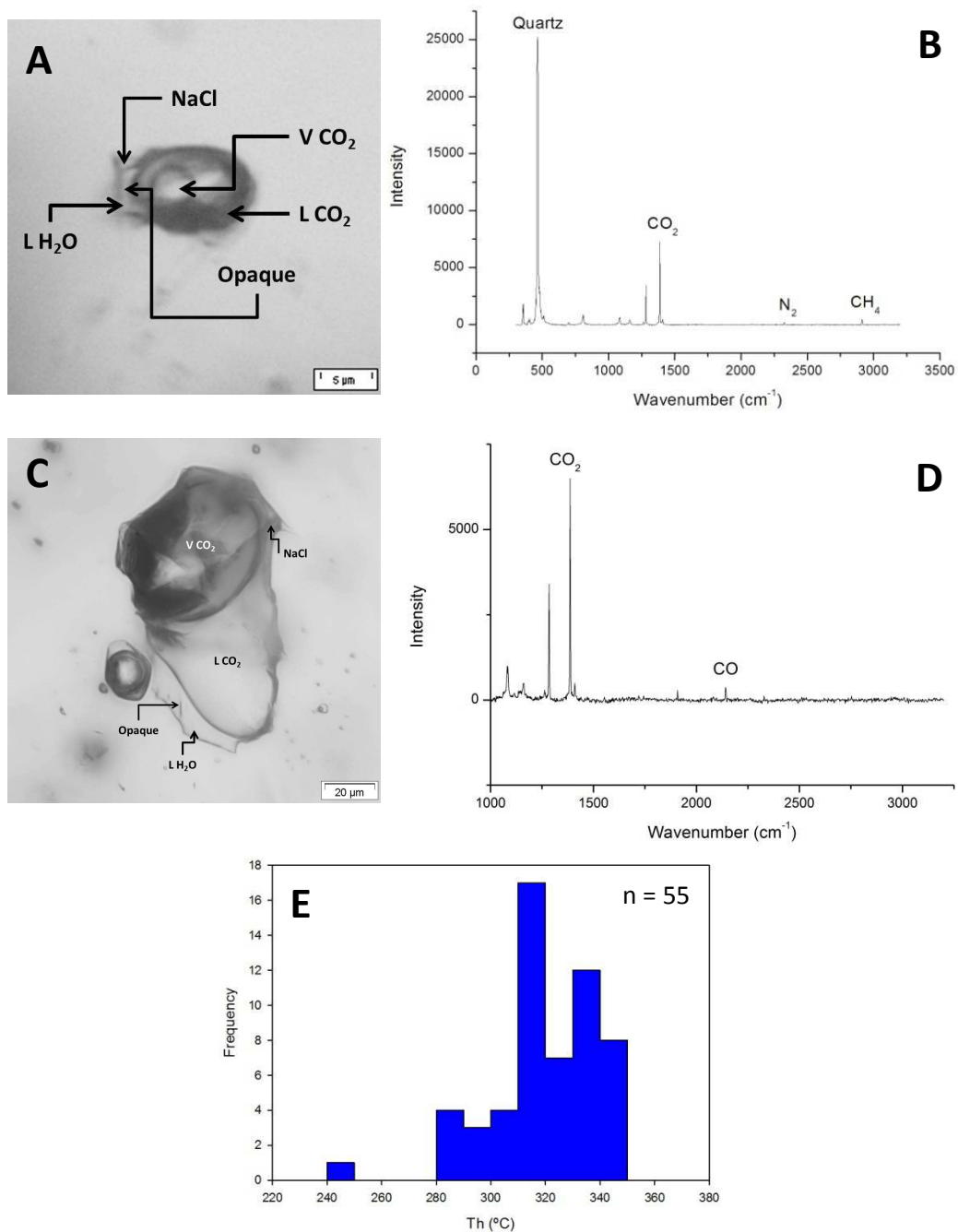


Figure 5.9: Type 1 fluid inclusion from an Uis pegmatite; A) Photomicrograph showing carbonic vapour, aqueous liquid and solid phases in a Type 1A fluid inclusion; B) Normalised spectrum of the vapour phase of that fluid inclusion obtained using Raman microspectroscopy, showing the composition of the vapour phase as CO₂, CH₄ and N₂; C) Photomicrograph showing carbonic vapour, aqueous liquid and solid phases in a Type 1B fluid inclusion; D) Normalised spectrum of the vapour phase of that fluid inclusion obtained using Raman microspectroscopy, showing the composition of the vapour phase as CO₂ and CO; E) Histogram showing the distribution of Th values for all Type 1 fluid inclusions.

PIXE analyses of Type 1A fluid inclusions indicate that they contain a number of elements, including Ca, Cl, Cu, Fe, K, and Zn (Figure 5.10). Unfortunately very few fluid inclusions were suitable for analysis, the exact amounts of these elements could not be quantified. Cu, Fe and Zn are most abundant in the vapour phase of the fluid inclusions, while Ca, Cl and K are evenly distributed throughout the inclusions.

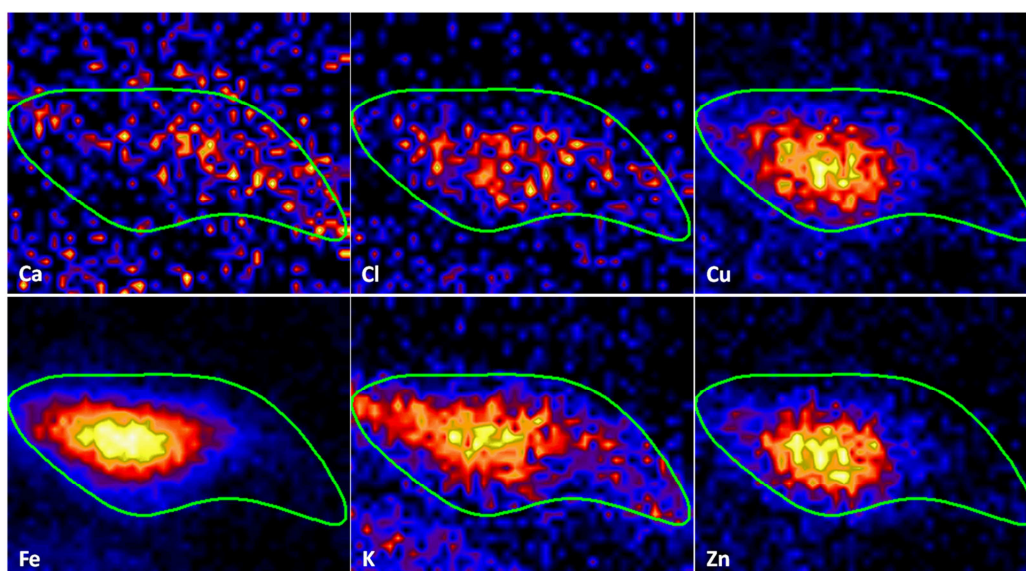


Figure 5.10: PIXE elemental map of an individual Type 1A fluid inclusion from an Uis Sn-bearing pegmatite. The green outline indicates the shape of the fluid inclusion, and warm colours indicate the presence and relative abundance of individual elements.

5.3.2.2.2 Type 5 fluid inclusions

Type 5 aqueous fluid inclusions (Figures 5.11A and B) are the most abundant inclusions present in all the samples analysed. Initial melting occurs between -22.5 °C and -20.3 °C indicating that the salt present in the fluid is NaCl. Ice melting temperatures are variable and range from -4.6 - -0.0 °C, indicating varying salinities ranging from low (0.7 equivalent wt % NaCl) to moderate (7.3 equivalent wt % NaCl). Type 5 inclusions homogenise to the liquid phase at relatively low temperatures averaging 145.6 °C (Figure 5.11C), and their bulk density is high, ranging from 0.9 - 1.0 g/cc.

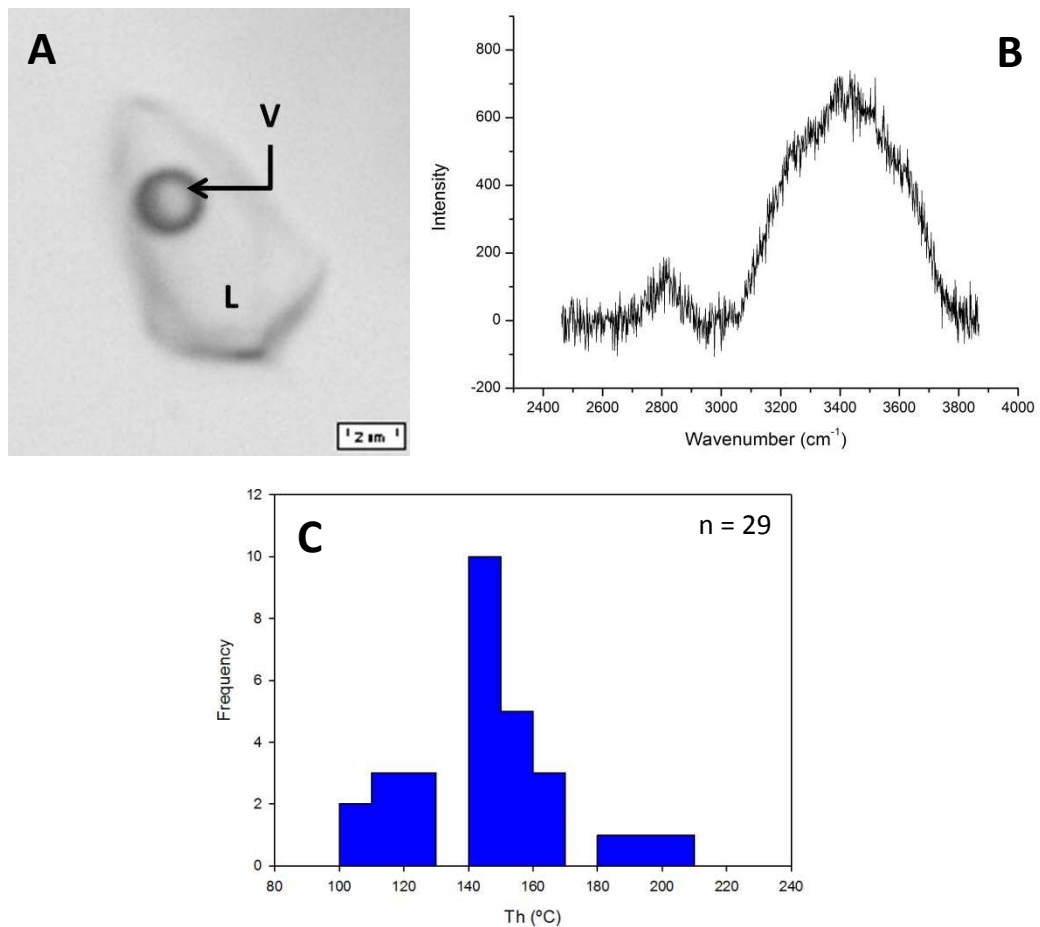


Figure 5.11: Type 5 fluid inclusion from an Uis pegmatite; A) Photomicrograph showing aqueous vapour, and liquid phases in the fluid inclusion; B) Normalised spectrum of the liquid phase of the fluid inclusion obtained using Raman microspectroscopy, showing the composition of the fluid inclusion as saline H₂O, expressed as a broad H₂O + NaCl feature from 3200 - 3800 cm⁻¹. Note that the broad peak at 2800 cm⁻¹ and the broad shoulder between 3600 and 3800 cm⁻¹ is likely to be an artefact caused by the presence of glue on the sample remaining from sample preparation; C) Histogram showing the distribution of Th values for Type 5 fluid inclusions.

5.3.2.3 Li-Sn-bearing pegmatites: Karlowa pegmatite

Similar to the Uis Sn-bearing pegmatites, Type 1 and Type 5 fluid inclusions were identified in the Li-Sn-bearing pegmatite selected for fluid inclusions analysis. Again, the fluid inclusions were measured in quartz samples which were taken both from the Wall and Core zones of the pegmatite. Microthermometric and Raman microspectroscopic analyses were conducted on the samples. Because of analytical complications, PIXE measurements of fluid inclusions in the Karlowa pegmatite could not be obtained.

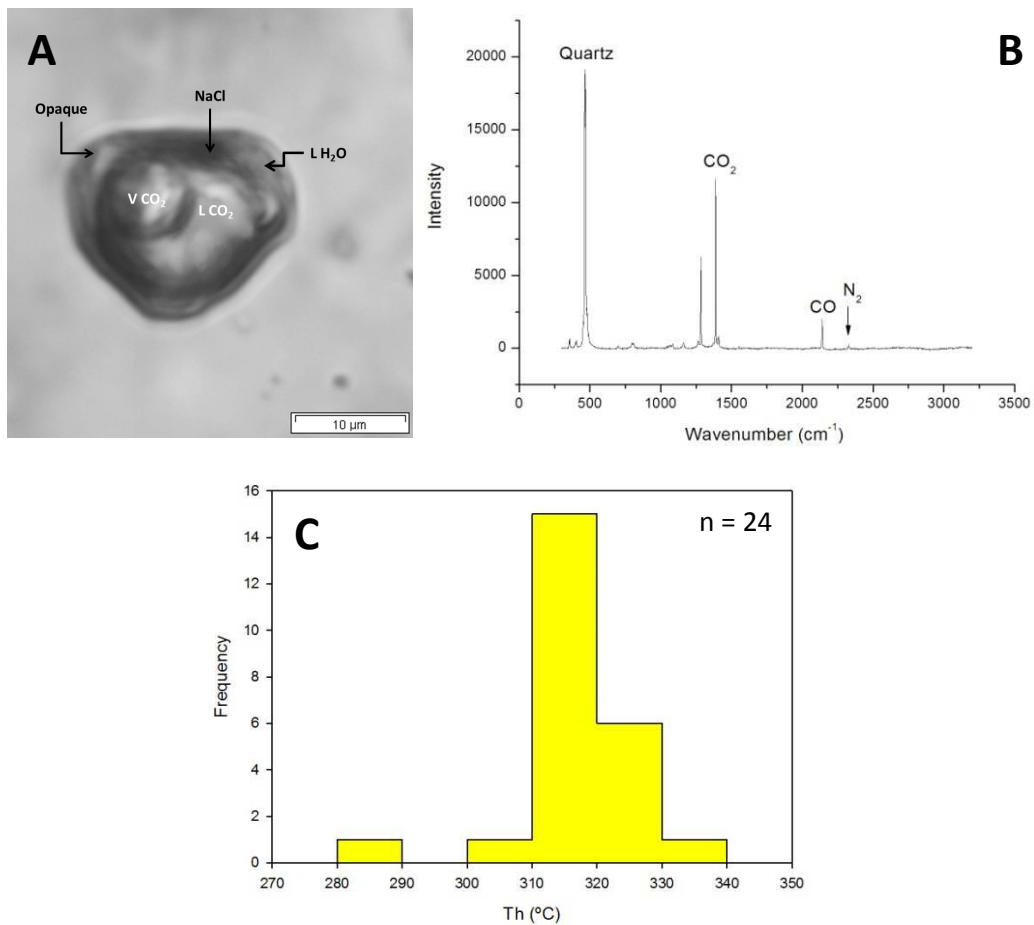


Figure 5.12: Type 1 fluid inclusion from a Karlowa pegmatite; A) Photomicrograph showing carbonic vapour, aqueous liquid and solid phases in a Type 1 fluid inclusion; B) Normalised spectrum of the vapour phase of that fluid inclusion obtained using Raman microspectroscopy, showing the composition of the vapour phase as CO₂, CO and N₂; C) Histogram showing the distribution of Th values for Type 1 fluid inclusions.

5.3.2.3.1 Type 1 fluid inclusions

The carbonic phase of the aqueo-carbonic Type 1 fluid inclusions (Figure 5.12A) in the Karlowa pegmatite comprises 20 – 30 % of the bulk composition of the inclusions. It shows melting temperatures between -57.7 °C and -57.3 °C, indicating the presence of components other than CO₂ in the system, an observation corroborated by Raman microspectroscopic data which indicate the presence of trace amounts of CH₄, CO and N₂ (Figure 5.12B). Again, the exact amounts of these trace components could not be calculated, however microthermometric data indicate that they are present in only negligible amounts (Thiéry *et al.*, 1994). Clathrate melting temperatures average 9.5 °C, and the carbonic phase homogenises to a liquid at temperatures ranging from 21.3 - 25.5 °C.

The aqueous phase of the inclusions comprises up to 70 % of individual inclusions. Initial melting temperatures range from -26.0 - -24.0 °C, and only one ice melting temperature could be obtained (-4.1 °C). The exact salinity of the inclusions could not be calculated due to the fact that they decrepitated before the melting temperature of halite could be measured, however the presence of the halite daughter crystal in the inclusions suggests that the salinity of the fluid was in excess of 26.3 equivalent wt % NaCl at the time of trapping. The density of these inclusions is high (0.9 g/cc), and the final homogenisation of Type 1 fluid inclusions ranges from 282.5 - 332.0 °C, and homogenisation is to the vapour phase.

5.3.2.3.2 Type 5 fluid inclusions

Type 5 aqueous fluid inclusions (Figure 5.13A) are composed of H₂O + NaCl as indicated by their initial melting temperatures which range from -21.8 - -21.1 °C, as well as spectra obtained using Raman microspectroscopy (Figure 5.13B). Ice melting temperatures are well constrained, averaging -3.0 °C, indicating that the salinity of these inclusions is low to moderate (4.3 - 5.9 equivalent wt % NaCl). The inclusions homogenise at relatively low temperatures averaging 180.5 °C (Figure 5.13C), and homogenisation is to the liquid phase. The bulk density of Type 5 fluid inclusions is high (0.5 g/cc).

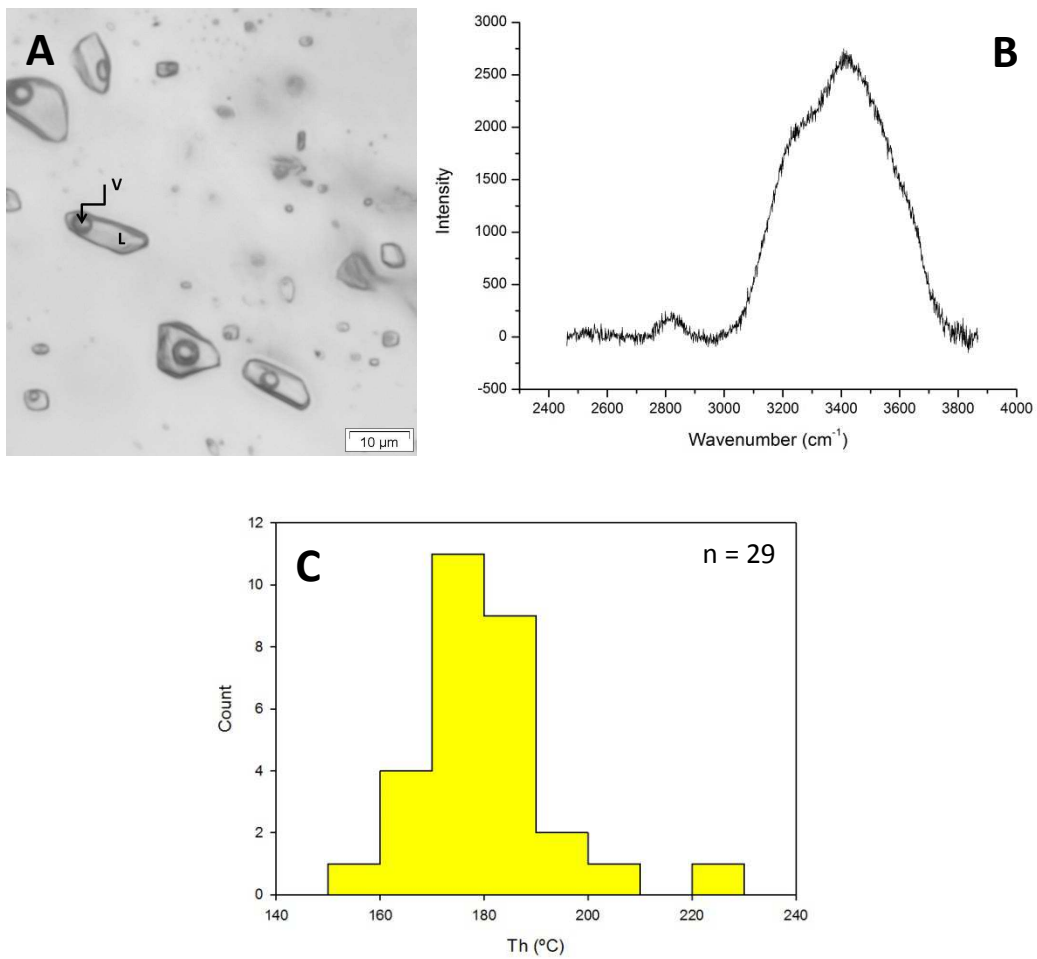


Figure 5.13: Type 5 fluid inclusion from a Karlowa pegmatite; A) Photomicrograph showing aqueous vapour, and liquid phases in the fluid inclusion; B) Normalised spectrum of the liquid phase of the fluid inclusion obtained using Raman microspectroscopy, showing the composition of the fluid inclusion as saline H₂O, expressed as a broad H₂O + NaCl feature from 3200 - 3800 cm⁻¹. Note that the broad peak at 2800 cm⁻¹ is likely to be an artefact caused by the presence of glue on the sample remaining from sample preparation; C) Histogram showing the distribution of Th values for Type 5 fluid inclusions.

5.3.2.4 Gem tourmaline-bearing pegmatites: Omapyu pegmatite

Type 1, 4 and 5 fluid inclusions were observed and measured in quartz from the Omapyu pegmatite. The samples were taken from the outer parts of the pegmatite. Inclusions were analysed using microthermometry, Raman microspectroscopy, and in this instance, PIXE.

5.3.2.4.1 Type 1 fluid inclusions

Type 1 aqueo-carbonic fluid inclusions in the Omapyu pegmatite (Figure 5.14A) are both small, averaging approximately 7.5 μm in length, and rare in comparison to the other fluid inclusion populations identified in the pegmatite.

The carbonic phase of these inclusions comprises 20 - 30 % of the bulk composition of the inclusions. The melting temperature of the carbonic phase ranges from -56.9 to -56.6 $^{\circ}\text{C}$, which, in conjunction with Raman microspectroscopic results (Figure 5.14B), indicates that it is composed of pure CO_2 . Clathrate melting ranges from 8.0 - 8.9 $^{\circ}\text{C}$, and the CO_2 homogenises to the liquid phase between 22.0 $^{\circ}\text{C}$ and 23.7 $^{\circ}\text{C}$.

The aqueous phase comprises up to 70 % of the inclusions, and shows initial melting temperatures between -26.2 $^{\circ}\text{C}$ and -24.4 $^{\circ}\text{C}$, with ice melting temperatures ranging from -6.5 - -4.6 $^{\circ}\text{C}$. Again, due to early decrepitation, the exact salinity of these inclusions cannot be determined owing to the fact that the melting temperature of NaCl cannot be recorded, however the presence of a halite crystal in the inclusions indicates that the salinity of the fluid is at least 26.3 equivalent wt % NaCl. Type 1 fluid inclusions homogenise to the liquid phase between 306.5 $^{\circ}\text{C}$ and 339.0 $^{\circ}\text{C}$ (Figure 5.14C), and the bulk density of the inclusions is high, averaging 0.9 g/cc.

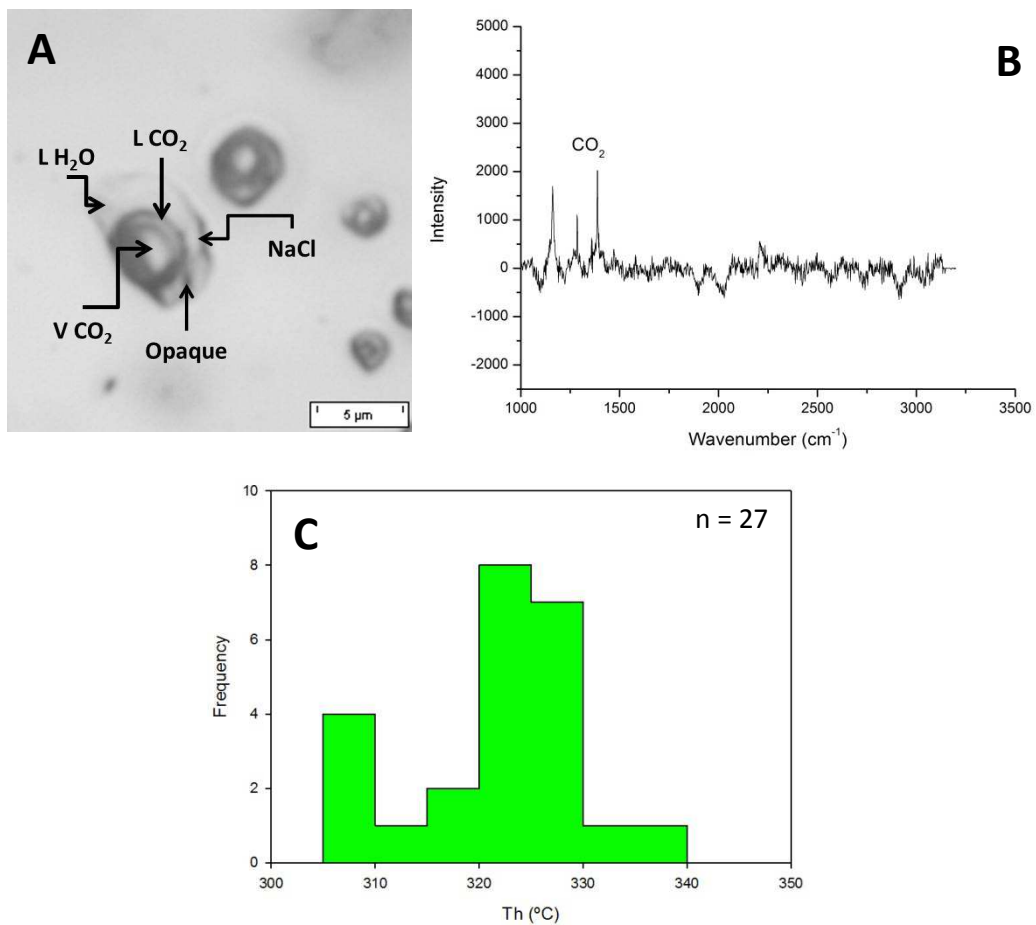


Figure 5.14: Type 1 fluid inclusion from the Omapyu pegmatite; A) Photomicrograph showing carbonic vapour, aqueous liquid and solid phases in a Type 1 fluid inclusion; B) Normalised spectrum of the vapour phase of that fluid inclusion obtained using Raman microspectroscopy, showing the composition of the vapour phase as pure CO₂; C) Histogram showing the distribution of Th values for Type 1 fluid inclusions.

PIXE analyses of Type 1 fluid inclusions indicate that they contain a number of elements, including Ca, K, Fe and Mn (Figure 5.15). Unfortunately very few fluid inclusions were suitable for analysis, the exact amounts of these elements could not be quantified. Ca, K, Fe and Mn appear to be concentrated in the vapour phase of the inclusions.

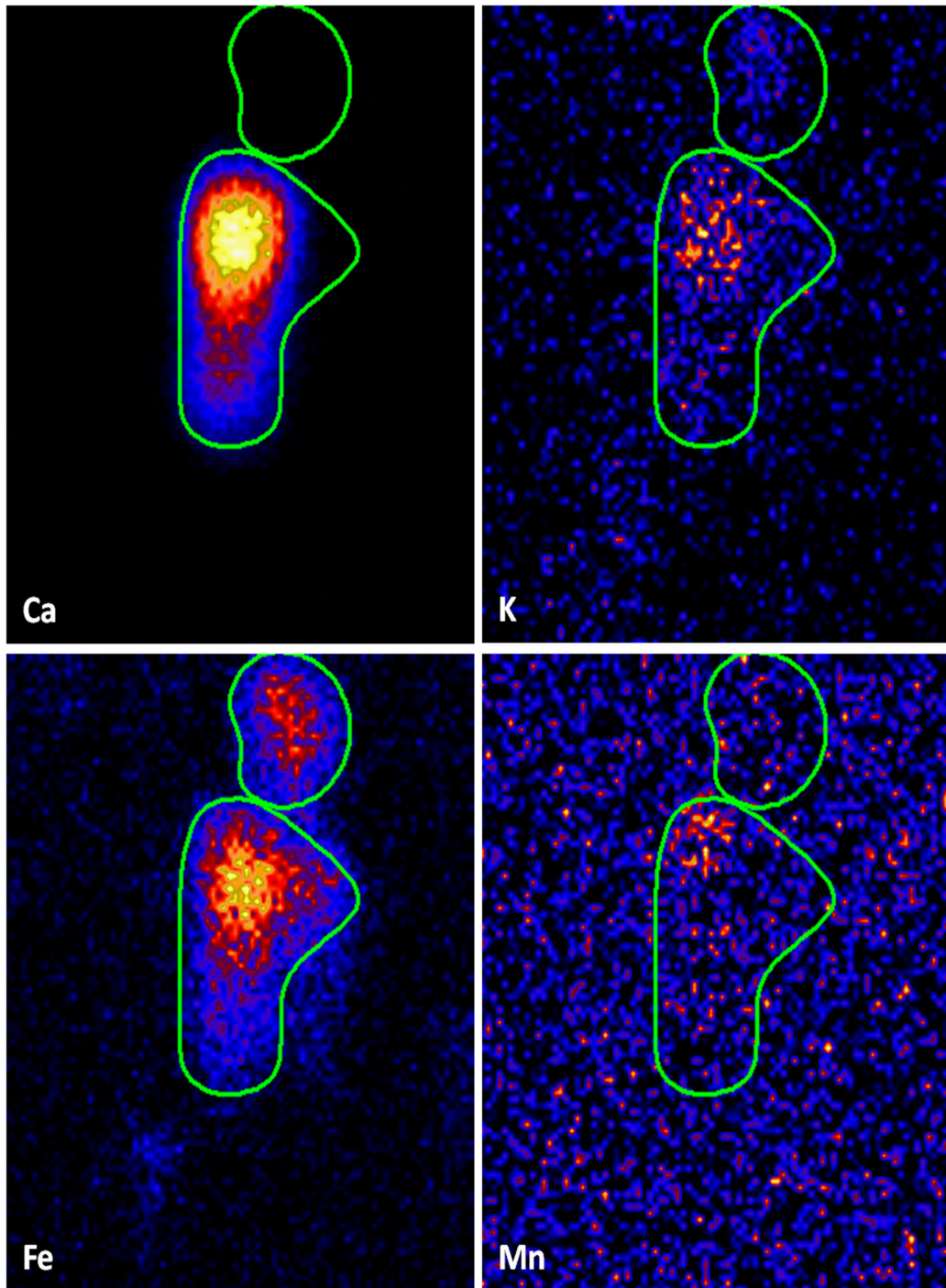


Figure 5.15: PIXE elemental map of a two Type 1 fluid inclusions from the Omapyu gem tourmaline-bearing pegmatite. The green outline indicates the shape of the fluid inclusion, and warm colours indicate the presence and relative abundance of individual elements.

5.3.2.4.2 Type 4 fluid inclusions

Type 4 carbonic fluid inclusions (Figure 5.16A) are abundant in the Omapyu pegmatite. Their melting temperature ranges from -56.9 - -57.5 °C, indicating that they should contain a trace amount of CH_4 , CO , or N_2 , however these gases were not identified with Raman microspectroscopy (Figure 5.16B). The density of these fluid inclusions is 0.7 g/cc, and they homogenise to the liquid phase at 23.1 – 23.8 °C (Figure 5.16C). Although the distribution of homogenisation temperatures appears to be highly variable in Figure 5.16C, they are actually well constrained, varying only by a maximum of 0.7 °C.

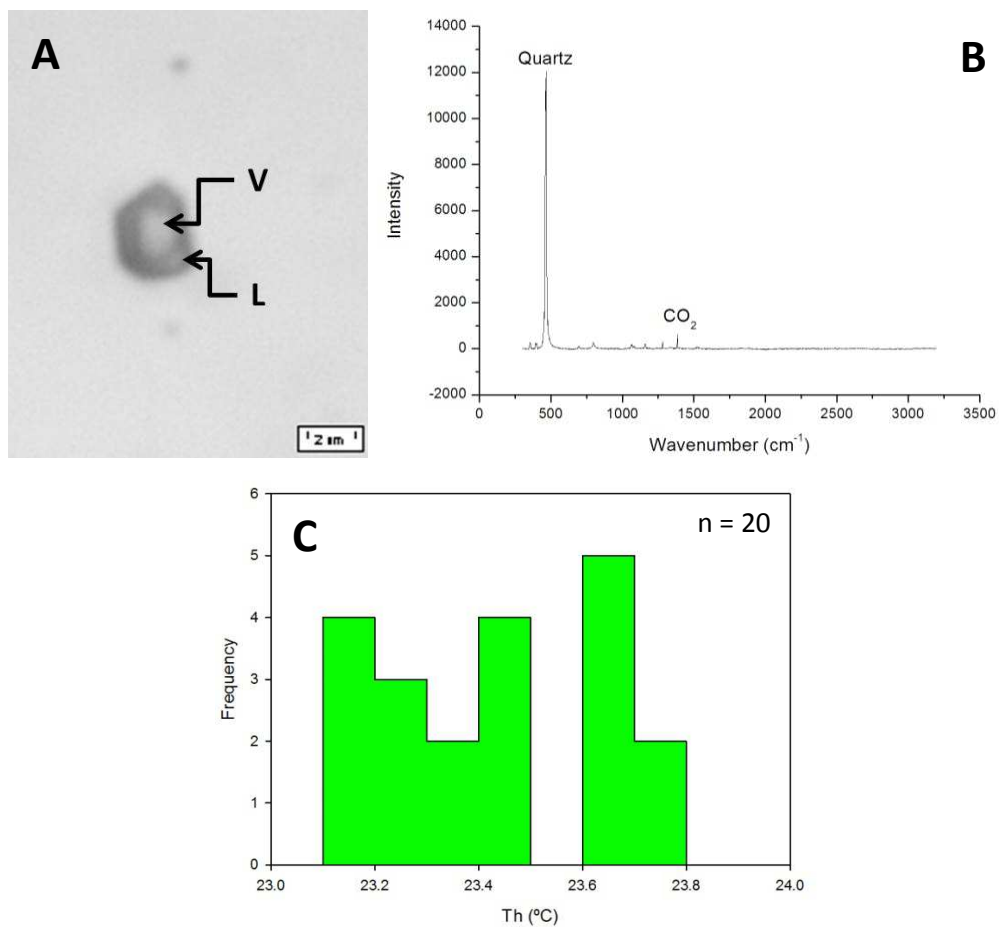


Figure 5.16: Type 4 fluid inclusion from the Omapyu pegmatite; A) Photomicrograph showing carbonic vapour and liquid phases in the fluid inclusion; B) Normalised spectrum of the vapour phase of that fluid inclusion obtained using Raman microspectroscopy, showing the composition of the vapour phase as pure CO_2 ; C) Histogram showing the distribution of Th values for Type 4 fluid inclusions.

5.3.2.4.3 Type 5 fluid inclusions

Like Type 4 inclusions, Type 5 aqueous fluid inclusions (Figure 5.17A) are abundant in the Omapyu pegmatite. Initial melting temperatures were particularly difficult to measure in these inclusions owing to their very small size averaging 6 μm , however those obtained range from -21.6 - -2.7 $^{\circ}\text{C}$, indicating that the inclusions are composed of $\text{H}_2\text{O} + \text{NaCl}$ (Figure 5.17B). Ice melting temperatures are variable, but average -0.2 $^{\circ}\text{C}$, and salinities range from 0.2 - 8.1 equivalent wt % NaCl. The inclusions homogenise to a liquid at ~ 123.3 $^{\circ}\text{C}$. The density of Type 5 inclusions is high, averaging 0.9 g/cc.

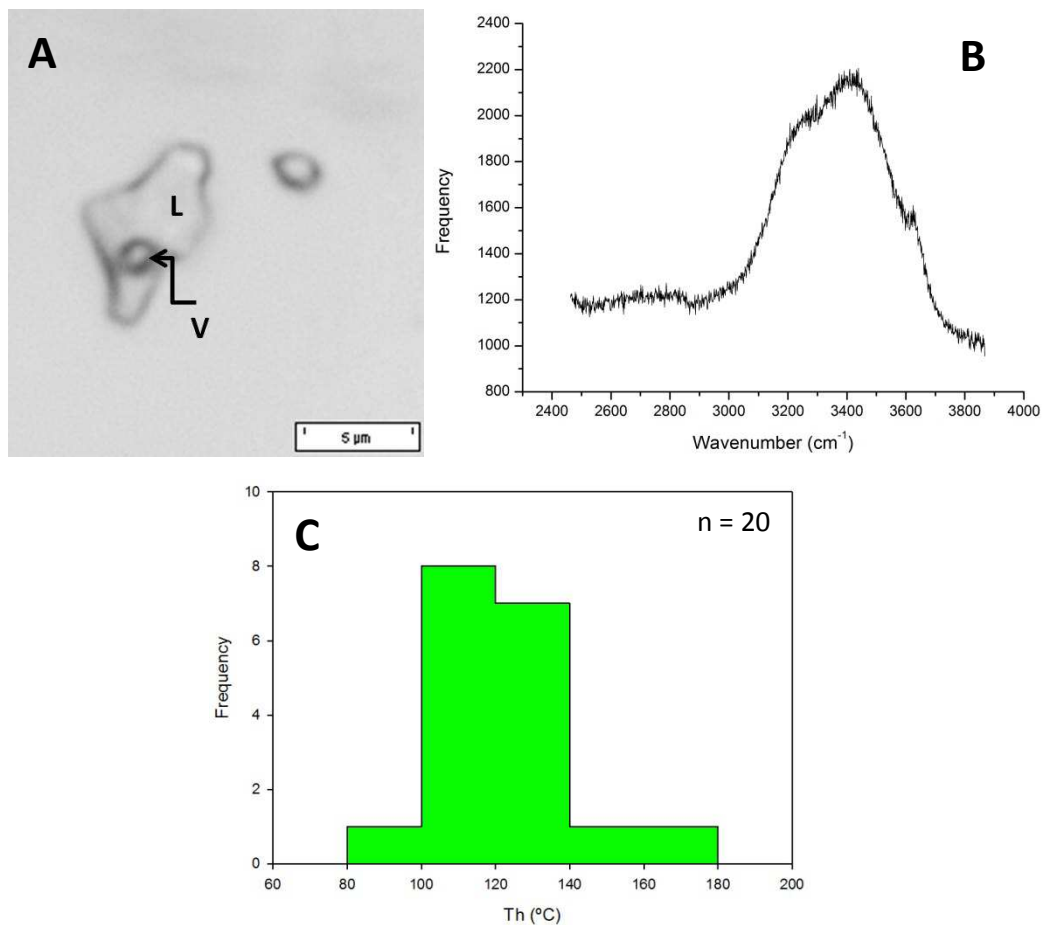


Figure 5.17: Type 5 fluid inclusion from the Omapyu pegmatite; A) Photomicrograph showing aqueous vapour, and liquid phases in the fluid inclusion; B) Spectrum of the liquid phase of the fluid inclusion obtained using Raman microspectroscopy, showing the composition of the fluid inclusion as saline H_2O , expressed as a broad $\text{H}_2\text{O} + \text{NaCl}$ feature from 3200 - 3800 cm^{-1} ; C) Histogram showing the distribution of Th values for Type 5 fluid inclusions.

5.3.2.5 U-bearing pegmatites: Valencia pegmatites (SLGs)

During this study, only Type 4 and 5 fluid inclusions were observed and measured. These were observed in quartz samples which were extracted from surface samples belonging to G. Freemantle, who conducted extensive fieldwork in the area in previous years. The samples were measured using microthermometry and Raman microspectroscopy. No suitable fluid inclusions were found for measurement using PIXE. Although no Type 1 fluid inclusions were identified in this study, Nex (1993) observed and recorded the characteristics of them, which have been summarised in this section.

2.3.2.5.1 Type 1 fluid inclusions

Nex (1993) noted the presence of aqueo-carbonic in samples taken from the SH and SJ areas at Rössing. These fluid inclusions share similar characteristics with the Type 1 fluid inclusions measured in the various pegmatites forming the subject of this study.

The carbonic phase of the inclusions melts between $-57.6\text{ }^{\circ}\text{C}$ and $-57.1\text{ }^{\circ}\text{C}$, and homogenises between $25.7\text{ }^{\circ}\text{C}$ and $31.5\text{ }^{\circ}\text{C}$ (Nex, 1993), although it is unclear whether this is to a liquid or vapour phase. Limited Raman microspectroscopic data indicate that the carbonic phase is composed of pure CO_2 . Final homogenisation temperatures range from $312 - 390\text{ }^{\circ}\text{C}$ (Nex, 1993), and again it is unknown to which phase this occurs.

2.3.2.5.2 Type 4 fluid inclusions

Type 4 fluid inclusions in the Valencia samples (Figure 5.18A) are pseudosecondary, rather than secondary, and are located in areas of fracturing in the samples. Their melting temperatures are very well constrained, and range from $-56.5 - -56.3\text{ }^{\circ}\text{C}$, which together with Raman microspectroscopic results (Figure 5.18B) indicate that they are composed of pure CO_2 . They homogenise to the liquid phase at variable temperatures between $4.8\text{ }^{\circ}\text{C}$ and $18.8\text{ }^{\circ}\text{C}$. Their density is high, averaging 0.8 g/cc .

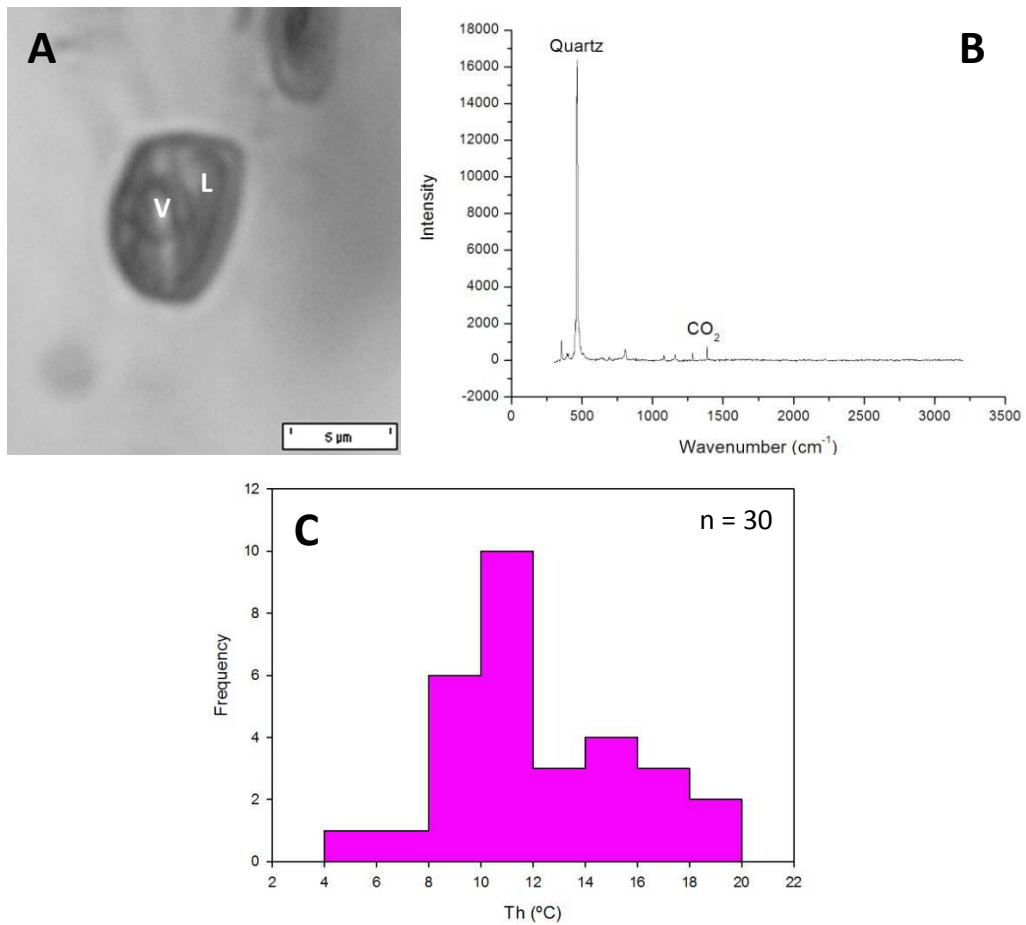


Figure 5.18: Type 4 fluid inclusion from a Valencia pegmatite; A) Photomicrograph showing carbonic vapour and liquid phases in the fluid inclusion; B) Normalised spectrum of the vapour phase of that fluid inclusion obtained using Raman microspectroscopy, showing the composition of the vapour phase as pure CO₂; C) Histogram showing the distribution of Th values for Type 4 fluid inclusions.

2.3.2.5.3 Type 5 fluid inclusions

Initial melting temperatures for aqueous Type 5 fluid inclusions (Figure 5.19A) average -21.1 °C, indicating that they comprise H₂O (Figure 5.19B) and NaCl. Ice melting temperatures range from -1.7 - -1.5 °C, and the salinity of the inclusions is low, ranging from 1.9 - 2.9 equivalent wt % NaCl. These inclusions homogenise to the liquid phase between 146.2 °C and 179.3 °C, and they are dense, with densities averaging 0.9 g/cc.

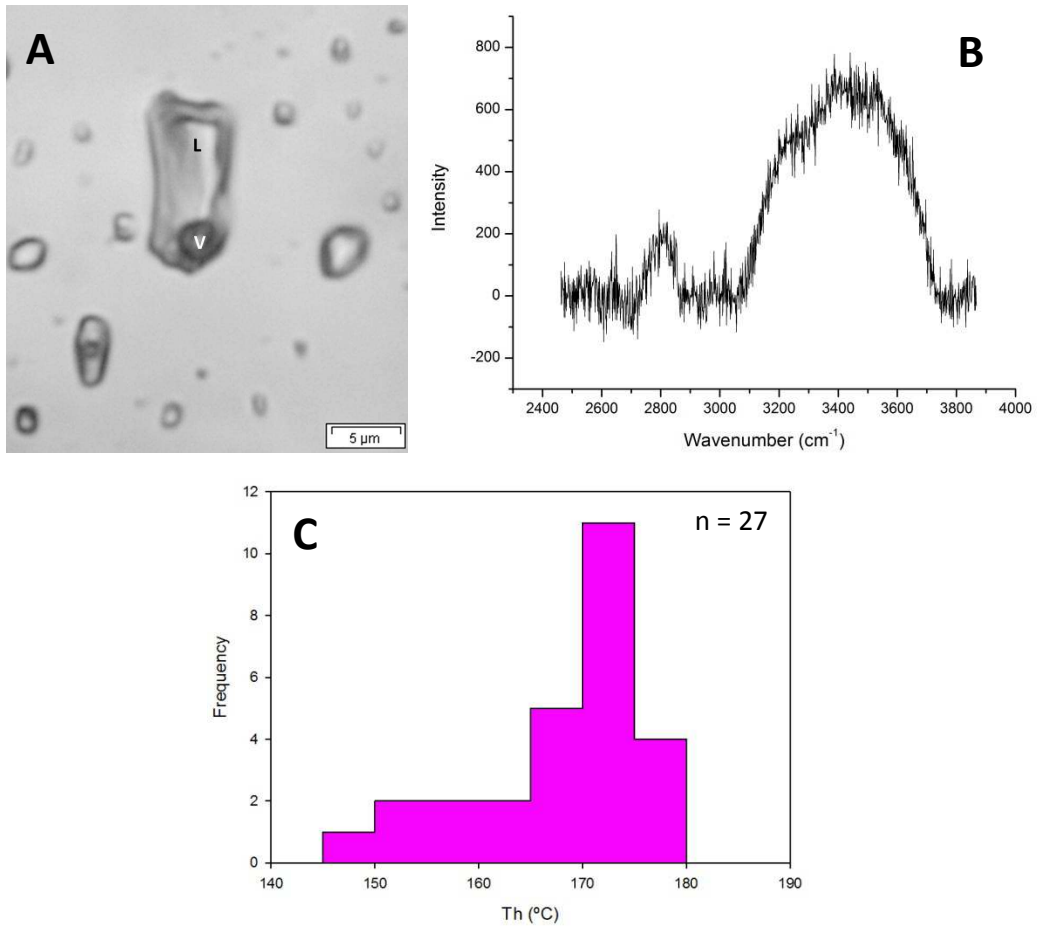


Figure 5.19: Type 5 fluid inclusion from a Valencia pegmatite; A) Photomicrograph showing carbonic vapour, and liquid phases in the fluid inclusion; B) Normalised spectrum of the liquid phase of the fluid inclusion obtained using Raman microspectroscopy, showing the composition of the fluid inclusion as saline H_2O , expressed as a broad $\text{H}_2\text{O} + \text{NaCl}$ feature from $3200 - 3800 \text{ cm}^{-1}$. Note that the broad peak at 2800 cm^{-1} is likely to be an artefact caused by the presence of glue on the sample remaining from sample preparation; C) Histogram showing the distribution of Th values for Type 5 fluid inclusions.

5.4 Discussion of results

Despite the strong zonation observed in some of the LCT pegmatites, as well as the differences in mineralisation between LCT and NYF pegmatites from different parts of the Damara Belt, all of the pegmatites appear to contain similar/the same fluid inclusions populations.

Cathodoluminescence results showed that the quartz samples measured for fluid inclusions are massive, containing only small, dark patches of recrystallization around healed fractures (e.g. Müller *et al.*, 2008), and in the absence of any growth zonation of the mineral, no fluid inclusions could unequivocally be classified as primary.

Both LCT and NYF pegmatites contain the earliest Type 1 pseudosecondary aqueo-carbonic and the latest aqueous secondary Type 5 fluid inclusions. The Type 1 inclusions show similar geochemical characteristics ($\text{H}_2\text{O} + \text{CO}_2 + \text{NaCl}$) across the different pegmatite types. Those measured in samples from Sn- and Li-Sn-bearing LCT pegmatites show some variation, both in terms of their composition i.e. they contain traces of constituents other than CO_2 , particularly CH_4 , CO , and N_2 , and in terms of their bulk density. Out of the populations measured, Type 1 inclusions are the most saline. In addition to these geochemical characteristics, Type 1 fluid inclusions across the different LCT and NYF pegmatites homogenise at similar temperatures, ranging from 315 - 330 °C (Figure 5.20).

Type 2 aqueous pseudosecondary fluid inclusions were only observed in the Li-Be-bearing pegmatites. The Th values of these inclusions differ from those measured in other inclusions populations; this and their occurrence as pseudosecondary clusters mean that their exact timing in relation to the other fluid inclusion populations remains unclear.

The greatest variability in the fluid inclusion assemblages present in individual pegmatites is most evident in their secondary fluid inclusion assemblages. Type 3 aqueo-carbonic fluid inclusions occurring in the Li-Be-bearing LCT pegmatites, and

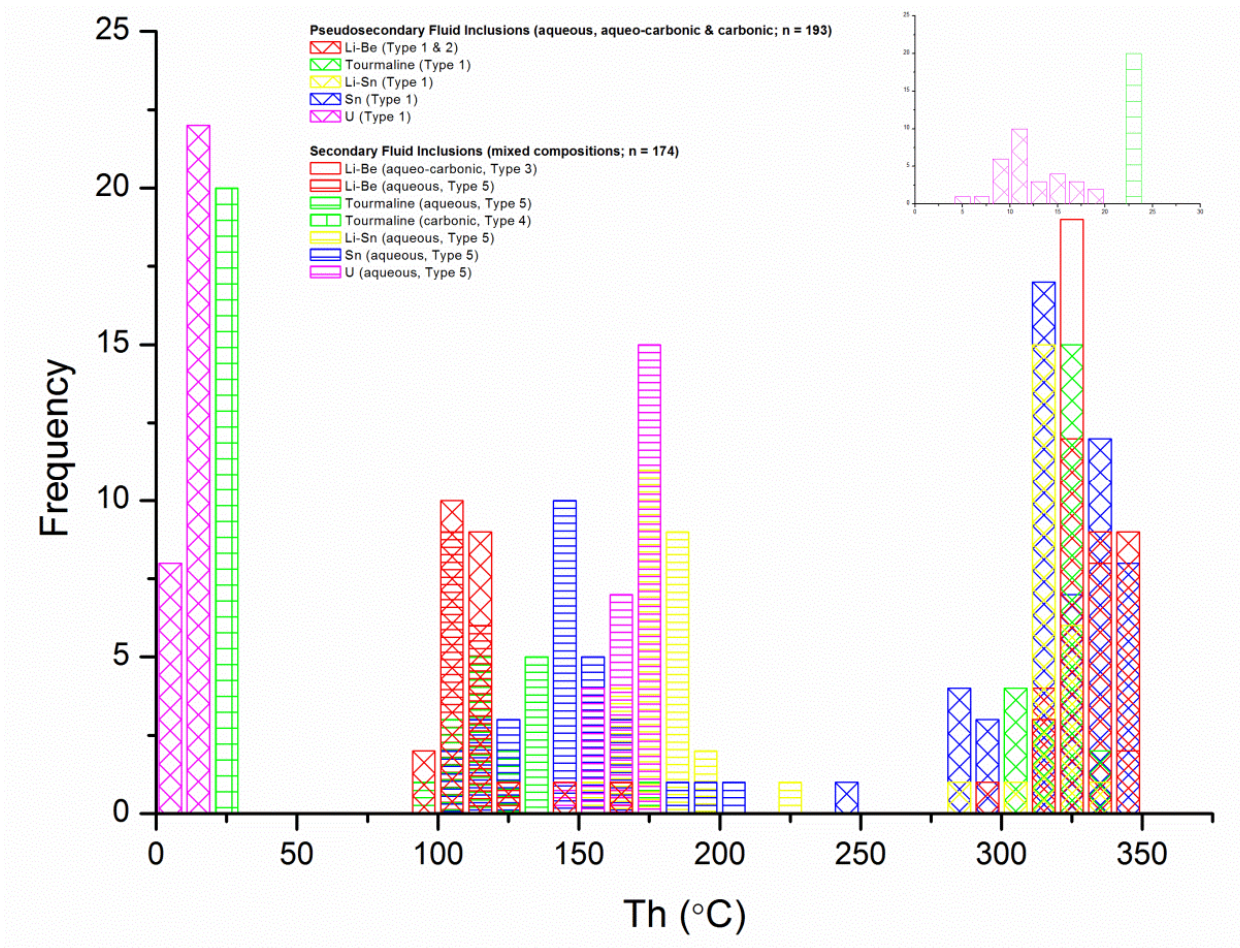


Figure 5.20: Homogenisation temperatures of all measured fluid inclusions (n = 367). The inset shows the distribution of homogenization temperatures for carbonic inclusions; those with higher Th are from NYF pegmatites, and those with lower temperatures are from LCT pegmatites.

Type 4 carbonic inclusions, which occur in gem tourmaline-bearing LCT pegmatites and U-bearing NYF pegmatites. In addition to this, the Type 4 inclusions in LCT and NYF pegmatites homogenise at different temperatures (Figure 5.20), and their respective densities differ, with lower density secondary inclusions occurring in the LCT pegmatites, and higher density pseudosecondary inclusions occurring in the LCT pegmatites.

Homogenisation data are again represented in Figure 5.21, however in this plot the data are separated only by relative timing i.e. pseudosecondary vs. secondary. The plot shows that there is an overlap in the homogenisation temperatures particularly of Type 1 and Type 3 fluid inclusions between ~ 300 °C and 350 °C (refer to Figure 5.20 for legend), and there is also a large cluster of data for Type 5 inclusions between 100 °C and 200 °C. Type 2 homogenisation temperatures are lower than those of bulk of Type 5 values, again indicating that the two populations are unrelated.

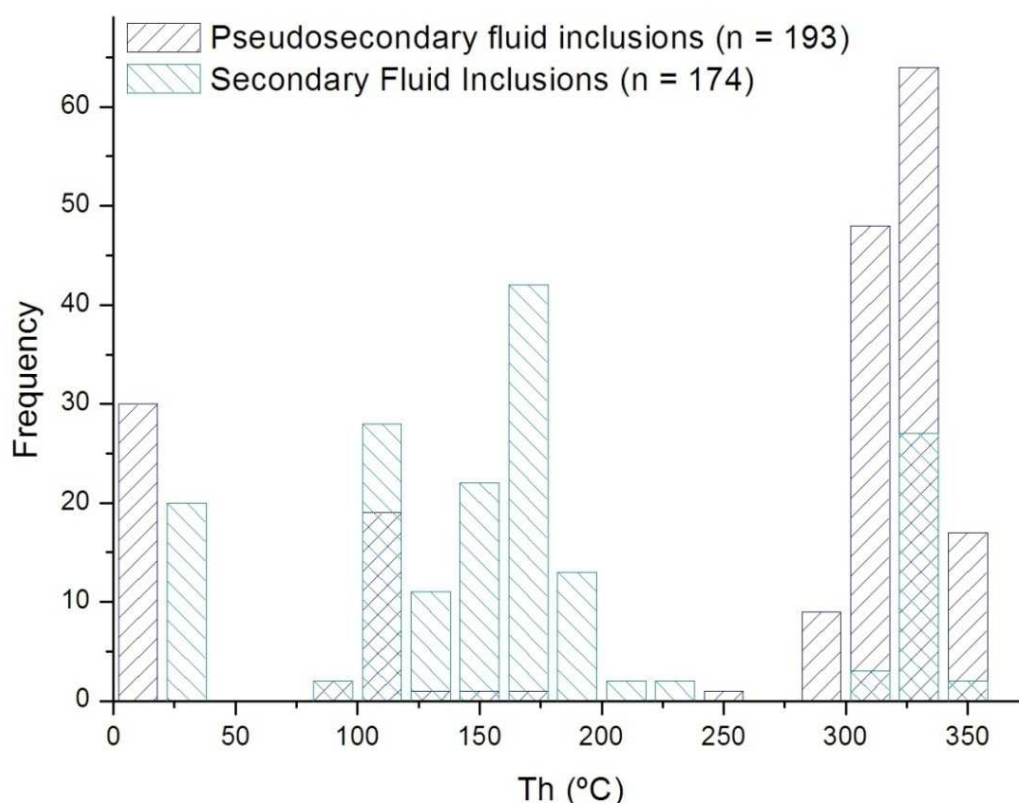


Figure 5.21: Homogenisation temperatures of all measured fluid inclusions, showing the relationship between the homogenization temperatures of pseudosecondary and secondary inclusions.

In addition to the overlap in homogenisation temperatures of pseudosecondary and secondary inclusions, the carbonic phases of Type 1, 3, and 4 fluid inclusions are of a similar density (~ 0.7 g/cc), even though in some deposits they contain trace amounts of constituents other than CO_2 , such as CH_4 , CO , and N_2 . Similarly, the density of Type 5 inclusions across different deposit types is similar (~ 1.0 g/cc).

5.5 Interpretation of results

Similar observations have been made of fluid inclusions populations in pegmatites in other localities (Trumbull, 1995; Alfonso and Melgarejo, 2008; Thomas *et al.*, 2009).

Trumbull (1995) identified three fluid inclusions populations in rare-element pegmatites in Swaziland; the first of these fluid inclusions populations comprises pseudosecondary to secondary, moderately saline, aqueo-carbonic inclusions, which homogenise at relatively low temperatures (~ 220 °C). The Type 2 fluid inclusions of Trumbull (1995) are also aqueo-carbonic and show similar petrographic relationships to the Type 1 inclusions. Like the Sn- and Li-Sn-bearing LCT pegmatites of this study, they contain minor amounts of CH_4 (Trumbull, 1995), and overall they show the greatest similarity in terms of composition and homogenisation temperature with the Type 1 fluid inclusions of the current study. The third population identified (Type 3) by Trumbull (1995) comprises saline aqueous inclusions, which bear a resemblance to the Type 2 inclusions identified in this study.

Alfonso and Melgarejo (2008) identified the same number of fluid inclusion populations of similar compositions and with similar homogenisation temperatures in the Cap de Creus zoned rare-element pegmatites in Spain. The Type A fluid inclusions of Alfonso and Melgarejo (2008) are geochemically similar to Type 1 fluid inclusions measured in this study. In addition to compositional similarities, they also homogenise at temperatures ranging from 320 - 370 °C, and also represent the earliest fluid inclusion population trapped in the pegmatites. Similar to this study, the later or secondary fluid inclusion assemblages show some variability across the

different types of pegmatites, however Type A inclusions are present in all the pegmatites.

Thomas *et al.* (2009) identified aqueo-carbonic and carbonic inclusions as an end-member variety of a number of melt and fluid inclusions populations which were identified in pegmatites from East Transbaikalia, Russia. Again, the aqueo-carbonic inclusions share several geochemical characteristics in common with the Type 1 fluid inclusions of this study, and the carbonic inclusions resemble Type 4 inclusions from this study.

The abundance and composition of fluids in magmatic systems are among the most valuable information that can be obtained from fluid inclusions (Roedder, 1984), and it is commonly accepted that the concentration of fluids in a residual melt results from the fractional crystallisation of peraluminous H₂O- and F-rich granite melts (Roedder, 1984; Thomas *et al.*, 2006).

Recent melt and fluid inclusion studies by Thomas and co-workers (2006, 2009, 2011, 2012) and Borisova *et al.* (2012) suggest that in addition to the accumulation of fluids during the late stages of crystallisation, with saturation a melt will be forced to separate into two conjugate immiscible melts, one peraluminous (Type A), and one peralkaline (Type B, usually only preserved as melt inclusions as a result of its reactivity throughout crystallisation), as well as a fluid phase. The late stage exsolution of hydrosaline fluids from felsic magmas in studies on granites and pegmatites has been reported by numerous authors e.g. Roedder and Coombs (1967), Roedder (1992), Frezzotti (1992), Lu and Lottermoser (1997); Linnen (1998); Kontak *et al.* (2001), Gagnon *et al.*, (2004), Alfonso and Melgarejo (2008), and Thomas *et al.* (2006, 2009, 2012).

The composition and salinity of such a fluid will be determined by the amount of fluxing components, or melt structure modifiers (Thomas *et al.* 2012), present as H₂O, OH⁻, CO₂, HCO₃⁻, CO₃²⁻, SO₄²⁻, PO₄³⁻, H₃BO₃, F, and Cl, as well as the elements Li, Na, K, Rb, Cs, and Be, in the melt, since these elements decrease the solubility of Cl⁻ in the

magma (London 1987, Thomas *et al.* 2000). Furthermore, Cl⁻ solubility in carbonic fluids is extremely low, and as such it will partition preferentially into the aqueous phase of a fluid exsolved from an aluminosilicate melt (De Vivo and Frezzotti, 1994; Webster and De Vivo, 2002).

5.5.1 Fluid evolution of LCT and NYF pegmatites from the Damara Belt

The overlap in the homogenisation temperatures between Type 1 and Type 3 fluid inclusions, and the similarities in the density of the carbonic phases in both aqueo-carbonic and carbonic inclusions suggest that the fluids identified have recorded the progressive evolution of a saline aqueo-carbonic fluid exsolved from the pegmatite melt during a single trapping event, and the much later ingress of a moderately saline aqueous fluid..

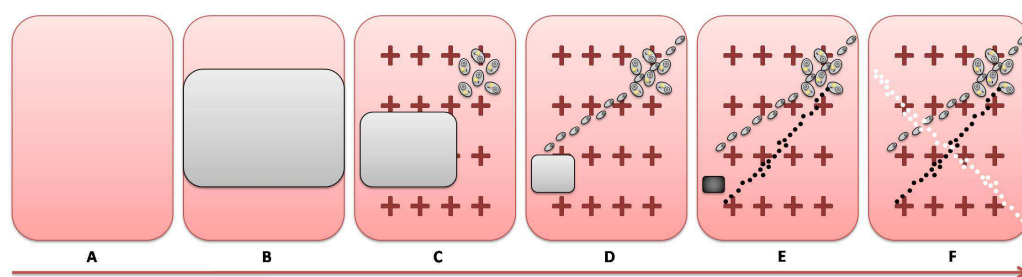


Figure 5.22: Schematic diagram of the evolution of fluids in Namibian pegmatites. See text for detailed explanation.

A model for the evolution of fluids in the Namibian pegmatites is illustrated in Figure 5.22. Here, a saline aqueo-carbonic fluid (grey box) exsolves from a late-stage pegmatite magma (pink box) rich in P, B, and F (Figure 5.22A & B). Fluxes present in the melt partition preferentially into the fluid phase, facilitating the accumulation of Cl⁻ in the fluid. As the pegmatite crystallises (pink box with crosses), multiphase aqueo-carbonic Type 1 fluid inclusions become trapped (Figure 5.22C). With progressive crystallisation, the fluid becomes less saline, and low salinity aqueo-carbonic Type 3 inclusions become trapped (Figure 5.22D); with time and crystallisation, eventually the Type 4 carbonic fluid remains (black box; Figure 5.22E).

The accumulation of Cl⁻ in the fluid would have been facilitated by P, B, and F, and other melt structure modifiers, evidence for which is present in the abundance of lepidolite, tourmaline, and a number of phosphate minerals, for example, in the wall and intermediate zones of the zoned pegmatites, and throughout unzoned bodies. Slight differences in the composition of the carbonic phase, i.e. the presence of trace amounts of CH₄, CO, and N₂ in the carbonic phase, is likely to be the result of mixing with some external fluid, such as a metamorphic fluid, derived from the country rock during emplacement (e.g. Linnen and Williams-Jones, 1994; Masoudi *et al.*, 2009; Thomas *et al.* (2009).

Much later, low-salinity Type 5 fluid inclusions circulate through the cooled and fully crystallised pegmatites; this fluid could be meteoric in origin, or it may be related to the intrusion of Mesozoic ring complexes, however identifying the exact origin of this fluid is beyond the scope of the current study.

This model for the evolution of the fluids in Namibian pegmatites is similar to that proposed by Alfonso and Melgarejo (2008) for the Cap de Creus zoned rare-element pegmatites in Spain. While it does account for the textural and geochemical characteristics of the Type 1, 3, 4, and 5 populations, it fails to include and clarify the timing of Type 2 inclusions. In addition to the exsolution of a saline aqueo-carbonic fluid during the crystallisation of the intermediate zones of the Cap de Creus pegmatites, Alfonso and Melgarejo (2008) found evidence of a later unmixing of the remaining fluid into a saline aqueous phase and a low-salinity aqueo-carbonic phase at temperatures ranging from 415 - 450 °C. While a similar process might be invoked for the trapping of Type 2 fluid inclusions, given their relatively low homogenisation temperatures (~ 100 - 115 °C) this would seem unlikely, therefore the origin and exact timing of the trapping of this fluid inclusion population remains unresolved.

Note that because the study of melt inclusions was beyond the scope of this study, evidence for a Type B peralkaline melt was not observed/recorded. This does not, however, negate the possibility of two melt-fluid immiscibility during the crystallisation of the pegmatites studied.

5.5.2: Implications for mineralisation

It is widely accepted that mineralisation in pegmatites is a result of magma geochemistry and reactivity rather than of fluid activity (e.g. Gagnon *et al.*, 2004; Borisova, 2012; Thomas *et al.*, 2009, 2011), however Thomas *et al.* (2009) and Borisova *et al.*, (2012) propose that volatile-rich melts are significantly involved in the transport and concentration of rare metals as a result of the affinity of rare metals for OH and F. They suggest that elevated concentrations of metals e.g. Sn, Be, Zn, Ga, Cd, Ta, Th, and U in these melts may be attributed the effects of melt structure modifiers (Thomas *et al.*, 2012), which depolymerise the melt and cause the formation of oxy-hydroxide and complex fluoride complexes which transport metals in the system (Borisova *et al.* 2012). Late-stage melt-melt-fluid immiscibility is also crucial in concentrating metals such as Be (e.g. Thomas *et al.*, 2011; Simmons *et al.*, 2012) to economic abundances, and to the degree crystals containing these metals could grow to such large dimensions as those observed in pegmatites. Any variations in metal concentrations would be a result of the effects of primary heterogeneities in the peraluminous pegmatite melt (Borisova *et al.*, 2012), and the reactivity of melt phases throughout transport and crystallisation of the magma, which would facilitate their contamination through contact with other melts or with country rock (Ackerman *et al.*, 2007; Thomas *et al.*, 2009).

Although the physical and chemical characteristics of a magma may have a greater effect on mineralisation in a pegmatite than the fluid geochemistry, the influence of exsolved fluids cannot be negated. The partitioning of an element into the fluid phase is dependent on the salinity of that fluid, such that an element like Sn, W or Ta will favour a hypersaline fluid rather than the coexisting melt (Roedder, 1984; Alfonso and Melgarejo, 2008). The hypersaline fluid could then transport the element as hydroxyl-Cl complexes, for example, (Kovalenko *et al.*, 1986), causing mineralisation to occur from the fluid in the latest stages of crystallisation e.g. in late-stage veins or greisens (e.g. Alonso and Melgarejo, 2008). This would facilitate economic mineralisation in pegmatites whose initial melt compositions would not otherwise do so.

In the case of the Namibian pegmatites there is evidence that mineralisation was from the melt (Li-Be- and U-bearing pegmatites), and a fluid (gem-tourmaline and Sn-bearing pegmatites) phase, as well as a combination of the two (Li-Sn-bearing pegmatites). In the Li-Be- and U-bearing pegmatites, mineralisation occurs in primary magmatic minerals e.g. petalite, lepidolite and beryl in the LCT bodies and uraninite and monazite in the NYF pegmatites, which formed during the crystallisation of the pegmatite bodies by magmatic processes.

Cassiterite mineralisation in the Sn-bearing pegmatites occurs primarily in greissenised patches indicating fluid activity. In addition to this the unusual trace element composition of the earliest fluids as observed particularly in Type 1 inclusions from the Uis pegmatites, suggests that the accessory Cu-sulphides and galena in these pegmatites are most likely to have been formed during the late stages of pegmatite crystallisation.

In the gem-tourmaline-bearing pegmatites, mineralisation occurs in miarolitic cavities. These cavities are known to form as a result of the accumulation of volatiles (Simmons, 2007; Simmons *et al.*, 2012; London, 2008). Again, the presence of rare accessory Mn-phosphates and Fe-sulphides in the pegmatites may also be attributed to fluid activity, as is suggested by the presence of Mn and Fe in solution in Type 1 fluid inclusions from these pegmatites.

The Li-Sn-bearing pegmatites from Karlowa show evidence of mineralisation both from magmatic processes and fluid activity. Magmatic mineralisation occurs in the form of Li-aluminosilicates, particularly spodumene, in these pegmatites. Again cassiterite mineralisation is most prominent in greissenised patches representing areas within the pegmatites where fluids would have accumulated and ultimately deposited economic metals.

5.6 Summary

This study provides the first fluid inclusions data for mineralised pegmatites in Namibia, with the exception on a study conducted by Nex (1993) on NYF SLGs in the Rössing area. Numerous fluid inclusion populations are present in quartz from the pegmatites. These, and the deposits in which they occur, are summarised in Table 5.1.

The earliest of these fluids is a saline aqueo-carbonic fluid which exsolved from the pegmatite magma during the late stages of crystallisation at a minimum temperature of 320 – 330 °C. With progressive crystallisation the fluid became less saline until eventually it evolved into a carbonic fluid, which was trapped as small, secondary trails cross-cutting the quartz. Because the fluid inclusion populations are so similar across the different types of pegmatites, it is unlikely that fluids alone are responsible for the differences in mineralisation which occur in different geographic locations, and therefore different stratigraphic heights, in the Damara Belt. Furthermore, given that the fluid inclusion populations in all of the pegmatites, irrespective of their geographic locations or metallogeny, are very similar; therefore, compared with published data, this would suggest a similar fluid evolution for many pegmatites, both in Namibia and around the world.

The pegmatite magmas are however likely to have been volatile- and melt modifier-rich which would facilitate enrichment in metals such as Sn, Be, U, and Th. Once saturation in volatiles occurred, a fluid exsolved from the melt, leaving more compatible elements to crystallise from the coexisting melt, while incompatible elements would partition into the fluid, and eventually crystallise from it.

CHAPTER 6

GEOCHEMICAL CHARACTERISTICS OF MINERALISED PEGMATITES AND THEIR COUNTRY ROCKS

6.1 Introduction

Major and trace element data provide a useful means of interpreting and understanding the evolution of magma generation in a given tectono-magmatic setting (see reviews in Rollinson, 1993; Winter, 2001). Chappell and White (1974) distinguished between I- and S-type granites based on the distinct geochemical trends observed in granites in Eastern Australia. I-type granites refer to those granitoids which are derived from the partial melting of mafic mantle material or lower crustal (infracrystal) material, while S-type refers to those derived from the partial melting of peraluminous sedimentary (supracrustal) source rocks. Later White (1979) expanded upon this classification scheme by proposing M-type granites, which form directly from a mantle source, and A-type granites, which are granitoids whose emplacement is unrelated to an orogenic event, and rather results from extension, which resulted in the S-I-A-M classification of granitic rocks. In the 1980s, Whalen *et al.* (1987) devised a method of distinguishing between I-, S-, and A-type granites by plotting $10000 \cdot \text{Ga}/\text{Al}$ against various trace and major element combinations.

Another widely used geochemical tectonic discrimination tool is that of Pearce *et al.* (1984), who found that Nb, Ta, Rb, Y, and combinations thereof, were useful in identifying four major (later five) major tectonic environments, syn-collisional (syn-COLG), post-collisional (post-COLG), within plate (WPG), ocean ridge (ORG), and volcanic arc (VAG) granites. This method of classifying granites is a popular means of identifying the tectonic setting of a granite whose tectonic environment has not been preserved (Frost *et al.*, 2001).

The granite classification scheme of Barbarin (1999) uses silicate mineralogy, and its relation to the A.S.I. of a given granite, to place the granite into one of six classes.

Each class is derived from a particular source type in a particular geodynamic environment. Muscovite and Cordierite Peraluminous Granites (MPG and CPG respectively) are proposed to be derived from crustal material during continent-continent collision, while K-rich Calc-alkaline (KCG) and Amphibole Calc-alkaline Granitoids (ACG) are of mixed crustal and mantle origin, and form during transitional regimes and subduction respectively. Arc Tholeiitic Granites (ATG) are proposed to be derived from the mantle during subduction, while Mid-Ocean Ridge Tholeiitic (RTG), and Peralkaline and Alkaline Granitoids (PAG), although also sourced from mantle material, are proposed to form during ocean spreading or continental doming and rifting.

Whole-rock samples were taken from the mineralised pegmatites under investigation in order to identify any particular geochemical characteristics they may possess, and to classify them in terms of those geochemical characteristics. Whole-rock country rock samples were also analysed in an effort to establish whether or not there are any significant geochemical similarities or differences between the pegmatites and their host rocks.

6.2 Methodology

6.2.1 Sample preparation

For whole-rock geochemical analyses samples were crushed and milled into fine powders and then submitted to the X-ray Fluorescence Spectrometry (XRF) facility at the Earth Lab, University of the Witwatersrand for major and trace element analysis. Whole-rock samples were also submitted to the Department of Geological Sciences at the University of Cape Town for trace element analysis using Inductively-Coupled Mass Spectrometry (ICP-MS). A sample inventory is presented in Appendix 1.

6.2.2 XRF analyses

Major elements were analysed using fused disks. First the finely milled rock powders were ignited at 1020 °C for 40 minutes to calculate the loss on ignition (LOI). Then the

samples were mixed with a commercially available pre-ignited flux at a ratio of 1:5 and fired for 50 minutes at 1020 °C. The mixture was then poured and mechanically pressed into an infinitely thick fused disk. The disks were placed in a Panalytical WDXRF which uses a Rh tube as the excitation source, and measured for major and trace elements.

6.2.3 ICP-MS analyses

6.2.3.1 Whole-rock trace element analyses

Trace element samples were prepared for analysis by dissolving 50 mg of rock powder in a 4:1 HF/HNO₃ acid mixture in sealed Savilex beakers on a hotplate for 48 hours. This was followed by evaporation to incipient dryness and two treatments of 2mL of concentrated HNO₃. The final dried product was then taken up in 5% HNO₃ solution containing 10 ppb Re, Rh, In, and Bi as internal standards. Standardisation was done against artificial multi-element standards. The samples were then measured using a Thermo-Fishers X-Series2 mass spectrometer.

6.2.3.2 Trace element analyses in quartz

The in situ analysis of trace elements (Li, Be, B, Ge, Na, Al, K, Ti and Fe) in quartz was done using Laser Ablation Inductively-Coupled Mass Spectroscopy (LA-ICP-MS) at the Geological Survey of Norway. Quartz wafers that had been prepared for fluid inclusion studies were used for the analyses. The ICP-MS used in this study is a Thermo Instruments ELEMENT XR with a NewWave 193 nm excimer laser probe. The laser was used at a repetition rate of 20 Hz, and pulse energy of 1.5–1.6 mJ with continuous ablation on an area of approximately 180 × 200 μm. The laser beam was adjusted to give a spot size of approximately 20 μm. External calibration was done using four silicate glass reference materials produced by the National Institute of Standards and Technology (NIST SRM 610, NIST SRM 612, NIST SRM 614, NIST SRM 616). Measurements on each sample were repeated three times.

Ti concentrations from the quartz samples were used to calculate crystallisation temperatures for the pegmatites according to the Ti-in-quartz geothermometer of

Wark and Watson (2006), later revised to a geothermobarometer by Thomas *et al.* (2010) and Huang and Audétat (2012):

$$T (^{\circ}\text{C}) = \frac{(-0.27943 \times 10^4) - 660.53(P^{0.35})}{\log Ti_{aTiO_2} - 5.6459} - 273$$

Ti is the concentration of Ti in quartz in ppm, and a_{TiO_2} is the activity of Ti in the system, assumed to be 1 where Ti-bearing phases have been identified in the rock. P , pressure, is constrained to 3 kbar following the work of Nex *et al.* (2001a). The results of the trace element analyses of quartz wafers can be found in Appendix 3.

6.3 Results

Major and trace element data for mineralised pegmatites are presented in Tables 6.1 and 6.2 respectively, while major element data for the country rock suite are presented in Table 6.3, and country rock trace element data in Table 6.4.

6.3.1 Li-Be-bearing pegmatites

6.3.1.1 Rubicon and Helicon pegmatites

Wall Zone samples from the Rubicon and Helicon pegmatites are highly siliceous, being composed of 70.96 - 79.90 wt % SiO_2 . Al_2O_3 is the second most abundant constituent of these samples, with values reaching up to 17.86 wt Al_2O_3 . Na_2O values are relatively high, but also variable, ranging from 4.77 - 10.15 wt % Na_2O . K_2O and CaO concentrations are low, with K_2O values reaching a maximum of 1.47 wt % K_2O , and CaO concentration measuring less than 0.25 wt % CaO . P_2O_5 concentrations are similar, ranging between 0.21 wt % P_2O_5 and 0.31 wt % P_2O_5 . While FeO concentrations are variable, they typically remain below 1.00 wt % FeO . The concentrations of all other major elements are typically very low (< 0.10 wt %). The Alumina Saturation Index (A.S.I., Shand, 1927) values of The Rubicon and Helicon pegmatites range from 1.02 - 1.30.

Li and Rb are the most abundant trace elements in the Rubicon pegmatites, although their concentrations are variable, ranging from 267.50 - 1178.00 ppm Li and 216.20 - 1545.00 Rb. The samples also contain appreciable, although variable, amounts of Zn (57.07 - 244.00 ppm) and Cs (17.55 - 106.20 ppm). Nb and Ta concentrations are typically less than 40 ppm Nb and 10 ppm Ta, however one sample, 2eRUB from the Rubicon pegmatite contains 154.7 ppm Nb and 51.51 ppm Ta. Sn concentrations are extremely variable, reaching a maximum value of ~30.00 ppm, and Ga concentrations, are significantly less variable, reaching a maximum of ~ 42 ppm. All other trace element abundances are very low (< 10 ppm), although Ti values do reach up to 39.97 ppm. Rb/Sr, and Rb/Ba ratios in Li-Be-bearing pegmatites are variable, ranging from ~ 100-887 and ~ 350-1061 respectively. Sr/Ba ratios typically range from < 1 to 3.67.

Ti measured in the quartz samples from the Rubicon and Helicon pegmatites are extremely variable, ranging from 0.00 - 102.90 ppm. The range of temperatures calculated from these concentrations is as variable, ranging from 405 - 763 °C (Table 6.5). With the exception of outlier data points, the temperatures generated from are fairly tightly constrained, and range from 390 - 463 °C.

Table 6.1: Whole-rock major element concentrations (in wt %) of LCT and NYF pegmatites (LOI = loss on ignition, A.S.I = Alumina Saturation Index).

Locality	Sample No.	SiO ₂	Al ₂ O ₃	Fe ₂ O ₃	FeO	MnO	MgO	CaO	Na ₂ O	K ₂ O	TiO ₂	P ₂ O ₅	Cr ₂ O ₃	NiO	TOTAL	LOI	A.S.I
Rubicon	2eRUB	70.96	17.86	0.02	0.19	0.05	0.05	0.25	10.15	0.33	0.01	0.31	0.00	0.00	100.16	0.43	1.02
Rubicon	2RUBp	76.29	14.40	0.10	0.82	0.14	0.04	0.19	6.00	1.40	0.02	0.21	0.00	0.00	99.60	0.88	1.23
Helicon	IHELg	75.53	15.28	0.07	0.57	0.03	0.06	0.22	6.39	1.36	0.01	0.28	0.00	0.00	99.79	0.80	1.23
Helicon	IHELm	79.90	12.65	0.08	0.66	0.06	0.03	0.16	4.77	1.47	0.01	0.21	0.00	0.00	100.00	0.89	1.30
Uis	IUIS3	70.72	17.36	0.07	0.55	0.04	0.11	2.21	3.15	2.82	0.04	2.25	0.00	0.00	99.31	3.04	1.42
Uis	IUIS10	77.90	16.11	0.08	0.61	0.02	0.13	0.74	0.15	3.08	0.02	0.58	0.00	0.00	99.41	3.51	3.27
Uis	IUIS3	68.05	17.30	0.03	0.20	0.03	0.05	0.83	2.46	8.78	0.02	1.70	0.00	0.00	99.44	1.31	1.15
Uis	IUIS6	70.50	17.06	0.03	0.27	0.02	0.05	1.59	6.68	1.29	0.02	2.09	0.00	0.00	99.60	1.62	1.12
Karlowa	IKAR7	91.09	5.29	0.03	0.25	0.01	0.03	0.42	2.21	0.45	0.01	0.11	0.00	0.00	99.91	0.57	1.08
Karlowa	IKAR17	71.37	17.69	0.02	0.12	0.02	0.05	0.16	9.76	0.49	0.01	0.14	0.00	0.00	99.81	0.37	1.05
Karlowa	IIKAR3	74.21	17.36	0.05	0.39	0.02	0.17	0.51	3.39	3.27	0.02	0.42	0.00	0.00	99.81	2.01	1.73
Karlowa	IIKAR7	63.56	20.21	0.03	0.22	0.05	0.25	3.06	6.87	1.87	0.02	3.26	0.00	0.00	99.40	2.33	1.07
Omapyu	OMA1	76.00	13.89	0.14	1.15	0.05	0.10	0.55	5.52	1.36	0.07	0.56	0.00	0.00	99.40	0.52	1.20
Omapyu	OMA2	74.02	14.33	0.30	2.41	0.05	0.13	0.29	2.47	4.02	0.12	0.40	0.01	0.00	98.55	0.51	1.60
Usakos	USK3	76.06	16.23	0.20	1.60	0.23	0.28	0.19	0.33	4.37	0.06	0.13	0.01	0.00	99.70	2.13	2.89
Usakos	USK 5	77.78	14.34	0.07	0.60	0.05	0.13	0.43	3.08	3.04	0.04	0.29	0.00	0.00	99.85	1.10	1.57
Valencia	VALG02	73.55	14.99	0.03	0.28	0.01	0.07	0.41	3.24	7.43	0.04	0.13	0.00	0.00	100.20	0.34	1.06
Valencia	VALG04	67.01	16.05	0.12	1.00	0.08	0.47	3.94	3.74	6.66	0.06	0.45	0.01	0.00	99.59	3.22	0.78
Valencia	VALG06	70.53	15.79	0.03	0.22	0.01	0.05	0.64	2.42	10.33	0.02	0.12	0.01	0.00	100.15	0.47	0.97
Valencia	VALG22	74.63	14.17	0.19	1.51	0.35	0.13	0.61	3.61	4.79	0.03	0.12	0.00	0.00	100.13	0.47	1.16
	Ave.	73.98	15.42	0.08	0.68	0.07	0.12	0.87	4.32	3.43	0.03	0.69	0.00	0.00	99.69	1.33	1.39
	σ	5.70	2.97	0.07	0.59	0.08	0.11	1.04	2.70	2.88	0.03	0.89	0.00	0.00	0.39	1.03	0.62

Table 6.2: Whole-rock trace element concentrations (in ppm) of LCT and NYF pegmatites. Concentrations below detection limit are denoted by “nd.”

Locality	Rubicon	Rubicon	Helicon	Helicon	Uis	Uis	Uis	Uis	Karlowa	Karlowa
Sample No.	2eRUB	2RUBp	IHELg	IHEL m	IUIS3	IUIS10	IUIS3	IUIS6	IKAR7	IKAR17
Li	267.50	1178.00	475.10	1001.00	1250.00	2159.00	1204.00	478.40	105.60	33.16
Sc	nd	nd	nd	nd	nd	nd	nd	nd	nd	nd
Ti	10.34	39.97	20.28	17.87	200.90	95.72	35.90	41.84	13.12	9.49
V	3.72	0.86	0.19	0.20	4.87	3.41	1.30	1.53	0.38	0.70
Cr	0.66	1.38	1.07	2.79	1.65	1.54	2.52	1.21	1.73	0.76
Co	0.27	0.11	0.03	0.15	nd	nd	nd	nd	0.33	0.15
Ni	0.83	0.55	0.95	1.04	nd	0.44	nd	nd	0.86	0.44
Cu	2.71	4.45	6.22	7.95	6.74	7.46	3.80	3.14	3.08	3.53
Zn	57.07	214.40	109.00	244.00	122.00	122.60	106.90	45.39	21.25	13.70
Ga	32.31	42.37	34.19	32.16	47.61	47.42	25.36	60.45	11.37	28.67
Rb	216.20	1545.00	791.30	1327.00	1003.00	1200.00	3598.00	821.80	214.20	125.90
Sr	2.20	4.10	1.90	1.50	1347.00	34.71	155.70	1587.00	7.19	8.42
Y	0.42	0.10	0.22	0.33	1.84	2.18	0.41	2.10	0.11	0.17
Zr	13.72	1.52	0.92	2.00	9.21	14.54	5.63	94.19	1.96	14.98
Nb	154.70	36.36	28.87	24.82	46.60	31.88	32.23	39.63	64.12	201.60
Sn	1.85	25.22	17.57	30.65	119.40	137.00	27.09	51.18	10.69	9.74
Cs	51.93	106.20	17.55	49.91	16.06	17.22	62.54	25.69	48.79	18.16
Ba	0.60	2.45	2.28	1.25	112.40	65.71	56.17	102.20	10.34	17.30
La	0.49	0.10	0.18	0.06	0.40	0.47	0.12	0.41	0.09	0.05
Ce	1.56	0.22	0.19	0.10	0.75	0.93	0.19	0.61	0.19	0.07
Pr	0.23	0.03	0.04	0.02	0.09	0.10	0.02	0.09	0.02	0.01
Nd	0.81	0.12	0.18	0.07	0.26	0.30	0.09	0.39	0.09	0.03

Table 6.2: continued

Sm	0.99	0.12	0.05	0.04	0.19	0.21	0.02	0.10	0.02	0.01
Eu	0.00	0.00	0.01	0.00	nd	nd	nd	0.02	0.00	0.01
Gd	0.85	0.12	0.06	0.08	0.24	0.27	0.04	0.16	0.02	0.02
Tb	0.11	0.01	0.01	0.02	0.07	0.09	0.01	0.03	0.00	0.01
Dy	0.18	0.02	0.04	0.08	0.37	0.41	0.06	0.22	0.02	0.02
Ho	0.01	0.00	0.01	0.01	0.05	0.05	0.01	0.04	0.00	0.01
Er	0.01	0.00	0.01	0.01	0.10	0.12	0.03	0.12	0.01	0.02
Tm	0.00	nd	0.00	0.00	0.02	0.02	0.01	0.02	0.00	0.01
Yb	0.02	0.01	0.01	0.01	0.11	0.14	0.04	0.17	0.01	0.04
Lu	0.00	0.00	0.00	0.00	0.01	0.02	0.01	0.02	0.00	0.01
Hf	2.48	0.24	0.12	0.23	0.47	0.58	0.49	8.64	0.27	2.26
Ta	51.51	7.49	4.28	7.11	15.73	6.78	34.34	42.54	52.80	337.60
W	3.48	3.96	2.23	1.93	4.96	4.21	1.91	3.88	0.47	1.13
Pb	5.22	8.28	2.59	1.13	10.73	3.96	32.22	7.34	2.25	8.86
Th	5.28	0.73	0.17	0.19	0.16	0.20	0.17	1.10	0.65	1.40
U	2.46	2.05	0.39	0.50	3.39	2.83	11.61	11.22	0.94	1.14
Rb/Sr	98.32	377.29	416.25	887.03	0.74	34.57	23.11	0.52	29.79	14.95
Rb/Ba	360.33	629.84	347.06	1060.75	8.92	18.26	64.06	8.04	20.72	7.28
Sr/Ba	3.67	1.67	0.83	1.20	11.98	0.53	2.77	15.53	0.70	0.49

Table 6.2: continued

Locality	Karlowa	Karlowa	Usakos	Usakos	Omapyu	Omapyu	Valencia	Valencia	Valencia	Valencia
Sample No.	IIKAR3	IIKAR7	USK3	USK 5	OMA1	OMA2	VALG02	VALG04	VALG06	VALG22
Li	126.30	112.90	173.60	150.50	96.04	100.20	16.68	3.86	13.49	8.86
Sc	nd	nd	6.98	6.24	2.51	5.75	nd	2.42	nd	8.01
Ti	79.89	92.31	296.90	202.90	283.10	605.80	192.70	236.00	33.30	104.60
V	2.23	0.85	1.73	0.44	0.46	0.77	2.18	9.98	0.33	3.72
Cr	2.02	0.83	1.40	1.16	1.12	1.88	1.00	2.86	0.94	1.06
Co	0.11	nd	0.57	nd	nd	0.25	0.10	nd	nd	0.21
Ni	0.72	nd	1.07	0.13	0.16	1.30	0.17	nd	nd	0.05
Cu	4.65	2.44	8.44	3.66	2.19	6.71	4.23	6.29	3.19	3.83
Zn	50.66	35.27	51.85	49.00	76.65	173.40	36.13	26.75	50.65	35.56
Ga	55.47	55.40	50.48	39.95	27.54	36.86	18.96	28.75	35.82	18.38
Rb	1565.00	501.70	585.40	458.00	254.50	573.80	362.80	288.80	385.50	217.70
Sr	50.12	4387.00	13.63	8.62	17.65	17.32	36.50	37.17	75.02	12.25
Y	0.07	0.37	3.18	1.74	5.06	0.10	7.41	11.97	6.95	27.09
Zr	4.15	9.55	12.22	2.49	26.93	6.41	48.05	0.74	9.19	30.87
Nb	100.10	30.91	115.80	60.18	47.83	119.20	7.23	3.93	1.29	19.31
Sn	125.70	47.09	53.93	10.15	8.62	11.20	5.24	1.58	0.27	3.66
Cs	240.10	61.68	14.79	20.53	32.17	32.91	20.59	10.29	6.66	3.17
Ba	9.25	686.70	37.14	6.41	12.96	25.12	118.30	173.10	563.00	39.96
La	0.04	0.39	0.55	0.50	1.29	0.16	4.53	10.20	2.24	4.12
Ce	0.06	0.33	1.23	1.05	2.67	0.22	8.51	20.33	4.27	8.36
Pr	0.01	0.04	0.15	0.12	0.32	0.02	0.95	2.33	0.61	0.92
Nd	0.02	0.18	0.51	0.42	1.04	0.05	3.20	8.71	2.99	2.87

Table 6.2: continued

Locality	Karlowa	Karlowa	Usakos	Usakos	Omapyu	Omapyu	Valencia	Valencia	Valencia	Valencia
Sample No.	IIKAR3	IIKAR7	USK3	USK 5	OMA1	OMA2	VALG02	VALG04	VALG06	VALG22
Sm	0.01	nd	0.22	0.21	0.47	0.01	0.78	2.14	0.87	0.86
Eu	0.00	nd	0.03	0.02	0.01	nd	0.23	0.59	0.31	0.11
Gd	0.01	0.06	0.26	0.26	0.54	0.01	0.77	2.05	1.09	0.92
Tb	0.00	0.01	0.07	0.07	0.16	0.00	0.17	0.35	0.18	0.31
Dy	0.01	0.04	0.55	0.38	1.02	0.02	1.17	2.15	1.23	3.54
Ho	0.00	0.01	0.09	0.05	0.13	0.00	0.24	0.42	0.25	0.99
Er	0.01	0.02	0.28	0.12	0.37	0.01	0.82	1.27	0.70	4.27
Tm	0.00	0.00	0.06	0.02	0.06	0.00	0.16	0.21	0.11	0.92
Yb	0.01	0.02	0.56	0.12	0.47	0.02	1.29	1.43	0.67	8.32
Lu	0.00	0.00	0.08	0.01	0.06	0.00	0.21	0.22	0.09	1.28
Hf	0.61	0.47	0.79	0.19	1.47	0.40	2.14	0.02	0.45	1.60
Ta	277.00	111.00	22.61	7.56	5.97	14.03	1.13	0.77	0.29	2.01
W	3.96	2.32	55.86	29.96	13.51	41.44	4.22	12.83	0.22	4.39
Pb	4.70	11.06	2.76	7.98	4.38	7.16	43.10	16.05	34.15	28.98
Th	0.13	1.34	1.16	0.39	0.95	0.59	5.47	0.07	0.66	7.39
U	0.72	1.73	3.80	1.17	3.72	4.15	2.84	1.03	2.15	3.89
Rb/Sr	31.23	0.11	42.95	53.14	14.42	33.13	9.94	7.77	5.13	17.77
Rb/Ba	169.24	0.73	15.76	71.44	19.64	22.84	3.07	1.67	0.68	5.45
Sr/Ba	5.42	6.39	0.37	1.34	1.36	0.69	0.31	0.21	0.13	0.31

Table 6.3: Whole-rock major element concentrations (in wt %) of country rock samples.

Locality	Sample No.	Rock Type	SiO ₂	Al ₂ O ₃	Fe ₂ O ₃	FeO	MnO	MgO	CaO	Na ₂ O	K ₂ O	TiO ₂	P ₂ O ₅	Cr ₂ O ₃	NiO	TOTAL	LOI
Rubicon	2RUBi	granodiorite	52.31	18.35	0.98	7.98	0.18	4.44	8.91	3.20	1.97	1.14	0.33	0.01	0.00	99.79	0.91
Rubicon	2RUBCR	granodiorite	60.71	16.78	0.76	6.18	0.13	2.62	5.48	3.04	2.73	1.06	0.29	0.00	0.00	99.79	0.65
Helicon	IHELn	banded marble	51.86	14.51	0.69	5.58	0.06	4.97	15.66	1.77	3.92	0.75	0.23	0.02	0.00	100.03	3.90
Helicon	IHEL0	banded marble	34.31	9.67	0.45	3.64	0.10	4.48	42.56	1.01	2.60	0.50	0.16	0.02	0.00	99.48	23.03
Uis	IUIS8	metapelite	62.36	18.98	0.83	6.73	0.11	3.74	0.81	0.74	4.40	0.90	0.21	0.02	0.01	99.84	5.61
Uis	IUIS11	metapelite	62.39	19.33	0.75	6.09	0.06	3.30	1.43	0.78	4.74	0.93	0.16	0.03	0.01	99.99	5.40
Uis	IUIS10	metapelite	63.69	18.50	0.70	5.70	0.08	3.30	1.19	1.34	4.36	0.86	0.15	0.01	0.01	99.89	3.43
Uis	IUIS11	metapelite	62.49	18.58	0.79	6.37	0.09	3.58	0.82	0.88	5.29	0.87	0.19	0.02	0.01	99.98	3.22
Karlowa	IKAR15	metapelite	79.31	10.60	0.39	3.12	0.05	1.56	0.29	0.05	2.79	0.69	0.19	0.01	0.00	99.06	2.21
Karlowa	IKAR16	metapelite	78.00	10.43	0.35	2.84	0.05	1.24	0.93	2.57	2.77	0.60	0.15	0.01	0.00	99.95	0.81
Karlowa	IICAR12	metapelite	75.62	11.70	0.44	3.53	0.05	1.71	1.15	2.60	2.20	0.64	0.15	0.01	0.00	99.80	1.48
Karlowa	IICAR 13	metapelite	77.64	10.88	0.34	2.75	0.04	1.40	0.78	3.80	1.51	0.64	0.17	0.00	0.00	99.94	0.58
Usakos	USK16	metapelite	61.19	17.98	0.74	5.97	0.16	3.90	2.33	3.12	3.67	0.80	0.13	0.02	0.01	100.01	1.77
Usakos	USK 22	metapelite	61.29	17.78	0.73	5.87	0.15	3.80	1.55	3.82	3.62	0.80	0.14	0.02	0.01	99.59	1.61
Omapyu	OMA5	marble	1.23	0.49	0.08	0.64	0.07	4.40	92.31	nd	0.23	0.06	0.72	0.03	0.00	100.24	42.81
Omapyu	OMA13	marble	4.10	1.27	0.06	0.52	0.03	1.80	90.73	0.20	0.25	0.10	0.23	0.04	0.00	99.31	41.73
Valencia	VA26-139	metapelite	74.56	9.00	1.20	9.73	0.08	1.12	1.38	1.01	1.29	0.41	0.16	0.00	0.00	99.94	1.16
Valencia	VA26-141	metapelite	60.07	19.44	0.89	7.19	0.10	4.56	0.77	1.58	4.07	0.88	0.21	0.03	0.01	99.80	2.02

Table 6.4: Whole-rock trace element concentrations (in wt %) of country rock samples. Concentrations below detection limit are denoted by “nd.”

Locality	Rubicon	Rubicon	Helicon	Helicon	Uis	Uis	Uis	Uis	Karlowa
Sample No.	2RUBi	2RUBCR	IHELn	IHEL0	IUIS8	IUIS11	IUIS10	IUIS11	IKAR15
Rock Type	granodiorite	granodiorite	marble	marble	metapelite	metapelite	metapelite	metapelite	metapelite
Li	43.07	24.37	37.19	132.70	919.80	661	343	295	2105
Sc	20.43	13.57	12.01	6.33	16.20	16.2	15.8	15.9	5.99
Ti	6239.00	6023.00	4185.00	2055.00	4854.00	4888	4754	4689	3805
V	233.70	143.00	109.50	51.10	146.70	142	142	146	66.3
Cr	30.72	11.43	59.23	38.25	99.66	97.9	95.6	93.9	43.2
Co	22.84	15.85	6.49	nd	16.26	12.9	11.1	13.9	5.23
Ni	5.77	nd	6.57	nd	42.22	39.8	41.7	42.4	13.8
Cu	104.70	29.93	20.35	4.79	41.68	22.3	10.6	47.6	8.13
Zn	127.90	118.80	128.50	102.50	154.60	144	131	135	60.3
Ga	40.86	40.16	35.95	22.04	40.44	43.0	42.0	43.3	27.8
Rb	65.90	93.54	145.90	82.47	204.50	237	197	283	1806
Sr	639.30	424.80	144.10	217.40	66.56	75.6	101	61.5	15.3
Y	21.28	26.70	32.04	17.87	29.43	24.2	25.8	26.7	24.7
Zr	43.13	21.13	110.40	57.02	145.90	161	144	142	144
Nb	12.53	15.04	13.10	6.31	13.36	14.4	13.8	13.5	9.99
Sn	1.77	1.79	5.54	2.46	5.19	13.2	5.12	15.3	46.4
Cs	2.34	3.16	12.03	14.46	33.32	32.6	93.7	107	1478
Ba	616.10	660.80	505.40	359.30	490.60	578	542	604	450
La	41.15	42.74	36.46	17.89	40.05	38.9	37.1	32.3	33.3
Ce	80.51	83.65	76.79	38.14	81.40	79.7	75.6	66.8	69.7
Pr	9.24	9.84	9.08	4.43	9.78	9.49	8.96	8.05	8.26

Table 6.4: continued

Locality	Rubicon	Rubicon	Helicon	Helicon	Uis	Uis	Uis	Uis	Karlowa
Sample No.	2RUBi	2RUBCR	IHELn	IHELo	IUIS8	IUIS11	IUIS10	IUIS11	IKAR15
Rock Type	granodiorite	granodiorite	marble	marble	metapelite	metapelite	metapelite	metapelite	metapelite
Nd	35.43	38.31	35.00	17.28	38.21	36.3	34.5	31.7	33.0
Sm	6.47	7.04	7.04	3.54	7.75	6.93	6.74	6.62	6.48
Eu	1.58	1.49	1.09	0.62	1.30	1.27	1.20	1.06	0.87
Gd	5.31	5.97	6.32	3.36	7.01	5.77	5.85	5.90	5.56
Tb	0.73	0.84	0.97	0.52	1.00	0.84	0.85	0.87	0.80
Dy	4.25	5.16	6.04	3.26	5.92	4.92	5.16	5.29	4.90
Ho	0.81	0.97	1.17	0.64	1.10	0.92	0.98	0.99	0.94
Er	2.27	2.80	3.34	1.85	3.16	2.67	2.85	2.85	2.65
Tm	0.33	0.40	0.48	0.27	0.45	0.39	0.41	0.42	0.40
Yb	1.96	2.57	3.12	1.72	3.00	2.67	2.88	2.82	2.56
Lu	0.30	0.38	0.44	0.25	0.44	0.40	0.42	0.42	0.38
Hf	1.34	0.99	3.25	1.62	4.10	4.83	4.08	4.02	4.76
Ta	0.56	0.90	0.99	0.43	0.97	1.04	1.01	1.00	1.92
W	0.62	0.48	2.43	13.45	3.76	12.7	4.64	10.9	2.60
Pb	12.64	19.39	18.90	9.75	16.75	20.3	17.9	11.8	4.35
Th	6.15	10.93	13.81	6.45	13.19	13.7	13.9	12.6	10.5
U	1.03	2.97	3.58	1.67	3.83	4.57	2.89	3.08	1.99

Table 6.4: continued

Locality	Karlowa	Karlowa	Karlowa	Usakos	Usakos	Omapyu	Omapyu	Valencia	Valencia
Sample No.	IKAR16	IIKAR12	IIKAR 13	USK16	USK 22	OMA5	OMA13	VA26-139	VA26-141
Rock Type	metapelite	metapelite	metapelite	metapelite	metapelite	marble	marble	metapelite	metapelite
Li	457	282	430	677	801	3.99	6.42	65.31	102.20
Sc	5.28	7.76	5.87	15.5	14.5	nd	0.44	5.28	19.80
Ti	3434	3622	3626	4719	4636	28.2	172	2270.00	4840.00
V	65.3	78.1	62.1	115	106	2.78	6.29	48.18	174.50
Cr	41.5	50.8	41.8	81.8	77.0	2.76	4.23	27.90	112.10
Co	5.99	8.78	7.68	16.8	17.3	nd	nd	11.25	23.25
Ni	13.6	18.5	14.0	38.8	36.5	nd	nd	15.90	54.02
Cu	20.4	34.1	10.3	11.6	6.53	3.78	4.50	148.30	44.69
Cs	38.8	413	704	47.7	65.3	1.62	0.53	10.88	9.00
Ba	638	280	249	464	444	21.4	28.6	231.10	659.10
La	29.4	27.2	27.5	46.0	39.6	0.85	3.06	25.58	34.59
Ce	62.0	57.4	58.2	93.5	80.8	1.85	5.63	51.26	70.22
Pr	7.29	6.73	6.84	10.8	9.30	0.24	0.78	5.76	8.72
Nd	29.1	27.0	27.5	40.8	35.1	1.09	3.27	21.30	34.71
Sm	5.78	5.49	5.55	7.76	6.73	0.24	0.66	4.04	7.16
Eu	0.93	1.07	1.03	1.43	1.32	0.06	0.13	0.70	1.25
Gd	4.79	4.61	5.09	6.64	5.72	0.24	0.62	3.65	6.08
Tb	0.64	0.64	0.74	0.96	0.90	0.04	0.08	0.56	0.87
Dy	3.78	3.75	4.61	5.56	4.70	0.23	0.51	3.48	5.00
Ho	0.69	0.67	0.89	1.06	0.91	0.05	0.10	0.68	0.89
Er	1.90	1.86	2.52	3.01	2.55	0.14	0.27	1.98	2.38

Table 6.4: continued

Locality	Karlowa	Karlowa	Karlowa	Usakos	Usakos	Omapyu	Omapyu	Valencia	Valencia
Sample No.	IKAR16	IIKAR12	IIKAR 13	USK16	USK 22	OMA5	OMA13	VA26-139	VA26-141
Rock Type	metapelite	metapelite	metapelite	metapelite	metapelite	marble	marble	metapelite	metapelite
Tm	0.29	0.27	0.36	0.43	0.43	0.02	0.04	0.28	0.33
Yb	1.85	1.76	2.42	2.85	2.42	0.11	0.23	1.89	2.09
Lu	0.28	0.26	0.35	0.42	0.43	0.02	0.04	0.28	0.30
Hf	3.64	3.02	3.80	4.68	4.56	0.04	0.14	2.01	1.82
Ta	0.70	0.86	0.70	0.88	1.10	nd	nd	0.77	0.78
W	2.09	1.70	1.89	2.15	6.06	0.07	0.11	1.00	0.41
Pb	29.6	33.1	18.4	38.9	19.0	3.99	3.23	4.39	18.31
Th	9.90	8.77	8.02	15.5	13.9	0.20	0.53	12.21	12.47
U	2.35	2.03	1.87	3.26	2.79	0.97	1.15	1.40	2.97

Table 6.5: Ti-in-quartz data for quartz samples from mineralised Namibian pegmatites. Cells highlighted in red show unreliable analyses. Temperatures that could not be calculated are denoted by “nd.”

Locality	Sample & Analysis No.	Ti (ppm)	T (°C)
Rubicon	IlgRUB-A	2.07	433
	IlgRUB-B	3.39	463
	IlgRUB-C	0.93	390
	IIRUB1-1-A	19.77	592
	IIRUB1-1-B	75.94	727
	IIRUB1-1-C	102.90	763
Helicon	1HEL1-1-A	1.23	405
	1HEL1-1-B	0.00	nd
	1HEL1-1-C	2.13	435
	1HEL4-1-A	0.00	nd
	1HEL4-1-B	0.00	nd
	1HEL4-1-C	0.00	nd
Uis	IUIS2-A	3.99	473
	IUIS2-B	2.91	453
	IUIS2-C	2.07	433
	IUIS4-A	1.29	407
	IUIS4-B	2.02	432
	IUIS4-C	2.10	434
	IUIS2-A	2.14	435
	IUIS2-B	2.38	441
	IUIS2-C	2.85	452
Karlowa	IKAR5-A	0.00	nd
	IKAR5-B	0.00	nd
	IKAR5-C	0.00	nd
	IIKAR1-A	5.77	498
	IIKAR1-B	10.91	544
	IIKAR1-C	11.14	546
Usakos	USK8-A	1.67	421
	USK8-B	2.18	436
	USK8-C	1.29	407
Omapyu	OMA4-A	29.71	629
	OMA4-B	20.98	598
	OMA4-C	19.23	590
	OMA6-A	12.84	557
	OMA6-B	9.75	535
	OMA6-C	11.44	548

Table 6.5: *continued*

Locality	Sample & Analysis No.	Ti (ppm)	T (°C)
Valencia	VALG04-A	50.26	670.89
	VALG04-B	37.06	640.59
	VALG04-C	35.29	635.92
	VALG06-A	41.54	651.70
	VALG06-B	33.46	630.86
	VALG06-C	35.50	636.46

6.2.1.2 Rubicon and Helicon country rocks

The Rubicon pegmatite has been emplaced into granodiorites of the Goas Suite. These rocks have relatively low silica values in comparison to the pegmatite samples, with concentrations up to 60.71 wt % SiO₂, and their alumina contents are quite high, up to 18.35 wt % Al₂O₃. Total Fe contents of the rocks are relatively high (up to 8.86 wt %), and CaO values are similar (up 8.91 wt %). Na₂O concentrations are typically in the region of ~ 3.00 wt % and MgO values are similar, although more variable, ranging from 2.62 - 4.44 wt %. TiO₂ values are low, reaching a maximum of 1.15 wt %, and all other major element concentrations are less than 1.00 wt % of the given element (refer to Table 6.3).

V, Cu, Zn, Sr and Ba are the most abundant trace element constituents of the granodiorites, each attaining up to a few 100 ppm (refer to Table 6.4). While Rb concentrations reach up to 93.54 ppm, most other trace elements, including Li, Sc, Zr and Ga, are below 50 ppm.

The Helicon pegmatite has intruded into Karibib marbles which contain some pelitic material. They are relatively rich in silica (up to 51.86 wt % SiO₂) and aluminium (up to 14.51 wt % Al₂O₃), and their CaO concentrations reach up to 42.56 wt %. They contain appreciable amounts of total Fe (3.64 - 5.58 wt %), MgO (4.48 - 4.97 wt %) and K₂O (2.60 - 3.92 wt %), while other elements typically constitute less than 1.50 wt % of the rock.

In terms of trace element concentrations, Ba reaches abundances of up to 505.40 ppm, while many other trace elements, including Zn, Rb, Sr and Zr typically range from 100 - 220 ppm each. Cu, Ga, Y, and Cr typically do not exceed ~ 50 ppm each, and most other elements occur in concentrations less than 20 ppm (refer to Table 6.4).

6.3.2 Sn-bearing pegmatites

6.3.2.1 Uis pegmatites

SiO₂ concentrations in the Uis pegmatites are high, with values up to 77.90 wt %. Al₂O₃, the second most abundant constituent of the samples, typically ranges from 16.11 - 17.36 wt %, and Na₂O, although variable, also reaches appreciable abundances (up to 6.68 wt %). K₂O generally ranges from 1.20 - 3.00 wt %, although an individual sample from an Uis pegmatite (IIUIS3) contains as much as 8.78 wt % K₂O. CaO and P₂O₅ concentrations are similar to each other, with both reaching values of up to 2.25 wt %. The A.S.I. values of the Uis pegmatites range from 1.12 - 3.27.

With respect to their trace element compositions, the Uis pegmatites contain as much as 2159 ppm Li, 3598 ppm Rb, and 1587 ppm Sr. Zn, Sn and Ba concentrations typically reach up to ~ 120 ppm, while Ga, Nb and Cs generally do not exceed 65 ppm. All other trace elements are present in negligible amounts (refer to Table 6.2). Rb/Sr ratios in the Uis pegmatites variable, ranging from 0.74 - 34.57, while Rb/Ba ratios range from 8.04 - 64.06. Sr/Ba ratios are also variable (0.53 - 15.53).

Ti concentrations in quartz range from 1.29 - 3.99 ppm, producing crystallisation temperatures of 433 - 473 °C for the Uis pegmatites (Table 6.5).

6.3.2.2 Uis country rocks

The Uis pegmatites have intruded into porphyroblastic pelitic metasedimentary rocks of the Amis River Formation. These metapelites contain ~ 62 wt % SiO₂, and appreciable amounts of Al₂O₃, with concentrations ranging from 18.50 - 19.33 wt % Al₂O₃. Total Fe concentrations reach as much as 7.48 wt % in the metapelites, which

also contain ~ 3 wt % MgO and ~ 5 wt % K₂O. TiO₂ concentrations do not exceed ~ 1 wt %.

The metapelites contain up to 920 ppm Li and 604 ppm Ba. V, Cr, Zn and Zr concentrations typically range from ~ 100 - ~ 150 ppm, and Rb concentrations are slightly higher, attaining values of up to ~ 300 ppm. The concentrations of the remaining trace elements in the element suite analysed usually do not exceed 50 ppm (refer to Table 6.2).

6.3.3 Li-Sn-bearing pegmatites

6.3.3.1 Karlowa pegmatites

The Karlowa pegmatites contain variable silica, with concentrations ranging from 63.56 wt % SiO₂ to as high as 91.09 wt % SiO₂. Their Al₂O₃ abundances are equally variable, with values occurring between 5.29 wt % Al₂O₃ and 20.21 wt % Al₂O₃. Na₂O abundances are up to 9.76 wt % Na₂O, while CaO and K₂O typically do not exceed 3.3 wt %. P₂O₅ concentrations are not generally higher than 0.5 wt %, however one sample, IKAR7, produced a value of 3.26 wt % P₂O₅. All other major element constituents are present in negligible amounts (refer to Table 6.1), and the A.S.I. values of the pegmatites range from 1.05 - 1.73.

Trace element concentrations in the Karlowa pegmatites are extremely variable. Rb (up to 1565 ppm) and Sr (up to 4387 ppm) are the most abundant trace elements in the Karlowa pegmatites. Elements such as Li, Nb and Sn values typically range between 100 ppm and 200 ppm, while Ba concentrations are up to 600 ppm and Ta concentrations reach ~ 330 ppm. All other trace elements are present in minor amounts (refer to Table 6.3). Although the Rb/Sr ratios of the Karlowa pegmatites show some variation, they typically range from ~ 15 - ~ 31, while Rb/Ba ratios show more scatter, ranging from 0.73 - 169.24. Sr/Ba values are also variable, ranging from 0.49 - 6.39.

Ti concentrations in quartz from the Karlowa pegmatites are somewhat variable, ranging from 0.00 - 11.14. Calculated crystallisation temperatures range from 498 - 546 °C (Table 6.5).

6.3.3.2 Karlowa country rocks

Like the Uis pegmatites, the Karlowa pegmatites have been emplaced in the metapelitic rocks of the Amis River Formation, although in the Karlowa area, they are not porphyroblastic. The metasediments are silica rich, containing up to 79.31 wt % SiO₂, and their Al₂O₃ concentrations range from 10.43 - 11.70 wt %. They contain appreciable amounts of total Fe (3.15 - 3.93 wt %) and K₂O (1.51 - 2.79 wt %), while MgO concentrations are slightly lower, ranging from 1.24 - 1.71 wt %. TiO₂ values are well constrained and fall between 0.60 wt % and 0.70 wt %, and all other elements are present only in negligible amounts.

Like the pegmatite samples, trace element concentrations in the metapelitic country rock suite are quite variable. Li, Rb and Cs concentrations are high in one country rock sample (2105 ppm Li, 1806 ppm Rb, and 1478 ppm Cs in IKAR15; refer to Table 6.4), although Li values typically range from 282 - 487 ppm, Rb values from ~ 100 ppm - 620 ppm, and Cs values from as low as 38 ppm to 704 ppm. Ba concentrations range from 250 - 648 ppm, Zn from 60 - 90 ppm, and Zr from 100 - 150 ppm, while the concentrations of other trace element generally do not exceed 50 ppm (refer to Table 6.4).

6.3.4 Gem tourmaline-bearing pegmatites: Usakos and Omapyu pegmatites

6.3.4.1 Usakos and Omapyu pegmatites

SiO₂ concentrations in the gem tourmaline-bearing pegmatites typically range from 74.02 - 77.78 wt %, with Al₂O₃ values reaching up to 16.23 wt %. Na₂O and K₂O are relatively low and variable, with concentrations ranging from 0.33 - 5.52 wt % Na₂O and 1.36 - 4.37 wt % K₂O. P₂O₅ concentrations do not exceed 0.50 wt %, and TiO₂ values are low, typically reaching a maximum of only 0.12 wt %. All other elements

form only minor constituents of the samples (refer to Table 6.1). A.S.I. values for the Usakos and Omapyu pegmatites range from 1.20 - 2.89.

Trace element concentrations in the gem tourmaline-bearing miarolitic pegmatites are generally low, with only Rb exceeding 250 ppm, and Li, Zn and Nb abundances attaining values greater than 100 ppm (refer to Table 6.2). All other elements analysed are present only in trace amounts. Rb/Sr ratios range from 14.42 - 53.14, and Rb/Ba values are similar, although slightly higher, ranging from 15.76 - 71.44. Sr/Ba ratios range from 0.37 - 1.36.

Ti concentrations in quartz wafers from the Usakos and Omapyu pegmatites are variable, ranging from 1.29 - 29.71 ppm, producing crystallisation temperatures in that range from between 407 °C and 629 °C (Table 6.5).

6.3.4.2 Usakos and Omapyu country rocks

The Usakos pegmatite has been emplaced into metapelitic country rocks belonging to the Kuiseb Formation. SiO₂ values are moderate (~ 61 wt %), while Al₂O₃ concentrations reach up to ~ 18 wt %. Total Fe concentrations are in the region of 6.64 wt %, while MgO, Na₂O and K₂O share similar values of ~ 3.50 wt % each. CaO values typically range from 1.55 - 2.33, and TiO₂ concentrations average 0.80 wt %.

The trace element composition of the metapelites is dominated by Li (677 - 801 ppm), and Ba (~ 450 ppm), while V, Zn and Zr generally reach up to 150 ppm each. Cr concentrations reach up to 82 ppm, however the concentrations of the remaining elements rarely exceeds 50 ppm, and most do not exceed 20 ppm (refer to Table 6.4).

The Omapyu pegmatite has intruded into Karibib marbles which are composed of 91 - 92 wt % CaO, with the next most abundant element being MgO, which attains variable concentrations of 1.80 - 4.40 wt %. SiO₂ and Al₂O₃ concentrations are low, ranging from 0.50 - 1.30 wt %, and all other elements generally do not exceed 0.5 wt % abundances.

Sr is the most abundant trace element in the marbles, attaining values of up to ~ 2580 ppm. Ba and Zn range from 20 - 60 ppm, and all other trace elements typically do not exceed concentrations of 10 ppm (refer to Table 6.2).

6.3.5 U-bearing pegmatites: Valencia pegmatites (SLGs)

6.3.5.1 Valencia pegmatites (SLGs)

The Valencia pegmatites (SLGs) are SiO₂- and Al₂O₃-rich, with values reaching up to ~ 75 wt % SiO₂ and ~ 16 wt % Al₂O₃. They contain appreciable amounts of K₂O, with values ranging from ~ 5 - 10 wt %, and Na₂O concentrations average 3.25 wt %. The remaining elements analysed are present only in negligible amounts < 1 wt %, and the A.S.I. values for these pegmatites are variable, ranging from 0.78 - 1.16.

Rb and Ba are the most abundant trace elements in the Valencia pegmatites, with values typically ranging from 100 – 250 ppm Rb and Ba concentrations reaching up to 563 ppm. Zn, Ga, Sr and Zr concentrations do not exceed 50 ppm, and all other trace elements typically do not exceed 20 ppm. U concentrations in the samples analysed are low, not exceeding 4 ppm. Rb/Sr ratios show some variability with values ranging from 5.13 - 17.77, while Rb/Ba values are slightly lower, ranging from 0.68 - 5.45. Sr/Ba ratios are much lower and more consistent, ranging from 0.13-0.31.

Quartz samples from the Valencia pegmatites contain between 34 ppm and 50 ppm Ti, yielding crystallisation temperatures ranging from 640 - 681 °C (Table 6.5).

6.3.5.2 Valencia country rocks

Although the Valencia pegmatites have been emplaced in a variety of different country rocks, only metapelitic samples of the Kuiseb Formation, taken from directly adjacent to two of the pegmatites, were analysed for the purpose of this study.

The metapelites are SiO₂-rich (60 - 75 wt %) and their Al₂O₃ contents are variable, ranging from 9 - 19 wt %. Total Fe concentrations range from 8 - 10 wt %, and MgO contents from 1 - 5 wt %, while all other elements are present in concentrations less than 1 wt %.

Li, V, Cu and Zn concentrations in the metapelites generally range from 50 - 150 ppm, while Rb and Ba attain values as high as 250 ppm and 660 ppm respectively. Most other elements are present in concentrations under 50 ppm, although the Zr content of the metapelites reaches up to 72 ppm.

6.4 Discussion of results

6.4.1 Major element composition of mineralised pegmatites

SiO₂ values are high in all pegmatite samples, ranging from 67.01 - 79.09 wt %, while Al₂O₃ is the next most abundant constituent of the pegmatite samples, ranging from 12.65 - 20.21 wt %. Sample IKAR7 from a Karlowa pegmatite (see Table 6.1) has both the highest SiO₂ and lowest Al₂O₃ values. Figure 6.1 illustrates that overall, the Al₂O₃ contents of the pegmatites decrease as SiO₂ contents increase.

Na₂O and K₂O show more variation across different pegmatites, with values ranging from 0.33 - 10.15 wt % and 0.33 - 10.33 wt % respectively. There does not appear to be any significant relationship between SiO₂ and Na₂O and K₂O (Figure 6.1), however Figure 6.1 does show that the highest K₂O values occur in the U-bearing NYF pegmatites, whereas K₂O values for the rare-metal i.e. Sn- and Li-Sn-bearing, and miarolitic LCT pegmatites are considerably lower. Generally K₂O > Na₂O, however this is not consistent, and in some samples, particularly those from the Li-Be-bearing LCT pegmatites (IIRUB and I HEL samples from the Rubicon and Helicon pegmatites respectively) Na₂O > K₂O. Overall CaO values are typically low, however they are quite variable, ranging from 0.16 - 3.94 wt %.

The Aluminium Saturation Index (A.S.I.; molar Al/CNK) across different pegmatites is relatively consistent and above 1.00, although two NYF pegmatites from the Valencia area (VALG04 and VALG06) have values less than 1.00. All other elements are present in amounts generally less than 1.00 wt %, with the exception of P_2O_5 , where values reach up to 3.26 wt % in Sn- and Li-Sn-bearing LCT pegmatites (Figure. 6.1).

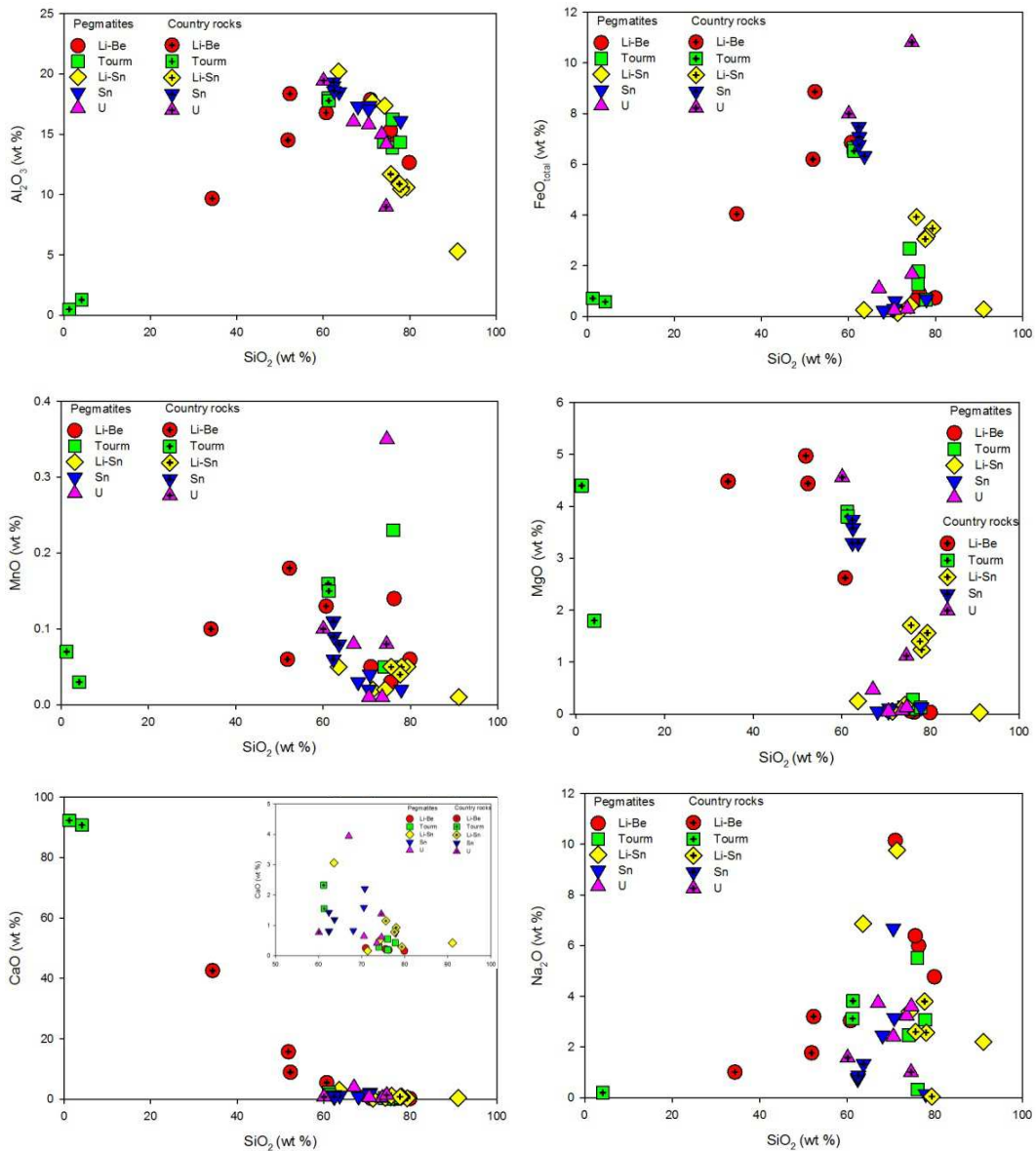


Figure 6.1: Major element plots for mineralised pegmatites and their country rocks.

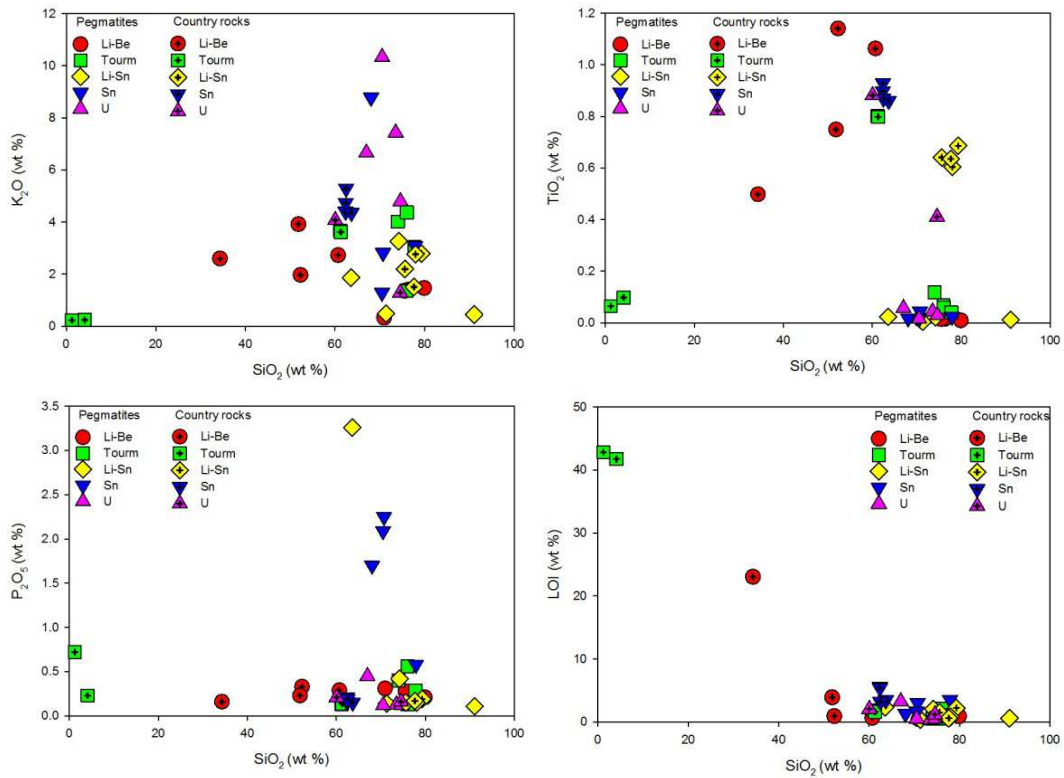


Figure 6.1: continued

6.4.2 Trace element composition of mineralised pegmatites

The concentrations of most trace elements are extremely variable, both in a given type/class of pegmatite, and among samples from a given deposit, with the concentrations of certain elements such as Li, Rb, Sr ranging from a few ppm to a few thousand ppm.

Figure 6.2 shows that there is no apparent relationship between silica content and trace element concentrations, however it is apparent that the LCT pegmatites are relatively enriched in Li, Cs, Ta, Rb, Nb, Zn, Ga, and W (Figures 6.2 and 6.3) in comparison to the uraniferous NYF pegmatites (SLGs). The NYF pegmatites are enriched in Y with respect to the LCT pegmatites, however, contrary to what may be expected of an NYF pegmatite, Nb concentrations in these rocks are lower than in the LCT pegmatites. U concentrations in these rocks are similar to those measured in LCT pegmatites, however they are enriched in Pb and Th in relation to the latter (Figure

6.3). V, Cr, Cu, Ni and Co concentrations are negligible, often below detection limit, in all the pegmatites.

Rb, Sr, and Ba ratios are highly variable, with the highest ratios (e.g. Rb/Sr > 800) occurring in the Li-Be-bearing pegmatites. Rb/Sr, Rb/Ba, and Sr/Ba ratios in the NYF pegmatites are consistently lower than those of LCT pegmatites, however in the values of some individual Li-Sn- and Sn-bearing pegmatites are as low as 0.11 (e.g. IIKAR 7 from a Karlowa pegmatite: Rb/Sr = 0.11).

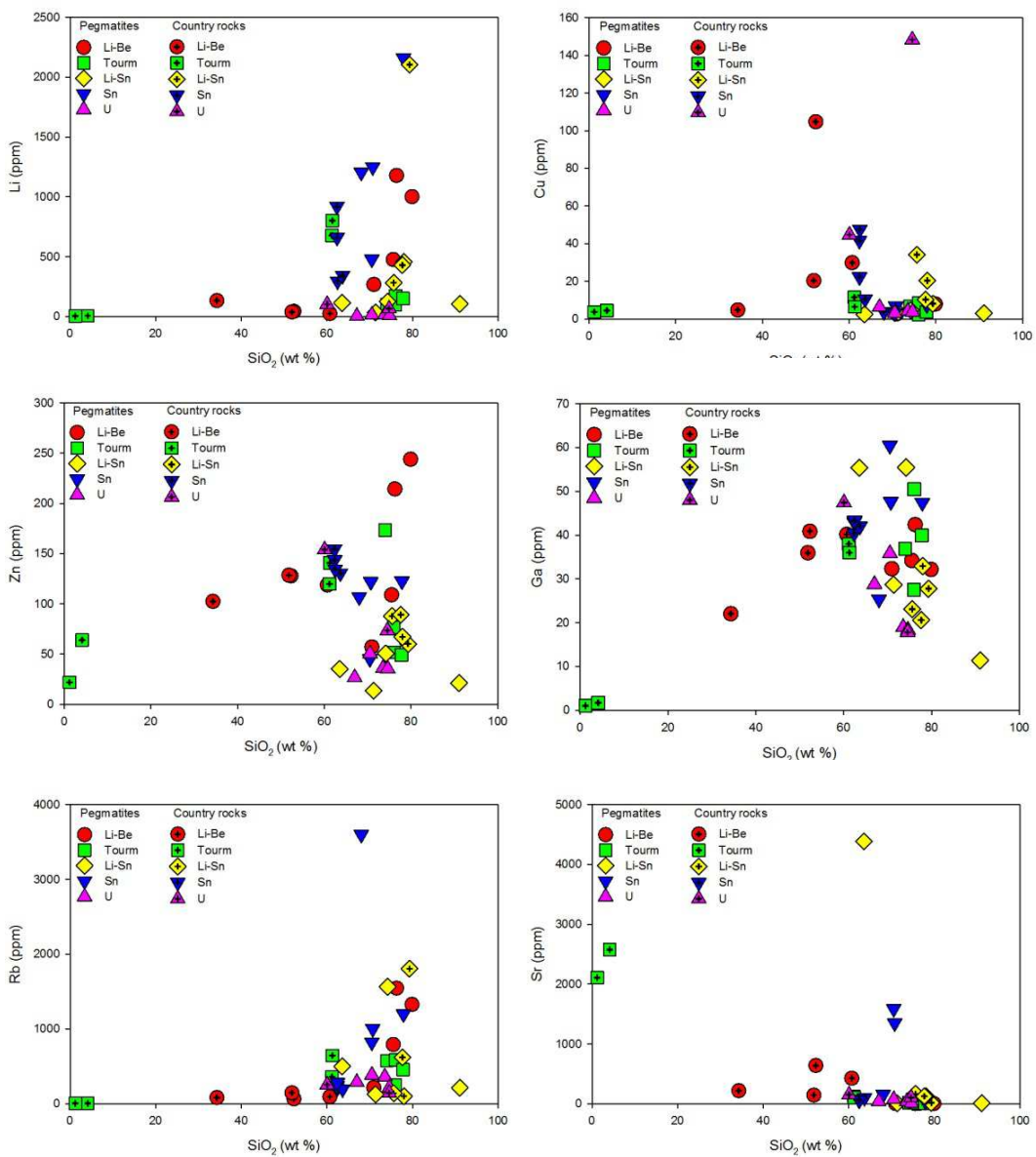


Figure 6.2: Selected trace element plots for mineralised pegmatites and their country rocks.

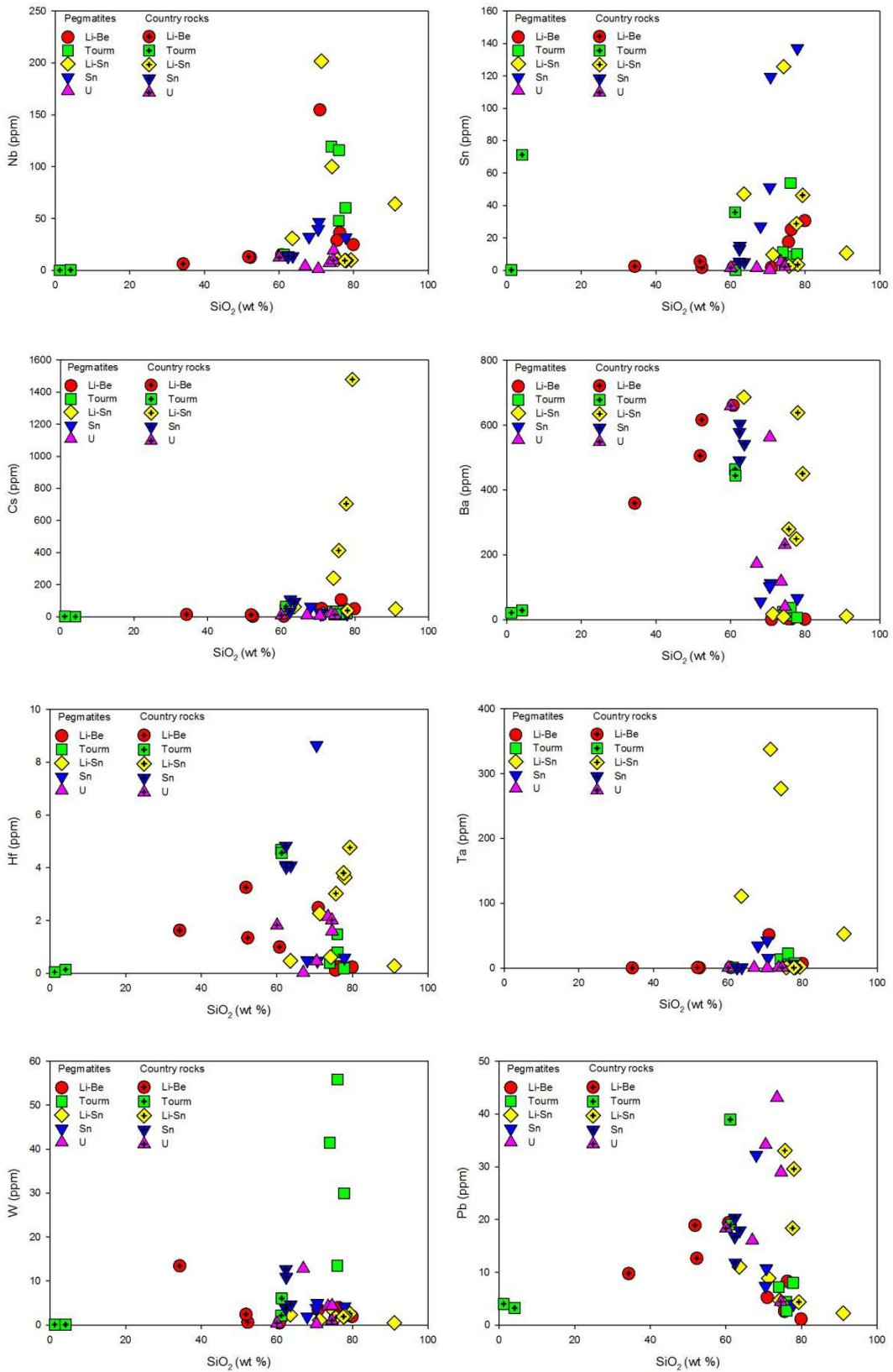


Figure 6.2: continued

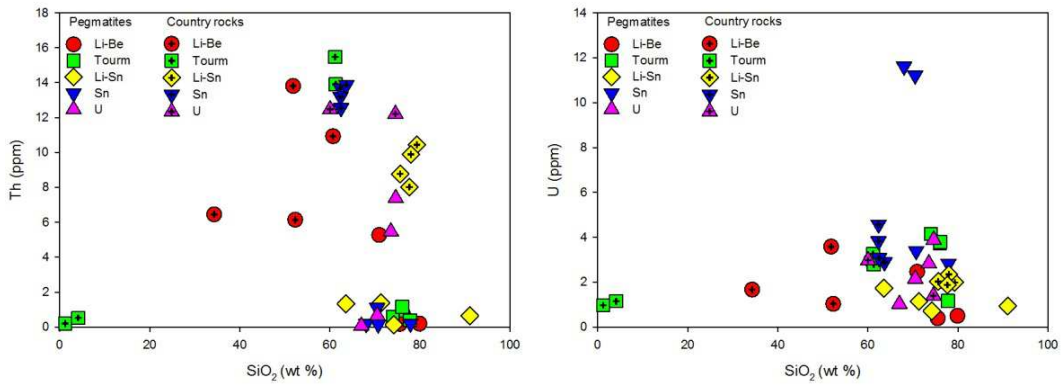


Figure 6.2: continued

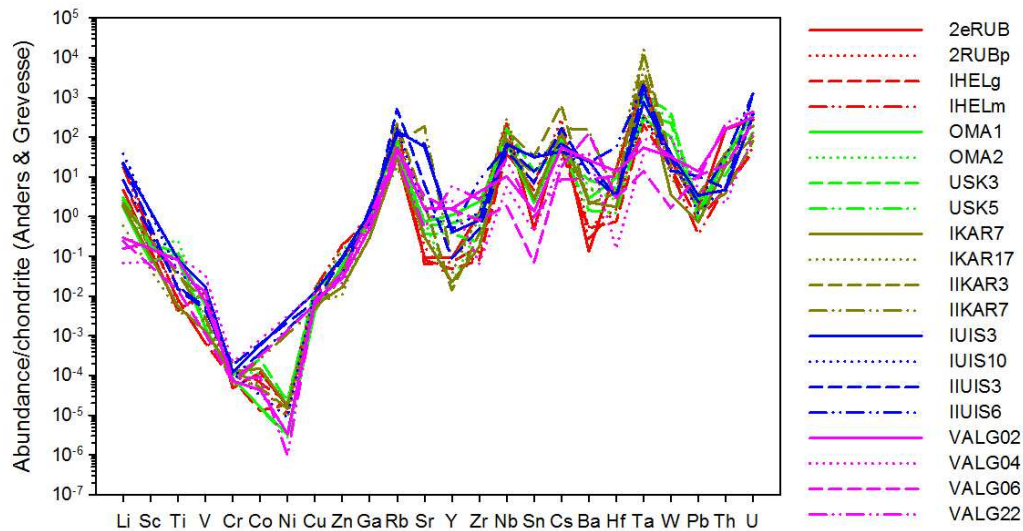


Figure 6.3: Chondrite-normalised trace element concentrations in mineralised pegmatites. Refer to Table 6.1 for sample localities.

It is significant to note that although the metallogeny of the pegmatites studied is different, trace element concentrations are overall very similar between them, regardless of their type or locality.

Chondrite-normalised rare earth element (REE) patterns are illustrated in Figure 6.4. REE concentrations in all types of mineralised pegmatite are highly variable, however it is clear that the REE pattern itself is similar between all the different LCT pegmatites analysed. Most of the LCT pegmatites show strong negative Eu anomalies, the most

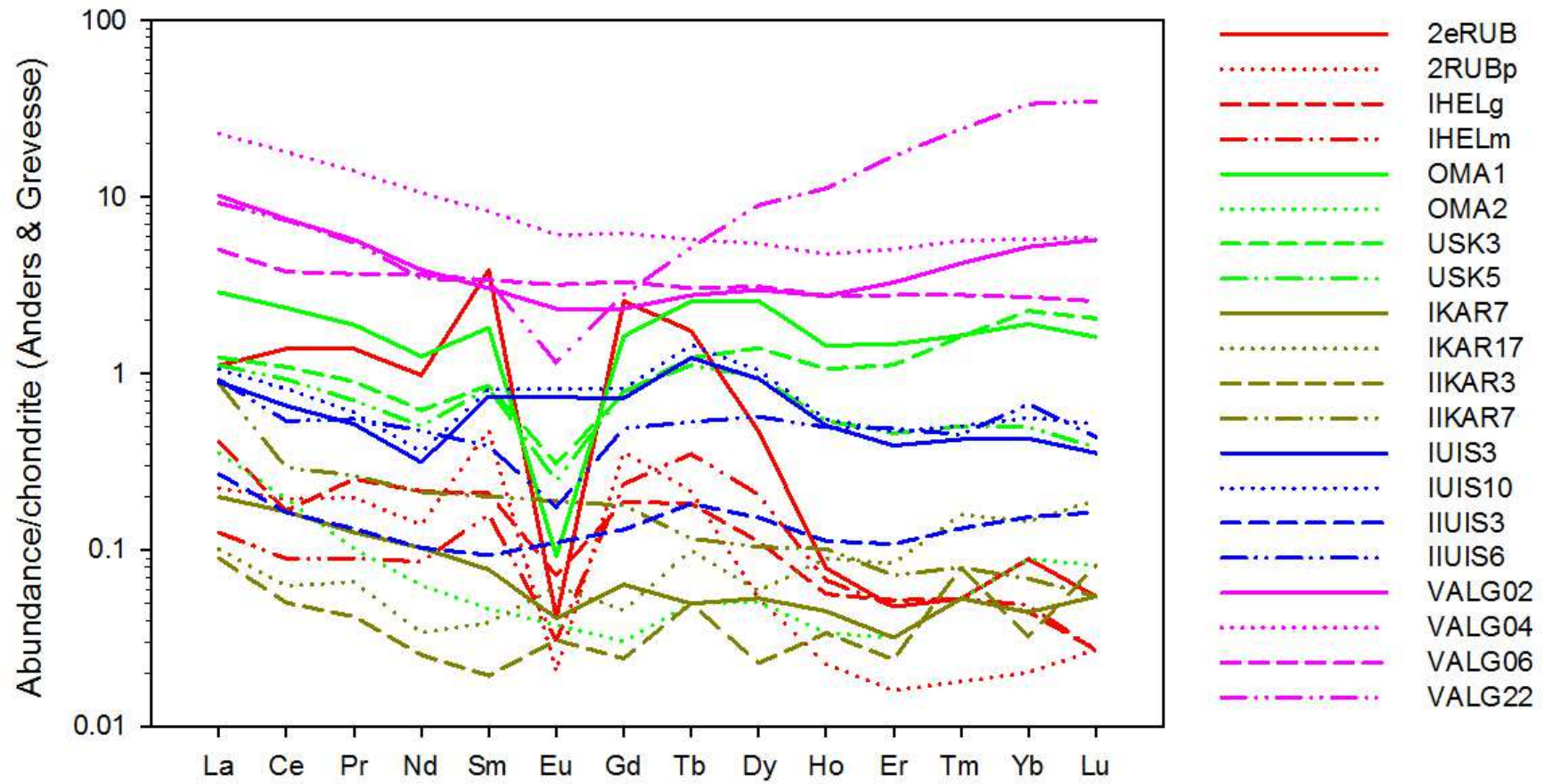


Figure 6.4: Chondrite-normalised REE data from mineralised pegmatite samples. Refer to Table 6.1 for sample localities.

pronounced of which are observed in the Li-Be- and Sn-bearing pegmatites. With the exception of the Li-Be-bearing pegmatites, which show a significant enrichment in LREE compared to HREE, all of the LCT pegmatites show a slight enrichment in HREE in comparison to LREE.

The NYF pegmatites are enriched in REE with respect to the LCT pegmatites, and although their REE patterns show some variation, they are generally flat, with the three Type C (refer to Chapter 4) samples showing a slight enrichment in LREE and a depletion in HREE. VALG22 from the Valencia area is a Type B SLG, and its REE characteristics are quite different from those of the Type C SLGs in that it shows a negative Eu anomaly and an enrichment in HREE relative to LREE.

The Ti values obtained from quartz wafers from all of the pegmatites are variable, ranging from 0.00 ppm in one of the Karlowa pegmatites, and in the Core zone of the Helicon pegmatite, to as high as 102.90 ppm in the Wall zone of the Rubicon pegmatite. The accuracy analyses for trace elements in quartz is highly susceptible to the thickness of the samples, and the presence of micro-inclusions, whether solid or fluid, in the samples (Müller *et al.*, 2003), the effects of which are seen in the dataset generated for this study. The highest Ti values, obtained from a single sample from the Rubicon pegmatite, are the result of the fact that during analysis the laser beam penetrated the entire thickness of the sample, and measured the Ti values of the sample holder, thus these values cannot be used in the calculation of crystallisation temperatures from Ti-in-quartz data.

The lowest crystallisation temperatures were measured in the Li-Be-bearing LCT pegmatites, whose temperatures range from 385 - 457 °C. Similar temperatures were obtained for the gem tourmaline-bearing LCT pegmatites, although some of the calculated temperatures for these temperatures are high (~ 620 °C) because of their elevated Ti-in-quartz concentrations. Similarly, the Sn-bearing LCT pegmatites give temperatures ranging from 402 - 467 °C, however the Li-Sn-bearing LCT pegmatites give slightly higher temperatures, ranging from 491 - 538 °C.

The U-bearing NYF pegmatites (SLGs) of the Valencia area have the highest Ti-in-quartz values, which consistently range from 35 - 50 ppm. These pegmatites, as a result, also have the highest crystallisation temperatures, which range from 631 - 671 °C.

6.4.3 Major element composition of country rocks

Major element data for country rock samples are illustrated in Figure 6.1. The country rocks into which mineralised pegmatites have intruded are diverse in terms of rock type and metamorphic grade, and therefore diverse in composition. The country rock sample suite is dominated by mica schists, however two of the pegmatite bodies, Helicon and Omapyu pegmatites, have intruded into marbles (either pure or interlayered with psammitic material), and one, Rubicon pegmatite, into granodiorite.

The highest SiO₂ values (75.62 - 79.31 wt %) are observed in the mica schists of the Amis River Formation, into which the Li-Sn-bearing pegmatites of the Karlowa swarm intruded. One sample, from the Valencia area (VA26-139), of the Kuiseb Formation is also rich in silica, with SiO₂ = 74.56 wt %. All other metapelitic samples are “knotted” schists and their SiO₂ values are significantly lower than those of samples that do not contain “knots”, with values ranging from 60.07 - 63.69 wt %. A similar trend is observed in the MgO and K₂O concentrations of the different metapelites, with “knotted” schists containing higher amounts of MgO (3.30 - 3.90 wt %) and K₂O (2.36 - 5.29 wt %) than metapelites without the quartz-biotite porphyroblasts (Figure 6.1).

There is an inverse relationship between SiO₂ content and Al₂O₃, with aluminium decreasing with increasing silica. FeO content are variable, ranging from 2.75 - 9.73 wt % and there is no apparent correlation between the iron content and the presence of “knots” in the metapelites.

The metapelites also contain appreciable, yet highly variable amounts of Na₂O, with concentrations ranging from 0.05 - 3.82 wt %. TiO₂ and CaO concentrations are low, yet variable (0.41 - 0.93 wt % and 0.29 - 2.33 wt % respectively), while MnO and P₂O₅

values are low with very little variation (0.04 - 0.16 wt % and 0.13 - 0.21 wt % respectively).

The pure marbles, into which the Omapyu pegmatites intruded, contain the lowest concentrations of SiO₂ (1.23 - 4.10 wt%) and CaO concentrations are in excess of 90 wt % (Figure 6.1). All other elements occur in trace amounts, less than 1.0 wt %, with the exception of MgO which is present in concentrations up to 4.40 wt %. The banded marbles, into which the Helicon pegmatites intruded, has significantly higher SiO₂ contents (34.31 - 51.86 wt%) and lower CaO contents (15.66 - 42.56 wt%). They also contain appreciable amounts of Al₂O₃ (9.67 - 14.51 wt %), FeO (3.64 - 5.58 wt %), and K₂O (2.60 - 3.92 wt %), while all other elements occur in minor amounts (< 1.00 wt %). Both the pure and banded marbles have the highest LOI values, with values reaching in excess of 40.00 wt % (Figure 6.1).

Silica values are intermediate in the granodiorites which host the Rubicon pegmatite, and they contain a significant amount of Al₂O₃, FeO, and CaO. Although MgO, Na₂O, and K₂O are less abundant than aluminium, iron, and calcium, they are still present in appreciable amounts. TiO₂ constitutes only approximately 1.00 wt % of the granodiorites, and P₂O₅, concentrations are negligible.

6.4.4 Trace element composition of country rocks

As is the case with the pegmatite samples, trace element concentrations in the country rock samples are highly variable, particularly with respect to Li, Rb, Sr, and Cs, where values range from a few ppm to a few thousand ppm. The variability of trace element concentrations occurs across all samples, regardless of the rock type, and concentrations do not appear to be consistent in similar rock types. Absolute concentrations of Li, Cu, Y, Zr, Ba, Hf, and Th, in particular, are significantly higher in the country rocks than in the pegmatites which have intruded into them.

Metapelitic country rocks, regardless of whether or not they contain quartz-biotite “knots” show similar trace element patterns regardless of the variability of their

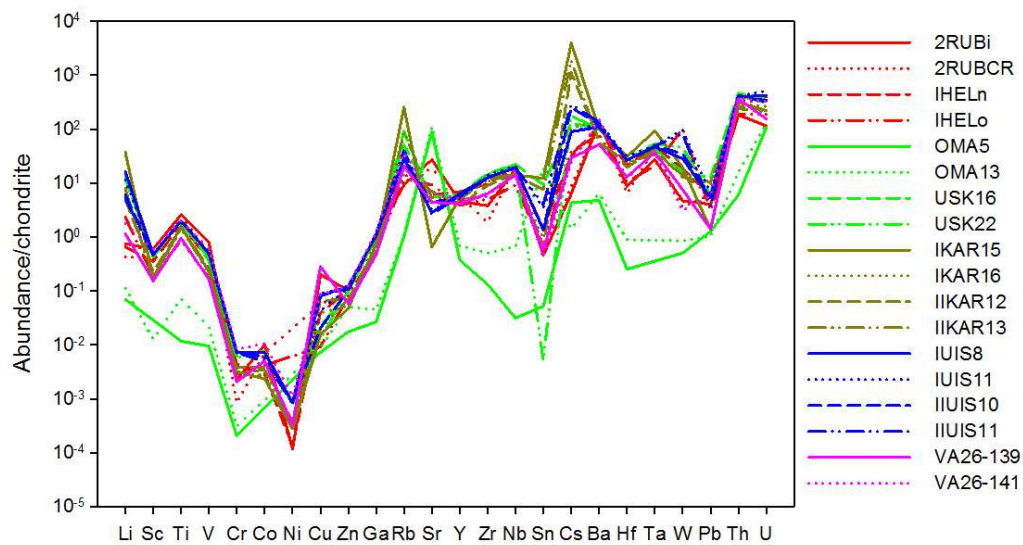


Figure 6.5: Chondrite-normalised trace element concentrations of country rocks into which mineralised pegmatites have intruded. For sample localities refer to Table 6.4.

absolute concentrations (Figure 6.2). They show strong enrichments in Rb, Cs, and Ta, particularly those into which the Li-Sn-bearing pegmatites have intruded. While concentrations are low, the country rocks from the Valencia area show a relative enrichment in Cu with respect to other metapelitic samples. All of the metapelites show a relative depletion in Pb and a slight enrichment in Th (Figure .65).

The granodiorites into which the Rubicon pegmatite has intruded show a similar trace element pattern to the metapelitic country rocks (Figure 6.5). They do, however, show a relative enrichment in Sr and a relative depletion in Zr in comparison to the metapelitic country rocks (Figure 6.5).

The lowest trace element concentrations occur in the pure marbles into which the Omapyu pegmatites have intruded (Figures. 6.2 and 6.5). They do, however, show a relative enrichment in Sr, which is lacking in the metapelitic and granodioritic country rocks, and do not show the strong relative depletion in Pb and enrichment in Th that the other country rock types show. The banded marble units appear to share the trace element characteristics of the metapelitic units rather than showing similarities with the pure marble samples.

All of the country rocks, regardless of rock type, display similar REE trends (Figure 6.6). Even though the pure marble units contain the lowest relative abundance of REE, they share all other characteristics with the metapelites and granodiorites, including a relative enrichment in LREE with respect to HREE, a pronounced Eu anomaly, and a slight enrichment in Gd. Apart from the relative abundance of REE, what distinguishes the marbles further from the other country rocks is the fact that they show a slight depletion in Yb with respect to other REE.

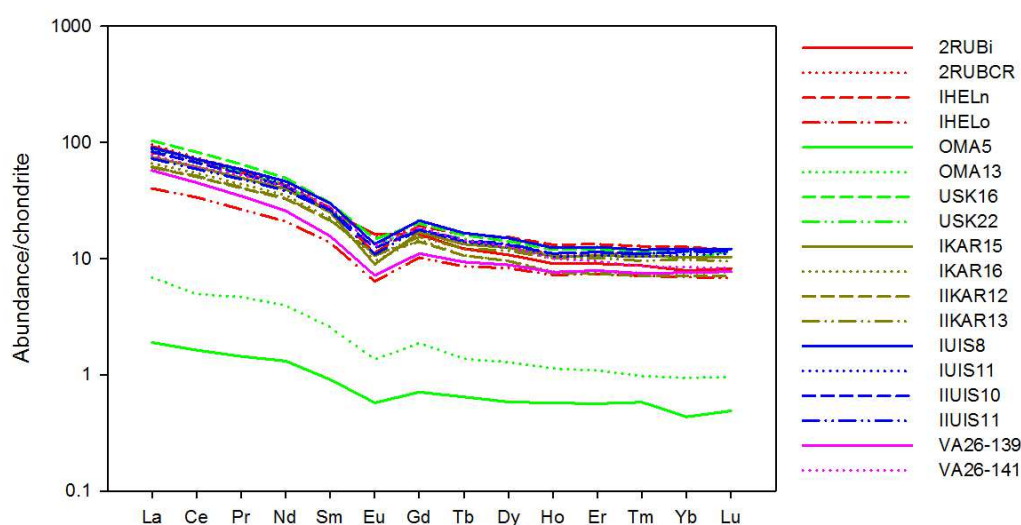


Figure 6.6: Chondrite-normalized REE data for country rock samples. For sample localities refer to Table 6.4.

6.5 Interpretation of results

The geochemical composition of the Li-Be-bearing, miarolitic, Li-Sn-, and Sn-bearing pegmatites is typical of that expected from LCT pegmatites, showing relative enrichments in Li, Rb, Sn, Ta, and Nb ($Ta > Nb$); and highly variable REE patterns at very low concentrations (< 10 times chondrite; Černý and Ercit, 2005). That of the U-bearing pegmatitic SLGs is also characteristic of NYF pegmatites, however the relative enrichments in Sc, Zr, and Nb are not as conspicuous as would be expected (Černý and Ercit, 2005). Nonetheless, the fact that $Nb > Ta$ and $LREE > 10$ times chondrite are indicative of their NYF character (Černý and Ercit, 2005). The variability and inconsistency of trace element data is also a result of the coarse-grained texture of the pegmatite samples, and their mineralogy, for example Li would be enriched in samples that contain coarse-grained spodumene (e.g. samples from Uis) and Sn enrichment

would occur in those samples containing significant cassiterite mineralisation (e.g. samples from Uis and Karlowa).

Major element geochemistry appears to be a direct result of the mineralogy of the samples analysed; for example, IKAR7 from a Karlowa pegmatite, contains SiO₂ in excess of 90.00 wt %, indicating that the sample contained a large amount of quartz. This deduction is corroborated by the inverse relationship between SiO₂ and Al₂O₃, which indicates that samples with relatively lower SiO₂ and relatively higher Al₂O₃ contents are composed of a greater proportion of feldspar. In addition to this, the Na₂O and K₂O contents of individual samples indicate what the dominant feldspar is in those samples, i.e. in the LCT pegmatites sodic feldspar, while potassic feldspar dominates the NYF pegmatites (SLGs). The fact that mineralogical differences are so easily identified in the geochemical data can be attributed to the difficulty in analysing pegmatite samples because of their typically extremely coarse-grained nature. In comparison to the very coarse-grained LCT pegmatite samples, the relatively finer-grained texture of the NYF pegmatites (SLG) samples has resulted in more consistent geochemical data.

A.S.I. values greater than 1.00 indicate that the majority of the pegmatites under investigation in this study are peraluminous (Shand, 1927; Černý and Ercit, 2005), and samples from the LCT sample suite, in particular, typically show this trend (Figure 6.7A and B). The values obtained for LCT pegmatites in this study are characteristic of A.S.I. values that would typically be expected for LCT pegmatites, and they correspond with similar data for LCT pegmatites in other parts of the world, such as those obtained by e.g. Antunes *et al.* (2009), who conducted geochemical analyses on LCT aplite-pegmatite veins in Central Portugal, and Gharib (2012) who analysed LCT pegmatites in the Abu Hab area, Egypt.

The peraluminous nature of the LCT pegmatites, along with their major element compositions (high SiO₂ and K₂O, low MgO, CaO and Na₂O) indicates that they have an S-Type affinity (Chappell and White, 1974). Furthermore, using the classification scheme of Barbarin (1999), all of the LCT pegmatites studied are Muscovite-bearing

Peraluminous Granites (MPGs). This classification corresponds with the S-type geochemical characteristics of the LCT population, and in addition to this, the geochemical behaviour of Rb, Sr, and Ba ratios i.e. high Rb/Sr and low Sr/Ba, suggest that these lithologies contain a significant metasedimentary component, or that they were derived from the partial melt of S-type basement material with a pre-existing S-type geochemical signature (Chappell and White, 1974; Harris and Inger, 1992; Barbarin, 1999; Jung *et al.*, 1999, 2003).

The A.S.I. values of the NYF sample suite are, however, more varied (Figure 6.7A and B). Two of the samples analysed, VALG02 and VALG22 from the Valencia area, have A.S.I. > 1, indicating that they are peraluminous (Shand, 1927), like the pegmatites of the LCT sample suite. The other two samples analysed, VALG04 (A.S.I. = 0.78) and VALG06 (A.S.I. = 0.97) from the Valencia area, have A.S.I. < 1, indicating that they, instead, are metaluminous (Shand, 1927; Figure 6.7A and B).

The geochemical characteristics of the U-bearing NYF pegmatites (SLGs) have been thoroughly examined in recent work by Freemantle (2012). Freemantle (2012) observed that there is significant variability in the A.S.I. of pegmatites not only from the Valencia area, but also from the nearby Goanikontes, Ida Dome, Hildenhof, and Rössing areas, and the data obtained from Valencia samples in this study behave accordingly. Although Freemantle (2012) did identify a few metaluminous SLGs (e.g. from the Rössing area), it was concluded that the majority of the Type C SLGs of the southern Central Zone are, in fact, peraluminous. Furthermore, this conclusion about the aluminosity of Type C SLGs studied by Freemantle (2012), and in this study, is in agreement with the findings of Jung *et al.* (2003), who identified only peraluminous NYF pegmatites (SLGs) in their study on granitoids exposed along the Khan River gorge.

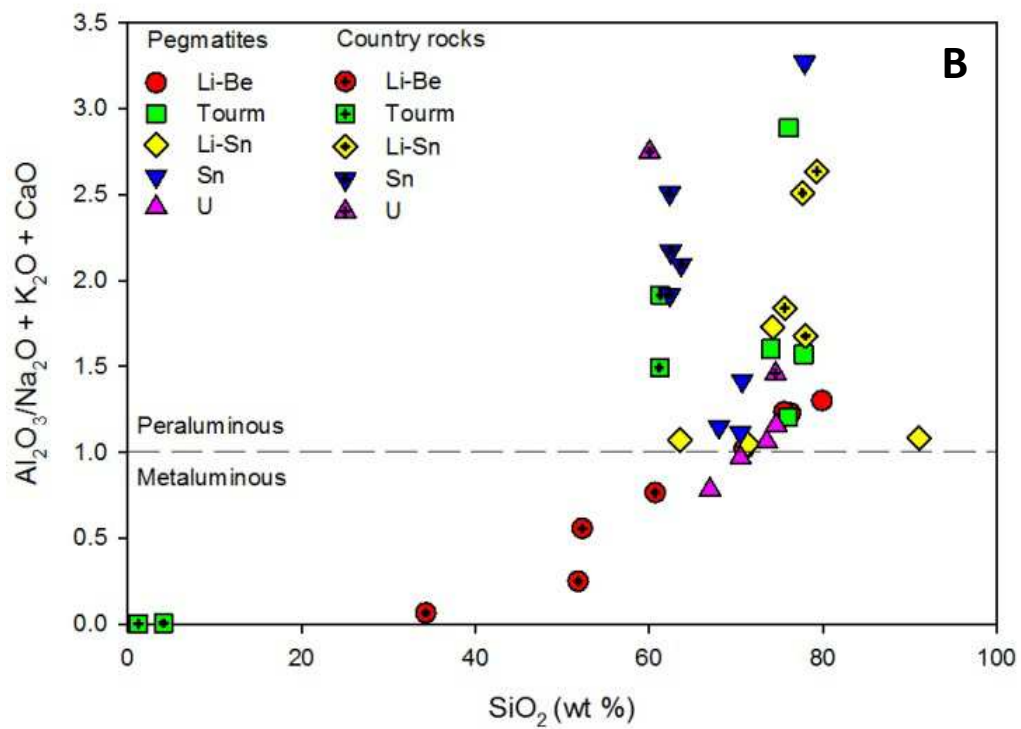
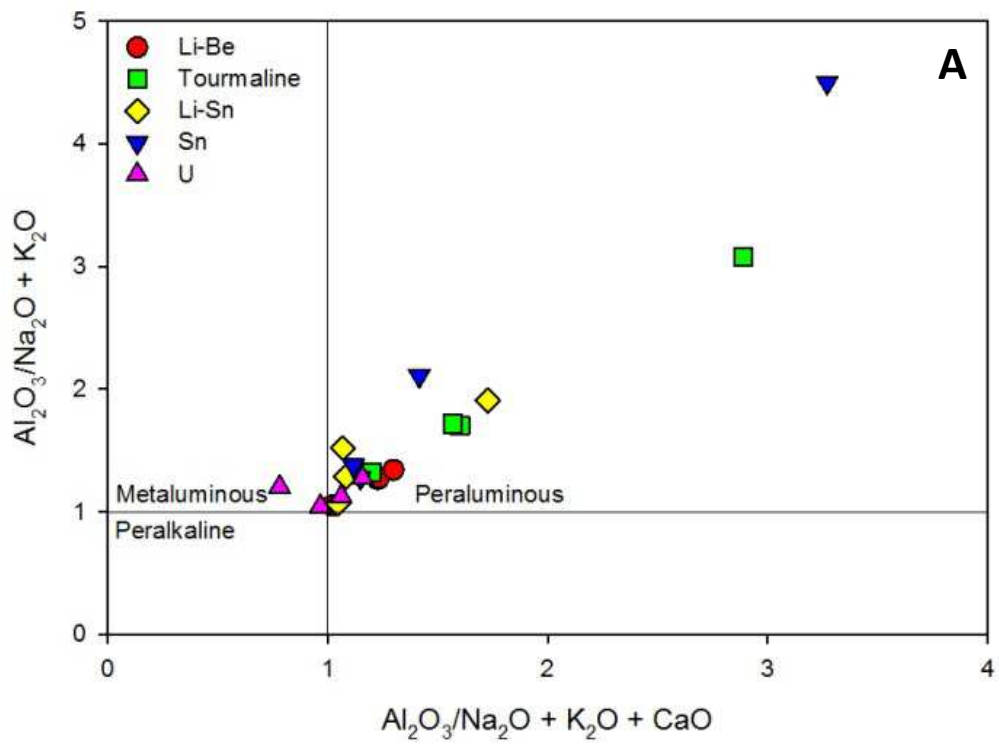


Figure 6.7: Aluminium Saturation Indices (molar $\text{Al}/(\text{Na} + \text{K} + \text{Ca})$) of mineralised pegmatites plotted A) against molar $\text{Al}/(\text{Na} + \text{K})$ and B) against silica. Both plots show clearly that the pegmatites, with the exception of two metaluminous SLGs, are peraluminous.

According to the classification scheme of Barbarin (1999), the NYF pegmatites (SLGs) can be classified as Biotite-bearing Peraluminous Granites, which fall within the CPG (Cordierite-bearing Peraluminous Granite) field, suggesting that they, or at least some of them, should contain a minor mantle component or I-type component (Chappell and White, 1974; Barbarin (1999). This is consistent with the interpretation of Jung *et al.* (2003) who, using Pb- and Sr-isotope data, invoked a meta-igneous source for the NYF pegmatites (SLGs) that they sampled from the Khan River gorge.

In an effort further to constrain the possible sources for the Namibian pegmatites, and further constrain their S- or I-type characteristics, geochemical data obtained from this study were plotted in the granite discrimination diagrams of Whalen *et al.* (1987; Figure 6.8). These diagrams, however, show great variability and inconsistency. When plotted against $10000 \cdot \text{Ga}/\text{Al}$ (ppm), Ce, Y, Zn, and Zr constrain most of the pegmatites and SLGs to the field of S- and I-type granites, however Nb and major elements like K_2O , CaO, Na_2O , and MgO place many of them within the field of A-type granites.

There does not appear to be any trend in which type of LCT pegmatite plots within the A-type granite field i.e. the data points are scattered. It is unusual that they should plot within this field since LCT pegmatites are typically S-type in nature (Martin and De Vito, 2005). Indeed it is more common for NYF pegmatites to have an A-type affinity (e.g. Martin and De Vito, 2005), however the NYF samples from this study plot within the S- and I-type fields of the granite discrimination diagrams. Thus the granite discrimination diagrams of Whalen *et al.* (1987) prove to be of little use in distinguishing between S- and I-type pegmatites in this study.

Given the S-type nature of almost all of the pegmatites studied here, it can be concluded that they were derived from the partial melting of a crustal source which contained a significant (meta)sedimentary component (e.g. Chappell and White, 1974; Barbarin, 1999; Jung *et al.*, 2003; Freemantle, 2012). Indeed it would appear that the pegmatites have similar trace element enrichments, if not similar abundances.

This observation is particularly true of the LCT pegmatites (Uis and Karlowa pegmatites) which have intruded into metapelitic units i.e. enrichments in Sn are observed both in the Uis and Karlowa pegmatites, and in their country rocks of the Amis River Formation. The same observation led Richards (1986) to conclude that the Uis pegmatites were in fact derived from the partial melting of their country rocks. However, in the absence of field evidence directly linking the pegmatites to the anatexis of their country rocks, it must be concluded that the pegmatite melts could not have been generated *in situ*, but that they must have migrated a short distance from their sources and been emplaced into pre-existing Damaran structures (e.g. Owen, 2011; Freemantle, 2012; Longridge, 2012).

The source of the Li-Be- and U-bearing pegmatites is not as clear, however. The Li-Be-bearing pegmatites have been intruded into granodiorites and marbles with which they share little geochemical affinity. In addition to this, the significant difference in age between the pegmatites (~ 506 Ma; Melcher *et al.*, 2013) and the granodiorite (~ 560 Ma; Milani, pers. comm., 2013) indicates that the Li-Be-bearing pegmatites do not represent the last, most fractionated fluid-rich phase of the granodioritic melt.

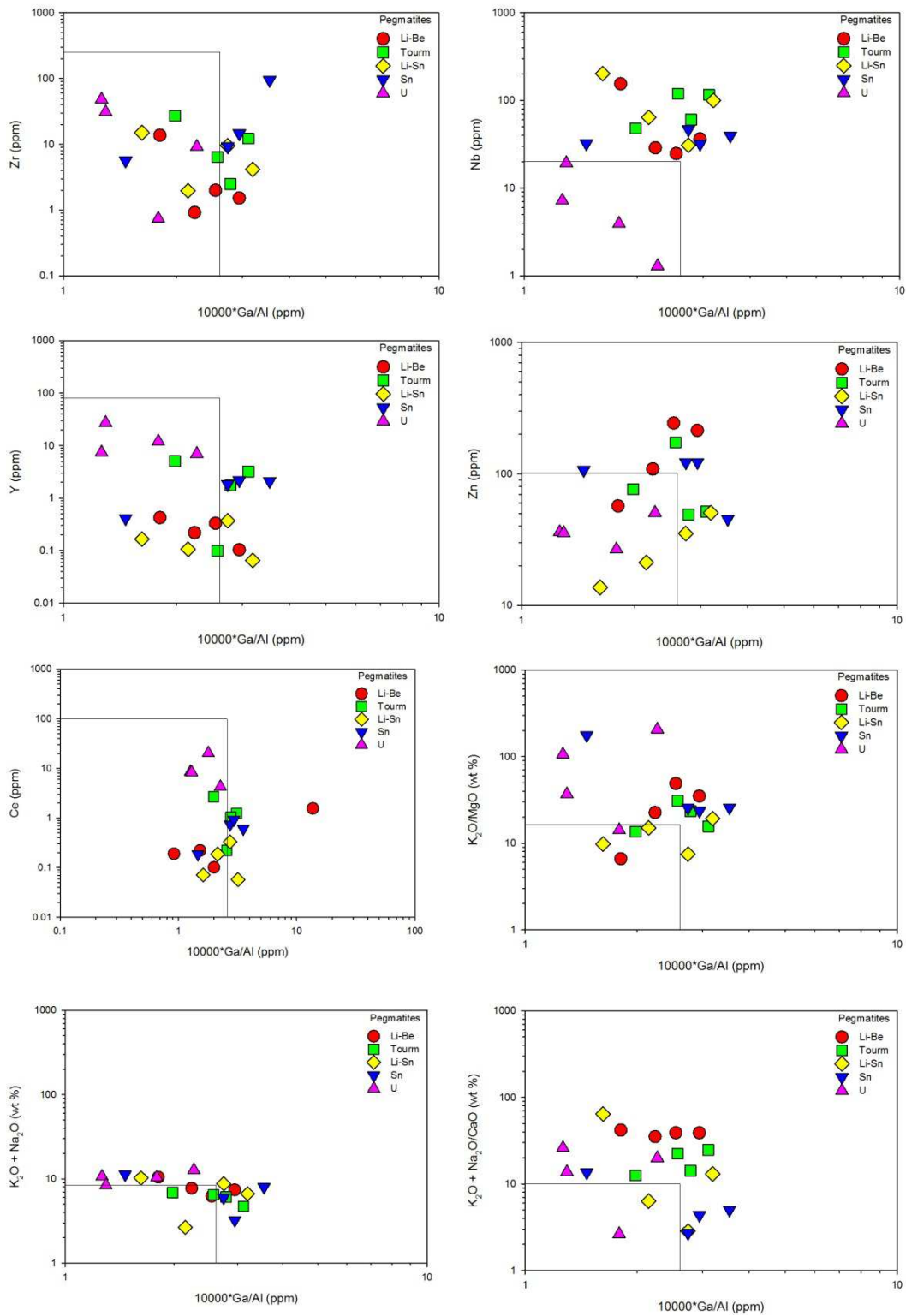


Figure 6.8: Geochemical granite discrimination diagrams for selected trace and major elements (modified after Whalen *et al.*, 1987). The box in the bottom left corner of each plot indicates the I- and S-type granite field while the remainder of the plot represents that of A-type granites.

Similarly, the U-bearing pegmatites in the Valencia area are much younger than other granitoids in the area (Longridge, 2012), thus they cannot represent the most fractionated end-product of plutonic granitic magmatism. In addition to this, while they do share some geochemical similarities with the metapelitic country rocks into which they have been emplaced, there is no field evidence to support their derivation from the *in situ* anatexis of these country rocks. These observations, along with Hf-isotope data, led Longridge (2012) to conclude that the NYF pegmatites in the southwestern parts of the Damara Belt were likely to have been derived from the partial melting of much older Kalahari Craton material which was subducted beneath the Congo Craton during the Damara Orogeny. Indeed this would be consistent with the hypothesis that these pegmatites were generated during the partial melt of an S-type meta-igneous (Jung *et al.*, 2003).

Thus, even if the pegmatite melts were not derived directly from the country rocks into which they have been emplaced, it is still possible that the country rocks may have influenced the mineralisation of the pegmatites to some degree by causing a relative enrichment in some elements e.g. Sn during pegmatite emplacement. The country rock suite also shows higher relative abundances in certain metals, such as Li, Cu, Y, Zr and Ba, and it may be possible that elements diffused outward from the pegmatites into their country rocks during their crystallisation. A more detailed analysis of country rocks with distance from the pegmatites would have to be done in order to clarify this, however.

In terms of the emplacement setting of the pegmatites, according to the bivariate Y + Nb vs. Rb tectonic discrimination diagram of Pearce *et al.* (1984), almost all of the pegmatites fall within the field of syn-collisional granites, with three samples plotting within the post-collisional granite field, and three samples plotting within, or on the boundary of, the within plate granite field (Figure 6.9). Field studies show that the pegmatites have not been subjected to Damara-aged deformation, thus their emplacement must have been post-collisional.

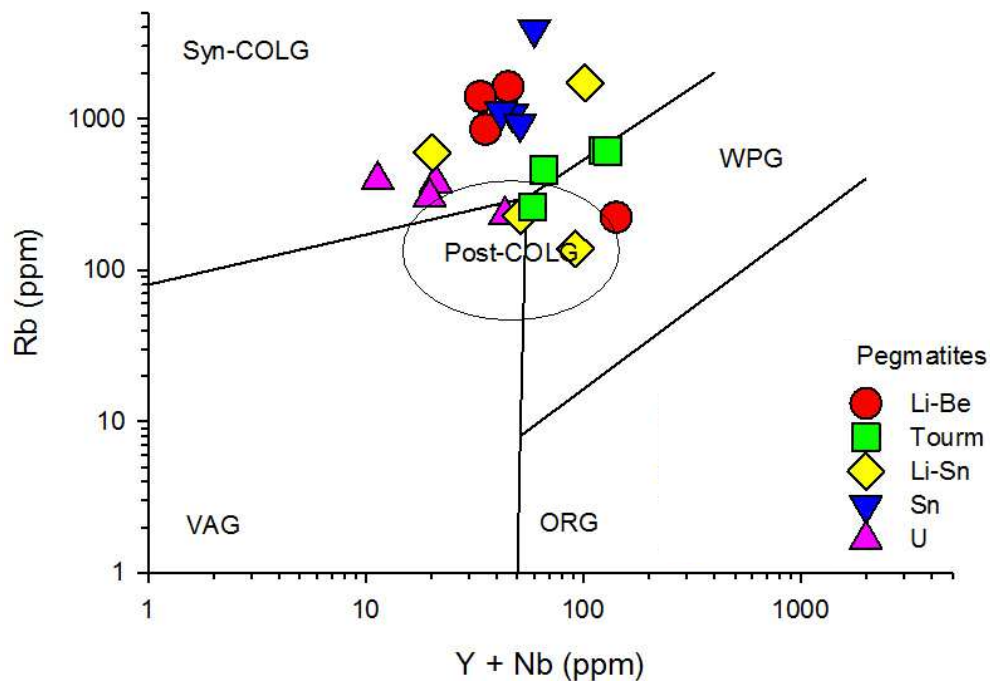


Figure 6.9: Y + Nb vs. Rb tectonic discrimination diagram for mineralised pegmatites; Syn-COLG = syn-collisional granite, Post-COLG = post-collisional granite, WPG = within plate granite, ORG = ocean-ridge granite, VAG = volcanic arc granite (modified after Pearce *et al.*, 1984).

The temperatures of pegmatite crystallisation obtained using Ti-in-quartz thermometry are consistent with the temperatures typically expected for hydrous granitic pegmatites (Nabalek *et al.*, 2010; Thomas *et al.*, 2012). Taylor *et al.* (1979) obtained temperatures of 525 - 625 °C, and in more recent studies, Müller *et al.* (2013) calculated crystallisation temperatures of ~ 612 °C for NYF pegmatites.

Although the temperatures obtained using Ti-in-quartz thermometry in this study are consistent with those typically accepted for pegmatite formation, the sample suite from this study does show some internal variation i.e. the temperatures obtained for the LCT sample suite appear generally to be ~ 150 - 200 °C lower than those obtained from the NYF sample suite.

6.6. Summary

The geochemical characteristics, including major and trace element enrichments, and REE patterns indicate that the Li-Be-, gem tourmaline-, Li-Sn, and Sn-bearing pegmatites are definitively LCT type pegmatites, while the U-bearing pegmatitic SLGs have an NYF affinity.

The peraluminous nature of the LCT population, as well as their Rb, Sr, and Ba characteristics, suggests an S-type origin for these pegmatites, and that they are likely to have been derived from the partial melting of biotite-bearing metapelitic rocks. The NYF pegmatites show mixed geochemical characteristics, with some being metaluminous and some being peraluminous. While the peraluminous NYF pegmatites, like the LCT suite, are likely to have been derived from the anatexis of metapelitic crustal material, the metaluminous NYF pegmatites may rather have been derived from the partial melting of an S-type meta-igneous source, such as older crustal material of the Kalahari Craton.

Although the country rock suites show similar geochemical characteristics with the pegmatites which have been emplaced into them, there is no field evidence to suggest that they were derived from *in situ* anatexis of the country rocks. It is more likely that anatexis occurred some distance away from where the pegmatites were ultimately emplaced, and that the melts migrated and were finally emplaced in pre-existing structures, possibly formed during Damaran deformation. Thus, while the immediate country rocks may have contributed to the overall enrichment of the pegmatites in certain elements, they may not have been the direct source of those metals.

The LCT pegmatites crystallised at temperatures ranging from ~ 460 - 560 °C, while the NYF pegmatites crystallised at higher temperatures, ranging from 640 - 680 °C, and the emplacement of the pegmatites was post-tectonic.

CHAPTER 7

O- AND H-ISOTOPE CHARACTERISTICS OF MINERALISED PEGMATITES AND THEIR COUNTRY ROCKS

7.1 Introduction

Stable isotope geochemistry refers to the study of the isotopic variation of elements that arises from physico-chemical, rather than radiogenic, processes (Rollinson, 1993; Faure and Mensing, 2005; Sharp, 2007). It provides a useful way to study light elements, such as H, C, N, O and S, which are often the principal constituents of geological fluids, but are difficult to study using other analytical techniques (Rollinson, 1993; Sharp, 2007). Stable isotopes are studied mainly because they can give an indication of processes by which isotopes are fractionated as a result of their mass; these processes may take the form of isotopic exchange reactions (equilibrium effects), kinetic processes, or physico-chemical processes (Sharp, 2007). For this study, O- and H-isotopes were studied in order to determine the temperatures of formation of mineralised Damaran pegmatites, as well as the isotope composition, and hence origin, of the fluid from which the pegmatites formed.

Oxygen and hydrogen are important components of the Earth's crust, and of magmatic systems. Studying the O- and H-isotope ratios in igneous rocks can give an indication of open-system behaviour during or after emplacement, they can be used as a monitor of crustal contamination, and they can be used to identify and quantify fluid-rock interaction (Taylor, 1978; Sharp, 2007). Furthermore, combining H- and O-isotope data allows one to determine the source of water present in a given system (Sheppard, 1977b; 1986).

7.2 Methodology

7.2.1 Sampling

Quartz, feldspar and muscovite samples were taken for the purposes of O- and H-isotope analyses. These minerals were sampled individually where possible so as to minimize sample preparation for the purposes of mineral separation, however care was taken to sample them from exactly the same locality. Whole-rock samples were also analysed; these were sampled from the Wall Zones of zoned pegmatites and from approximately 1 m within unzoned pegmatites in an attempt to sample homogeneously textured material of a representatively “granitic” composition i.e. quartz + feldspar + muscovite.

7.2.2 Sample preparation

Mineral separates of quartz, feldspar (plagioclase and potassic feldspar), and mica (muscovite and biotite) were prepared by milling and sieving samples of each mineral to a grain size of 90 - 125 μm , running them through a Frantz magnetic barrier separator at 0.6, 1.2 and 2 A to remove magnetic impurities, and then handpicking them to remove any remaining impurities. After this, 1 - 5 g of material were milled into powder.

7.2.3 Analytical techniques

Oxygen- and Hydrogen-isotope ratios were determined on 10 mg quartz, feldspar, mica, whole-rock, and country rocks samples at the Department of Geological Sciences, University of Cape Town. The $\delta^{18}\text{O}$ values were determined after drying powdered material at 50 $^{\circ}\text{C}$, and degassing them under vacuum on conventional silicate lines for 2 hours at 200 $^{\circ}\text{C}$. Quartz and whole-rock powders were reacted with ClF_3 (oxidising agent) for 3 hours at 500 - 550 $^{\circ}\text{C}$, and the O_2 was converted to CO_2 using a hot platinised carbon rod. Duplicate internal standards (Murchison Line Quartz, MQ; $\delta^{18}\text{O} = 10.1 \text{‰}$) were run with each batch of samples. An average value for MQ was used to normalise the raw data to the SMOW scale. The method for

oxygen extraction from silicates has been described in detail by Vennemann and Smith (1990), Harris and Erlank (1992), and Harris *et al.* (2002).

The method of Vennemann and O'Neil (1993) was used to determine Hydrogen-isotope ratios of fine-grained mica samples. The samples were degassed at 200 °C on the vacuum line prior to decrepitation at 500 °C. Two water standards, CTMP2010 ($\delta D = -7.4 \text{ ‰}$) and RMW ($\delta D = -131.4 \text{ ‰}$) were used to normalise the data to the SMOW scale and to correct for compression respectively. The water extracted from samples was collected in quartz tubes containing Indiana Zn, and these tubes were heated to 450 °C to reduce the water immediately prior to analysis on the mass spectrometer. The CO₂ and H₂O gases were introduced into a Finnegan MAT252 mass spectrometer via break-seal tubes, and samples were analysed in dual inlet mode.

Data are reported in the delta (δ) notation relative to Standard Mean Ocean Water (SMOW):

$$\delta = \left(\frac{R_x - R_{std}}{R_{std}} \right) \times 1000$$

R is the ratio of the abundance of heavy to light isotope, x denotes the sample, and std denotes the standard. For more information on the technique and data reporting standards see Appendix 1.

Fractionation between a mineral pair, A and B is quantified by the fractionation factor (α_{A-B}), which is defined as follows:

$$\alpha_{A-B} = \frac{1000 + \delta^{18}O_A}{1000 + \delta^{18}O_B}$$

Fractionation can also be expressed as $1000\ln\alpha$ as a result of the fact that $1000\ln(X) = X$ and Δ_{A-B} such that:

$$\Delta_{A-B} = \delta_A - \delta_B \approx 1000 \ln \alpha_{A-B}$$

The O-isotope ratios of quartz and feldspar separates were used to calculate temperatures of equilibration and pegmatite crystallisation using the equation (Chiba *et al.*, 1989):

$$1000 \ln \alpha_{qz-fs} = A \times \frac{10^6}{T^2}$$

α_{qz-fs} is the fractionation factor of quartz and feldspar, A is the mineral-mineral fractionation coefficient, in this case determined by Chiba *et al.* (1989), and T is the temperature in Kelvin.

7.3 Results

All $\delta^{18}\text{O}$ values for quartz, feldspar, whole-rock, and country rock samples are presented in Table 7.1, and δD values for mica samples (muscovite and biotite) in Table 7.2.

7.3.1 Oxygen- and Hydrogen-isotope results

7.3.1.1 Li-Be-bearing pegmatites: Rubicon and Helicon pegmatites

O-isotope ratios in quartz from the Rubicon pegmatite range between 11.2 ‰ and 12.4 ‰, and ratios obtained from quartz in the Helicon pegmatite are similar, ranging from 12.1 - 12.6 ‰. In both pegmatites, there does not appear to be any systematic variation between the $\delta^{18}\text{O}$ values of samples taken from the Wall zones and those taken in the Core zones of the pegmatites (Figure 7.1). The $\delta^{18}\text{O}$ values of plagioclase in the pegmatites is slightly lower and slightly more variable than those obtained from quartz, with values ranging from 9.9 - 12.7 ‰ in the Rubicon pegmatite and from 10.9 - 12.4 ‰ in the Helicon pegmatite.

The $\delta^{18}\text{O}$ values obtained from whole-rock samples fall within a similar range to those measured in quartz and feldspar, although they are slightly higher, with values ranging

between 10.4 ‰ and 10.6 ‰ in the Rubicon pegmatite, and 11.2 ‰ and 11.5 ‰ in the Helicon pegmatite.

Country rock samples show the greatest variability in $\delta^{18}\text{O}$ values. The values of the Goas granodiorites into which the Rubicon pegmatite has been emplaced are low in comparison to pegmatite values, ranging from 8.8 - 9.1 ‰. Marble samples taken from adjacent to the Helicon pegmatite are significantly higher than this ranging from 16.9 - 17.2 ‰.

Temperatures obtained using O-isotope thermometry on quartz-feldspar pairs suggests crystallisation temperatures of $\sim 470 - 527$ °C ($\Delta_{\text{q-f}} = 1.5 - 1.7$) for Rubicon and a higher temperature of 630 °C for Helicon ($\Delta_{\text{q-f}} = 1.2$).

The H-isotope ratios of muscovite from the Rubicon pegmatite range from -63 - -67 ‰, and they contain as much as 2.84 wt % water. Muscovites from the Helicon pegmatite have δD values between -78 ‰ and -91 ‰, and they contain between 1.88 wt % water and 3.66 wt % water.

7.3.1.2 Sn-bearing pegmatites: Uis pegmatites

The $\delta^{18}\text{O}$ values of quartz from the two Uis pegmatites sampled range from 15.0 - 15.8 ‰. Feldspar $\delta^{18}\text{O}$ values in the two bodies are similar, although more variable, ranging from 13.6 - 15.1 ‰, while whole-rock O-isotope ratios range from 13.5 - 14.5 ‰.

The $\delta^{18}\text{O}$ values of “knotted” metapelitic country rocks from adjacent to the Uis area are again very similar to the values obtained for quartz and feldspar, ranging from 13.2 - 13.6 ‰.

Quartz-feldspar pairs yield temperatures of 537 - 1348 °C ($\Delta_{\text{q-f}} = 0.4 - 1.5$) for the crystallisation of the pegmatites.

The H-isotope ratios of muscovites from the Uis pegmatites range from -60 - -67 ‰, and they contain up to 4.12 wt % water.

7.3.1.3 Li-Sn-bearing pegmatites: Karlowa pegmatites

The O-isotope ratios of quartz in pegmatites from the Karlowa area show little variation, and range from 14.8 - 15.2 ‰. The $\delta^{18}\text{O}$ values for feldspars in the pegmatites are more variable, and slightly lower, ranging from 13.0 - 14.0 ‰, and whole-rock samples for these pegmatites show the most variability, with values ranging between 12.7 ‰ to 15.2 ‰.

The metapelites into which the pegmatites intruded fall between the lowest pegmatitic feldspar $\delta^{18}\text{O}$ value ($\delta^{18}\text{O} = 12.7$ ‰), and the highest quartz $\delta^{18}\text{O}$ value ($\delta^{18}\text{O} = 15.2$), and typically range from 13.8 - 14.4 ‰.

Temperatures obtained for the crystallisation of the pegmatites are variable, and are typically between 396 °C and 713 °C ($\Delta_{q-f} = 1.0 - 2.1$).

The δD values of muscovites from the Karlowa pegmatites are variable, ranging from -44 - -69 ‰, and their water contents are also quite variable, ranging from 1.19 - 4.16 wt % water.

Table 7.1: $\delta^{18}\text{O}$ values for quartz, feldspar, and whole-rock LCT and NYF pegmatite samples, as well as adjacent country rocks. Note that (c) indicates samples taken from massive quartz core zones of zoned pegmatites.

Locality	Quartz		Feldspar		Whole-rock		Country Rock		Δ_{q-f}	T (°C)	
	Sample No.	$\delta^{18}\text{O}$ (‰)	Sample No.	Type	$\delta^{18}\text{O}$ (‰)	Sample No.	$\delta^{18}\text{O}$ (‰)	Sample No.			$\delta^{18}\text{O}$ (‰)
Rubicon	IIRUB1-1	12.4	2aIIRUB	Plag	10.7	2eRUB	10.4			1.7	472
	2gRUB(c)	11.7									
	2RUBm	11.2	2RUBl	Plag	12.7	2RUBp	10.6	2RUBCR	9.1	-1.5	
	2RUBo	11.4	2RUBo	Plag	9.9			2RUBi	8.8	1.5	526.96
Helicon	I HEL1-1	12.4	IHELf	Plag	12.4	IHELg	11.5			-0.1	
	IHEL4-1(c)	12.1									
	IHELh	12.1	IHELi	Plag	10.9	IHElm	11.2	IHELn	17.2	1.2	630
	IHELj	12.2	IHELk	Plag	12.2			IHELl	16.9	0.1	4004
Uis	IUIS2	14.8	IUIS1	Plag	13.6	IUIS3	14.5			1.2	611
	IUIS6	15.1	IUIS6	Plag	15.1	IUIS10	13.5	IUIS8	13.2	-0.1	
	IUIS7	15.1	IUIS7	Plag	14.3			IUIS11	13.3	0.8	807
	IUIS2	15.0	IUIS2	Plag	13.6	IUIS3	14.2			1.5	536
	IUIS4	15.8	IUIS5	Plag	15.5	IUIS6	14.4	IUIS10	13.5	0.4	1348
	IUIS8	15.8	IUIS9	Plag	14.7			IUIS 11	13.6	1.1	642
Karlova	IKAR5	15.0	IKAR8	Plag	13.7	IKAR7	15.2			1.3	588
	IKAR8/9	15.2	IKAR8/9	Plag	13.4	IKAR17	12.7	IICAR15	13.8	1.9	442
	IKAR11	15.0	IKAR12	Plag	14.0			IICAR16	14.4	1.0	713
	IICAR1	14.8	IICAR3	Plag	13.0	IICAR3	13.9			1.8	457
	IICAR4	15.1	IICAR6	Plag	13.0	IICAR7	12.8	IICAR12	14.2	2.1	395

Table 7.1: continued

Quartz		Feldspar			Whole-Rock		Country Rock		Δ_{q-f}	T (°C)	
Locality	Sample No.	$\delta^{18}\text{O}$ (‰)	Sample No.	Type	$\delta^{18}\text{O}$ (‰)	Sample No.	$\delta^{18}\text{O}$ (‰)	Sample No.	$\delta^{18}\text{O}$ (‰)		
Usakos	IIKAR11	14.9	IIKAR10	Plag	13.3			IIKAR13	13.8	1.7	480
	USK3	16.0	USK3	Plag	14.9	USK3	15.5			1.1	656
	USK9(c)	15.5									
	USK17	15.2	USK18	Plag	15.0	USK5	15.2	USK16	13.9	0.1	2359
	USK20	15.3	USK21	Plag	14.6			USK22	13.2	0.7	902
Omapyu	OMA4	16.0	OMA4	Plag	14.4	OMA2	14.5			1.6	509
	OMA9	15.5	OMA10	Plag	13.9	OMA1	14.7	OMA5	19.8	1.5	513
	OMA11	15.4	OMA12	Plag	13.7			OMA13	15.8	1.8	464
Valencia	VALG02	14.8	VALG02	Ksp	13.6	VALG02	12.4	VA26-141	13.3	1.3	599
	VALG04	11.5	VALG04	Ksp	10.4	VALG04	10.8			1.1	655
	VALG06	12.7	VALG06	Ksp	12.5	VALG06	11.8			0.1	2427
	VALG22	12.9	VALG22	Ksp	12.8	VALG22	13.1	VA26-139	14.1	0.0	4499
Mean		14.1			13.3		13.1		14.0	1.0	1072
σ		1.6			1.5		1.7		2.5	0.8	1118

Table 7.2: δD values for muscovite and biotite samples from LCT and NYF pegmatite samples.

Locality	Mica			
	Sample No.	Type	δD	wt % water
Rubicon	Ile2RUBm	Musc	-67	2.84
	2RUBj	Musc	-66	2.57
	2 RUBO	Musc	-63	2.76
Helicon	IHELg	Musc	-91	3.34
	IHELj	Musc	-83	1.88
	IHELI	Musc	-78	3.66
Uis	IUIS3	Musc	-60	4.10
	IUIS6	Musc	-62	4.12
	IUIS7	Musc	-63	2.99
	IUIS3	Musc	-62	4.04
	IUIS5	Musc	-64	2.08
	IUIS7	Musc	-67	3.70
Karlowa	IKAR10	Musc	-55	1.19
	IKAR13	Musc	-68	3.78
	IIKAR3	Musc	-44	2.52
	IIKAR8	Musc	-59	3.07
	IIKAR9	Musc	-69	4.16
Usakos	USK3	Musc	-57	3.88
	USK15	Musc	-71	4.22
	USK23	Musc	-106	0.68
Omapyu	OMA2	Musc	-67	4.11
	OMA8	Musc	-79	4.08
	OMA11	Musc	-70	3.70
Valencia	VALG02	Musc	-75	2.75
	VALG04	Biotite	-42	3.87
	VALG22	Musc	-63	1.37
Mean			-67	3.13
σ			13	1.02

7.3.1.4 Gem-tourmaline-bearing pegmatites: Usakos and Omapyu pegmatites

$\delta^{18}\text{O}$ values from quartz in the Usakos pegmatite range from 15.2 - 16.0 ‰, and there does not appear to be any variation in O-isotope ratios in the Wall and Core zones of the pegmatite. O-isotope ratios in quartz from the Omapyu pegmatite are similar, and are also typically between 15.4 ‰ and 16.0 ‰. Plagioclase from the Usakos pegmatite produced slightly lower $\delta^{18}\text{O}$ values (14.6 - 15.0 ‰) than quartz from the same deposit, and similarly values in the Omapyu pegmatite range from 13.7 - 14.4 ‰. Whole-rock sample from the Usakos and Omapyu pegmatites also have O-isotope ratios similar to those of the quartz-feldspar pairs, with values ranging from 15.2 - 15.5 ‰ in the Usakos pegmatite, and 14.5 - 14.7 ‰ in the Omapyu pegmatite.

Country rock samples taken adjacent to the gem-tourmaline-bearing pegmatites are highly variable in their O-isotope ratios. The metapelites into which the Usakos pegmatite intruded have similar, although slightly lower, $\delta^{18}\text{O}$ to the pegmatite itself ($\delta^{18}\text{O} = 13.2 - 13.9$ ‰). In contrast, the $\delta^{18}\text{O}$ values of the marbles into which the Omapyu pegmatite has intruded are significantly higher than those obtained from the pegmatite, ranging from 15.8 - 19.8 ‰.

The temperatures obtained from quartz-feldspar pairs for the crystallisation of the Usakos and Omapyu pegmatites are highly variable. Values calculated for Usakos are very high, falling between 650 °C and 2360 °C ($\Delta_{\text{q-f}} = 0.1 - 1.1$), while those from Omapyu are considerably lower (464 – 513 °C; $\Delta_{\text{q-f}} = 1.5 - 1.8$).

H-isotope ratios in muscovite from the Usakos pegmatite are highly variable (-57 to -106 ‰), and water contents in the muscovites are equally variable, ranging from 0.68 - 4.22 wt % water. The δD values of muscovites from the Omapyu pegmatite are less variable, ranging from -67 to -79 ‰, and their water contents reach as much as 4.11 wt % water.

7.3.1.5 U-bearing pegmatites (SLGs): Valencia pegmatites (SLGs)

The O-isotope ratios obtained for quartz in the NYF pegmatites of the Valencia area show some variability, and typically range from 11.5 - 14.8 ‰. Similarly, the $\delta^{18}\text{O}$ values of potassic feldspars from the pegmatites, range from 10.4 - 13.6 ‰. Whole-rock samples from these pegmatites yield very similar O-isotope ratios (11.8 - 13.0 ‰).

The metapelites which are in contact with these pegmatites show slightly higher $\delta^{18}\text{O}$ values than the pegmatites themselves (13.3 - 14.1 ‰).

O-isotope thermometry yields temperatures of 600 - 4500 °C ($\Delta_{q-f} = 0.0 - 1.3$) for the crystallisation of the Valencia NYF pegmatites. The cause of excessively high temperature values are discussed in further detail in section 7.4.

H-isotope ratios of micas from the Valencia pegmatites/SLGs show some variability. δD values for muscovites range from -63 - -75 ‰, and the $\delta\text{D} = -42$ ‰ for the biotite sample that was analysed. The muscovite sample contain less (1.37 - 2.75 wt % water) than the biotite sample, which contains 3.87 wt % water.

7.4 Discussion of results

Overall, O-isotope ratios in quartz from all LCT and NYF pegmatites range between 11.18 ‰ and 16.00 ‰ (mean = 14.1 ‰). In addition to this the $\delta^{18}\text{O}$ values of samples taken from the Wall zone and the massive quartz Core zone of individual zoned pegmatite bodies show there is no systematic variation in O-isotope ratios in different parts of the pegmatites. The highest $\delta^{18}\text{O}$ values are observed in the unzoned to weakly-zoned miarolitic gem-tourmaline-, Sn, and Li-Sn LCT pegmatites ($\delta^{18}\text{O} = 14.8$ ‰ - 16.0 ‰; Group B), while lower values are observed in the zoned LCT Li-Be-bearing pegmatites, and U-bearing NYF SLGs ($\delta^{18}\text{O} = 11.2 - 12.9$ ‰; Group A). A histogram of $\delta^{18}\text{O}$ values in quartz shows that there is a strong bimodal distribution of the data (Figure 7.1).

The $\delta^{18}\text{O}$ values of feldspar (albite in LCT pegmatite samples and potassic feldspar in the NYF pegmatite samples) are slightly lower than those in quartz, ranging from 9.9 - 15.5 ‰ (mean $\delta^{18}\text{O} = 13.3$ ‰), and the whole-rock $\delta^{18}\text{O}$ values have a similar range (10.2 - 15.5 ‰; mean $\delta^{18}\text{O} = 13.1$ ‰). A bimodal distribution of $\delta^{18}\text{O}$ values in feldspar is also apparent, if not as strongly as in quartz, and the distribution of values in whole-rock samples appears to be random (Figure 7.1).

Whole-rock $\delta^{18}\text{O}$ ratios are fairly variable, with the lowest values occurring in the Li-Be-bearing LCT and U-bearing NYF pegmatites (SLGs; $\delta^{18}\text{O} = \pm 10.5$ ‰). The highest whole-rock $\delta^{18}\text{O}$ values are found in the Usakos pegmatite ($\delta^{18}\text{O} = 15.5$ ‰). Figure 7.1 shows that there is a fair amount of variability in the O-isotope ratios of whole-rock samples from all of the pegmatites sampled, and there does not appear to be any trend in their values between different pegmatite types.

The greatest variability in $\delta^{18}\text{O}$ values is observed in samples from the country rock suite (8.8 - 19.8 ‰; Figure 7.1). The lowest $\delta^{18}\text{O}$ values are those of the granodiorites in contact with the Rubicon pegmatite, while the highest belong to the marbles into which the Helicon (Li-Be-bearing LCT) and Omapyu (gem tourmaline-bearing LCT) pegmatites have intruded. The O-isotope ratios of the metapelitic country rocks into which the Uis (Sn-bearing LCT), Karlowa (Li-Sn-bearing LCT), Usakos (gem-tourmaline-bearing LCT), and Valencia (U-bearing NYF) pegmatites have intruded fall within a relatively narrow range between 13.2 ‰ and 14.2 ‰.

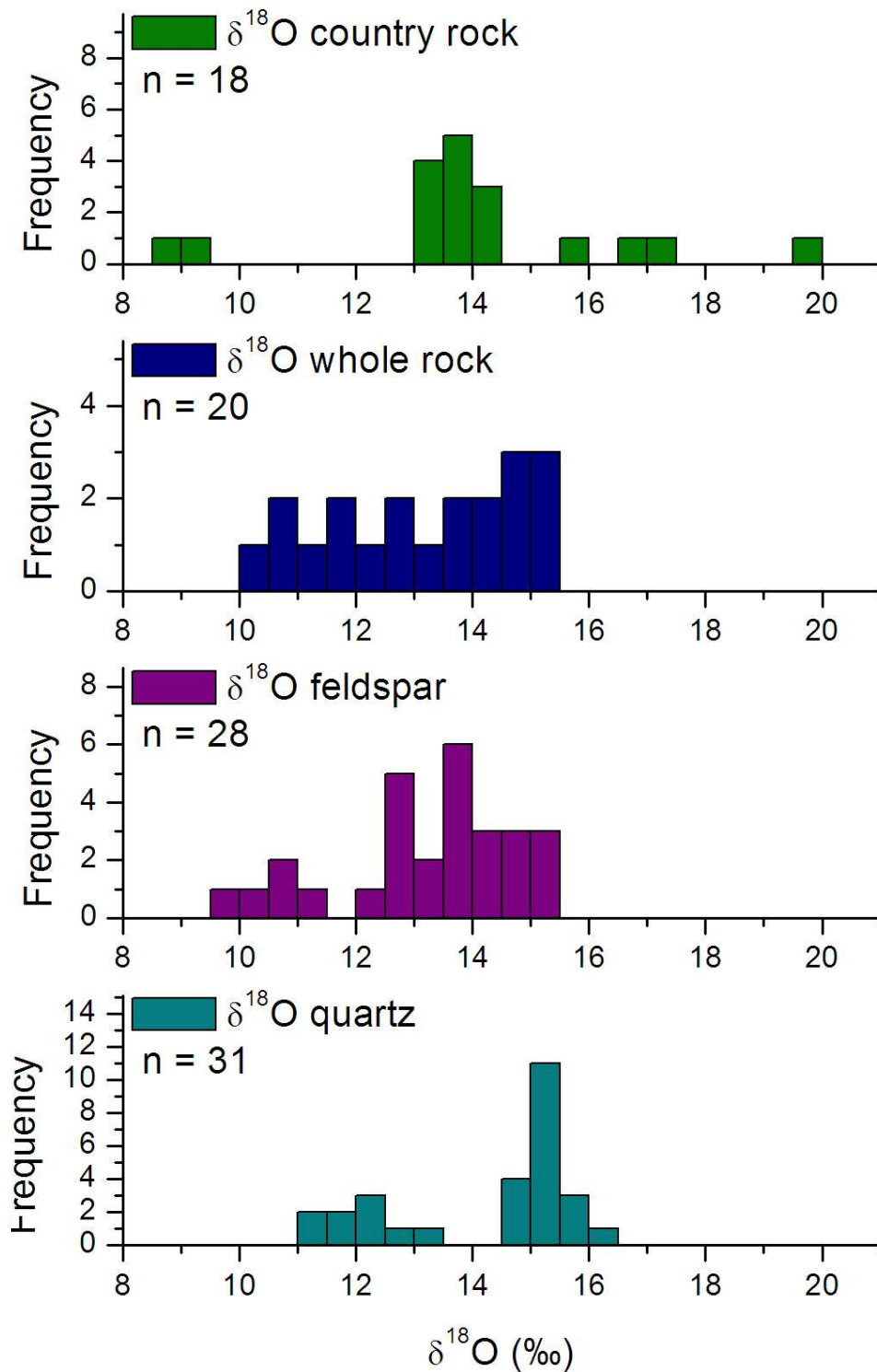


Figure 7.1: Histograms showing the distribution of $\delta^{18}\text{O}$ values measured in quartz, feldspar, whole-rock, and country rock samples from mineralised pegmatites and SLGs in Namibia.

Figure 7.2 shows O-isotope ratios in quartz in relation to O-isotope ratios in feldspar, whole-rock, and country rock samples. The data plot mostly within the range defined by the 400 °C - 700 °C isotherms ($\Delta_{\text{qz-fs}} = 0$ ‰ refers to the isotherm along which the O-isotope ratios between a given mineral pair are the same, and as such a temperature cannot be calculated), indicating that most mineral pairs were in O-isotope equilibrium at the temperatures of formation of the pegmatites, with the exception of one feldspar sample (2RUBI) from Rubicon pegmatite which has an elevated $\delta^{18}\text{O}$ value for feldspar in relation to other samples from the body, and some whole-rock samples from the Sn- and Li-Sn bearing pegmatites. Quartz and whole-rock $\delta^{18}\text{O}$ values also generally show isotopic equilibrium. It is interesting to note that the pegmatites with higher $\delta^{18}\text{O}$ values are in isotopic equilibrium with their country rocks, regardless of the composition of those country rocks, while those with lower values show disequilibrium with their country rocks.

Typically, $\Delta_{\text{qz-fs}}$ fall between 1 and 2 ‰ (ranging from -1.5 ‰ - +1.9 ‰; mean $\Delta_{\text{qz-fs}} = 1.0$ ‰), with the majority of mineral pairs falling within the range of 1.0 - 1.5 ‰. Individual feldspar samples have high $\delta^{18}\text{O}$ values to the extent that $\Delta_{\text{qz-fs}}$ values are negative.

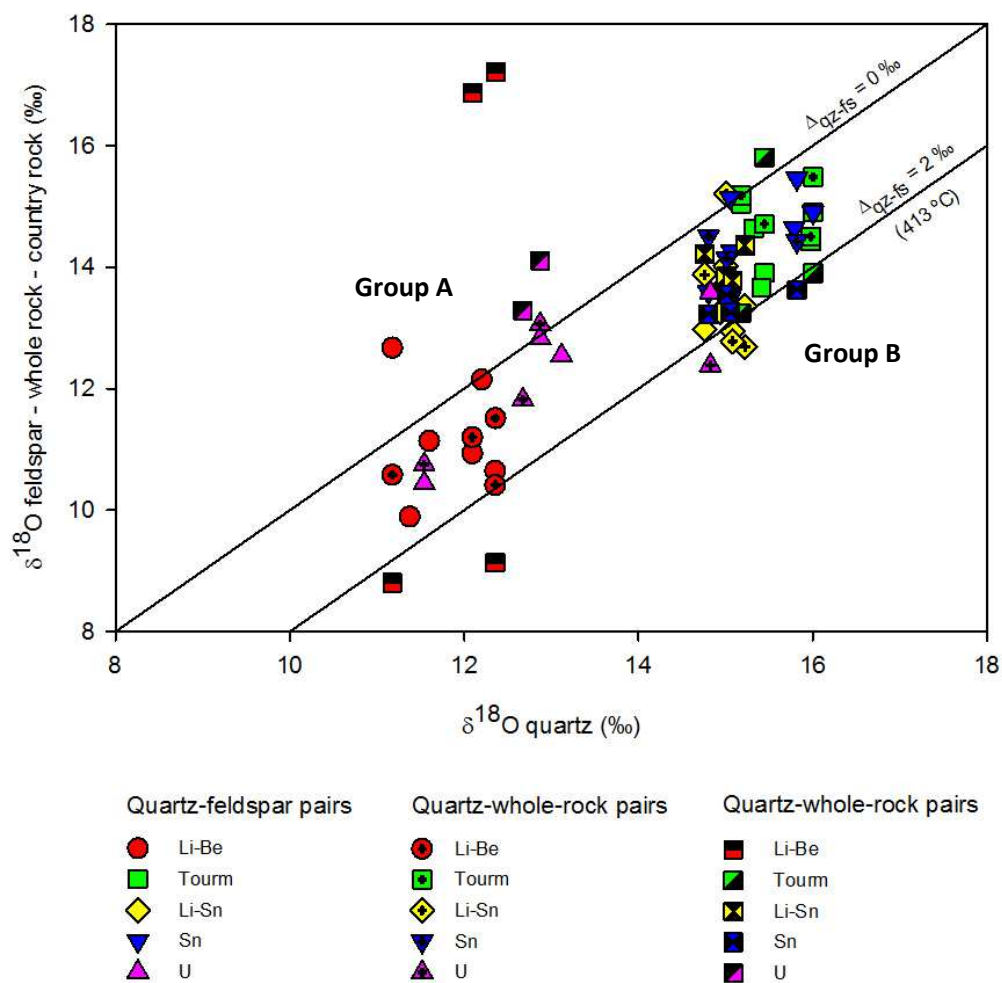


Figure 7.2: Plot of $\delta^{18}\text{O}$ values of quartz (qz) plotted against $\delta^{18}\text{O}$ values of feldspar (fs), whole-rock (wr), and country rock (cr) samples. Note that symbol colours refer to different deposit types. Refer to text for descriptions of Group A and Group B pegmatites.

A range of equilibrium temperatures were obtained for the pegmatites using the O-isotope geothermometry equations and coefficients of Chiba *et al.* (1989). The temperatures acquired from quartz feldspar pairs in all of the pegmatites range from 396 °C to 4499 °C. Excessively high temperatures are the result of very low per mil differences between the O-isotope ratios of quartz and feldspar, indicating that this mineral pair is of limited use in O-isotope geothermometry (Taylor, 1978; Valley, 1986; Sharp, 2007). The

reason for this is that feldspars are highly susceptible to alteration, which can produce significant errors on the $\delta^{18}\text{O}$ values obtained for feldspars and subsequently yield fairly large temperature ranges (Taylor, 1978; Valley, 1986; Sharp, 2007). The feldspars for mineral pairs where $1000\ln\alpha_{\text{qz-fs}} > 1$ were less altered, therefore their $\delta^{18}\text{O}$ were more reliable; the calculated temperatures of pegmatite crystallisation for these pairs range from 395.54 °C - 656.83 °C (mean = 541.05 °C).

δD values show a normal distribution (Figure 7.3), with the majority of samples ranging between -60 ‰ and -70 ‰ (mean = -67. ‰). The highest δD value is that of biotite from VALG04, a pegmatitic SLG from Valencia, which is also the only biotite sample analysed.

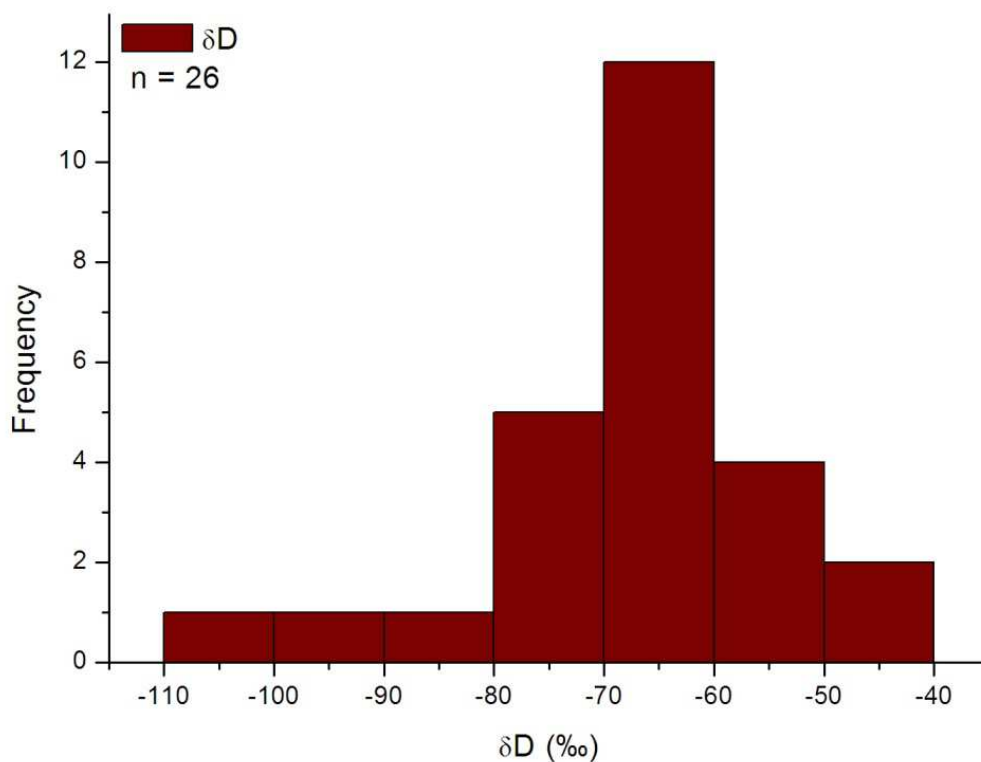


Figure 7.3: Histogram showing the distribution of δD values measured in micas from mineralised pegmatites and SLGs in Namibia.

The water contents of mica samples are variable, and the distribution of samples is highly variable, however most sample seem to contain between 1.19 – 4.22 wt % water (Figure

7.4). The lowest water content corresponds with the lowest δD , measured in muscovite from a miarolitic gem-bearing pegmatite (sample USK23 from Usakos; Table 7.2). All other δD values for muscovites sampled from pegmatites of this type fall within the range of $\delta D = -50$ - -80 ‰. The greatest consistency in water content among all the samples is also observed in pegmatites of this type, with water contents ranging from 3.34 - 4.22 wt % water (Figure 7.4).

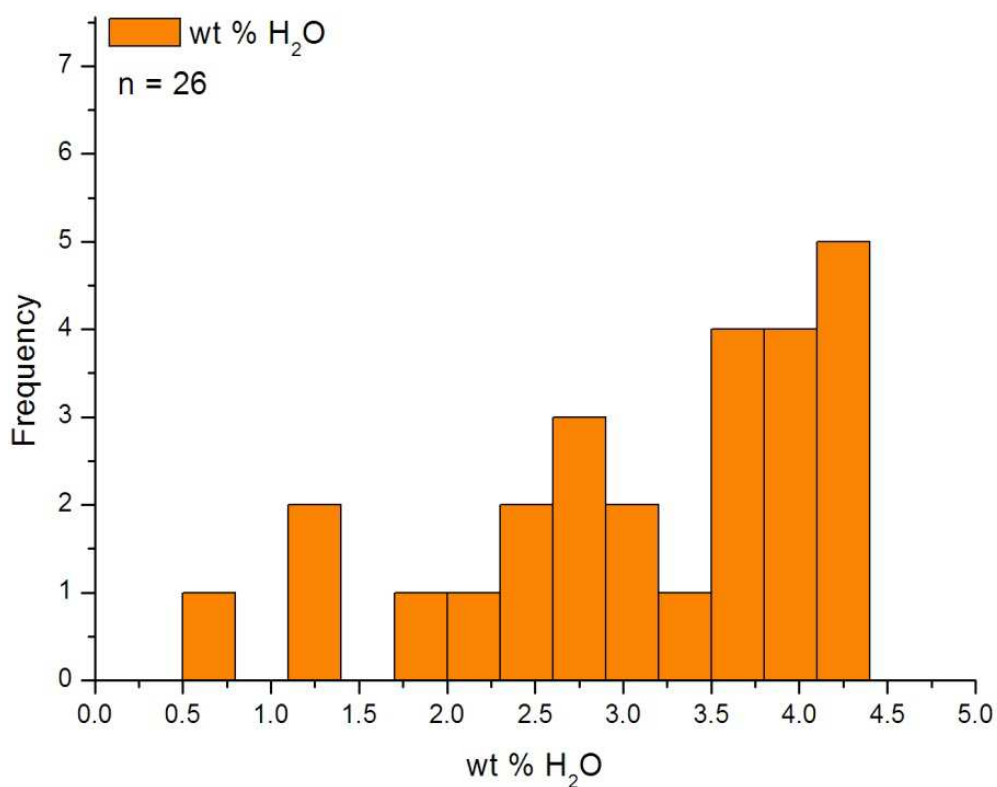


Figure 7.4: Histogram showing the water content measured in muscovites and biotites from mineralised pegmatites and SLGs in Namibia. All samples are muscovite, except for VALG04 from Valencia, which is biotite (wt % H₂O = 3.87).

7.5 Interpretation of results

Very little work has been done on the stable isotope systematics of pegmatites, therefore, assuming that pegmatites represent the last fraction of melt in a granitic system, the interpretation of their isotopic composition should be similar to that of any other magmatic rock (Damm *et al.*, 1992). As such, three processes must be considered in identifying their origins, namely a) the nature of the source material that is partially melted to produce the magma, b) differentiation processes, including fractional crystallisation and assimilation, c) loss of volatiles during crystallisation, and d) post-crystallisation fluid-rock interaction (Taylor, 1978; Damm *et al.*, 1992).

Taylor *et al.* (1979) produced one of the first and few stable isotope studies on pegmatites, which included $\delta^{18}\text{O}$ and δD values for quartz, feldspars, micas and tourmaline from eight LCT pegmatites, and the country rocks immediately adjacent to them, in San Diego County, California. They identified two groups (A and B) of pegmatites, with $\delta^{18}\text{O}_{\text{qz}} = \pm 8.5 - 10.5 \text{ ‰}$, and highly variable H-isotope ratios of $\delta\text{D}_{\text{ms}} = -35 - -100 \text{ ‰}$. The country rock suite in this study consisted of noritic, dioritic, and tonalitic rocks, and Taylor *et al.* (1979) concluded that the pegmatites tended to show a Group A or B affinity depending on the lithology into which they had been emplaced i.e. pegmatites emplaced into norites and gabbros showed Group A O-isotope characteristics, which those emplaced into tonalities showed Group B O-isotope characteristics.

More recent work by Jung *et al.* (2000, 2003) produced whole-rock O-isotope ratios ranging between 11.5 ‰ and 15.5 ‰ for NYF pegmatites (SLGs) sampled in the Khan River valley in the vicinity of the Valencia area. The study did not include any H-isotope data. The $\delta^{18}\text{O}$ values metapelitic and migmatitic country rocks in the area typically range from 11.6 - 13.0 ‰. Similar to the conclusions drawn by Taylor *et al.* (1979), Jung *et al.* (2000, 2003) concluded that the O-isotope characteristics of the NYF pegmatites (SLGs) were affected by those of the country rocks into which they had been emplaced.

While the $\delta^{18}\text{O}$ and δD values measured in silicates and whole-rocks samples from mineralised pegmatites of this study are significantly higher than those of isotopically "normal" granites, which typically range from $\delta^{18}\text{O} = 6 - 10 \text{ ‰}$ and $\delta\text{D} = -40 - -85 \text{ ‰}$ (Taylor, 1978; Sharp, 2007), they are in accordance with data obtained for Pan-African Namibian granites (Jung *et al.*, 2000; 2003; Figures 7.5 and 7.6).

In terms of the internal evolution of the pegmatites, the $\delta^{18}\text{O}$ values of quartz from the Wall zones of zoned pegmatites differ from those obtained from the massive quartz Core zones of those pegmatites by 0.5 - 1.0 ‰ (refer to Table 6.1). This indicates that the high $\delta^{18}\text{O}$ ratios of the pegmatites are not restricted to a narrow zone of isotopic exchange between the contact of the pegmatites with their high $\delta^{18}\text{O}$ metasedimentary lithologies (e.g. Shieh and Taylor, 1969), and also suggests that processes of differentiation did not have an effect on the O-isotope ratios of the zoned pegmatites. For mineral pairs where $1000\ln\alpha_{\text{qz-fs}} > 1$, calculated temperatures of crystallisation range from 396 to 657 °C (mean = 541 °C).

These temperatures are very similar to those obtained by Taylor *et al.* (1979), which range from 525 - 625 °C in miarolitic LCT pegmatites. They are also in accordance with the results of O-isotope geothermometry conducted by Walker *et al.* (1986) on the Tin Mountain pegmatite in South Dakota (USA), which yielded temperatures, although variable, ranging from 550 - 650 °C. In more recent study of NYF pegmatites from Evje-lveland in Norway, Müller *et al.* (2013) calculated crystallisation temperatures of $\sim 612 \text{ °C}$. Thus the temperatures of crystallisation for the Namibian pegmatites under investigation are in agreement with, if not slightly higher than (Nabalek *et al.*, 2010), temperatures expected for pegmatite magmas.

A number of possibilities exist which could account for the O-isotope systematics of the pegmatites under investigation. The first of these is low-temperature hydrothermal circulation which not only would have elevated the $\delta^{18}\text{O}$ values of the pegmatites, but would also have caused disequilibrium between certain of the quartz-feldspar pairs

analysed (e.g. samples IHEL1-1 qz and IHELf fs from the Helicon LCT pegmatite; refer to Table 7.1) through the alteration of the feldspars, producing negative $\Delta_{\text{qz-fs}}$ values. Typically, however, $\Delta_{\text{qz-fs}}$ values fall between 1 and 2 ‰ (ranging from -1.5 ‰ - +1.9 ‰; mean $\Delta_{\text{qz-fs}} = 1.0$ ‰), with the majority of mineral pairs falling within the range of 1.0 - 1.5 ‰, which is consistent with equilibrium in a closed system (e.g. Shieh, 1985; Harris *et al.*, 1997; Jung *et al.*, 2000; Harris and Ashwal, 2002; refer to Figure 7.2), thus only samples that plot outside of this range may have been affected by fluid-rock interaction.

In addition to this, all of the pegmatites show a positive correlation between their Alumina Saturation Indices (A.S.I.; refer to Chapter 6, Table 6.1) and O-isotope ratios (Figure 7.5). The most pronounced of these is observed in the Group A pegmatites, whereas the relationship between the two variables in the Group B pegmatites is somewhat random. According to Jung *et al.* (2000) the positive correlation between pegmatites and their respective A.S.I. values, as illustrated in Figure 7.5, is indicative of primary $\delta^{18}\text{O}$ values. As such, this negates alteration and isotopic exchange with high $\delta^{18}\text{O}$ country rocks as the cause of elevated $\delta^{18}\text{O}$ values. Thus it is most likely that the pegmatites and Damaran granites (e.g. Jung *et al.*, 2000; 2003) were derived from the partial melting or assimilation of high $\delta^{18}\text{O}$ crustal material (Taylor, 1978; Jung *et al.*, 2000).

Figure 7.6 shows that the high $\delta^{18}\text{O}$ values of silicate and whole-rock samples, with the exception of one feldspar sample (2RUBo: $\delta^{18}\text{O} = 9.9$ ‰) place all of the pegmatites within the O-isotope range of S-type granites, thus the second possibility that could account for the elevated O-isotope ratios of the pegmatites is that they may be a result of the source material of the pegmatites. The strong bimodal distribution of $\delta^{18}\text{O}$ in quartz, and to some degree in feldspar (refer to Figure 7.2), suggests however, that while all of the pegmatites share a common S-type signature, Group A and Group B pegmatites could not have shared a common source, or that there were different processes at work at the source of the two groups of pegmatites. Furthermore, the isotopic disequilibrium between Group A pegmatites and their country rocks, and isotopic equilibrium between

Group B pegmatites and their country rocks show that there were differences in fluids and fluid-rock interaction at the time of emplacement of the two subsets of pegmatite.

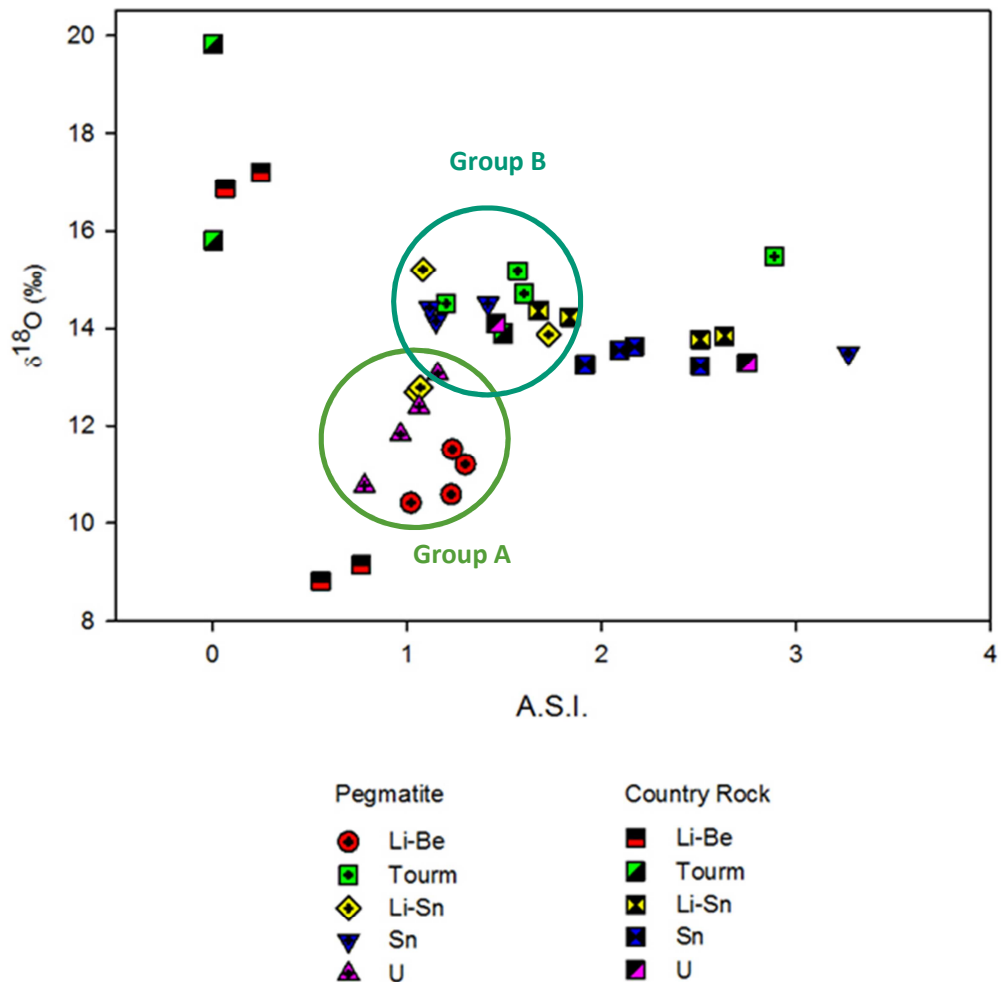


Figure 7.5: Whole-rock $\delta^{18}\text{O}$ values vs. Alumina Saturation Index (A.S.I.) of pegmatites and their country rocks.

Group A pegmatites do not show isotopic equilibrium with their granodioritic, marble, and metapelitic country rocks (refer to Figure 7.2). Although their O-isotope ratios indicate that they formed from the anatexis of crustal material, the fact that these ratios are not elevated much above the $\delta^{18}\text{O}$ values of I-type granitic rocks (Taylor, 1978), suggests that

there is an I-type component to their source, i.e. their source rock may be an S-type metaigneous rock, such as Abbabis basement material.

Longridge (2012) explored the possibility, using Hf-isotope data, that the NYF pegmatites (SLGs) were sourced from the recycling of Mesoproterozoic (Kibaran-aged) rocks of the Abbabis Complex from the Congo Craton, however the isotopic data contradicted this hypothesis. As an alternative, it was suggested that the late Damaran granitoids, including the NYF pegmatites, were rather sourced from Kalahari Craton crustal material, a model initially proposed by Barnes and Sawyer (1980). Similar data have been collected from various granitoids, including earlier Goas Suite granodiorites and Salem granites, which also indicates their derivation from the partial melting of Eburnian and/or Kibaran crustal material (Milani, pers. comm., 2013).

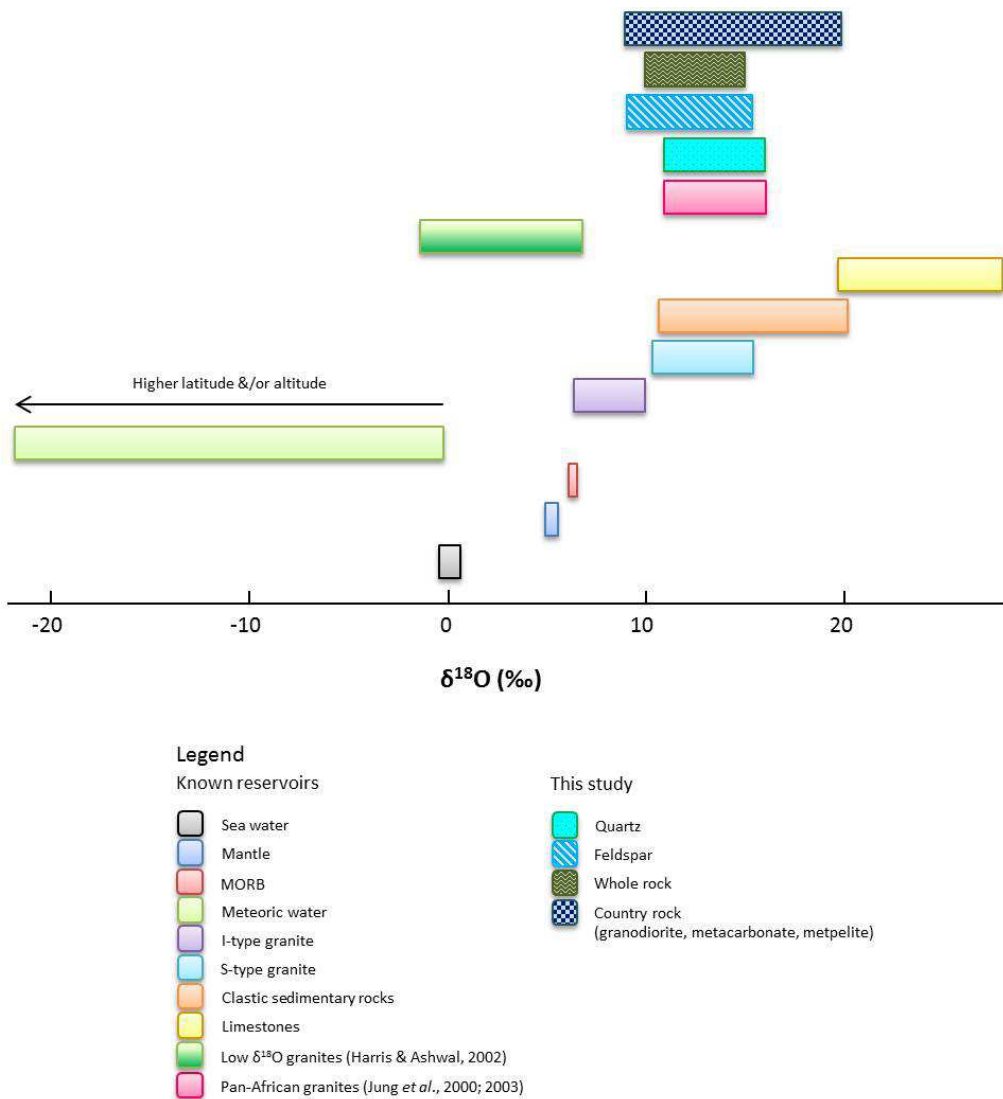


Figure 7.6: $\delta^{18}\text{O}$ ranges for known geological reservoirs, including I- and S-type granites, clastic sedimentary rocks, carbonates, low $\delta^{18}\text{O}$ granites (e.g. Harris and Ashwal, 2002), and Pan-African granites from the Damara Belt (Jung *et al.*, 2000; 2003). Samples from this study fall within the range of higher $\delta^{18}\text{O}$ I-type granites, and S-type granites (modified after Hoefs, 2009).

Therefore it is possible that the Group A pegmatites were derived from the partial melting and recycling of juvenile Mesoproterozoic to Palaeoproterozoic crust on the Kalahari Craton, which was subducted below the Congo Craton during the Pan-African Orogeny (Longridge, 2012). One NYF pegmatite sample, however (VALG02, Type C_t pegmatite from Valencia) has a higher $\delta^{18}\text{O}$ value ($\delta^{18}\text{O} = 14.8 \text{ ‰}$) for quartz than those measured from

the NYF pegmatites. This would imply that not all of the NYF pegmatites were sourced from the same crustal material, or may reflect heterogeneity in the source. Further stable isotope studies would need to be conducted in order to resolve this however.

Group B pegmatites are more clearly S-type in character. The high $\delta^{18}\text{O}$ values recorded in these pegmatites necessitates their derivation from high $\delta^{18}\text{O}$ metapelites/carbonates, or at least isotopic exchange with, or equilibration with fluids from, high $\delta^{18}\text{O}$ metapelites/carbonates (Taylor, 1978, 1980; Macey and Harris, 2006).

Figure 7.2 also shows that country rock samples taken near the contacts of these pegmatites, although possessing slightly higher $\delta^{18}\text{O}$ values, have similar $\delta^{18}\text{O}$ values to the pegmatites samples. This, in conjunction with field observation and the absence of any obvious relation to a potential source pluton in the area, would suggest that these Group B pegmatites i.e. Sn-, Li-Sn, and miarolitic gem-bearing pegmatites, were derived from the metapelites into which they intruded. In the case of pegmatites emplaced into carbonates because of the high reactivity of the country rocks, it is possible that the pegmatite melt may have equilibrated with the surrounding country rock, some of which may have been incorporated into the pegmatite magma, thus elevating the O-isotope ratios of these pegmatites significantly (Taylor, 1978, 1980; Macey and Harris, 2006).

δD values for isotopically "normal" granites typically fall within the narrow range of $\delta\text{D} = -40$ to -85 ‰ (Taylor, 1978); Figure 7.7 illustrates how δD values for micas obtained in this study relate to the values of known geological reservoirs. The values measured in this study are, however, higher than the ranges typical of whole-rock pegmatite samples, which range from $\delta\text{D} = -35$ to -60 ‰ (Taylor, 1978).

O- and H-isotope data show that the $\delta^{18}\text{O}$ values of Pan-African pegmatites and pegmatitic SLGs from the Damara Belt are at least 2 ‰ higher in $\delta^{18}\text{O}$ than primary magmatic

waters¹, falling within, and slightly adjacent to, the field of Cornubian magmatic water² (Sheppard, 1977a), with some data points lying at various positions outside of this field (Figure 7.8). It is not uncommon for $\delta^{18}\text{O}$ values of igneous rocks to be high enough to push measured water compositions out of a recognised isotopic-composition field; indeed this is the basis for the Cornubian magmatic water field of Sheppard (1977a), and other such cases have been documented by earlier workers, particularly in calc-alkaline and volcanic provinces in Italy e.g. Taylor and Turi (1976), Turi and Taylor (1976) and Lombardi and Sheppard (1977).

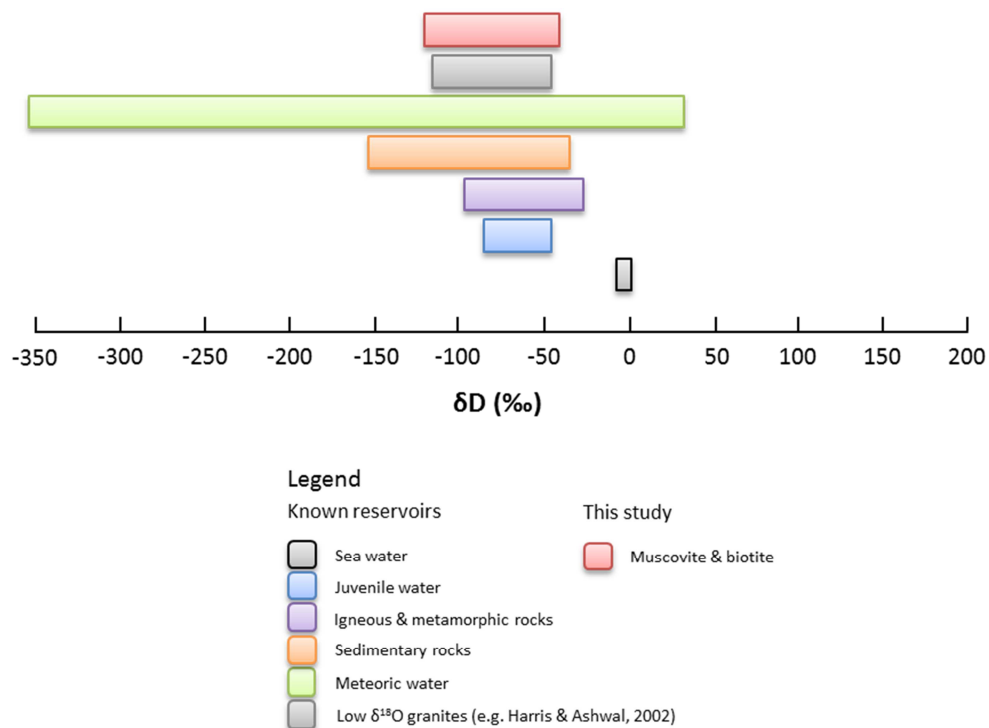


Figure 7.7: δD ranges for known geological reservoirs, including sea water, juvenile water, igneous and metamorphic rocks, low $\delta^{18}\text{O}$ granites, and meteoric water. Juvenile water refers to water derived from the degassing of the mantle, remnants of which may be preserved in OH-bearing minerals derived from the mantle. This type of water is assumed not to have been affected by surface/atmospheric processes. δD values for Pan-African granites other than from this study are not available (modified after Taylor, 1978, Sheppard, 1986, and Hoefs, 2009).

¹ Primary magmatic waters refer to waters, measured from igneous rocks, that have equilibrated with a magma regardless of their origin (Sheppard, 1986).

² Cornubian magmatic water was defined by Sheppard (1977a) and refers to the isotopic composition of magmatic waters from the high $\delta^{18}\text{O}$ Cornubian batholith in SW England.

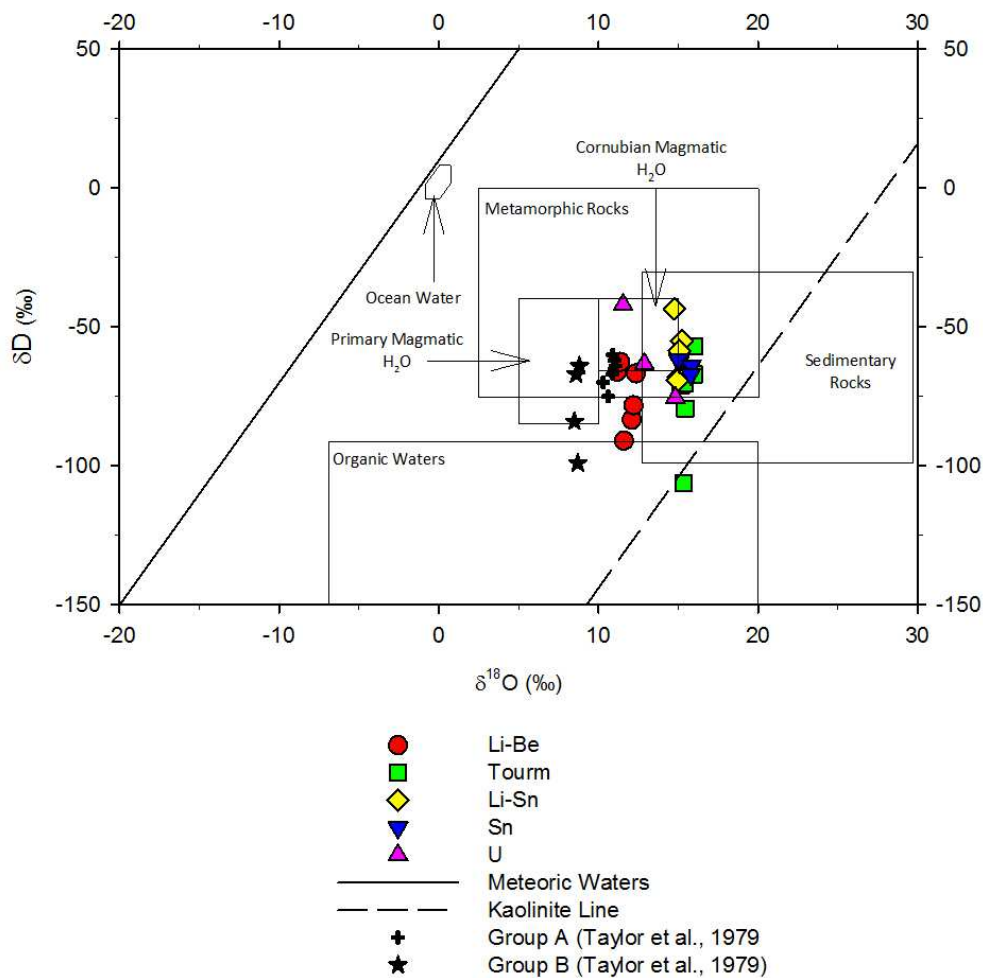


Figure 7.8: Plot of $\delta^{18}\text{O}$ and δD values obtained from silicate minerals in mineralised pegmatites from Namibia, and from the study of Taylor *et al.*, (1979) outlining the ranges of ocean water, metamorphic water, sedimentary rocks, organic water, primary magmatic water, and Cornubian magmatic water, in relation to the meteoric water line, and Savin and Epstein's (1970) kaolinite line of weathering (modified after Taylor, 1978).

The data for all of the pegmatites analysed for this study are also higher than the O- and H-isotope ratios of selected Group A and Group B LCT pegmatites from the study of Taylor *et al.* (1979), which both plot within the fields for primary and Cornubian magmatic waters. Given that the pegmatites from this study which have the highest $\delta^{18}\text{O}$ values have intruded into high $\delta^{18}\text{O}$ metapelites and carbonates, it is not unusual that their O-

isotope ratios fall outside of the recognised field for primary magmatic water. The pegmatites, particularly those with higher $\delta^{18}\text{O}$ values, also plot within the field of metamorphic water, suggesting the possibility that late-stage pegmatite magmas may have mixed with metamorphic fluids at some stage during the formation of the pegmatites.

With respect to δD values, while some of them are lower than those that define Sheppard's (1977a) Cornubian magmatic water field, they do fall within the accepted range for primary magmatic waters, with the exception of one muscovite sample from the Usakos pegmatite (USK23; $\delta\text{D} = -106\text{‰}$) and one from the Helicon pegmatite (IHELg; $\delta\text{D} = -90\text{‰}$) which plot at lower δD values, indicating that they may have been subjected to weathering or to degassing. Degassing i.e. the loss of H_2O leading to the crystallisation of hydrous minerals with ever-decreasing δD values, would also result in a decline in the water contents of these hydrous minerals.

This trend is observed in Figure 7.9 which shows δD in relation to the water content of muscovite and biotite. While the decrease in water content is strongly apparent in all of the micas analysed, the expected decrease in δD is less so (with the exception of the miarolitic gem-bearing pegmatites, green squares). This suggests that degassing may not be responsible for the decrease in water content, and that it may rather be a result of weathering.

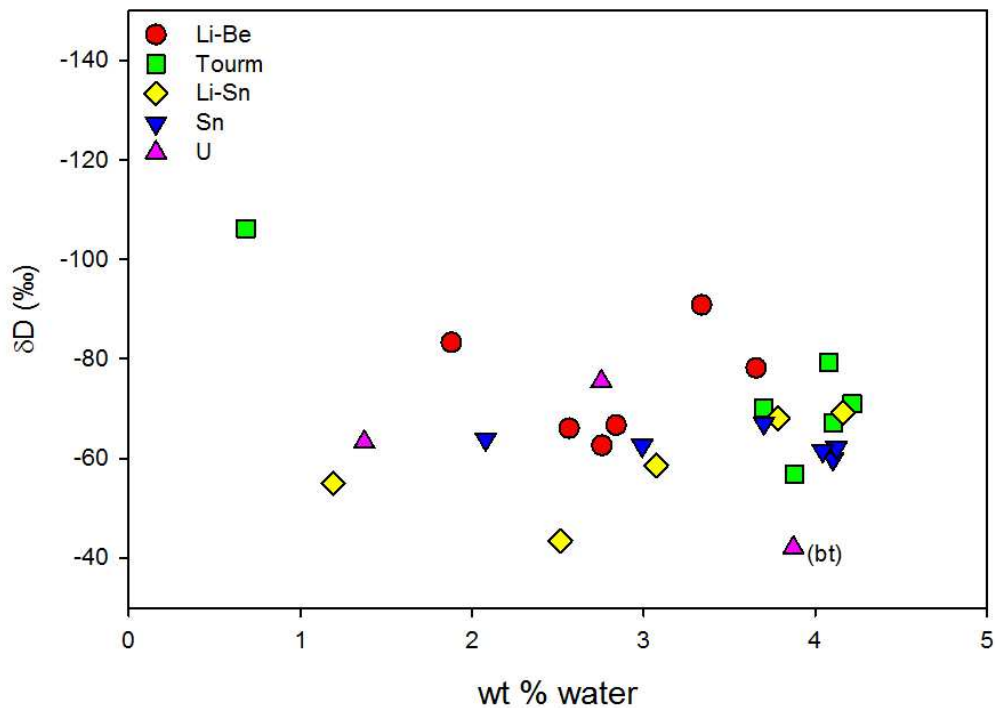


Figure 7.9: Plot of δD values vs. the water content of micas. Note that different symbol colours refer to different deposit types. All values are for muscovite, except for one biotite sample (bt).

7.6 Summary

The $\delta^{18}O$ values retained in quartz and feldspar from mineralised pegmatites in Namibia are higher than the values of O-isotope ratios for mineral separates obtained in the few studies published on the topic (e.g. Taylor *et al.*, 1979). They do, however correspond with the values obtained for Pan-African granites, including some U-bearing NYF pegmatites (SLGs) in Namibia, which were obtained by Jung *et al.* (2000; 2003).

Interaction with a hydrothermal fluid is unlikely to be responsible for the slightly elevated $\delta^{18}O$ values of the pegmatites, since mineral pairs show equilibrium at pegmatite crystallisation temperatures, which, based on O-isotope geothermometry, average 541 °C

for the pegmatites. It is more likely that the O-isotope characteristics of the Namibian pegmatites were inherited from their source lithologies, a hypothesis supported by the fact that all of the pegmatites under investigation have $\delta^{18}\text{O}$ values characteristic of S-type granites.

O-isotope ratios in quartz, and to some degree in feldspar, show a bimodal distribution, indicating that the pegmatites under investigation fall into two distinct categories, Group A and Group B, based on their O-isotope characteristics.

Group A pegmatites include Li-Be-bearing LCT pegmatites and U-bearing NYF pegmatites (Type C SLGs). Their $\delta^{18}\text{O}$ values range from 11.2 - 12.9 ‰, and these pegmatites are not in isotopic equilibrium with their country rocks. This would suggest that Group A pegmatites were not derived from their host rocks lithologies, and that the country rocks have not had an effect on the $\delta^{18}\text{O}$ values of these pegmatites through isotopic exchange. Rather it is likely that these pegmatites were derived from the partial melting of non-pelitic crustal material, such as crustal material from the subducted Kalahari Craton, from which granitic melt may have been generated during the Pan-African Damara Orogeny.

Group B pegmatites include Sn-, Li-Sn, and gem tourmaline-bearing LCT pegmatites. They have higher $\delta^{18}\text{O}$ values ($\delta^{18}\text{O} = 15.5 - 17.0$ ‰) than Group A pegmatites, and thus have a more obvious S-type affinity. All Group A pegmatites show isotopic equilibrium with the metapelites and metacarbonates into which they were emplaced. They are likely to have been derived from the partial melting of the metapelites into which they intruded. The highest $\delta^{18}\text{O}$ values are observed in pegmatites which have intruded into Damaran metacarbonates. While the partial melting of the metacarbonates may not be the source of these pegmatites, it is likely that magmatic fluids from the pegmatite system equilibrated with the carbonate country rocks, and the high reactivity of the carbonates would have resulted in much higher $\delta^{18}\text{O}$ values for these pegmatites.

The $\delta^{18}\text{O}$ values are too high for the pegmatite waters to fall within the recognised field of primary magmatic water, and some plot within the field of metamorphic water. This would suggest that the fluids in late stage pegmatite magmas may have mixed with metamorphic waters. δD values generally fall within the range of primary magmatic waters, although some are lower than the expected values for this field. While degassing might be responsible for this trend, no clearly systematic decrease in δD with decreasing water content is observed, therefore low δD values in the data set are likely to be the result of weathering.

CHAPTER 8

DISCUSSION AND CONCLUSIONS

8.1 Introduction

The aim of this thesis has been to gain an understanding of the relationship between the different types of Pan-African-aged pegmatites at different geographic locations, and therefore stratigraphic levels in the Damara Belt. This was done by investigating what role fluids may have played in mineralisation in the pegmatites i.e. whether or not the differences observed in mineralisation are a result of fluid geochemistry and activity, or whether the differences observed are in fact the product of geochemical differences at the sources of the pegmatites.

Table 8.1 summarises the geochemical and emplacement characteristics of the Namibian pegmatites and their country rocks. This summary shows that the geochemical characteristics and temperatures of the pegmatites are independent of the regional metamorphic grade, with the exception of the Karlowa pegmatites whose crystallisation temperatures are the same as regional peak metamorphic temperatures.

8.2 Crystallisation temperatures of the Damaran pegmatites

One common characteristic of pegmatites is their low crystallisation temperatures, which typically ranges from ~ 350 - 450 °C, 200 - 300 °C below the liquidus temperatures for their felsic magmatic compositions (London, 2008; Nabalek *et al.*, 2010).

O-isotope geothermometry using quartz-feldspar pairs, and Ti-in-quartz thermometry have proven to be useful and consistent geothermometers, which appear to provide reliable temperature data for the Damaran pegmatites.

Table 8.1: Summary of geochemical and structural characteristics of mineralised Namibian pegmatites. Metamorphic conditions cited from Puhan (1983), Steven (1993), Goscombe *et al.* (2004), Kisters *et al.* (2004), and Longridge (2012).

Locality	Pegmatite Family	Pegmatite Class	Mineralisation	Minor elements	Aluminosity	Temperature	Metamorphic Environment	Relation to Granite	Structural Features
Rubicon	LCT	Rare-element	Li-Be	Li, Rb, Cs, Nb > Ta	A.S.I. > 1	~ 430 °C	Lower amphibolite facies (560 - 650 °C at 3 ± 1 kbar)	None	Cross-cutting
Helicon	LCT	Rare-element	Li-Be	Li, Rb, Cs, Nb > Ta	A.S.I. > 1	~ 420 °C	Lower amphibolite facies (560 - 650 °C at 3 ± 1 kbar)	None	Cross-cutting
Uis	LCT	Rare-element	Sn, W, Ta	Li, Rb, Cs, Ta > Nb, Sn, W	A.S.I. > 1	~ 440 °C	Upper greenschist facies (540 - 570 °C at 2 - 3 kbar)	None	Cross-cutting
Karlowa	LCT	Rare-element	Sn, W, Ta, Li	Li, Rb, Sr, Cs, Ta > Nb, Sn, W	A.S.I. > 1	~ 530 °C	Upper greenschist facies (540 - 570 °C at 2 - 3 kbar)	None	Cross-cutting
Usakos	LCT	Miarolitic	Tourmaline	Li, Ti, Rb, Cs, Ta > Nb, W	A.S.I. > 1	~ 420 °C	Lower amphibolite facies (560 - 650 °C at 3 ± 1 kbar)	None	Cross-cutting
Omapyu	LCT	Miarolitic	Tourmaline	Li, Ti, Rb, Cs, Ta > Nb, W	A.S.I. > 1	~ 575 °C	Lower amphibolite facies (560 - 650 °C at 3 ± 1 kbar)	None	Cross-cutting
Valencia	NYF	Abyssal	U	Ti, V, Rb, Y, Nb, Cs, Ba, Th, U	A.S.I. > 1 & A.S.I. < 1	~ 655 °C	Granulite facies (750 - 850 °C at 5.0-6.0 kbar)	None	Cross-cutting

The geothermometers indicate that the Damaran pegmatites show two distinct trends in terms of their crystallisation temperatures. Firstly, there is little variation in the crystallisation temperatures observed between the various (Li-Be- vs. Li-Sn- vs. Sn- vs. gem tourmaline bearing) LCT pegmatites (see Table 8.1), and their temperatures are well constrained, ranging from ~430 - 575 °C. The crystallisation temperatures calculated for the NYF pegmatites are also well-constrained, averaging 655 °C.

The second trend that the crystallisation temperatures show is that the LCT pegmatites appear to crystallise at significantly, and consistently lower temperatures than the NYF pegmatites. The same trend is observed in pegmatites from other parts of the world, with studies on LCT pegmatites yielding temperatures of 525 - 625 °C (Taylor *et al.*, 1979), and those on NYF pegmatites yielding temperatures around 600 °C (Müller *et al.*, 2003).

Fluid inclusions do not appear to be useful indicators of pegmatite crystallisation temperatures, with temperatures from the earliest saline aqueo-carbonic populations giving temperatures consistently 100 - 120 °C less than those calculated using the O-isotope and Ti-in-quartz thermometers. Furthermore, the determination of fluid inclusion trapping temperatures in pegmatites is fraught with complications which result from the hydrous nature of pegmatites, which have a tendency to “stew in their own juice,” a phrase which Richard Jahns is known to have used in several descriptions of pegmatite formation. This action has caused the earliest fluid inclusion populations and textures to be destroyed, therefore the initial crystallisation conditions of the pegmatites cannot be determined using fluid inclusion thermometry.

8.3 Late-stage evolution of the Damaran pegmatites: Implications for mineralisation

Fluid inclusion studies of Damaran pegmatites have provided evidence for the exsolution of a saline aqueo-carbonic fluid from the pegmatite melt during the late stages of pegmatite crystallisation, and have preserved various stages in the evolution

of this fluid. Recent studies e.g. Gagnon *et al.* (2004), Borisova *et al.* (2012) and Thomas *et al.* (2009, 2011) have shown that magma geochemistry and reactivity may play a greater role in the mineralisation of pegmatites than fluid activity. However, this does not rule out the contribution of fluids to mineralisation in pegmatites containing, for example, appreciable amounts of Sn, which is incorporated into hydroxyl-Cl complexes in hypersaline fluids and crystallises at the very latest stages of pegmatite formation (Kovalenko *et al.*, 1986; Alfonso and Melgarejo, 2008).

The Damaran pegmatites show that both magma and fluid geochemistry are responsible for mineralisation in these bodies. In the LCT Li-Be-bearing pegmatites, magmatic mineralisation occurs as massive lepidolite in the low- and high-grade Lepidolite Zones, giant petalite crystals in the Petalite Zone, and large beryl crystals in the Beryl Zone. The fact that the minerals occur in discreet zones defined by their presence is also indicative that their deposition is the result of pegmatite crystallisation. Thus it is most likely that magmatic processes are responsible for Li and Be mineralisation in the Rubicon and Helicon LCT pegmatites.

In the U-bearing NYF pegmatites (SLGs) from the Valencia area, mineralisation occurs in primary magmatic minerals e.g. uraninite, as well as in secondary phases such as B-uranophane (Freemantle, 2012). Thus there is evidence both for mineralisation related to magmatic processes, as well as a secondary enrichment resulting from fluid flow along jointing/fractures within the pegmatites (SLGs). It remains unclear exactly which generation of fluid inclusion was responsible for the secondary enrichment, however at temperatures ranging from 200 - 300 °C, chloride and fluoride complexes of U^{6+} and U^{4+} are important for the transport of metals under both oxidising and reducing conditions (Skirrow *et al.*, 2009), thus it is possible that the saline aqueo-carbonic Type 1 or saline aqueous Type 5 fluid inclusions (refer to Chapter 5) may be responsible for this process in the NYF pegmatites (SLGs).

A similar occurrence of mineralisation is observed in the Uis Sn-bearing LCT pegmatites, where cassiterite mineralisation does occur sporadically throughout the pegmatite bodies as a magmatic mineral, however the greatest proportion of

mineralisation is found in greisenised patches, indicating a relationship between greisenisation i.e. fluid activity, and mineralisation. Furthermore, the presence of metals such as Cu and Zn in earlier pseudosecondary inclusions in these pegmatites indicates that these late-stage fluids are also responsible for the mineralisation of rare accessory phases, for example Zn- and Cu-sulphides in these pegmatites.

Similarly, the Li-Sn-bearing LCT pegmatites from the Karlowa swarm are mineralised with both Li-phases such as spodumene and the Sn-phase, cassiterite. Like petalite and lepidolite in the Li-Be-pegmatites, spodumene in the Li-Sn-bearing pegmatites is a magmatic phase which would have crystallised during the fractional crystallisation of the pegmatites. While cassiterite also occurs sporadically as a primary phase, Sn mineralisation occurs predominantly in greisenised patches, similar to the occurrences observed at Uis. This would suggest that the initial melt contained sufficient Li and Sn to facilitate Li-aluminosilicate and cassiterite crystallisation from the magma, however most of the Sn partitioned in the exsolved fluid from which cassiterite later crystallised in greisens.

Lastly, in the gem-tourmaline-bearing LCT pegmatites, mineralisation occurs in miarolitic cavities, the typical style of gem mineralisation in any gem-bearing pegmatite (Simmons, 2007; Simmons *et al.*, 2012; London, 2008). The formation of pockets is well-documented (e.g. Simmons *et al.*, 2012); miarolitic cavities or pockets develop in shallow-level pegmatites in which the saturation of volatiles is achieved at the latest stages of crystallisation, and high quality gem minerals are able to crystallise in a fluid-rich space conducive to their growth (Simmons, 2007; Simmons *et al.*, 2012; London, 2008).

The Namibian pegmatites thus illustrate that both magmatic processes and the exsolution of fluids from the magma during the late stages of crystallisation play an important role in the concentration of minerals to economic levels in these deposits. Since the compositional characteristics of the fluids measured do not differ significantly across the different type of pegmatites they cannot solely be responsible for the differences in mineralisation that are observed at different geographic

locations, and therefore stratigraphic levels in the Damara Belt. As such, alternative causes for these differences, for example, different source lithologies, need to be explored.

8.4 Potential sources of Damaran pegmatite magmas

A number of possibilities exist that could account for the geochemical differences, and differing types of mineralisation observed in the different pegmatites of the Damara Belt. Many workers have shown that there is a relationship between pegmatites in a given swarm/field and a source pluton; the pegmatites become more fractionated and geochemically complex with distance from a source pluton (see reviews in London, 2008). In the absence of measurable field relationships, however, regional zoning on an orogen-wide scale cannot easily be proven to be the cause of the spatial distribution of mineralisation observed in the Namibian pegmatites as there is, at present, no way to test the hypothesis.

Other workers (e.g. Deniel *et al.*, 1987) have suggested that the geographic/stratigraphic variations observed in, or between, pegmatite swarms may represent magma pulses from a deep-seated magma, or that they may rather be discreet batches of melt derived from different sources (Jung *et al.*, 2000; Freemantle, 2012). Given the geochemical and isotopic characteristics of the pegmatites under investigation, it would seem plausible that the source material, or processes at the source of the pegmatite melts, may have been responsible for their elemental and isotopic systematics.

With respect to the pegmatites studied, all, with the exception of two NYF samples from the Valencia area, are peraluminous. This geochemical variation in the NYF pegmatites is corroborated by recent work conducted by Freemantle (2012), who studied the mineralogical and geochemical variations between different SLG types (A - F) from different locations within the Central Zone, and concluded that Type C SLGs from the Valencia, such as those sampled for this study, are metaluminous to peraluminous.

The peraluminous nature of the LCT and some of the NYF pegmatites indicates that they must have been derived from the partial melting of crustal material, such as metapelites (Chappell and White, 1974; McDermott *et al.*, 1996; Chappell *et al.*, 2012). However, the metaluminous nature of some of the NYF pegmatites would indicate that they do not share a common/similar source with the rest of the pegmatites comprising the sample suite of this study (Chappell *et al.*, 2012).

In addition to the variations observed in the aluminium saturation of all of the studied pegmatites, the O-isotope ratios of quartz and feldspars from the pegmatites give some insight into potential sources for the pegmatite melts. All are higher than 10 ‰, suggesting that they all have an S-type affinity. Some models for the development of the S-type characteristic in highly felsic rocks invoke fractionation as the dominant process responsible for the elemental variations observed in these rocks (e.g. Phillips *et al.*, 1981; Miller and Mittlefehldt, 1982; Mittlefehldt & Miller, 1983). However, in the absence of any obvious relation to a potential source pluton, it would appear that the geochemical characteristics e.g. low CaO and Na₂O and high large ion lithophile element contents, in addition to the high O-isotope ratios of the pegmatites under investigation are the result of the composition of their source rocks, which are likely to have been a biotite-bearing metapelitic or garnet-bearing metaigneous in nature (London and Evensen, 2002; McDermott *et al.*, 1996; Jung *et al.*, 1998; 1999; 2003).

It is commonly accepted that LCT pegmatites are derived from the anatexis of crustal sources (Černý, 1991a) via the hydrous partial melting of the subducting slab during orogenesis (Martin and De Vito, 2005), causing O-isotope ratios to exceed 10 ‰. NYF pegmatites, however, are generally expected to be subaluminous to metaluminous, possessing O-isotope ratios in the region of 8 ‰; as such, mantle or juvenile undepleted crustal sources are typically invoked as their sources (Černý, 1991a). Thus, while the LCT pegmatites of the sample suite behave geochemically in an unsurprising manner, the geochemical behaviour of the NYF pegmatites remains somewhat enigmatic, and suggests that processes at the source, and the source material itself, have influenced the geochemical characteristics of the NYF pegmatites.

High $\delta^{18}\text{O}$ NYF pegmatites, although rare, have been documented. De Vito *et al.* (2006) obtained $\delta^{18}\text{O}$ values of ~ 15 ‰ from amazonitic potassic feldspar from the Anjanabonoina NYF pegmatite in central Madagascar. Similar O-isotope ratios for feldspars and tourmalines have been measured in other Madagascan pegmatites (Martin and De Vito, 2005), reinforcing the hypothesis that NYF pegmatites can indeed be anatectic in origin, contrary to the commonly held belief that they are customarily related to gabbro-granite sequences.

With respect to the Namibian pegmatites, the bimodal distribution of $\delta^{18}\text{O}$ values also indicates that there are two subsets of pegmatites which could thus potentially have been derived from different crustal sources. The pegmatites with lower O-isotope ratios ($\delta^{18}\text{O} = 10 - 12$ ‰) are the U-bearing NYF pegmatites and the Li-Be-bearing LCT pegmatites. While Li, Cs, Rb, Be and Ba would typically have been derived from muscovite and/or clay minerals, and Ta and Nb from ilmenite, in a metapelitic source, the presence of Be as beryl in the LCT pegmatites, and absence thereof in the NYF pegmatites provides a clue as to what their source rocks may alternatively have been (Martin and De Vito, 2005; London, 2008).

Beryllium can be highly enriched or depleted in an S-type magma depending on whether melting occurred within the cordierite (\pm andalusite) stability field or within the garnet + sillimanite/kyanite stability field (London and Evensen, 2002; Evensen and London, 2003). Cordierite in the restite will cause Be to remain in the restite due to its high compatibility with the mineral (Evensen and London, 2003), therefore Be-bearing pegmatites should not originate from a cordierite-bearing source. At higher pressures/temperatures, however, where cordierite is unstable, Be will preferentially partition into muscovite, the breakdown of which would liberate Be into the melt (London and Evensen, 2002), thus it is plausible that the Li-Be-bearing LCT pegmatites were derived from a garnet-bearing S-type source (imparting elements such as P and B to the melt to facilitate the crystallisation of phosphates and tourmaline) such as a metaigneous rock or even basement material.

A complication arises, however, from the fact that the NYF pegmatites, while possessing the geochemical hallmarks e.g. high Ti, U, Th, REE and F, of their pegmatite family (see reviews in Černý *et al.*, 2012), have an S-type affinity (metaluminous to peraluminous, and $\delta^{18}\text{O} > 10 \text{ ‰}$) as opposed to an A-type affinity as has been suggested should be the case (Černý, 1991a; Černý and Ercit, 2005). Furthermore, they contain phosphates such as monazite and the C-type SLGs contain abundant tourmaline, suggesting again that they contain a metapelitic component. Haack *et al.* (1980; 1984), based on Rb/Sr and $\delta^{18}\text{O}$ data, invoked melting of the Damaran intra-crustal sedimentary lithologies as a source for the U-enriched melts of the southern Central Zone, however Nex *et al.* (2001b) pointed out that if the pegmatites cross-cut all the lithologies of the southern Central Zone it is impossible for them to have been derived from the metasediments. The origin of NYF pegmatites remains obscure, however O-isotope data from this study suggest that it is possible that the pegmatites were derived then from an S-type metagneous source, such as quartzo-feldspathic pre-Damaran crustal material from the subducted Kalahari Craton (Longridge, 2012).

Although pertaining to a different suite of rocks, this interpretation of the potential sources of the Li-Be-bearing and U-bearing pegmatites corresponds with recent unpublished Hf-isotope data on granodiorites, particularly of the Goas Suite in the CZ, obtained by Milani (pers. comm. 2013). The isotopic data suggest that these earlier Damaran granitoids were also generated by the recycling and mixing of older (the Eburnean, 2.2 - 1.8 Ga, component of which was probably the most active) crustal material, which itself had an S-type affinity. Thus it is plausible that later Damaran granitoids and pegmatites were derived from similar sources, which would also account for the isotopic disequilibrium that the Li-Be and U-bearing pegmatites studied show with their country rocks (refer to Chapter 7).

The Damaran pegmatites with higher $\delta^{18}\text{O}$ values ($\delta^{18}\text{O} = 14 - 16 \text{ ‰}$) are the LCT Sn-, Li-Sn, and mirolitic gem-tourmaline-bearing bodies. Their high O-isotope ratios indicate that they crystallised from S-type melts likely derived from the partial melting of mica-rich metapelitic rocks (McDermott *et al.*, 1996 Jung *et al.*, 1998, 1999, 2000, 2003; London, 2008). The presence of xenoliths within many of these pegmatites, as

well as the equilibrium observed between $\delta^{18}\text{O}$ of pegmatitic quartz and bulk country rock samples also points not only towards the incorporation of metapelitic crustal material into the pegmatite melts, but the derivation of these pegmatites from their biotite-rich metapelitic country rocks (with the exception of the miarolitic gem-tourmaline-bearing pegmatites, which were probably derived from metapelites, but emplaced in metacarbonates).

Micas in the metapelitic source rocks would act as a reservoir for elements such as Li, Rb, Cs, Be, and Ba while Ta would be sourced from the breakdown of ilmenite (London, 2008). The Li-Sn-, Sn-, and gem-tourmaline-bearing pegmatites, with higher O-isotope values, are conspicuously absent in beryllium mineralisation; this characteristic may be attributed to the retention of Be being in porphyroblastic cordierite (London and Evensen, 2002; Evensen and London, 2003; London, 2008), now pseudomorphic intergrowths of quartz-biotite as “knotten” in the schistose metapelitic country rocks.

Phosphorous and boron would also have been derived from the Damaran metapelites. In pegmatites where B was not incorporated in abundant tourmaline e.g. Uis and Karlowa Sn- and Li-Sn-bearing pegmatites, it would have been lost to the country rocks causing the precipitation, by metasomatism between the B-rich fluid and country rock, of tourmaline in the vicinity of the contacts, as has been observed in the Uis and Karlowa areas (Richards, 1986; Diehl, 1993; London, 2008).

Tin in these pegmatites could also have been derived from the source/country metapelites, which have been shown to contain appreciable amounts of Sn (Richards, 1986; Diehl, 1993).

8.5 Melt generation and magma transport

According to Jung *et al.* (1999), a granitic melt intruding into, and crystallising in, metapelitic units can be a source of both fluid and heat promoting the melting of surrounding country rocks; large-scale melting of amphibolite grade rocks, like those in the Central Zone, can be achieved providing these criteria are met. The temperatures required to achieve such melting are typically in excess of 750 °C (e.g. Jung *et al.* 1999). The temperature of pegmatitic melts is, however, typically much lower (450 - 550 °C; London, 2008; Nabalek *et al.*, 2010) than the solidus temperatures of “regular” granitic melts (~ 750 °C; Winter, 2001), therefore insufficient to act as the heat engine driving crustal anatexis.

Thus given the crystallisation temperatures obtained using Ti-in-quartz and O-isotope thermometry, which range from ~ 450 °C for the LCT pegmatites and ~ 650 °C for the NYF pegmatites, it would seem that pegmatite emplacement itself could not have been the only mechanism responsible for the partial melting of Damaran metapelites.

Aside from the low temperatures of the Namibian pegmatites, field observation has shown that none of them is surrounded by contact aureoles. This would indicate that the pegmatite magmas were the result of metamorphism rather than its cause (Chamberlain and Sonder, 1990; Longridge, 2012). Furthermore there is an absence of linear trends in major and trace elements between the pegmatites and their surrounding country rocks, a trend which would be expected in the instance of the separation of melt from restite, and the subsequent fractional crystallisation of that melt (Jung *et al.*, 1999).

According to Longridge (2012), however, peak metamorphic conditions in the Damara Belt, caused by crustal relaxation and orogenic collapse, reached up to 850 °C (Longridge, 2012), a temperature which would be high enough to facilitate the fluid-absent melting of biotite within the metapelitic and metagneous rocks of the Damara Belt. This process could therefore account for the voluminous anatexis in particularly the Central Zone of the Damara Belt. Based on this hypothesis, Longridge (2012)

proposed that the SLGs and pegmatites of the Central Zone were generated during, or immediately after, peak metamorphic conditions were attained (510 - 505 Ma), and were emplaced slightly after the thermal peak during the development of D₃ upright, NE-trending folds (510 - 490 Ma; Figure 8.1).

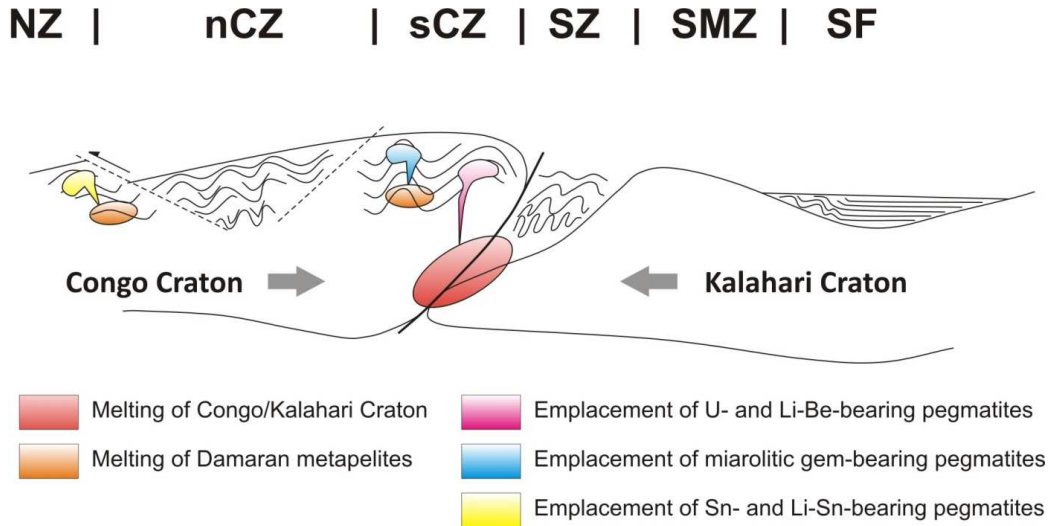


Figure 8.1: Tectonic model for sources of melt generation and emplacement of post-collisional (505 - 490 Ma) pegmatites in the Damara Belt (modified after Longridge, 2012).

While anatexis of the source lithologies of the pegmatite melts may have occurred at depth during peak metamorphism, the geochemical behaviour of the Damaran pegmatites indicates that it is unlikely the pegmatite magmas were retained in deep-seated magma chambers for a prolonged period before they were expelled into higher levels of the crust (Jung *et al.*, 1998). The abundance of H₂O, P, B, F in the melt would have reduced the viscosity of the pegmatite magmas, and, coupled with the temperature of the host rocks at the time of melt generation and emplacement, would have facilitated their rapid ascent through the crust, even at the undercooled temperatures typical of pegmatite magmas (Jung *et al.*, 1998; Nabalek *et al.*, 2010).

8.6 Discrepancies in the classification of LCT and NYF pegmatites

Currently the most popular classification scheme of pegmatites is that of Černý and Ercit (2005), which relates the different classes and subclasses of pegmatites to their depth of emplacement (see Chapter 2; Martin and De Vito, 2005).

While many advances have been made in pegmatology, especially in the fields of mineralogy, mineral geochemistry, and experimental petrology, there is a conspicuous absence of detailed work done on an important aspect in understanding pegmatite systems, that being “the interplay of tectonic setting and petrological processes, insofar as they affect patterns of crystallization in granitic pegmatites” (Martin, 2007).

8.6.1 Complications in relating pegmatite geochemistry to tectonic processes

It has been suggested that LCT pegmatites are the products of the progressive fractionation and ascent through the crust of a mass of magma generated at the base of the crust by the hydrous melting of the mantle wedge during subduction (Martin and Devito, 2005; Martin, 2007; Martin *et al.*, 2009). These magmas are metaluminous to peraluminous i.e. they exhibit crustal as well as mixed mantle-crustal signatures, and contain crustally derived enrichments in Li, P, and B.

In contrast, NYF pegmatites are proposed to form in extensional environments where the crust is underlain by anomalous mantle material which is actively degassing. Aqueous and carbonic fluids mobilise REE, alkali elements, U, Th, Ta, Nb, Ti and Zr and metasomatise the crust before the emplacement of an ocean island type basalt which enhances anatexis in the middle crust during its ascent through the crust (Martin and De Vito, 2005; Martin, 2007; Martin *et al.*, 2009). The resultant magmas are metaluminous to mildly peralkaline, and with progressive fractionation they crystallise to form NYF pegmatites (Martin and De Vito, 2005; Martin, 2007). Similar to their LCT counterparts, NYF pegmatites may be derived purely from a crustal source, or from the mixing of crustal and mantle derived material (see reviews in Martin *et al.*, 2009).

The Namibian pegmatites pose an interesting conundrum with regards to the pegmatite emplacement models proposed by Martin (2007) and Martin *et al.* (2005; 2009). If LCT pegmatites are supposed to form due to subduction, the Namibian LCT pegmatites should have similar ages to the oldest granitoids of the Damara Belt, specifically the Goas granodiorites and Salem granites, which have recently been dated at $\sim 540 - 560$ Ma (U-Pb in zircons) by Milani (2013; Refer to Chapter 1). Dated LCT pegmatites from Namibia have however produced much younger ages (505.5 ± 2.6 Ma; Davis, 2007; 492 ± 11 Ma; Steven, 1993), similar to the ages obtained for uraniferous NYF pegmatites in the sCZ and ($508 - 509$ Ma; Briquieu *et al.*, 1980; Longridge *et al.*, 2009; Longridge, 2012). Thus the LCT and NYF pegmatites of the Damara Belt are coeval.

In addition to this, although most of the pegmatites plot within the syn-collisional granite field in the tectonic discrimination diagram for granites that was developed by Pearce *et al.* (1984; refer to Chapter 6), field observations indicate that both LCT and NYF are post-collisional, having been emplaced during a period of orogenic collapse and cooling of the mid-crust, and there is no evidence for syn-tectonic deformation.

The juxtaposition of coeval post-tectonic LCT and NYF pegmatites is not unique to Namibia, and several occurrences have been documented throughout the African continent.

8.6.1.1 Kibaran pegmatites in South Africa

The Kibaran Namaqualand Complex in South Africa represents the accretion of several exotic terranes at ~ 1.0 Ga. This tectonic process was accompanied by extensive deformation, with voluminous syn- and post-tectonic magmatism taking place between 1200 Ma and 930 Ma (Cornell *et al.*, 2006).

The pegmatites of the Richtersveld are hosted within the Orange River pegmatite belt, which spans 450 km from Richtersveld in the west to the Kenhardt area in the east, and their occurrences were mapped in detail by Hugo (1969). There are two types of pegmatite in the Richtersveld; zoned LCT pegmatites enriched in Li, Be, Sn, Ta, and Nb

are found in the western parts of the belt. These pegmatites contain a typical LCT assemblage of beryl, Li-aluminosilicates, columbite-tantalite minerals, and cassiterite (Hugo, 1969).

The LCT pegmatites have been emplaced into the same terrane as coeval NYF pegmatites, which are unzoned and contain corundum, andalusite, and apatite mineralisation, or REE-bearing phases such as gadolinite (Hugo, 1969). The NYF pegmatites are more abundant in the eastern parts of the Orange River pegmatite belt (Von Knorring and Condliffe, 1987).

8.6.1.2 Pan-African pegmatites Mozambique

The Mozambique Belt is the result of the collision of east and west Gondwana during the consolidation of the Gondwana supercontinent ~ 550 - 600 Ma. Later tectonic extension and plutonism in the northeastern parts of Mozambique occurred ~ 520 - 515 Ma (Ueda *et al.*, 2012).

In the Mozambique Belt, LCT pegmatites abundant in columbite-tantalite, spodumene, lepidolite, tourmaline, aquamarine and beryl occur in the same terrane as coeval NYF pegmatites, which contain topaz, euxenite and monazite, reflecting their REE and U enrichments (Von Knorring and Condliffe, 1987).

8.6.2 Factors to consider in interpreting the geochemical signatures of pegmatites

Both the Kibaran pegmatites of the Richtersveld, and the Pan-African pegmatites of the Mozambique Belt show that it is possible for pegmatites of the same age, related to the same tectonic event, can be emplaced in the same terrane. Given these examples, it would appear that the model of Martin and De Vito (2005), which relates the geochemical and mineralogical characteristics of LCT and NYF pegmatites, and their emplacement during collisional and extensional tectonic regimes respectively, fails to account for the field relationships observed between LCT and NYF pegmatites throughout the southern African continent.

This study has shown that the source of a pegmatite magma has a significant influence on what geochemical characteristics the pegmatites in a given pegmatite field will have. Furthermore, it appears that in some cases the sources of pegmatite melts change with time. Indeed detailed geochemical studies on the Namibian uraniferous NYF pegmatites have shown that different generations of pegmatite have different trace element signatures, suggesting that not all generations of pegmatites were sourced from the same material even though they were emplaced within a relatively short space of time (Freemantle, 2012).

The country rocks through which pegmatites migrated prior to emplacement will also have played a role in the geochemical variability of a given pegmatite population. This study, particularly the O-isotope results, has shown that, particularly in the case of the Sn-, Li-Sn-, and gem tourmaline-bearing LCT pegmatites, the country rocks into which the pegmatites have been emplaced had an influence on the geochemical signatures of those pegmatites. This, and the presence of metapelitic xenoliths in the pegmatites, indicates that country rock material is incorporated in the pegmatite system during emplacement, affecting the overall composition of the pegmatites. In addition to this, enrichment of a particular element in a pegmatite may be a reflection of province-scale enrichment in that element, which subsequently becomes accentuated in highly evolved pegmatites as a result of crustal recycling.

8.6.3 Suggestions for future work and revisions of pegmatite classification schemes

The current classification schemes of pegmatites are riddled with complications; it has been demonstrated that geochemical characteristics (e.g. aluminosity) and mineral assemblages are far too sensitive to subtle variations across individual pegmatites of a pegmatite field to prove useful as a means of classification.

Furthermore, the Namibian pegmatites have shown that relating LCT and NYF pegmatite families and their mineralogy to their depths of emplacement, based on the metamorphic grade of the country rocks, is equally ineffective as a classification scheme. Similarly, the suggestion that the two families are simply the product of different tectonic regimes falls short in classifying pegmatites of both families which

share a common structural setting. Nonetheless, the two pegmatite families are mineralogically distinct from each other, a fact that cannot be ignored.

Typically, classification schemes have been applied to individual pegmatites, and usually those which represent the most evolved parts of the pegmatite system. As a result, the relationship between these highly evolved end-member bodies and the hundreds of coeval, less evolved bodies is usually ignored. It would be useful to study these relationships for many reasons, including gaining a better understanding of the structural setting of pegmatites emplacement on a regional scale, as well as understanding the geochemical characteristics of a pegmatite field on a regional scale.

This study has shown that one of the most pronounced differences between LCT and NYF pegmatites is their Ti-in-quartz values (Ti-in quartz < 10 in LCT pegmatites and Ti-in quartz > 30 in NYF pegmatites in this study), and by extension their temperature of crystallisation, an observation consistent with the those made by Fersman (1931) who identified similar geochemical differences in pegmatites. LCT pegmatites from the Namibian sample suite gave consistently lower temperatures than the NYF samples, a difference detected using multiple geothermometers. It could therefore be useful, and potentially enlightening, to test the hypothesis that the mineralogical differences between LCT and NYF pegmatites are the products of temperature differences on a regional scale. It could also be useful to determine whether the differences between the two pegmatite families are the product of differences in the geochemical parameters e.g. Ti-in-quartz values that are used to calculate temperatures using geothermobarometry. In addition to this, the search for, and study of, melt inclusions within the Damaran pegmatites may provide valuable information regarding the fluid evolution of these rocks.

This thesis has also demonstrated that there is very little understanding of magma generation and the emplacement of pegmatites on a regional scale. Indeed conclusions pertaining to orogen-scale tectonics cannot be drawn with certainty if only individual, highly fractionated end-member bodies are studied, therefore future studies should be conducted on a regional scale.

REFERENCES

- Abdel-Rahman, A.-F.M. and Martin, R.F. (1990). The Mount Gharib A-type granite, Nubian Shield: petrogenesis and role of metasomatism at the source. *Contributions to Mineralogy and Petrology* **104**, 173 - 183.
- Abraham, I. M. (2009). Geology and spatial distribution of uranium mineralisation in the SK anomaly area, Rössing area, Namibia. Unpublished M.Sc. thesis, University of the Witwatersrand, pp 184.
- Ackerman, L., Zachariáš and Pudilová, M. (2007). P-T and fluid evolution of barren and lithium pegmatites from Vlastějovice, Bohemian Massif, Czech Republic. *International Journal of Earth Sciences (Geologische Rundschau* **96**, 623 - 638.
- Alfonso, P. and Melgarejo, J.C. (2008). Fluid evolution in the zoned rare-element pegmatite field at Cap de Creus, Catalonia, Spain. *The Canadian Mineralogist* **46**, 597 - 617.
- Allsopp, H. L., Barton, E. S., Kröner, A., Welke, H. J. & Burger, A. J. (1983). Emplacement versus inherited isotopic age patterns: a Rb-Sr and U-Pb study of Salem-type granites in the central Damara Belt. In: Miller, R. McG. (Ed.) *Evolution of the Damara Orogen*. Special Publications of the Geological Society of South Africa **11**, 281 - 287.
- Antunes, I.M.H.R., Neiva, A.M.R., Silva, M.M.V.G., Ramos, J.M.F. and Silva, P.B. (2009). Geochemistry of Li-bearing aplite-pegmatite veins from Cabeço Queimado and associated granitic rocks (Segura, Central Portugal). *Estudos Geológicos* **19(2)**, 40 - 44.
- Archer, D.G. (1992). Thermodynamic Properties of the NaCl+H₂O System. II. Thermodynamic Properties of NaCl(aq), NaCl·2H₂O(cr), and Phase Equilibria. *Journal of Physical and Chemical Reference Data* **21(4)**, 793 - 829.

- Badenhorst, F.P. (1992). *The lithostratigraphy of areas 2115B and D in the Central Zone of the Damara Orogen, Namibia: with emphasis on facies changes and regional correlation*. Unpublished M.Sc. thesis, University of Port Elizabeth, pp 124.
- Bakker R.J. (2003). Package *FLUIDS 1*. Computer programs for analysis of fluid inclusion data and for modelling bulk fluid properties. *Chemical Geology*, **194**, 3 - 23.
- Barbarin, B. (1999). A review of the relationships between granitoid types, their origins, and their geodynamic environments. *Lithos* **46**, 605 - 626.
- Barnes, J.F.H. (1981). Some aspects of the tectonic history of the Khan-Swakop region of the Damara Belt, Namibia. PhD. Thesis, University of Leeds, UK, pp 340.
- Barnes, S.J. and Sawyer, E.W. (1980). An alternative model for the Damara Mobile Belt. Ocean crust subduction and continental convergence. *Precambrian Research* **13**, 297 - 336.
- Basson, I.J. and Greenway, G. (2004). The Rössing uranium deposit: a product of late-kinematic localization of uraniferous granites in the Central Zone of the Damara Orogen, Namibia. *Journal of African Earth Sciences* **38**, 413 - 435.
- Berning, J. (1986). The Rössing uranium deposit, South West Africa/Namibia. In Anhaeusser, C.R. and Maske, S. (Eds). *Mineral Deposits of Southern Africa* **2**, Geological Society of South Africa, Johannesburg, 1819 - 1832.
- Blaine, J.L. (1977). Tectonic evolution of the Waldau Ridge structure and the Okahandja Lineament in part of the Central Damara Orogen, west of Okahandja, South West Africa. *Bulletin of the Precambrian Research Unit, University of Cape Town* **21**, pp 99.

- Blaxland, A., Gohn, E., Haack, U. & Hoffer, E. (1979). Rb/Sr ages of late-tectonic granites in the Damara Orogen, Southwest Africa/Namibia. *Neues Jahrbuch für Mineralogie, Monatshefte* **11**, 498 - 508.
- Bodnar, R.J. (1993). Revised equation and table for determining the freezing point depression of H₂O-NaCl solutions. *Geochimica et Cosmochimica Acta* **57**, 683 - 684.
- Bodnar, R.J. (2003a). Introduction to fluid inclusions *In* Samson, I. Anderson, A. & Marshall, D. *Fluid Inclusions: Analysis & Interpretation*, Short Course **32**, Mineralogical Association of Canada, Vancouver, 1 - 8.
- Bodnar, R.J. (2003b). Reequilibration of fluid inclusions *In* Samson, I. Anderson, A. & Marshall, D. *Fluid Inclusions: Analysis & Interpretation*, Short Course **32**, Mineralogical Association of Canada, Vancouver, 213 - 231.
- Borisova, A.Y., Thomas, R., Salvi, S., Candaudap, F., Lanzasova, A. and Chmeleff, J. (2012). Tin and associated metal and metalloid geochemistry by femtosecond LA-ICP-QMS microanalysis of pegmatite-leucogranite melt and fluid inclusions: new evidence for melt-melt-fluid immiscibility. *Mineralogical Magazine* **76(1)**, 91 - 113.
- Brandt, R. (1987). A revised stratigraphy for the Abbabis Complex in the Abbabis Inlier, Namibia. *South African Journal of Geology* **90**, 314 - 323.
- Breitkopf, J.H. and Maiden, K.J. (1986). A volcanogenic exhalative iron formation in the Southern Margin Zone of the Damara Orogen. *Communication of the Geological Survey of South West Africa/Namibia* **2**, 131 - 143.
- Briqueu, L., Lancelot, J.P., Valois, J.P. and Walgenwitz, F. (1980). Géochronologie U-Pb d'un type de minéralisation uranifère: les alaskites de Goanikontes (Namibie)

et leur encaissant. *Bulletin du Centre de Recherches-Production, Elf-Aquitaine* **4**, 759 - 811.

Buddington, A.F. (1959). Granite emplacement with special reference to North America. *Geological Society of America Bulletin* **70**, 671 - 747.

Burke E.A.J. (2001). Raman microspectrometry of fluid inclusions. *Lithos* **55**, 139 - 158.

Burruss, R.C. (2003). Raman spectroscopy of fluid inclusions *In* Samson, I. Anderson, A. & Marshall, D. *Fluid Inclusions: Analysis & Interpretation*, Short Course **32**, Mineralogical Association of Canada, Vancouver, 279 - 289.

Bühn, B., Stanistreet, I.G. and Okrusch, M. (1992). Late Proterozoic outer shelf manganese and iron deposits at Otjosondu (Namibia) related to Damara oceanic opening. *Economic Geology* **87**, 1393 - 1411.

Bühn, B., Okrusch, M., Woermann, E., Lehnert, K. & Hoernes, S. (1995). Metamorphic evolution of Neoproterozoic manganese formations and their country rocks at Otjosondu, Namibia. *Journal of Petrology* **36**, 463 - 496.

Cahen, L., Snelling, N.J., Delhal, J. And Vail, J.R. (1984). *The geochronology and evolution of Africa*. Oxford University Press, London, pp 512.

Cameron, E.N., Jahns, R.H., McNair, A.H. and Page, L.R. (1949). Internal structure of granitic pegmatites. *Economic Geology Monograph* **2**.

Černý, P. (1990). Distribution, affiliation and derivation of rare-element granitic pegmatites in the Canadian Shield, *Geologische Rundschau*, **79**, 183 - 226.

Černý, P. (1991a). Rare-element granitic pegmatites. Part I: Anatomy and Internal Evolution of Pegmatite deposits. *Geoscience Canada* **18**, 29 - 46.

- Černý, P. (1991b). Rare-element granitic pegmatites. Part II: regional to global environments and petrogenesis. *Geoscience Canada* **18**, 49 - 62.
- Černý, P. (1992). Geochemical and petrogenetic features of mineralisation in rare-element granitic pegmatites in the light of current research. *Applied Geochemistry* **7**, 393 - 416.
- Černý, P. (2005). The Tanco rare-element pegmatite deposit, Manitoba: regional context, internal anatomy, and global comparison *In* Linnen, R. and Samson, I. (Eds). Rare Element Geochemistry of Ore Deposits. *Geological Association of Canada, Short Course Handbook* **17**, 127 - 158.
- Černý, P. and Ercit, T.S. (2005). The classification of granitic pegmatites revisited. *The Canadian Mineralogist* **43(6)**, 2005 - 2026.
- Černý, P., Trueman, D.L., Ziehlke, D.V., Goad, B.E, and Paul, B.J. (1981). The Cat Lake - Winnipeg River and the Wekusko Lake pegmatite fields, Manitoba. *Manitoba Department of Energy and Mines Mineral Resources Division, Economic Geology Report* **ER80-1**.
- Černý, P., London, D. and Novák, M. (2012). Granitic Pegmatites as Reflections of their Sources. *Elements: An International Magazine of Mineralogy, Geochemistry, and Petrology* **8(4)**, 289 - 294.
- Chappell, B.W. and White, A.J.R. (1974). Two contrasting granite types. *Pacific Geology* **8**, 173 - 174.
- Chappell, B.W. and White, A.J.R. (1992). I- and S-type granites in the Lachlan Fold Belt. *Transactions of the Royal Society of Edinburgh, Earth Sciences* **86**, 1 - 26.
- Chappell, B.W. and White, A.J.R. (2001). Two contrasting granite types: 25 years later. *Australian Journal of Earth Sciences* **48**, 489 - 499.

- Chappell, B.W., Bryant, C.J. and Wyborn, D. (2012). Peraluminous I-type granites. *Lithos* **153**, 142 - 153.
- Chakoumakos, B. and Lumpkin, G.R. (1990). Pressure-temperature constraints on the crystallisation of the Harding pegmatite, Taos County, New Mexico. *Canadian Mineralogist* **28**, 287 - 298.
- Chamberlain, C. P. & Sonder, L. J. (1990). Heat-Producing Elements and the Thermal and Baric Patterns of Metamorphic Belts. *Science* **250**, 763 - 769.
- Chiba, H., Chacko, T., Clayton, R.N. and Goldsmith, J.R. (1989). Oxygen isotope fractionations involving diopside, forsterite, magnetite, and calcite: Application to geothermometry. *Geochimica et Cosmochimica Acta* **53**, 2985 - 2995.
- Clifford, T.N. (1967). The Damaran episode in the Upper Proterozoic-Lower Palaeozoic structural history of southern Africa. *Geological Society of America Special Paper* **92**, pp 100.
- Cornell, D.H., Thomas, R.J., Moen, H.F.G., Reid, D.L., Moore, J.M. and Gibson, R.L. (2006). The Namaqua-Natal Province *In* Johnson, M.R., Anhaeusser, C.R., and Thomas, R.J. (Eds.) *The Geology of South Africa*. Geological Society of South Africa, Johannesburg/Council for Geoscience, Pretoria, 325 - 379.
- Corner, B. (1982). An interpretation of the aeromagnetic data covering portion of the Damara Orogenic Belt with special reference to the occurrence of uraniferous granite. Unpublished Ph.D. Thesis, University of the Witwatersrand, pp 115.
- Corner, B. and Henthorn, D.I. (1978). Results of a palaeomagnetic survey undertaken in the Damara mobile belt, South West Africa, with special reference to the magnetisation of the uraniferous pegmatitic granites. Report PEL-260 Pelindaba, Atomic Energy Board South Africa.

- Coward, M.P. (1983). The tectonic history of the Damaran Belt. *Special Publication of the Geological Society of South Africa* **11**, 409 - 421.
- Damm, K-W., Harmon, R.S., Heppner, P-M., Dornsiepen, U. (1992). Stable isotope constraints on the origin of the Cabo de Creus garnet-tourmaline pegmatites, Massif des Alberes, Eastern Pyrenees, Spain. *Geological Journal* **27**, 75 - 86.
- Davies, C.J. and Coward, M.P. (1982). The structural evolution of the Gariiep Arc in southern Namibia (South West Africa). *Precambrian Research* **17**, 173 - 198.
- Deniel, C., Vidal, P., Fernandez, A., LeFort, P. and Peucat, J.-J. (1987). Isotopic study of the Manaslu granite, Himalaya, Nepal.: inferences on the age and source of Himalayan leucogranites. *Contributions to Mineralogy and Petrology* **96**, 78 - 92.
- De Kock, G. S. (1991). The mafic Audawib Suite in the Central Damara orogeny of Namibia: geochemical evidence for volcanic arc volcanism. *Journal of African Earth Science* **12**, 593 - 599.
- De Kock, G. S. and Botha, B. J. V. (1988). Komontwikkeling in die Damara-orogeen gedurende die afsetting van die Okomis-en Omusemaformasies aan die basis van die Swakopgroep, in die gebied suid-oos van Karibib, Namibia. *South African Journal of Geology* **91**, 83 - 96.
- De Kock, G.S. Eglinton, B., Armstrong, R.A., Harmer, R.E. and Walraven, F. (2000). U-Pb and Pb-Pb ages of the Naauwpoort rhyolite, Kawakeup leptite and Okongava Diorite: implications for the onset of rifting and orogenesis in the Damara Belt, Namibia. *Communications of the Geological Survey of Namibia, Henno Martin Volume* **12**, 81 - 88.

- De Kock, G.S. (2001). A reappraisal of the Namibian Damara stratigraphy in part of the Southern Swakop Terrane and its implications to basin evolution. *South African Journal of Geology* **104**, 115 - 136.
- De Vito, C., Pezzotta, F., Ferrini, V. and Aurisicchio, C. (2006). Ti–Nb–Ta oxides in the Anjanabonoina pegmatite, central Madagascar: a record of magmatic and postmagmatic events. *Canadian Mineralogist*. **44**, 87 - 103.
- De Vivo, B. and Frezzotti, M.L. (1994). Evidence for magmatic immiscibility in Italian subvolcanic systems *In* De Vivo, B. and Frezzotti, M.L. (Eds). Short course of the IMA working group "Inclusions in minerals". Virginia Polytechnic Institute, Blacksburg, Virginia, 345 - 362.
- Dewaele, S., Henjes-Kunst, F., Melcher, F., Sitnikova, M., Burgess, R., Gerdes, A., Fernandez, M.A., De Clercq, F., Muchez, P. and Lehmann, B. (2011). Late Neoproterozoic overprinting of the cassiterite and columbite-tantalite bearing pegmatites of the Gatumba area, Rwanda (Central Africa). *Journal of African Earth Sciences* **61**, 10 - 26.
- Diehl, B.J.M. (1990). The Cape Cross - Uis pegmatite belt, Namibia: Geology, mineralisation, Rb - Sr isotopic characteristics and petrogenetic implications of rare metal pegmatites. Open File Report, Geological Survey of Namibia, pp 29.
- Diehl, B.T.M. (1992a). Tin. *In* Miller, R. McG. *Mineral Resources of Namibia*, Ministry of Mines and Energy, Geological Survey of Namibia, Windhoek, 2.8, 1 - 30.
- Diehl, B.T.M. (1992b). Lithium, beryllium and caesium. *In* Miller, R. McG. *Mineral Resources of Namibia*, Ministry of Mines and Energy, Geological Survey of Namibia, Windhoek, 6.15, 1 - 18.

- Diehl, B.T.M. (1992c). Niobium and tantalum. In Miller, R. McG. *Mineral Resources of Namibia*, Ministry of Mines and Energy, Geological Survey of Namibia, Windhoek, 3.5, 1 - 20.
- Diehl, M. (1993). Rare metal pegmatites of the Cape Cross-Uis pegmatites belt, Namibia: geology, mineralisation, rubidium-strontium characteristics and petrogenesis. *Journal of African Earth Sciences* **17(2)**, 167 - 181.
- Diehl, B.J.M. and Schneider, G.I.C. (1990). Geology and mineralisation of the Rubicon Pegmatite, Namibia. Geological Survey of Namibia Open File Report, 20 pp.
- Ercit, T.S. (2005). REE-enriched granitic pegmatites In Linnen, R.L. and Samson, I.M. (Eds). Rare-element Geochemistry and Mineral Deposits. *Geological Association of Canada Short Course Notes* **17**, 175 - 199.
- Evensen, J.M. and London, D. (2003). Experimental partitioning of Be and other trace elements between cordierite and silicic melt, and the chemical signature of S-type granite. *Contributions to Mineralogy and Petrology* **144**, 739 - 757.
- Faure, G. and Mensing, T.M. (2005). *Isotopes: Principles and Applications 3rd Edition*, Wiley, Hoboken, NJ, pp 691- 873.
- Fersman, A.F. (1931). *Les pegmatites, leur importance scientifique et pratique*. Académie des sciences de l'U.R.S.S, Leningrad, pp 675.
- Freemantle, G. (2012). Granite-hosted Uranium Deposits of the Central Damara Orogen, Namibia. Unpublished M.Sc. thesis, University of the Witwatersrand.
- Frezzotti, M.L. (1992). Magmatic immiscibility and fluid phase evolution in the Mount Genis granite (southeastern Sardinia, Italy). *Geochimica et Cosmochimica Acta* **56**, 21 - 33.

- Frezzotti, M.L., Tecce, F. and Casagli, A. (2012). Raman spectroscopy for fluid inclusion analysis. *Journal of Geochemical Exploration* **112**, 1 - 20.
- Frimmel, H.E. (2009a). Configuration of Pan-African orogenic belts in Southwestern Africa. In Gaucher, C., Sial, A.N., Halverson, G.P., Frimmel, H.E. (Eds.). *Neoproterozoic-Cambrian tectonics, global change and evolution: a focus on southwestern Gondwana*. Developments in Precambrian Geology **16**, Elsevier, 145 - 151.
- Frimmel, H.E., McG. Miller, R. (2009b). Continental rifting. Neoproterozoic to Early Palaeozoic evolution of Southwestern Africa. In Gaucher, C., Sial, A.N., Halverson, G.P., Frimmel, H.E. (Eds.). *Neoproterozoic-Cambrian tectonics, global change and evolution: a focus on southwestern Gondwana*. Developments in Precambrian Geology **16**, Elsevier, 153 - 159.
- Frimmel, H.E., Fölling, P.G. and Eriksson, P. (2002). Neoproterozoic tectonic and climatic evolution recorded in the Gariep Belt, Namibia and South Africa. *Basin Research* **14**, 55 - 67.
- Frimmel, H.E., Basei, M.S. and Gaucher, C. (2011). Neoproterozoic geodynamic evolution of SW-Gondwana: a southern African perspective. *International Journal of Earth Sciences* **100**, 323 - 354.
- Frost, B.R., Barnes, C.G., Collins, W.J., Arculus, R.J., Ellis, D.J. and Frost C.D. (2001). A geochemical classification for granitic rocks. *Journal of Petrology* **42(11)**, 2033 - 2048.
- Gagnon, J.E., Samson, I.M., Fryer, B.J. and Williams-Jones, A.E. (2004). The composition and origin of hydrothermal fluids in a NYF-type granitic pegmatite, South Platte District, Colorado: evidence from LA-ICP-MS analysis of fluorite- and quartz-hosted fluid inclusions. *The Canadian Mineralogist* **42**, 1331 - 1355.

- Gaucher, C., Frimmel, H.E., Germs, G.J.B. (2009). Tectonic events and palaeogeographic evolution of southwestern Gondwana in the Neoproterozoic and Cambrian *In* Gaucher, C., Sial, A.N., Halverson, G.P. and Frimmel, H.E. (Eds). *Neoproterozoic-Cambrian tectonics, global change and evolution: a focus on southwestern Gondwana*, Developments in Precambrian Geology **16**, 295 - 316.
- Germs, G.J.B., Miller, R.McG., Frimmel, H.E., Gaucher, C. (2009). Syn-to late-orogenic sedimentary basins of southwestern Africa. Neoproterozoic to Early Palaeozoic evolution of Southwestern Africa. *In* Gaucher, C., Sial, A.N., Halverson, G.P., Frimmel, H.E. (Eds.). *Neoproterozoic-Cambrian tectonics, global change and evolution: a focus on southwestern Gondwana*. Developments in Precambrian Geology **16**, Elsevier, 183 - 203.
- Gharib, M. E. (2012). Origin and evolution of magmatic garnet-bearing pegmatites and associated granitoids, Abu Had, South Eastern Desert, Egypt: Inference from petrology and geochemistry. *Journal of American Science* **8(10)**, 536 - 554.
- Goscombe, B., Hand, M., Gray, D. and Mawby, J. (2003a). The metamorphic architecture of a transpressional orogen: the Kaoko Belt, Namibia. *Journal of Petrology* **44(4)**, 679 - 711.
- Goscombe, B., Hand, M. and Gray, D. (2003b). Structure of the Kaoko Belt, Namibia: progressive evolution of a classic transpressional orogen. *Journal of Structural Geology* **25**, 1049 - 1081.
- Goscombe, B., Gray, D. and Hand, M. (2004). Variation in metamorphic style along the northern margin of the Damara Orogen. *Journal of Petrology* **45(6)**, 1261 - 1295.

- Goscombe, B., Gray, D.R., Armstrong, R., Foster, D.A. and Vogl, J. (2005). Event geochronology of the Pan-African Kaoko Belt, Namibia. *Precambrian Research* **140**, 1 - 41.
- Ginsburg, A.I., Timofeyev, I.N. and Feldman, L.G. (1979). Principles of geology of the granitic pegmatites: Nedra Moscow, pp 296. [in Russian]
- Ginsburg, A.I. (1984). The geological condition of the location and the formation of granitic pegmatites. *27th International Geological Congress Proceedings* **15**, 245 - 260.
- Glover, A.S., Rogers, W.Z. and Barton, J.E. (2012). Granitic Pegmatites: Storehouses of Industrial Minerals. *Elements: An International Magazine of Mineralogy, Geochemistry, and Petrology* **8(4)**, 269 - 273.
- Goldstein, R.H. (2003). Petrographic analysis of fluid inclusions *In* Samson, I. Anderson, A. & Marshall, D. *Fluid Inclusions: Analysis & Interpretation*, Short Course **32**, Mineralogical Association of Canada, Vancouver, 9 - 53.
- Gray, D. R., D. A. Foster, Goscombe, B., Passchier, C.W. and Trouw, R.A.J. (2006). $^{40}\text{Ar}/^{39}\text{Ar}$ thermochronology of the Pan-African Damara Orogen, Namibia, with implications for tectonothermal and geodynamic evolution. *Precambrian Research* **150(1-2)**, 49 - 72.
- Gray, D.R., Foster, D.A., Meert, J.G., Goscombe, B.D., Armstrong, R.A., Trouw, R.A.J. and Passchier, C.W. (2008). A Damara Orogen perspective on the assembly of southwestern Gondwana. *Geological Society of London Special Publication* **294**, 257 - 278.
- Grotzinger, J.P. and Miller, R.McG. (2008). Nama Group *In* Miller, R. McG. *The Geology of Namibia* **2**, Ministry of Mines and Energy, Geological Survey, Windhoek, 13-229 - 13-272.

- Haack, U. and Gohn, E. (1988). Rb-Sr data on some pegmatites in the Damara Orogen, Namibia. *Communications of the Geological Survey of South West Africa/Namibia* **4**, 13 - 17.
- Haack, U., John, E. and Klein, J.A. (1980). Rb/Sr ages of granitic rocks along the middle reaches of the Omaruru River and the timing of orogenic events in the Damara Belt (Namibia). *Contributions to Mineralogy and Petrology* **74**, 349 - 360.
- Haack, U., Heinrichs, H., Boneß, M. and Schneider, A. (1984). The loss of metals from pelites during regional metamorphism. *Contributions to Mineralogy and Petrology* **85**, 116 - 132.
- Halverson, G.P., Hoffman, P.F., Schrag, D.P., Maloof, A.C., and Rice, A.H.N. (2005). Towards a Neoproterozoic composite carbon isotope record. *Geological Society of America Bulletin* **117**, 1181 - 1207.
- Harris, C. and Ashwal, L.D. (2002). The origin of low $\delta^{18}\text{O}$ granites and related rocks from the Seychelles. *Contributions to Mineralogy and Petrology* **143**, 366 - 376.
- Harris, C. and Erlank, A.J. (1992). The production of large-volume, low- $\delta^{18}\text{O}$ rhyolites during the rifting of Africa and Antarctica: the Lebombo Monocline, southern Africa. *Geochimica et Cosmochimica Acta* **56**, 3561 - 3570.
- Harris, N.B.W. and Inger, S. (1992). Trace element modelling of pelite-derived granites. *Contributions to Mineralogy and Petrology* **110**, 46 - 56.
- Harris, C., Faure, K., Diamond, R.E. and Scheepers, R. (1997). Oxygen and hydrogen isotope geochemistry of S- and I-type granitoids: the Cape Granite suite, South Africa. *Chemical Geology* **143**, 95 - 114.

- Harris, C., Johnstone, W.P. and Phillips, D. (2002). Petrogenesis of the Mesozoic Sistefjell syenite intrusion, Dronning Maud Land, Antarctica and surrounding low- $\delta^{18}\text{O}$ lavas. *South African Journal of Geology* **105**, 205 - 226.
- Hawkesworth, C.J. and Marlow, A.G. (1983). Isotope evolution of the Damara orogenic belt. *Special Publication of the Geological Society of South Africa* **11**, 397 - 407.
- Hawkesworth, C. J., Gledhill, A. R., Roddick, J. C., Miller, R. McG. & Kröner, A. (1983). Rb-Sr and $40\text{Ar}/39\text{Ar}$ studies bearing on models for the thermal evolution of the Damara Belt, Namibia. In Miller, R. McG. (Ed.) *Evolution of the Damara Orogen*. Special Publications of the Geological Society of South Africa **11**, 323 - 338.
- Heinrich, E. W. (1958). Rare-earth pegmatites of the South Platte-Lake George area, Douglas, Teller, and Park Counties, Colorado [abs.]. *Geological Society of America Bulletin* **69**, 1579 - 1580.
- Henry, G. (1992). *The sedimentary evolution of the Damara Sequence in the lower Khan River valley, Namibia*. Unpublished Ph.D. thesis, University of the Witwatersrand, Johannesburg.
- Hoefs, J. (2009). *Stable Isotope Geochemistry 6th Edition*, Springer-Verlag, Berlin, pp 285.
- Hoffman, P. F. (2005). On Cryogenian (Neoproterozoic) ice-sheet dynamics and the limitations of the glacial sedimentary record. *South African Journal of Geology* **108**, 557 - 577.
- Hoffman, P.F., Hawkins, D.P., Isachsen, C.E. and Bowring, S.A. (1996). Precise U-Pb zircon ages for early Damaran magmatism in the Summas Mountains and Welwitschia Inlier, northern Damara Belt, Namibia. *Communications of the Geological Survey of Namibia* **11**, 47 - 52.

- Hoffmann, K.-H. (1983). Lithostratigraphy and facies of the Swakop Group of the southern Damara Belt, South West Africa/Namibia. *Special Publication of the Geological Society of South Africa* **11**, 43 - 63.
- Hoffmann, K.-H. (1987). Application of tectonostratigraphic terrane analysis in the Damara Province of central and northern Namibia. *In: Hartnady, C.J.H. (Ed.). Proceedings and Abstracts of the Alex L. du Toit Golden Jubilee Conference on Tectonostratigraphic Terrane Analysis, 17 October, Cape Town, Precambrian Research Unit, University of Cape Town, 25 - 27.*
- Hoffmann, K.-H. (1989). New aspects of lithostratigraphic subdivision and correlation of late Proterozoic to early Cambrian rocks of the southern Damara Belt, and their correlation with the central and northern Damara Belt and the Gariep Belt. *Communications of the Geological Survey of Namibia* **5**, 59 - 67.
- Hoffmann, K.-H., Condon, D.J., Bowring, S.A. and Crowley, J.L. (2004) U-Pb zircon date from the Neoproterozoic Ghaub Formation, Namibia: Constraints on Marinoan glaciation. *Geology* **32**, 817 - 820.
- Horstmann, U.E., Ahrendt, H., Clauer, N. and Porada, H. (1990). The metamorphic history of the Damara Orogen based on K/Ar data of detrital white micas from the Nama Group, Namibia. *Precambrian Research* **48**, 41 - 61.
- Huang R. and Audétat A. (2012). The titanium-in-quartz (TitaniQ) thermobarometer: a critical examination and re-calibration. *Geochimica et Cosmochimica Acta* **84**, 75 - 89.
- Hugo, P.J. (1969). The pegmatites of the Kenhardt and Gordonias Districts, Cape Province. *Memoir of the Geological Survey of South Africa* **58**, pp 94.

- Jacob, R.E. (1974). Geology and metamorphic petrology of part of the Damara Orogen along the lower Swakop River, South West Africa. Chamber of Mines, Precambrian Research Unit, University of Cape Town **17**, pp 117.
- Jacob, R.E., Snowden, P.A. and Bunting, F.J.L. (1983). Geology and structural development of the Tumas basement dome and its cover rocks. *In* Miller, R. McG. (Ed.) *Evolution of the Damara Orogen*. Special Publications of the Geological Society of South Africa **11**, 157 - 172.
- Jacob R.E. and Kruger F.J. (1994). Age of hydrothermal tin mineralization in the region northwest of the Brandberg, Namibia. *In*: Abstract Volume, *Proterozoic crustal and metallogenic evolution*, Geological Society and Geological Survey of Namibia, p 34.
- Jacob, R.E., Moore, K.M. and Armstrong, R.A. (2000). Zircon and titanite age determination from igneous rocks in the Karibib District, Namibia: implications for Navachab vein-style gold mineralisation. *Communications of the Geological Survey of Namibia* **12**, 157 - 166.
- Jahns R.H., and Burnham, C.W. (1969). Experimental studies of pegmatite genesis I: A model for the derivation and crystallization of granitic pegmatites. *Economic Geology* **64**, 843 – 864.
- Johnson, S. D., Poujol, M. & Kisters, A. F. M. (2006). Constraining the timing and migration of collisional tectonics in the Damara Belt, Namibia: U-Pb zircon ages for the syntectonic Salem-type Stinkbank granite. *South African Journal of Geology* **109**, 611-624.
- Jung, S. and Mezger, K. (2003). U-Pb garnet chronometry in high-grade rocks; case studies from the central Damara Orogen (Namibia) and implications for the interpretation of Sm-Nd garnet ages and the role of high U-Th inclusions. *Contributions to Mineralogy Petrology* **146**, 382 - 396.

- Jung, S., Mezger, K. and Hoernes, S. (1998). Petrology and geochemistry of syn- to post-collisional metaluminous A-type granites - a major and trace element and Nd-Sr-Pb-O isotope study from the Proterozoic Damara Belt, Namibia. *Lithos* **45**, 147 - 175.
- Jung, S., Hoernes, S., Masberg, P. and Hoffer, E. (1999). The petrogenesis of some migmatites and granites (Central Damara Orogen, Namibia): evidence of disequilibrium melting, wall-rock contamination and crystal fractionation. *Journal of Petrology* **40(8)**, 1241 - 1209.
- Jung, S., Hoernes, S. and Mezger, K. (2000). Geochronology and petrogenesis of Pan-African, syn-tectonic, S-type and post-tectonic A-type granite (Namibia): products of melting of crustal sources, fractional crystallisation and wall rock entrainment. *Lithos* **50**, 259 - 287.
- Jung, S., Hoernes, S. and Mezger, K. (2002). Synorogenic melting of mafic lower crust: constraints from geochronology, petrology and Sr, Nd, Pb and O isotope geochemistry of quartz diorites (Damara orogen, Namibia). *Contributions to Mineralogy and Petrology* **143**, 551 - 566.
- Jung, S., Mezger, K. and Hoernes, S. (2003). Petrology of basement-dominated terranes II. Contrasting isotopic (Sr, Nd, Pb and O) signatures of basement-derived granites and constraints on the source region of granite (Damara orogen, Namibia). *Chemical Geology* **199**, 1 - 28.
- Jung, S., Hoffer, E., and Hoernes, S. (2007). Neoproterozoic rift-related syenites (Northern Damara Belt, Namibia): geochemical and Nd-Sr-Pb-O isotope constraints for mantle sources and petrogenesis. *Lithos* **96**, 415 - 435.
- Kasch, K.W. (1983). Regional P-T variations in the Damara Orogen with particular reference to early high-pressure metamorphism along the southern margin. *In*

- Miller, R.McG. (Ed.). Evolution of the Damara Orogen of South West Africa/ Namibia. *Geological Society of South Africa Special Publication* **11**, 243 - 253.
- Keller, P., Robles, E.R., Pérez, A.P. and Fontan, F. (1999). Chemistry, paragenesis and significance of tourmaline in pegmatites of the Southern Tin Belt, central Namibia. *Chemical Geology* **158**, 203 - 225.
- Kennedy, W.Q. (1964). The structural differentiation of Africa in the Pan-African (\pm 500 m.y.) tectonic episode, *8th Annual Report of the Research Institute of African Geology*, University of Leeds, 9 - 11.
- Killick, A.M. (1986). A review of the economic geology of northern South West Africa/Namibia. In Anhaeusser, C.R. and Maske, S. (Eds). *Mineral Deposits of Southern Africa* **2**, Geological Society of South Africa, Johannesburg, 1709 - 1717.
- Killick, A.M. (2000). The Matchless Belt and associated sulphide mineral deposits, Damara Orogen, Namibia. *Communications of the Geological Survey of Namibia* **12**, 73 - 80.
- Kinnaird, J.A. and Nex, P.A.M. (2007). A review of geological controls on uranium mineralisation in sheeted leucogranites within the Damara Orogen, Namibia. *Applied Earth Science* **116(2)**, 68 - 85.
- Kisters, A.F.M. (2005). Controls of gold-quartz vein formation during regional folding in amphibolite-facies, marble-dominated metasediments of the Navachab Gold Mine in the Pan-African Damara Belt, Namibia. *South African Journal of Geology* **108**, 365 - 380.
- Kisters, A.F.M., Jordaan, L.S. and Neumaier, K. (2004). Thrust-related dome structures in the Karibib district and the origin of orthogonal fabric domains in the south

Central Zone of the Pan-African Damara belt, Namibia. *Precambrian Research* **133**, 283 - 303.

Kontak, D.J., Ansdell, K., Dostal, J., Halter, W., Martin, R. and Williams-Jones, A.E. (2001). The nature and origin of pegmatites in fluorine-rich leucogranite, East Kemptville tin deposit, Nova Scotia, Canada. *Transactions of the Royal Society of Edinburgh, Earth Sciences* **92**, 173 - 200.

Kovalenko, N.I., Ryzhenko, B.N., Barsukov, V.L., Klintsova, A.P., Velyukhanova, T.K., Volynets, M.P. and Kytayeva, L.P. (1986). The solubility of cassiterite in HCl + NaCl(KCl) solutions at 550 °C and 1000 atm under fixed redox conditions. *Geochemistry International* **23**, 1 - 16.

Kröner, A. (1982). Rb-Sr geochronology and tectonic evolution of the Pan-African Damara belt of Namibia, south-western Africa. *American Journal of Science* **282**, 1471-1507.

Kröner, A. and Hawkesworth, C. (1977). Late Pan-African emplacement ages for Rössing alaskitic granite, 20th *Annual Report of the Research Institute of African Geology*, University of Leeds, 14 - 17.

Kröner, A., Retief, E. A., Compston, W., Jacob, R. E. & Burger., A. J. (1991). Single-Age and conventional zircon dating of remobilised basement gneisses in the central Damara belt of Namibia. *South African Journal of Geology* **94**, 379 - 387.

Landes, K.K. (1933). Origin and classification of pegmatites. *American Mineralogist* **22**, 33 - 56.

Lehtonen, M. I., Manninen, T. E. T. & Schreiber, U. M. (1995). *The geology of the area between the Khan river and the Coast, and in the vicinity of Omdel Dam*. Mapping Report and geochemical study, Finnish-Namibian Geological mapping and maps project. Map 2215A.

- Lehtonen, M. I., Manninen, T. E. T. & Schreiber, U. M. (1996). Report on the lithostratigraphy of the area between the Swakop, Khan and lower Omaruru Rivers, Namib Desert. *Communications of the Geological Survey of Namibia* **11**, 65 - 75.
- Lenharo, S.L.R., Pollard, P.J. and Born, H. (2003). Petrology and textural evolution of granites associated with tin and rare metals mineralisation at the Pitinga mine, Amazonas, Brazil. *Lithos* **66**, 37 - 61.
- Linnen, R.L. (1998). Depth of emplacement, fluid provenance and metallogeny in granitic terranes: a comparison of western Thailand with other tin belts. *Mineralium Deposita* **33**, 461 - 476.
- Linnen, R.L. and Williams-Jones, A.E. (1994). The evolution of pegmatite-hosted tungsten mineralisation at Nong Sua, Thailand: evidence from fluid inclusions and stable isotopes. *Geochimica et Cosmochimica Acta* **58**, 735 - 747.
- Linnen, R.L., v. Lichtervelde, M. and Černý, P. (2012). Granitic Pegmatites as Sources of Strategic Metals. *Elements: An International Magazine of Mineralogy, Geochemistry, and Petrology* **8(4)**, 275 - 280.
- Lombardi, G. and Sheppard, S.M.F. (1977). Petrographic and isotopic studies of the altered acid volcanics of the Tolfa-Cerite area, Italy: The genesis of clays. *Clay Minerals* **12**, 147 - 162.
- London, D. (1987). Internal differentiation of rare-element pegmatites: effects of boron, phosphorus and fluorine. *Geochimica et Cosmochimica Acta* **51**, 403 - 420.
- London, D. (1995). Geochemical features of peraluminous granites, pegmatites, and rhyolites as sources of lithophile metal deposits *In* Thompson, J.F.H. (Ed.).

Magmas, Fluids and Ore Deposits. *Mineralogical Association of Canada Short Course Handbook* **23**, 175 - 202.

London, D. (2005). Geochemistry of alkalis and alkali earths in ore-forming granites, pegmatites, and rhyolites *In* Linnen, R. and Samson, I. (Eds). Rare Element Geochemistry of Ore Deposits. *Geological Association of Canada, Short Course Handbook* **17**, 17 - 43.

London, D. (2008). Pegmatites. *Canadian Mineralogist Special publication* **10**, pp 347.

London, D. (2009). The origin of primary textures in granitic pegmatites. *Canadian Mineralogist* **47**, 697 - 724.

London, D. and Evensen, J.M. (2002). Beryllium in silicic magmas and the origin of beryl-bearing pegmatites *In* Grew, E.S. (Ed.). Beryllium: Mineralogy, petrology and geochemistry. *Reviews in Mineralogy and Geochemistry* **50**, 445 - 486.

London, D. and Kontak, D.J. (2012). Granitic Pegmatites: Scientific Wonders and Economic Bonanzas. *Elements: An International Magazine of Mineralogy, Geochemistry, and Petrology* **8(4)**, 257 - 261.

London, D. and Morgan VI, G.B.(2012). The Pegmatite Puzzle. *Elements: An International Magazine of Mineralogy, Geochemistry, and Petrology* **8(4)**, 263 - 268.

Longridge, L. (2012). Tectonothermal Evolution of the southwestern Central Zone, Damara Belt, Namibia. Unpublished Ph.D. thesis, University of the Witwatersrand, pp 524.

Longridge, L., Gibson, R.L., Kinnaird, J.A. and Armstrong, R.A. (2009). Timing of deformation and granite emplacement in the Central Zone of the Damara Orogen, Namibia. SEG-GSSA Student Conference, Johannesburg, South Africa.

- Lu, J. and Lottermoser, B.G. (1997). Petrogenesis of rare-element pegmatites in the Olary Bloc, South Australia. Part 2. Fluid inclusion study. *Mineralogy and Petrology* **59**, 21 - 41.
- Macey, P.H. (2003). The characteristics of regional-scale fluids, fluid flow and hydrothermal mineralization in meta-sedimentary terranes: a stable isotope and fluid inclusion study of the Zerrissene Group meta turbidites and Sn–W deposits, Brandberg West area, Neoproterozoic Damara Orogen, central western Namibia. Unpublished Ph.D. thesis, University of Cape Town, pp 332.
- Macey, P. and Harris, C. (2006). Stable isotope and fluid inclusion evidence for the origin of the Brandberg West area Sn-W vein deposits, NW Namibia. *Mineralium Deposita* **41**, 671 - 690.
- Marlow, A. (1983). Geology and Rb-Sr geochronology of mineralised and radioactive granites and alaskites, Namibia *In* Miller, R.McG. (Ed.). *Evolution of the Damara Orogen of South West Africa/Namibia*, Special Publication of the Geological Society of South Africa **11**, pp 515.
- Marsh, J. (1973). Relationships between transform directions and alkaline igneous lineaments in Africa and South America. *Earth and Planetary Science Letters* **18**, 317 - 327.
- Martin, R.F. (2007). The importance of tectonic setting in understanding granitic pegmatites. *Granitic Pegmatites: The State of the Art - International Symposium*.
- Martin, H. and Porada, H. (1977). The intracratonic branch of the Damara Orogen in South West Africa. I. Discussion of geodynamic models. II. Discussion of relationships with the Pan-African Mobile Belt system. *Precambrian Research* **5**, 311 - 338 and 339 - 357.

- Martin, R.F. and De Vito, C. (2005). The patterns of enrichment in felsic pegmatites ultimately depend on tectonic setting. *Canadian Mineralogist*, **43**, 2027 - 2048.
- Martin, R.F., De Vito, C and Sokolov, M. (2009). Pegmatites and pegmatites, just like granites and granites: apples and oranges are just not the same! *Estudios Geológicos* **19(2)**, 11 - 14.
- Masberg, H.P., Hoffer, E. And Hoernes, S. (1992). Microfabrics indicating granulite-facies metamorphism in the low-pressure central Damara Orogen, Namibia. *Precambrian Research* **55**, 243 - 257.
- Masoudi, F., Mehrabi, B., Rezai Aghdam, M. and Yardley, B.W.D. (2009). The nature of fluids during pegmatite development in metamorphic terranes: evidence from Hamadan Complex, Sanandaj-Sirjan Metamorphic Zone, Iran. *Journal of the Geological Society of India* **73**, 407 - 418.
- McDermott, F. (1986). *Granite petrogenesis and crustal evolution studies in the Damara Pan-African orogenic belt, Namibia*. Unpublished Ph.D. Thesis, The Open University.
- McDermott, F., Harris, N.B.W. and Hawkesworth, C.J. (1996). Geochemical constraints on crustal anatexis: a case study from the Pan-African Damara granitoids of Namibia. *Contributions to mineralogy and Petrology* **123**, 406 - 423.
- Melcher, F., Graupner, T., Gäbler, H-E., Sitnikova, M., Henjes-Kunst, F., Oberthür, T. Gerdes, A. and Dewaele, S. (2013). Tantalum-(niobium-tin) mineralisation in African pegmatites and rare metal granites: Constraints from Ta-Nb oxide mineralogy, geochronology and U-Pb geochronology. *Ore Geology Reviews*, in press.

- Miller, R.McG. (1979). The Okahandja Lineament, a fundamental tectonic boundary in the Damara Orogen of South West Africa/Namibia. *Transactions of the Geological Society of South Africa* **82**, 349 - 361.
- Miller, R.McG. (1992a). Mineral exploration targets in Namibia. In Miller, R. McG. *Mineral Resources of Namibia*, Ministry of Mines and Energy, Geological Survey of Namibia, Windhoek, 1.1, 1 - 8.
- Miller, R.McG. (1992b). Stratigraphy. In Miller, R. McG. *Mineral Resources of Namibia*, Ministry of Mines and Energy, Geological Survey of Namibia, Windhoek, 1.2, 1 - 22.
- Miller, R.McG. (1983). The Pan-African Damara Orogen of South West Africa/Namibia. In Miller, R. McG. (Ed.). *Evolution of the Damara Orogen of South West Africa/Namibia. Geological Society of South Africa Special Publication* **11**, 431 - 515.
- Miller, R.McG. (2008). Neoproterozoic and early Palaeozoic rocks of the Damara Orogen. In Miller, R. McG. *The Geology of Namibia* **2**, Ministry of Mines and Energy, Geological Survey, Windhoek, 13-1 - 13-410.
- Miller, C. F. & Mittlefehldt, D. W. (1982). Depletion of light rare earth elements in felsic magmas. *Geology* **10**, 129 -133.
- Miller, R.McG. and Frimmel, H.E. (2009). Syn- to post-orogenic magmatism. Neoproterozoic evolution of southwestern Africa. In Gaucher, C., Sial, A.N., Halverson, G.P. and Frimmel, H.E. (Eds). *Neoproterozoic-Cambrian tectonics, global change and evolution: a focus on southwestern Gondwana*, *Developments in Precambrian Geology* **16**, 219 - 226.
- Miller, R.McG., Frimmel, H.E., Will, T.M. (2009a). Geodynamic synthesis of the Damara Orogen *sensu lato*. Neoproterozoic to Early Palaeozoic evolution of Southwestern Africa In Gaucher, C., Sial, A.N., Halverson, G.P., Frimmel, H.E.

(Eds.). *Neoproterozoic-Cambrian tectonics, global change and evolution: a focus on southwestern Gondwana*. *Developments in Precambrian Geology* **16**, Elsevier, 231 - 235.

Miller, R.McG., Frimmel, H.E., Halverson, G.P. (2009b). Passive continental margin evolution. Neoproterozoic to Early Palaeozoic evolution of Southwestern Africa. In Gaucher, C., Sial, A.N., Halverson, G.P., Frimmel, H.E. (Eds.). *Neoproterozoic-Cambrian tectonics, global change and evolution: a focus on southwestern Gondwana*. *Developments in Precambrian Geology* **16**, Elsevier, 161 - 181.

Mittlefehldt, D.W. and Miller, C. F. (1983). Geochemistry of the Seawater Grenville Province of Seawater Wash pluton, California: implications for 'anomalous' trace element behaviour during differentiation of felsic magmas. *Geochimica et Cosmochimica Acta* **47**, 109 - 124.

Morgan VI, G.B. and London, D. (1999). Crystallisation of the Little Three layered pegmatite-aplite dike, Ramona District, California. *Contributions to Mineralogy and Petrology* **102**, 281 - 297.

Müller, A., Wiedenbeck, M., v.d. Kerkhof, A.M., Kronz, A. and Simon, K. (2003). Trace elements in quartz - a combined electron microprobe, secondary ion mass spectrometry, laser-ablation ICP-MS, and cathodoluminescence study. *European Journal of Mineralogy* **15**, 747 - 765.

Müller, A., Ihlen, P.M. and Kronz, A. (2008). Quartz chemistry in polygeneration Sveconorwegian pegmatites, Froland, Norway. *European Journal of Mineralogy* **20**, 447 - 463.

Müller, A., Snook, B., Spratt, J., Williamson, B. and Seltmann, R. (2013). "Amazonite" – "Cleavelandite" replacement units in NYF-type pegmatites - residual fluids or

immiscible melts. *Abstract. PEG 2013: The 6th International Symposium on Granitic Pegmatites*, 96 - 97.

Nabalek, P.I., Whittington, A.G. and Sirbescu, M-L, C. (2010). The role of H₂O in rapid emplacement and crystallisation of granite pegmatites: resolving the paradox of large crystals in highly undercooled melts. *Contributions to Mineralogy and Petrology* **160**, 313 - 325.

Nagel, R. (1999). *Eine Milliarde Jahre geologischer Entwicklung am NW-Rand des Kalahari Kratons*. Unpublished Ph.D. thesis, University of Göttingen, pp 171.

Nash, C.R. (1971). Metamorphic petrology of the SJ area, Swakopmund District, South West Africa, Chamber of Mines, Precambrian Research Unit University of Cape Town **9**, pp 77.

Nex, P.A.M. (1993). Preliminary report on the "structural setting and emplacement history of granitic sheets in the Goanikontes area, Namibia. *University of Cork Department of Geology Report Series 8/93*, pp 19.

Nex, P. (1997). Tectono-metamorphic setting and evolution of granitic sheets in the Goanikontes area, Namibia. Unpublished Ph.D. Thesis, University College Cork, National University of Ireland, pp 322.

Nex, P.A.M. and Kinnaird, J.A. (1995). Granites and their mineralisation in the Swakop River area around Goanikontes, Namibia. *Communications of the Geological Survey of Namibia* **10**, 51 - 56.

Nex, P.A.M., Oliver, G.J.H. and Kinnaird, J.A. (2001a). Spinel-bearing assemblages and the P-T-t evolution of the Central Zone of the Damara Orogen, Namibia. *Journal of African Earth Sciences* **32(3)**, 471 - 489.

- Nex, P.A.M., Kinnaird, J.A. and Oliver, J.H. (2001b). Petrology, geochemistry and uranium mineralisation of post-collisional magmatism around Goanikontes, southern Central Zone, Damaran Orogen, Namibia. *Journal of African Earth Sciences* **33**, 481 - 502.
- Nex, P.A.M., Herd, D. and Kinnaird, J.A. (2002). Fluid extraction from quartz in sheeted leucogranites as a monitor to styles of uranium mineralisation: an example from the Rössing area, Namibia. *Geochemistry: Exploration, Environment, Analysis* **22**, 83 - 96.
- Oliver, G.J.H. (1995). The Central Zone of the Damara Orogen, Namibia, as a deep metamorphic core complex. *Communications of the Geological Survey of Namibia* **10**, 33 - 41.
- Owen, G.J. (2011). *Geology of the Kranzberg Syncline and emplacement controls of the Usakos Pegmatite Field, Damara Belt, Namibia*. Unpublished M.Sc. Thesis, University of Stellenbosch, pp 168.
- Paciullo, F.V.P., Ribeiro, A., Trouw, R.A.J. and Passchier, C.W. (2007). Facies and facies association of the siliciclastic Brak River and carbonate Gemsbok formations in the Lower Ugab River valley, Namibia, W. Africa. *Journal of African Earth Sciences* **47**, 121 - 134.
- Pearce, J.A., Harris, N.B.W. and Tindle, A.G. (1984). Trace element discrimination diagrams for the tectonic interpretation of granitic rocks. *Journal of Petrology* **25(4)**, 956 - 983.
- Pezzotta, F. (1999). Madagascar; a mineral and gemstone paradise. *ExtraLapis* **1**.
- Phillips, G. N., Wall, V. J. & Clemens, J. D. (1981). Petrology of the Strathbogie batholith—a cordierite bearing granite. *Canadian Mineralogist* **19**, 47 - 63.

- Poli, L. C. (1997). *Mid-crustal geodynamics of the Southern Central Zone, Damara Orogen, Namibia*. Unpublished Ph.D. thesis. University of St Andrews, Scotland.
- Poli, L.C. and Oliver, G.J.H., (2001). Constrictional deformation in the Central Zone of the Damara Orogen Namibia. *Journal of African Earth Sciences* **33**, 303 - 312.
- Porada, H., Ahrendt, H., Behr, H.-J. And Weber, K. (1983). The join of the coastal and intracontinental branches of the Damara Orogen, Namibia, South West Africa *In* Martin, H. and Eder, F.W. (Eds). *Intracontinental Fold Belts*, Springer Verlag, Berlin, 901 - 912.
- Porada, H. (1979). The Damara-Ribeiro Orogen of the Pan-African-Brasiliano cycle in Namibia (South West Africa) and Brazil as interpreted in terms of continental collision. *Tectonophysics* **57**, 237 - 265.
- Prave, A.R. (1996). Tale of three cratons: tectonostratigraphic anatomy of the Damara Orogen in northwestern Namibia and the assembly of Gondwana. *Geology* **24**, 1115 - 1118.
- Puhan, D. (1983). Temperature and pressure of metamorphism in the central Damara Orogen *In* Miller, R. McG. (Ed.). *Evolution of the Damara Orogen of South West Africa/ Namibia. Geological Society of South Africa Special Publication* **11**, 219 - 223.
- Reuning, E. (1923). Pegmatite und Pegmatitminerale in Sudwestafrika. *Zeitschrift für Kristallographie* **58**, 448 - 459.
- Richards, T.E. (1986). Geological characteristics of rare-metal pegmatites of the Uis type in the Damara orogen, South West Africa/Namibia. *In* Anhaeusser, C.R. and Maske, S. (Eds). *Mineral Deposits of Southern Africa* **2**, Geological Society of South Africa, Johannesburg, 1845 - 1862.

- Rinaud, C., Master, S., Armstrong, R. A. & Robb, L. J. (2005). Geochronology and nature of the Palaeoproterozoic basement in the Central African Copperbelt (Zambia and the Democratic Republic of Congo), with regional implications. *Journal of African Earth Sciences* **42**, 1-31.
- Roedder, E. (1984). Fluid Inclusions. *Reviews in Mineralogy* **12**, Mineralogical Society of America, Chelsea, MI, pp 646.
- Roedder, E. (1992). Fluid inclusions evidence for immiscibility in magmatic differentiation. *Geochimica et Cosmochimica Acta* **56**, 5 - 20.
- Roedder, E. and Coombs, D.S. (1967). Immiscibility in granitic melts, indicated by fluid inclusions in ejected granitic blocks from Ascension Island. *Journal of Petrology* **8**, 417 - 451.
- Roering, C. (1963). Pegmatite investigations in the Karibib district, South West Africa. Unpublished Ph.D. thesis, University of the Witwatersrand.
- Roering, C. and Gevers, T.W. (1964). Lithium- and beryllium-bearing pegmatites in the Karibib District, South West Africa. In Haughton, S.H. (Ed.). *The Geology of Some Ore Deposits in Southern Africa*, Geological Society of South Africa **2**, 462 - 495.
- Rollinson, H. (1993). *Using Geochemical Data: Evaluation, Presentation, Interpretation*, Pearson Prentice Hall, Essex, pp 352.
- Rumvegeri, B. T. (1991). Tectonic significance of Kibaran structures in Central and eastern Africa. *Journal of African Earth Sciences* **13**, 267 - 276.
- Ryan, C. (1999). Advances in fluid inclusion analysis using the nuclear microprobe. *Nuclear Instruments and Methods in Physics Research B* **158**, 523 - 532.

- Savin, S.M. and Epstein, S. (1970). The oxygen and hydrogen isotope geochemistry of clay minerals. *Geochimica et Cosmochimica Acta* **34**, 25 - 42.
- Sawyer, E. W. (1976). *The geology of an area south-east of Walvis Bay: Lithology, sedimentation and field relationships*. Geological Survey of Namibia Regional Geology Reports **3**.
- Sawyer, E.W. (1981). Damaran structural and metamorphic geology of an area southeast of Walvis Bay, SWA/Namibia. *Memoirs of the Geological Survey of South West Africa* **8**, pp 94.
- Schneider, G.I.C. and Seeger, K.G. (1992). Semi-precious stones. In Miller, R. McG. *Mineral Resources of Namibia*, Ministry of Mines and Energy, Geological Survey of Namibia, Windhoek, 5.2, 1 - 16.
- Shand, S.J. (1927). *Eruptive Rocks*. John Wiley. New York.
- Sharp, Z. (2007) *Principles of Stable Isotope Geochemistry* Pearson Prentice Hall, Upper Saddle River, NJ, pp 344.
- Sheppard, S.M.F. (1977a). The Cornubian batholith, SW England: D/H and $^{18}\text{O}/^{16}\text{O}$ studies of kaolinite and other alteration minerals. *Journal of the Geological Society* **133**, 573 - 591.
- Sheppard, S.M.F. (1977b). Identification of the origin of reforming solutions by the use of stable isotopes. *Geological Society of London Special Publication* **7**, 25 - 41.
- Sheppard, S.M.F. (1986). Characterisation and isotopic variation in natural waters In Valley J.W., Taylor, H.P. and O'Neil, J.R. (Eds). Stable isotopes in high temperature geological processes, *Reviews in Mineralogy* **16**, Mineralogical Society of America, Chelsea, MI, 165 - 183.

- Shepherd T.J., Rankin A.H. and Alderton D.H.M. (1985). *A practical guide to fluid inclusion studies*. Blackie, Glasgow, pp 235.
- Shieh, Y.N. (1985). High-¹⁸O granitic plutons from the Frontenac Axis, Grenville Province of Ontario, Canada. *Geochimica et Cosmochimica Acta* **49**, 117 - 123.
- Shieh, Y.N. and Taylor, H.P. (1969). Oxygen and carbon isotope studies of contact metamorphism of carbonate rocks. *Journal of Petrology* **10(2)**, 307 - 331.
- Simmons, W.B. (2007). Chapter 8: Gem-bearing pegmatites In Groat, L.A. *Geology of Gem Deposits*, Short Course Series **37**, Mineralogical Association of Canada, Québec, 169 - 206.
- Simmons, W.B., Pezzotta, F., Shigley, J.E. and Beurlen, H. (2012). Granitic pegmatites as sources of coloured gemstones. *Elements: An International Magazine of Mineralogy, Geochemistry, and Petrology* **8(4)**, 281 - 287.
- Singh, P.K. (2007). Tantalite exploration in "Block A" of Uis region, Namibia. *Trabajos de Geologia* **27**, 41 - 69.
- Singh, P.K. (2008). Revelation of tin and niobium occurrences in southern Uis region of Namibia through a geological reconnaissance study. *Trabajos de Geologia* **28**, 33 - 39.
- Singh, P.K. (2009). Occurrence of low grade concentration of niobium and tantalum in the granites of Eastern Uis region of Namibia: An exploration based study. *Journal of Geology and Mining Research* **1(3)**, 67 - 75.
- Skirrow, R.G., Jaireth, S., Huston, D.L., Bastrakov, E.N., Schofield, A., van der Wielen, S.E. and Barnicoat, A.C. (2009). Uranium mineral systems: Processes, exploration criteria and a new deposit framework. *Geoscience Australia Record* 2009/20, pp 44.

- Skjerlie, K.P. and Johnston, A.D. (1992). Vapor-absent melting at 10kbar of a biotite- and amphibole-bearing tonalitic gneiss: Implications for the generation of A-type granites. *Geology* **20**, 263 - 266.
- Smith, D.A.M. (1965). The geology of the area around the Khan and Swakop Rivers in Namibia. *Memoir of the Geological Survey of South Africa* **3**, pp 113.
- South African Committee for Stratigraphy (SACS). (1980). The Damara Sequence. *In* Stratigraphy of Southern Africa. I. Lithostratigraphy of South Africa, South West Africa/Namibia and the Republics of Bophuthatswana, Transkei and Venda. *Handbook of the Geological Survey of South Africa* **8**, 415 - 423.
- Stanistreet, I.G., Kukla, P.A. and Henry, G. (1991). Sedimentary basinal responses to a Late Precambrian Wilson Cycle: the Damara Orogen and Nama Foreland, Namibia. *Journal of African Earth Science* **13**, 141 - 156.
- Steven, N.M. (1993). *A study of epigenetic mineralisation in the Central Zone of the Damara Orogen, Namibia, with special reference to gold, tungsten, tin and rare-earth elements*. Memoirs of the Geological Survey of Namibia **16**, pp 166.
- Steven, N. M. (1994). Note: Mafic dykes in the pre-Damara basement, southeast of Usakos, central Namibia. *Communications of the Geological Survey of Namibia* **9**, 92 - 95.
- Steven, N.M., Armstrong, R.A. and Moore, J.M. (1993). New Rb-Sr data from the Central Zone of the Damara Orogen, Namibia. *Communications of the Geological Survey of Namibia* **8**, 5 - 14.
- Sun, Q., Zhao, L, Li, N. and Liu, J. (2010). Raman spectroscopic study for the determination of Cl⁻ concentration (molarity scale) in aqueous solutions: Application to fluid inclusions. *Chemical Geology* **272**, 55 - 61.

- Swart, R. (1992). The sedimentology of the Zerrissene turbidite system, Damara Orogen, Namibia. *Memoirs of the Geological Society of Namibia* **13**, pp 54.
- Taylor, H.P. (1978). Oxygen and hydrogen isotope studies of plutonic granitic rocks. *Earth and Planetary Science Letters* **38**, 177 - 210.
- Taylor, HP. (1980). The effects of assimilation of country rocks by magmas on $^{18}\text{O}/^{16}\text{O}$ and $^{87}\text{Sr}/^{86}\text{Sr}$ systematics in igneous rocks. *Earth and Planetary Science Letters* **47**, 243 - 254.
- Taylor, H.P. and Turi, B. (1976). High- ^{18}O igneous rocks from the Tuscan Magmatic Province, Italy. *Contributions to Mineralogy and Petrology* **55**, 33 - 54.
- Taylor, B.E., Foord, E.E. and Friedrichsen, H. (1979). Stable isotope and fluid inclusions studies of gem-bearing granitic pegmatite-aplite dikes, San Diego Co., California. *Contributions to Mineralogy and Petrology* **68**, 187 - 205.
- Tack, L., Williams, I. and Bowden, P. (2002). SHRIMP constraints on early post-collisional granitoids of the Ida Dome, central Damara (Pan-African) Belt, western Namibia. *Abstract, 11th IAGOD Quadrennial Symposium and Geocongress, Windhoek, Namibia*. Geological Survey of Namibia.
- Thiéry, R., van den Kerkhof, A.M. and Dubessy, J. (1994). V-X properties of $\text{CH}_4\text{-CO}_2$ and $\text{CO}_2\text{-N}_2$ fluid inclusions: Modelling for $T < 31$ degrees C and $P < 400$ bars. *European Journal of Mineralogy* **6**, 753 - 771.
- Thomas, R., Webster, J.D. and Heinrich, W. (2000). Melt inclusions in pegmatitic quartz: complete miscibility between silicate melts and hydrosaline fluids at low pressure. *Contributions to Mineralogy and Petrology* **139**, 394 - 401.
- Thomas, R., Webster, J.D., Rhede, D., Seifert, W., Rickers, K., Förster, H.-J, Heinrich, W. and Davidson, P. (2006). The transition from peraluminous to peralkaline

granitic melts: Evidence from the melt inclusions and accessory minerals. *Lithos* **91**, 137 - 149.

Thomas, R., Davidson, P., and Badanina, E. (2009). A melt and fluid inclusions assemblage in beryl from pegmatite in the Orlovka amazonite granite, East Transbaikalia, Russia: implications for pegmatite-forming melt systems. *Mineralogy and Petrology* **96**, 29 - 140.

Thomas, J.B., Watson, E.B., Spear, F., Shermella, P.T., Nayak, S.K. and Lanzirotti, A. (2010). Titanium under pressure: the effect of pressure and temperature on the solubility of Ti in quartz. *Contributions to Mineralogy and Petrology* **160**, 743 - 759.

Thomas, R., Webster, J.D. and Davidson, P. (2011). Be-daughter minerals in fluid and melt inclusions: implications for the enrichment of Be in granite-pegmatite systems. *Contributions to Mineralogy and Petrology* **161**, 483 - 495.

Thomas, R., Davidson, P. and Beurlen, H. (2012). The competing models for the origin and internal evolution of granitic pegmatites in the light of melt and fluid inclusion research. *Mineralogy and Petrology* **106**, 55 - 73.

Tkachev, A.V. (2011). Evolution of metallogeny of granitic pegmatites associated with orogens throughout geologic time. In Sial, A.N., Bettencourt, J.S., De Campos, C.P. (Eds). Granite-Related Ore Deposits. *Geological Society of London Special Publication* **350**, 7 - 23.

Trumbull, R.B. (1995). A fluid inclusion study of the Sinceni rare-element pegmatites of Swaziland. *Mineralogy and Petrology* **55**, 85 - 102.

Turi, B. and Taylor, H.P. (1976). Oxygen isotope studies of potassic volcanic rocks of the Roman Province, Central Italy. *Contributions to Mineralogy and Petrology* **55**, 1 - 31.







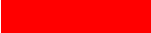
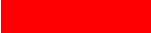




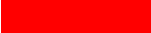











- Ueda, K., Jacobs, J., Thomas, R.J., Kosler, J., Jourdan, F. and Matola R. (2012) Delamination-induced late-tectonic deformation and high-grade metamorphism of the Proterozoic Nampula Complex, Mozambique. *Precambrian Research* **196 - 197**, 275 - 294.
- Unrug, R. (1996). The assembly of Gondwanaland. *Episodes* **19**, 11 - 20.
- Valley, J.W. (1986). Stable isotope geochemistry of metamorphic rocks waters *In* Valley J.W., Taylor, H.P. and O'Neil, J.R. (Eds). *Stable Isotopes in high temperature geological processes*, Reviews in Mineralogy **16**, Mineralogical Society of America, Chelsea, Michigan, 445 - 489.
- Varlamoff, N. (1972). Central and West African rare-metal granitic pegmatites, related aplites, quartz veins and minerals deposits. *Mineralium Deposita* **7**, 202 - 216.
- Vennemann, T.W. and Smith, H.S. (1990). The rate and temperature of reaction of ClF_3 with silicate minerals, and their relevance to oxygen isotope analysis. *Chemical Geology* **86**, 83 - 88.
- Vennemann, T.W. and O'Neil, J.R. (1993). A simple and inexpensive method of hydrogen isotope and water analysis of minerals and rocks based on zinc reagent. *Chemical Geology (Isotope Geosciences Section)* **103**, 227 - 234.
- Von Knorring, O. and Condliffe, E. (1987). Mineralised pegmatites in Africa. *Geological Journal* **22 (thematic issue)**, 253 - 270.
- Wagner, G.F. (1989). Systematic variation in the tin content of pegmatites in western central Namibia. *Journal of Geochemical Exploration* **34**, 1 - 19.
- Walker, R.J., Hanson, G.N., Papike, J.J., O'Neil, J.R. and Laul, J.C. (1986). Internal evolution of the Tin Mountain pegmatite, Black Hills, South Dakota. *American Mineralogist* **71**, 440 - 459.

- Wark, D.A. and Watson, E.B. (2006). TitaniQ: a titanium-in-quartz geothermometer. *Contributions to Mineralogy and Petrology* **152** 743 - 754.
- Webber, K.L., Falster, A.U., Simmons, W.B and Foord, E.E. (1997). The role of diffusion-controlled oscillatory nucleation in the formation of line rock in pegmatite-aplite dikes. *Journal of Petrology* **38**, 1777 - 1791.
- Webber, K.L., Simmons, W.B., Falster, A.U. and Foord, E.E. (1999). Cooling rates and crystallisation dynamics of shallow level pegmatite-aplite dikes, San Diego County, California. *American Mineralogist* **84**, 708 - 717.
- Webster, J.D. and De Vivo, B. (2002). Experimental and modelled solubilities of chlorine in aluminosilicate melts, consequences of magma evolution, and implications for exsolution of hydrous chloride melt at Mt. Somma - Vesuvius. *American Mineralogist* **87**, 1046 - 1061.
- Whalen, J.B., Currie, K. L. and Chappell, B.W. (1987). A-type granites: geochemical characteristics, discrimination and petrogenesis. *Contributions to Mineralogy and Petrology* **95**, 407 - 419.
- White, A.J.R. (1979). Sources of granite magmas. *Geological Society of America Abstract Programmes* **11**, 539.
- Will, T.M., Miller, R.McG., and Frimmel, H.E. (2009). Orogenic tectono-thermal evolution. Neoproterozoic to Early Palaeozoic evolution of Southwestern Africa. In Gaucher, C., Sial, A.N., Halverson, G.P., Frimmel, H.E. (Eds.). *Neoproterozoic-Cambrian tectonics, global change and evolution: a focus on southwestern Gondwana*. Developments in Precambrian Geology **16**, Elsevier, 205 - 218.
- Winter, J.D. (2001). *An Introduction to Igneous and Metamorphic Petrology*. Prentice Hall, New Jersey, pp 697.

Woolley, A.R. (1987) Lithosphere metasomatism and the petrogenesis of the Chilwa Province of alkaline igneous rocks and carbonatites, Malawi. *Journal of African Earth Sciences* **6** 891 – 898.

Appendix 1: Sample Inventory

Table A1: List of samples, samples prepared and what data were obtained from them.

GPS Coordinates	Sample No.	Zone	Description	Thin Section	Wafer	Microthermometry	Stable Isotopes	Majors	Trace	REE
Rubicon										
33 K 602720 7555284	IIRUB1-1	wall zone	perth+msc+qtz							
33 K 602724 7555290	IIRUB1-2	wall zone	qtz							
33 K 602704 7555306	IIRUB2-1	beryl zone	qtz							
33 K 602680 7555307	IIRUB2-2	low-grade lep ore	qtz+alb+lep							
33 K 602687 7555308	IIRUB2-3	low-grade lep ore	qtz+alb+lep							
33 K 602738 7555297	IIRUB3-1	low-grade lep ore	qtz+alb+lep							
33 K 602738 7555297	IIRUB3-2	low-grade lep ore	qtz+alb+lep							
33 K 602733 7555307	IIRUB3-3	low-grade lep ore	qtz+alb+lep							
33 K 602709 7555329	IIRUB4-1, 4-2	qtz core	qtz							
33 K 602760 7555368	IIRUB5-1	petalite zone	pet+qtz							
33 K 602760 7555368	IIRUB5-2	petalite zone	pet+qtz							
33 K 602760 7555368	IIRUB5-3	petalite zone	pet+qtz							
33 K 602757 7555292	IIRUB6-1	high-grade lep ore	lep ore							
33 K 602723 7555305	IlaRUB	wall zone	perth+msc+qtz+alb							
33 K 602723 7555305	IlbRUB	wall zone	perth+msc+qtz+alb							
33 K 602723 7555305	IlcRUB	wall zone	perth+msc+qtz+alb							
33 K 602723 7555305	IldRUB	wall zone	perth+msc+qtz+alb							
33 K 602723 7555305	IleRUB	wall zone	perth+msc+qtz+alb							
33 K 602650 7555378	IIfRUB	low-grade lep ore	alb+lep+qtz							
33 K 602643 7555392	IlgRUB	qtz core	qtz							
33 K 602643 7555392	IlhRUB	wall zone	perth							
33 K 602626 7555302	2RUBi	granodiorite	plag + hbl + bt							
33 K 602694 7555295	2RUBj	wall zone	musc							
33 K 602692 7555300	2RUBk	wall zone	qtz							
33 K 602658 7555299	2RUBl	wall zone	fsp							
33 K 602658 7555299	2RUBm	wall zone	qtz							

GPS Coordinates	Sample No.	Zone	Description	Thin Section	Wafer	Microthermometry	Stable Isotopes	Majors	Trace	REE
33 K 602673 7555312	2RUBo	wall zone	qtz + musc + alb							
33 K 597139 7557440	2RUBp	wall zone	qtz + musc + alb							
33 K 597133 7557437	2RUBCR	granodiorite								
Helicon										
33 K 605922 7561519	IHEL1-1	wall zone	qtz+musc+alb							
33 K 605922 7561519	IHEL1-2	wall zone	qtz+musc+alb							
33 K 605846 7561573	IHEL2-1	contact+wall zone	tourm+musc+qtz+alb							
33 K 605833 7561568	IHEL3-1	wall zone	tourm+musc+qtz+alb							
33 K 605833 7561568	IHEL3-2	wall zone	qtz							
33 K 605833 7561568	IHEL3-3	wall zone	tourm+musc+qtz+alb							
33 K 605833 7561568	IHEL3-4	wall zone	tourm+musc+qtz+alb							
33 K 605756 7561564	IHEL5-1	lep ore	qtz+lep+alb							
33 K 605765 7561560	IHEL4-1	qtz core	qtz							
33 K 605739 7561564	IHELa	low-grade lep ore	qtz+alb+lep							
33 K 605753 7561531	IHELe	wall zone	qtz+alb+musc							
33 K 605753 7561531	IHELf	wall zone	qtz+alb+musc							
33 K 605753 7561531	IHELg	wall zone	qtz+alb+musc							
33 K 605852 7561514	IHELh	wall zone	qtz							
33 K 605852 7561514	IHELi	wall zone	fsp							
33 K 605852 7561514	IHELj	wall zone	musc + qtz							
33 K 605881 7561523	IHELk	wall zone	fsp							
33 K 605913 7561535	IHELl	wall zone	musc							
33 K 605913 7561535	IHELm	wall zone	qtz + musc + alb							
33 K 605729 7561658	IHELn	Karibib Fm	marble							
33 K 605850 7561584	IHELo	Karibib Fm	marble							
Uis										
33 K 487930 7653565	IUIS1		tourm+alb+qtz+musc							

GPS Coordinates	Sample No.	Zone	Description	Thin Section	Wafer	Microthermometry	Stable Isotopes	Majors	Trace	REE
33 K 487895 7653550	IUIS2		qtz	■	■	■	■			
33 K 487895 7653550	IUIS3		alb+qtz greisen				■	■	■	■
33 K 487868 7653543	IUIS4		qtz+alb							
33 K 487868 7653543	IUIS5		qtz+alb+msc+cass	■						
33 K 487868 7653543	IUIS6	wall zone	musc+qtz+alb+mgt (?)				■			
33 K 487868 7653543	IUIS7	wall zone	musc+qtz+alb+mgt (?)				■			
33 K 487868 7653543	IUIS9	wall zone	musc+qtz+alb+mgt (?)				■			
33 K 488085 7653561	IUIS8	Kuiseb Fm	qtz-bt knotted schist				■	■	■	■
33 K 487900 7653546	IUIS10	wall zone	qtz+musc+alb				■			
33 K 487936 7653601	IUIS11	Kuiseb Fm	qtz-bt knotted schist				■	■	■	■
33 K 487820 7653289	IUIS1		qtz+alb+msc+tourm							
33 K 487839 7653296	IUIS2		qtz	■			■			
33 K 487839 7653296	IUIS3		columbite-tantalite				■	■	■	■
33 K 487965 7653276	IUIS4	wall zone	qtz				■			
33 K 487965 7653276	IUIS5	wall zone	alb+musc				■			
33 K 487990 7653264	IUIS6	wall zone	alb+musc+qtz+opaque	■			■	■	■	■
33 K 487990 7653264	IUIS 7	wall zone	musc				■			
33 K 487990 7653264	IUIS8	wall zone	qtz				■	■	■	■
33 K 487990 7653264	IUIS9	wall zone	qtz + alb				■			
33 K 487973 7653316	IUIS10	Kuiseb Fm	qtz-bt knotted schist	■			■	■	■	■
33 K 487973 7653316	IUIS11	Kuiseb Fm	qtz-bt knotted schist	■			■	■	■	■
33 K 480200 7643719	IKAR1		qtz+alb+cassit greisen	■						
Karlowa										
33 K 480200 7643719	IKAR2		qtz	■						
33 K 480200 7643719	IKAR3		spod							
33 K 480200 7643719	IKAR4		qtz+alb+cassit greisen							
33 K 480200 7643719	IKAR5		qtz	■	■	■	■			
33 K 480203 7643720	IKAR6		qtz							

GPS Coordinates	Sample No.	Zone	Description	Thin Section	Wafer	Microthermometry	Stable Isotopes	Majors	Trace	REE
33 K 480203 7643720	IKAR7		qtz + alb + ap							
33 K 480203 7643720	IKAR8		qtz+alb+cassit greisen							
33 K 480183 7643715	IKAR 8/9	wall zone	qtz + alb							
33 K 480183 7643715	IKAR10	wall zone	musc							
33 K 560911 7549997	IKAR11	wall zone	qtz							
33 K 560911 7549997	IKAR12	wall zone	alb							
33 K 560911 7549997	IKAR13	wall zone	musc							
33 K 560911 7549997	IKAR14	wall zone	musc							
33 K 560894 7549993	IKAR15	Kuiseb Fm								
33 K 480185 7643688	IKAR16	Kuiseb Fm								
33 K 480185 7643688	IKAR17	wall zone	qtz+musc+alb							
33 K 477610 7640782	I IKAR1	qtz core	qtz							
33 K 477610 7640782	I IKAR2		alb+musc+qtz+spod							
33 K 477629 7640795	I IKAR3		qtz+musc+alb							
33 K 477645 7640796	I IKAR4	wall zone	qtz							
33 K 477645 7640796	I IKAR5	wall zone	musc							
33 K 477645 7640796	I IKAR6	wall zone	alb							
33 K 477645 7640796	I IKAR7	wall zone	qtz+musc+alb							
33 K 477645 7640796	I IKAR8	border zone	qtz+musc							
33 K 477627 7640780	I IKAR9	wall zone	musc							
33 K 477627 7640780	I IKAR10	wall zone	alb							
33 K 477627 7640780	I IKAR11	wall zone	qtz							
33 K 477627 7640780	I IKAR12	contact	schist							
33 K 477627 7640780	I IKAR13	contact	quartzite							
Usakos										
33 K 563516 7566178	USK1	border	qtz+musc+tourm							
33 K 563516 7566178	USK2	border	qtz+musc+tourm							
33 K 563516 7566178	USK3	border	qtz+musc+tourm							

GPS Coordinates	Sample No.	Zone	Description	Thin Section	Wafer	Microthermometry	Stable Isotopes	Majors	Trace	REE
33 K 563516 7566178	USK4	wall	qtz+alb+msc+tourm							
33 K 563516 7566178	USK5	wall	qtz+alb+msc+tourm							
33 K 563514 7566182	USK6	intermediate	alb+qtz+tourm							
33 K 563514 7566182	USK7	intermediate	alb+qtz+tourm							
33 K 563514 7566182	USK8	qtz core	qtz							
33 K 563514 7566182	USK9	qtz core	qtz							
33 K 563514 7566182	USK10	qtz core	qtz							
33 K 563511 7566132	USK11	qtz core	qtz							
33 K 563511 7566132	USK12	qtz core	montebrasite							
33 K 563511 7566132	USK13	qtz core	fsp							
33 K 563511 7566132	USK14	qtz core	fsp							
33 K 563740 7566229	USK15	border zone	qtz + musc + tourm							
33 K 563537 7566171	USK16	Kuiseb Fm	qtz-bt knotted schist							
33 K 563535 7566137	USK17	wall zone	qtz							
33 K 563522 7566150	USK18	wall zone	fsp							
33 K 563519 7566107	USK19	wall zone	qtz							
33 K 563452 7566070	USK20	wall zone	qtz							
33 K 563505 7566159	USK21	wall zone	fsp							
33 K 563499 7566127	USK22	Kuiseb Fm	qtz-bt knotted schist							
33 K 572378 7560625	USK23	wall zone	musc							
Omapyu										
33 K 620083 7601603	OMA1	peg 4	qtz+alb+tourm							
33 K 620080 7601603	OMA2	border zone	qtz+alb+tourm							
33 K 620080 7601603	OMA3	border zone	qtz+alb+tourm							
33 K 620080 7601603	OMA4	border zone	qtz+alb+tourm							
33 K 619983 7601521	OMA5	Karibib Fm	marble							
33 K 619983 7601521	OMA6	intermediate	qtz+alb+tourm							
33 K 619983 7601521	OMA7	intermediate	qtz+alb+tourm							

GPS Coordinates	Sample No.	Zone	Description	Thin Section	Wafer	Microthermometry	Stable Isotopes	Majors	Trace	REE
33 K 620079 7601598	OMA8	wall zone	musc				■			
33 K 620079 7601598	OMA9	wall zone	qtz							
33 K 620079 7601598	OMA10	wall zone	ksp							
33 K 620078 7601591	OMA11	wall zone	qtz + musc							
33 K 620078 7601591	OMA12	wall zone	alb							
33 K 620098 7601631	OMA13	Karibib Fm	marble	■				■	■	
Valencia										
33K 524768 7530557	VALG02	C-type SLG	ksp+tourm+qtz	■			■	■	■	■
33K 524927 7529966	VALG04	C-type SLG	ksp+tourm+qtz+bt		■	■				
33K 523502 7529135	VALG06	C-type SLG	ksp+tourm+qtz							
33K 524215 7527761	VALG22	B-type SLG	plag+ksp+bt+grt							
33K 524088 7528841	VA 26 - 139	metapelite	qt-bt schist							
33K 524337 7528800	VA 26 - 141	metapelite	qt-bt schist							

Appendix 2: Microthermometry Data

Table A2.1: Microthermometry data for Type 1 fluid inclusions from Rubicon pegmatite. All temperature data in °C.

Filic No.	Size (µm)	D.F. CO2	D.F. H2O	Tf H2O	Tf CO2	Tm CO2	Tm i	Tm ice	Tm cl	Th CO2	Mode of homogenisation	Th total	Mode of homogenisation	Bulk p (g/cc)	NaCl (wt %)
2	9.60	0.62	0.38	-40.5	-95.5	-56.5	-20.8	-3.3	7.2	31.1	L + V → L	326.9	L + V → L	0.7	5.5
3	9.60	0.60	0.40	-40.5	-95.8	-56.5	-21.0	-3.1	6.7	31.1	L + V → L			0.7	5.2
5	8.71	0.60	0.40	-39.0	-95.1	-56.5	-20.0	-3.1	7.1	31.1	L + V → L	324.6	L + V → L	0.7	5.2
6	7.86	0.61	0.39		-94.4	-56.4	-19.0	-3.0	6.5	31.1	L + V → L	318.6	L + V → L	0.7	5.0
9	15.53	0.63	0.37	-41.1	-94.5	-56.4	-20.7	-2.8	6.8	31.0	L + V → L	344.6	L + V → L	0.7	4.7
10	9.97	0.54	0.46	-39.6	-95.6	-56.5	-20.2	-3.0	6.9	30.8	L + V → L	325.1	L + V → L	0.8	5.0
11	28.14	0.56	0.44	-44.9	-94.8	-56.4	-19.8	-3.0	6.9	31.1	L + V → L	327.0	L + V → L	0.8	5.0
12	11.53	0.66	0.34	-42.0	-95.2	-56.4	-20.1	-3.1	6.8	31.1	L + V → L	323.8	L + V → L	0.7	5.2
13	5.01	0.53	0.47	-39.4	-94.8	-56.4	-18.8	-3.0	6.9	30.8	L + V → L	320.4	L + V → L	0.8	5.0
14	7.45	0.61	0.39	-40.3	-95.8	-56.5	-20.0	-3.0	7.3	29.8	L + V → L			0.8	5.0
15	6.15	0.56	0.44	-43.8	-95.3	-56.5	-21.1	-3.0	7.0	30.9	L + V → L			0.8	5.0
16	5.89	0.56	0.44	-45.4	-95.9	-56.5		-3.1	6.8	30.8	L + V → L			0.8	5.2
17	5.89	0.61	0.39	-42.3	-95.8	-56.4	-20.4	-3.1	7.0	30.3	L + V → L			0.8	5.2
20	16.04	0.56	0.44	-38.8	-95.2	-56.4		-2.8	7.0	31.1	L + V → L			0.8	4.7
21	6.67	0.55	0.45		-94.8	-56.6	-22.3	-3.0	6.9	30.9	L + V → L	336.8	L + V → L	0.8	5.0
22	4.23	0.66	0.34		-95.5	-56.4	-20.6	-3.1	7.1	31.1	L + V → L	333.1	L + V → L	0.7	5.2
23	7.18	0.53	0.47	-41.6	-95.6	-56.5	-20.8	-3.1	6.9	31.0	L + V → L			0.8	5.2
24	8.32	0.66	0.34	-41.8	-95.8	-56.4	-20.5	-3.3	6.9	31.1	L + V → L	322.4	L + V → L	0.7	5.5
25	4.62	0.58	0.42	-41.8	-96.5	-56.4	-21.1	-3.1	7.1	31.1	L + V → L	342.4	L + V → L	0.7	5.2
26	5.12	0.50	0.50	-40.8		-56.3	-20.9	-2.8	6.9	31.1	L + V → L	336.2	L + V → L	0.8	4.7
27	7.31	0.50	0.50	-40.5	-94.5	-56.4		-2.9	6.9	31.0	L + V → L	340.8	L + V → L	0.8	4.9
28	5.01	0.56	0.44		-95.9	-56.4	-19.8	-2.9	7.0	31.0	L + V → L	337.2	L + V → L	0.8	4.9
29	5.01	0.59	0.41		-95.7	-56.6	-21.1	-3.0	7.1	31.1	L + V → L	342.1	L + V → L	0.7	4.9
30	7.56	0.55	0.45	-32.9	-94.6	-56.4	-20.6	-2.8	7.2	31.1	L + V → L	326.3	L + V → L	0.8	4.7

Finc No.	Size (µm)	D.F. CO2	D.F. H2O	Tf H2O	Tf CO2	Tm CO2	Tm i	Tm ice	Tm cl	Th CO2	Mode of homogenisation	Th total	Mode of homogenisation	Bulk p (g/cc)	NaCl (wt %)
32	10.46	0.52	0.48	-43.3	-94.2	-56.4	-21.9	-3.0	7.2	31.1	L + V → L	290.5	L + V → L	0.8	5.0
33	9.87	0.60	0.40	-39.1	-95.1	-56.5	-21.4	-2.9	7.2	31.1	L + V → L	340.7	L + V → L	0.7	4.9
34	6.15	0.60	0.40	-32.9	-95.8	-56.5	-21.9	-2.9	6.9	30.9	L + V → L	336.6	L + V → L	0.7	4.9
35	5.76	0.62	0.38	-41.9	-95.8	-56.5	-20.2	-2.5	7.5	30.9	L + V → L	324.5	L + V → L	0.7	4.2
36	13.83	0.56	0.44	-43.2	-94.7	-56.4	-19.2	-3.3	7.6	31.1	L + V → L	323.0	L + V → L	0.8	5.5
37	18.35	0.51	0.49	-43.6	-94.1	-56.5	-20.4	-3.4	7.5	31.0	L + V → L	313.4	L + V → L	0.8	5.6
38	13.62	0.64	0.36	-41.0	-95.5	-56.2	-20.6	-2.6	7.1	31.1	L + V → L	343.1	L + V → L	0.7	4.4
39	6.40	0.60	0.40		-95.1	-56.5	-20.3	-2.9	6.4	31.1	L + V → L	317.9	L + V → L	0.7	4.9
40	8.72	0.58	0.42	-42.6	-95.0	-56.5	-21.6	-3.0	6.8	30.9	L + V → L	337.8	L + V → L	0.7	5.0
41	8.96	0.61	0.39	-39.1	-94.5	-56.3	-18.5	-2.9	6.5	30.8	L + V → L	337.1	L + V → L	0.7	4.9
42	6.53	0.56	0.44	-39.1	-95.5	-56.5	-19.0	-2.9	7.2	31.0	L + V → L	348.8	L + V → L	0.8	4.9
43	25.23	0.54	0.46	-40.3	-94.5	-56.5	-21.7	-2.4	7.2	31.1	L + V → L	348.0	L + V → L	0.8	4.1
44	12.08	0.53	0.47	-40.7	-95.6	-56.5	-21.9	-2.5	7.3	31.0	L + V → L	320.6	L + V → L	0.8	4.2
46				-41.2	-95.6	-56.5	-21.1	-2.9	7.1		L + V → L	310.1	L + V → L		
47	16.47	0.63	0.37	-42.9	-94.0	-56.4		-2.9	7.0	31.1	L + V → L			0.7	4.9
48	5.77	0.53	0.47	-30.9	-95.3	-56.5	-21.6	-3.0	7.2	31.1	L + V → L	329.4	L + V → L	0.8	5.0
49	5.00	0.67	0.33		-95.6	-56.4	-21.2	-2.8	6.7	31.1	L + V → L	333.6	L + V → L	0.7	4.7
50	5.12	0.70	0.30		-96.0	-56.4	-20.2	-3.3	6.3	30.9	L + V → L	336.5	L + V → L	0.7	5.5
53	19.00	0.57	0.43		-95.2	-56.5	-21.1	-3.0	7.1	31.1	L + V → L	343.0	L + V → L	0.7	5.0
AVE	9.66	0.58	0.42	-40.6	-95.2	-56.4	-20.6	-3.0	7.0	31.0		330.4		0.7	5.0

Table A2.2: Microthermometry data for Type 2 fluid inclusions from Rubicon pegmatite. All temperature data in °C.

FliNC No.	Size (µm)	D.F. v	D.F. l	Tf H2O	Tm i	Tm ice	Th H2O	Mode of homegenisation	ρ (g/cc)	NaCl (wt %)
1	15.74	0.21	0.79	-35.5	-23.0	-0.1	107.7	L + V → L	1.0	0.2
2	13.49	0.24	0.76	-33.6	-24.0	0.5	112.6	L + V → L	0.9	-
4	12.16	0.27	0.73	-29.7	-24.0	0.1	116.5	L + V → L	0.9	-
5	11.41	0.18	0.82	-34.0	-23.9	-0.8	105.1	L + V → L	1.0	1.4
6	14.39	0.22	0.78	-34.1	-23.7	-0.1	122.6	L + V → L	0.9	0.2
7	11.57	0.26	0.74	-33.8	-23.6	0.1	119.8	L + V → L	0.9	-
8	24.09	0.19	0.81	-31.9	-23.5	-2.2	119.7	L + V → L	1.0	3.7
9	8.22	0.25	0.75	-31.2	-23.5	-2.1	91.9	L + V → L	1.0	3.5
10	14.47	0.18	0.82	-31.8	-23.6	-1.1	114.2	L + V → L	1.0	1.9
11	9.66	0.20	0.80	-34.7	-23.1	-1.0	114.5	L + V → L	1.0	1.7
12	18.89	0.19	0.81	-34.9	-23.3	0.8	100.6	L + V → L	1.0	-
13	10.59	0.27	0.73	-33.6	-23.7	0.0	93.7	L + V → L	1.0	-
14	10.93	0.22	0.78	-29.9	-23.3	-0.4	105.6	L + V → L	1.0	0.7
15	16.79	0.18	0.82	-33.6	-23.3	-1.3	112.7	L + V → L	1.0	2.2
16	22.18	0.20	0.80	-31.9	-23.9	-2.7	105.8	L + V → L	1.0	4.5
17	18.31	0.20	0.80	-32.0	-22.8	-0.3	112.9	L + V → L	1.0	0.5
18	11.80	0.21	0.79	-33.6	-23.8	0.3	118.2	L + V → L	0.9	-
19	8.91	0.25	0.75	-30.4	-23.4	2.2	103.8	L + V → L	1.0	-
20	12.24	0.28	0.72	-32.5	-23.9	-2.5	148.0	L + V → L	0.9	4.2
21	17.40	0.23	0.77	-33.9	-23.7	-0.2	103.2	L + V → L	1.0	0.4
22	13.13	0.19	0.81	-35.3	-23.4	1.2	101.8	L + V → L	1.0	-
23	12.82	0.26	0.74	-33.7	-24.6	3.8				-
24	8.81	0.26	0.74	-33.2	-23.7	-2.8				-
25	8.86	0.30	0.70	-32.5	-23.7	-2.5	168.9	L + V → L	0.9	4.2
26	12.62	0.23	0.77	-34.3	-23.4	-0.5				-
27	15.31	0.19	0.81	-33.4	-23.5	-1.7	108.8	L + V → L	1.0	2.9
28	8.98	0.21	0.79	-34.8	-24.0	1.0	107.0	L + V → L	1.0	-
AVE	13.47	0.22	0.78	-33.1	-23.6	-0.5	113.2		1.0	2.1

Table A2.3: Microthermometry data for Type 3 fluid inclusions from Rubicon pegmatite. All temperature data in °C.

Finc No.	Size (µm)	D.F. CO2	D.F. H2O	Tf H2O	Tf CO2	Tm CO2	Tm i	Tm ice	Tm cl	Th CO2	Mode of homogenisation	Th Total	Mode of homogenisation	Bulk ρ (g/cc)	NaCl (wt %)
1	19.71	0.26	0.74	-42.3	-98.8	-56.7	-20.0	no data	7.0	30.9	L + V → L				-
2	10.00	0.30	0.70	-41.6	-97.8	-56.7	-22.1	0.6	7.3	30.8	L + V → L	325.8	L + V → L	0.9	-
3	7.01	0.21	0.79	-42.5	-95.4	-56.6	-22.1	no data	7.2	30.9	L + V → L	324.8	L + V → L	0.9	-
4	5.20	0.66	0.34	no data	-96.2	-54.2	-23.1	-1.0	7.2	30.9	L + V → L	321.8	L + V → L	0.7	1.8
5	3.44	0.45	0.55	-46.9	-95.5	-56.5	-25.9	-0.6	7.2	30.9	L + V → L	338.3	L + V → L	0.8	1.1
6	6.33	0.61	0.39	-43.0	-95.9	-56.6	-22.9	no data	7.2	30.8	L + V → L	322.2	L + V → L	0.7	-
7	3.52	0.47	0.53	-41.7	-95.9	-56.4	no data	-0.6	7.0	30.8	L + V → L	319.5	L + V → L	0.8	1.1
8	3.22	0.36	0.64	no data	-95.7	-56.6	-25.4	no data	7.1	30.8	L + V → L	319.5	L + V → L	0.8	-
9	4.90	0.48	0.52	no data	-95.6	-56.6	-24.1	no data	6.9	30.9	L + V → L	325.6	L + V → L	0.8	-
10	2.08	0.49	0.51	no data	-96.8	-56.6	-23.0	no data	6.9	30.9	L + V → L	325.8	L + V → L	0.8	-
11	5.03	0.56	0.44	-43.1	-95.6	-56.4	-24.0	no data	6.9	30.7	L + V → L	329.9	L + V → L	0.8	-
12	3.85	0.40	0.60	no data	-95.9	-56.5	-21.1	no data	6.8	30.9	L + V → L	329.6	L + V → L	0.8	-
13			1.00	-41.3	-95.6	-56.5	-22.2	no data	7.6	30.5	L + V → L				-
14	3.21	0.47	0.53	-40.7	-94.5	-56.5	no data	1.3	7.6	30.8	L + V → L	326.0	L + V → L	0.8	-
15	2.67	0.36	0.64	no data	-96.5	-56.5	-21.7	no data	no data	30.9	L + V → L	328.6	L + V → L	0.8	-
16	3.04	0.40	0.60	no data	-96.7	-56.5	no data	2.1	6.9	30.9	L + V → L	330.7	L + V → L	0.8	-
17	4.68	0.41	0.59	-40.6	-96.2	-56.5	-22.2	0.2	no data	30.9	L + V → L	324.3	L + V → L	0.8	-
18	5.06	0.51	0.49	-41.2	-96.3	-56.5	-24.2	no data	6.8	30.9	L + V → L	330.9	L + V → L	0.8	-
19	8.09	0.67	0.33	-42.8	-95.5	-56.5	-22.3	no data	7.0	30.9	L + V → L	331.2	L + V → L	0.7	-
20	5.73	0.61	0.39	-43.6	-95.8	-56.5	-21.2	no data	6.9	30.9	L + V → L	340.7	L + V → L	0.7	-
21	5.12	0.57	0.43	no data	-96.2	-56.5	no data	no data	7.7	30.8	L + V → L	326.4	L + V → L	0.7	-
22	4.49	0.73	0.27	-40.8	-95.2	-56.5	-21.5	no data	7.0	30.9	L + V → L	324.7	L + V → L	0.7	-
23	4.51	0.63	0.37	no data	-96.1	-56.5	no data	no data	6.9	30.9	L + V → L	226.0	L + V → L	0.7	-

Finc No.	Size (µm)	D.F. CO2	D.F. H2O	Tf H2O	Tf CO2	Tm CO2	Tm i	Tm ice	Tm cl	Th CO2	Mode of homogenisation	Th Total	Mode of homogenisation	Bulk ρ (g/cc)	NaCl (wt %)
24	4.26	0.74	0.26	-40.0	-95.9	-56.5	no data	no data	6.9	30.9	L + V → L	323.2	L + V → L	0.6	-
25	6.00	0.57	0.43	-43.4	-95.3	-56.4	-20.1	no data	6.7	30.9	L + V → L	329.9	L + V → L	0.7	-
26	6.01	0.52	0.48	-43.0	-95.5	-56.5	-20.0	no data	6.9	30.9	L + V → L	324.4	L + V → L	0.8	-
27	5.84	0.53	0.47	-43.0	-95.5	-56.5	no data	no data	7.0	30.9	L + V → L	316.1	L + V → L	0.8	-
28	3.04	0.55	0.45	no data	-96.1	-56.5	-25.1	no data	6.8	30.9	L + V → L	331.8	L + V → L	0.7	-
29	4.25	0.52	0.48		-96.3	-56.4	-20.2	no data	7.2	30.9	L + V → L	327.8	L + V → L	0.8	-
30	6.93	0.54	0.46	no data	-95.8	-56.5	-20.2	no data	6.8	30.9	L + V → L	326.2	L + V → L	0.7	-
31	3.56	0.57	0.43	no data	-96.5	-56.5	-23.1	no data	7.5	30.9	L + V → L	339.6	L + V → L	0.7	-
32	10.32	0.48	0.52	-40.2	-96.6	-56.6	-22.4	no data	7.1	30.8	L + V → L	346.6	L + V → L	0.8	-
33	5.84	0.58	0.42	-44.7	-95.6	no data	-22.8	no data	7.6	30.9	L + V → L	334.1	L + V → L	0.7	-
34	4.02	0.49	0.51	-38.1	no data	-56.8	-20.7	no data	6.4	30.9	L + V → L	325.2	L + V → L	0.8	-
35	5.96	0.49	0.51	-39.1	-95.6	-56.6	-20.2	no data	7.7	30.8	L + V → L	330.1	L + V → L	0.8	-
AVE	5.50	0.51	0.51	-41.98	-96.01	-56.46	-22.3	0.3	7.1	30.9		325.1		0.8	1.3

Table A2.4: Microthermometry data for Type 5 fluid inclusions from Rubicon pegmatite. All temperature data in °C.

FliNC No.	Size (µm)	D.F. v	D.F. l	Tf H2O	Tm i	Tm ice	Tm ice new	Th H2O	Mode of homegenisation	ρ (g/cc)	NaCl (wt %)
1	9.20	0.18	0.82	-40.1	-26.4	2.6	-6.7	117.5	L + V → L	1.0	10.1
2	8.01	0.23	0.77	-38.5	-25.5	2.5	-4.1	100.4	L + V → L	1.0	6.6
3	8.67	0.24	0.76	-39.5	-25.8	4.4	-3.1	104.5	L + V → L	1.0	5.1
4	6.71	0.22	0.78	-39.4	-24.2	4.2	-3.8	111.6	L + V → L	1.0	6.2
5	4.48	0.22	0.78	-40.8	-25.1	3.2	-4.1	104.8	L + V → L	1.0	6.6
6	5.70	0.15	0.85	-39.6	-25.5	2.8	-4.6	105.6	L + V → L	1.0	7.3
7	5.22	0.17	0.83	-40.8	-24.5	3.9	-3.9	105.6	L + V → L	1.0	6.3
8	9.54	0.16	0.84	-40.7	-26.9	3.8	-3.8	104.8	L + V → L	1.0	6.2
9	7.46	0.16	0.84	-41.9	-26.6	3.9	-3.9	117.0	L + V → L	1.0	6.3
10	4.49	0.20	0.80	-42.0	-25.8	3.0	-4.3	125.1	L + V → L	1.0	6.9
11	7.67	0.16	0.84	-41.0	-26.2	3.1	-3.3	118.4	L + V → L	1.0	5.4
12	7.68	0.15	0.85	-41.3	-26.3	-0.8	-4.2	161.1	L + V → L	1.0	6.7
13	6.06	0.19	0.81	-41.8	-26.5	4.1	-4.1	113.9	L + V → L	1.0	6.6
14	5.51	0.19	0.81	-41.6	-26.0	4.1	-4.2	105.1	L + V → L	1.0	6.7
15	7.14	0.16	0.84	-41.9	-26.2	4.6	-4.6				7.3
16	5.68	0.17	0.83	-40.5	-26.3	3.6	-3.6	112.4	L + V → L	1.0	5.9
17	7.35	0.18	0.82	-41.5	-27.2	4.6	-4.6	102.1	L + V → L	1.0	7.3
18	7.79	0.20	0.80	-41.3	-25.6	2.9	-4.5				7.2
19	9.68	0.15	0.85	-41.2	-26.9	4.8	-4.8	107.0	L + V → L	1.0	7.6
20	8.38	0.14	0.86	-40.9	-25.8	no data	-4.8	97.1	L + V → L	1.0	7.6
AVE	7.12	0.18	0.82	-40.8	-26.0	3.4	-4.3	111.9		1.0	6.8

Table A2.5: Microthermometry data for Type 1A fluid inclusions from an Uis pegmatite. All temperature data in °C.

Flihc No.	Size (µm)	D.F. CO2	D.F. H2O	Tf H2O	Tf CO2	Tm CO2	Tm i	Tm ice	Tm cl	Th CO2	Mode of Homoge-nisation	Th Total	Mode of Homoge-nisation	Bulk ρ
1	15.96	0.76	0.24	-29.7	-96.8	-57.5	-24.4	no data	5.5	24.5	L + V → L	315.2	L + V → V	0.8
2	16.15	0.86	0.14	-29.6	-97.3	-57.5	-21.5	no data	4.6	24.2	L + V → L	301.7	L + V → V	0.8
3	14.66	0.71	0.29	no data	-96.3	-57.5	-21.7	no data	6.1	24.5	L + V → L	308.3	L + V → V	0.8
4	14.14	0.77	0.23	-28.1	-96.8	-57.4	-25.8	no data	7.7	25.2	L + V → L			0.8
5	13.09	0.82	0.18	-29.5	-95.5	-57.4	-24.0	no data	no data	24.9	L + V → L			0.8
6	10.90	0.59	0.41	-29.9	-97.8	-57.7	-24.8	no data	8.0	24.8	L + V → L	329.2	L + V → V	0.8
7	9.51	0.70	0.30	-33.8	-97.7	-57.5	-24.6	no data	5.8	24.6	L + V → L	322.8	L + V → V	0.8
8	9.03	0.82	0.18	-31.4	-95.9	-57.7	-26.4	no data	no data	24.6	L + V → L	315.7	L + V → V	0.8
9	11.03	0.56	0.44	-32.7	-97.4	-57.5	-23.8	no data	8.3	24.9	L + V → L	304.8	L + V → V	0.8
10	12.88	0.65	0.35	-28.8	-96.0	-57.5	-26.3	no data	7.9	24.1	L + V → L	304.1	L + V → V	0.9
11	11.86	0.77	0.23	-29.6	-97.3	-57.5	-27.3	no data	8.5	24.4	L + V → L	321.0	L + V → V	0.8
12	9.33	0.78	0.22	-29.1	-97.2	-57.5	-24.8	no data	no data	23.3	L + V → L	313.5	L + V → V	0.8
13	12.04	0.77	0.23	-29.6	-97.0	-57.3	-26.1	no data	8.2	24.2	L + V → L	338.8	L + V → V	0.8
14	5.83	0.70	0.30	-28.9	-96.4	-57.4	-25.9	no data	8.1	24.1	L + V → L	332.2	L + V → V	0.8
15	15.58	0.59	0.41	-30.1	-97.4	-57.3	-26.3	no data	8.9	25.6	L + V → L	331.0	L + V → V	0.8
16	21.87	0.67	0.33	-29.3	-96.9	-57.4	no data	no data	8.9	23.8	L + V → L	319.6	L + V → V	0.9
17	7.87	0.75	0.25	no data	-97.8	-57.3	-24.7	no data	8.9	23.4	L + V → L	328.1	L + V → V	0.8
18	25.69	0.47	0.53	-31.2	-96.4	-57.8	-23.1	no data	8.5	23.7	L + V → L	321.1	L + V → V	0.9
19	19.78	0.98	0.02	no data	-97.0	-57.5	-26.4	no data	8.6	25.4	L + V → L	318.8	L + V → V	0.7
20	27.44	0.72	0.28	-29.9	-93.3	-57.7	-26.7	no data	8.7	22.9	L + V → L	314.4	L + V → V	0.9
21	9.92	0.81	0.19	-30.1	-97.1	-57.7	-25.2	no data	no data	24.1	L + V → L	decrep ~280°		0.8
22	15.59	0.48	0.52	-29.4	-98.7	-58.0	-25.2	0.2	8.1	no data	L + V → L	334.1	L + V → L	
23	16.46	0.69	0.31	-30.2	-96.6	-57.6	-26.3	no data	9.1	25.4	L + V → L	294.8	L + V → V	0.8
24	8.42	0.62	0.38	no data	-94.2	-57.6	-27.6	no data	9.0	24.9	L + V → L	319.9	L + V → V	0.8
25	13.34	0.67	0.33	-30.0	-97.2	-57.7	-26.1	no data	8.1	25.7	L + V → L	326.6	L + V → V	0.8

Flinc No.	Size (μm)	D.F. CO2	D.F. H2O	Tf H2O	Tf CO2	Tm CO2	Tm i	Tm ice	Tm cl	Th CO2	Mode of Homogenisation	Th Total	Mode of Homogenisation	Bulk ρ
26	6.73	0.83	0.17	no data	-97.7	-57.5	-26.4	no data	8.9	24.1	L + V \rightarrow L	319.8	L + V \rightarrow V	0.8
27	8.07	0.75	0.25	-30.1	-97.4	-57.5	-25.1	no data	8.8	24.6	L + V \rightarrow L	317.8	L + V \rightarrow V	0.8
28	5.47	0.63	0.37	-30.1	-98.4	-57.4	-26.9	no data	8.7	25.0	L + V \rightarrow L	318.2	L + V \rightarrow V	0.8
29	8.96	0.87	0.13	-30.3	-97.5	-57.5	-25.5	no data	8.8	24.3	L + V \rightarrow L	311.6	L + V \rightarrow V	0.8
30	10.12	0.78	0.22	-29.1	-97.2	-57.4	-26.0	no data	9.0	24.9	L + V \rightarrow L	319.9	L + V \rightarrow V	0.8
31	6.89	0.76	0.24	-30.3	-97.7	-57.5	-26.4	no data	8.5	24.6	L + V \rightarrow L	313.1	L + V \rightarrow V	0.8
32	7.42	0.73	0.27	-33.5	-97.7	-57.6	-25.9	no data	9.1	23.4	L + V \rightarrow L	314.2	L + V \rightarrow V	0.9
33	18.36	0.81	0.19	-29.9	-97.7	-57.9	-24.9	no data	8.5	24.5	L + V \rightarrow L	312.0	L + V \rightarrow V	0.8
34	20.26	0.65	0.35	-28.9	-97.8	-58.2	no data	no data	8.7	21.8	L + V \rightarrow L	319.9	L + V \rightarrow V	0.9
AVE	12.96	0.72	0.28	-30.1	-97.0	-57.6	-25.4	0.2	8.2	24.4		318.14		0.8

Table A2.6: Microthermometry data for Type 1B fluid inclusions from an Uis pegmatite. All temperature data in °C.

Fliuc No.	Size (µm)	D.F. CO2	D.F. H2O	Tf H2O	Tf CO2	Tm CO2	Tm i	Tm ice	Tm cl	Th CO2	Mode of Homoge-nisation	Th Total	Mode of Homoge-nisation	Bulk p
1	56.36	0.73	0.27	-29.0	-96.1	-57.5	-25.3	no data	7.9	26.3	L + V → V	281.5	L + V → V	0.5
2	21.35	0.73	0.27	-29.9	-97.0	-57.4	-23.9	no data	7.8	26.5	L + V → V	297.7	L + V → V	0.5
3	23.06	0.81	0.19	-29.1	-96.4	-57.4	-26.3	no data	8.5	26.4	L + V → V	283.2	L + V → V	0.5
4	35.36	0.60	0.40	no data	-94.2	-57.2	-26.6	no data	9.0	26.2	L + V → V	343.9	L + V → V	0.6
5	13.11	0.67	0.33	-29.6	-96.9	-57.2	-26.6	no data	7.5	26.7	L + V → V	280.5	L + V → V	0.6
6	22.81	0.71	0.29	no data	-96.3	-57.4	-27.0	no data	8.4	26.2	L + V → V	339.9	L + V → V	0.5
7	13.28	0.71	0.29	-29.4	-96.7	-57.4	-26.3	no data	8.7	26.3	L + V → V	341.1	L + V → V	0.5
8	11.86	0.68	0.32	-29.1	-96.8	-57.5	-26.0	no data	8.7	26.4	L + V → V	343.6	L + V → V	0.6
9	13.45	0.72	0.28	-29.6	-96.1	-57.5	no data	no data	8.4	25.7	L + V → V	336.1	L + V → V	0.5
10	19.01	0.69	0.31	-28.9	-96.7	-57.6	-27.0	no data	8.7	26.3	L + V → V	341.3	L + V → V	0.6
11	8.11	0.71	0.29	-30.0	no data	-57.1	-26.9	no data	8.7	27.8	L + V → V	335.7	L + V → V	0.6
12	70.40	0.88	0.12	-28.0	-95.2	-56.9	-26.6	no data	8.8	28.5	L + V → V	242.8	L + V → V	0.5
13	15.90	0.77	0.23	-29.3	-96.6	-57.4	-25.5	no data	8.6	26.4	L + V → V	347.0	L + V → V	0.5
14	14.44	0.73	0.27	-28.9	-96.8	-57.4	-26.2	no data	8.9	26.9	L + V → V	335.2	L + V → V	0.5
15	20.10	0.76	0.24	-29.8	-97.0	-57.5	-26.2	no data	8.8	26.4	L + V → V			0.5
16	24.87	0.75	0.25	-29.0	-96.4	-57.4	-24.3	no data	8.7	26.4	L + V → V	293.4	L + V → V	0.5
17	19.74	0.77	0.23	-29.6	-96.9	-57.4	no data	no data	8.6	26.6	L + V → V	323.2	L + V → V	0.5
18	12.37	0.65	0.35	no data	-96.8	-57.1	-26.8	no data	8.9	26.5	L + V → V	337.8	L + V → V	0.6
19	16.82	0.74	0.26	no data	-97.4	-57.4	-25.5	no data	8.5	26.2	L + V → V	341.1	L + V → V	0.5
20	25.60	0.70	0.30	-31.7	-95.0	-57.2	-25.9	no data	8.1	26.5	L + V → V	339.5	L + V → V	0.6
21	36.68	0.79	0.21	-28.6	-96.3	-57.3	-26.3	no data	8.1	26.4	L + V → V	317.8	L + V → V	0.5
22	17.00	0.64	0.36	-30.2	-96.7	-57.3	-25.4	no data	8.4	26.5	L + V → V	335.8	L + V → V	0.6
23	19.00	0.67	0.33	-29.9	-96.6	-57.4	-25.2	no data	8.3	26.4	L + V → V	286.0	L + V → V	0.6
24	15.56	0.71	0.29	no data	-93.3	-57.4	-25.8	no data	8.6	26.3	L + V → V	339.9	L + V → V	0.5
25	18.44	0.76	0.24	-28.9	-96.8	-57.4	-26.3	no data	8.5	26.3	L + V → V	340.0	L + V → V	0.5

Finc No.	Size (µm)	D.F. CO2	D.F. H2O	Tf H2O	Tf CO2	Tm CO2	Tm i	Tm ice	Tm cl	Th CO2	Mode of Homogenisation	Th Total	Mode of Homogenisation	Bulk p
26	16.82	0.73	0.27	-30.5	-96.3	-57.3	no data	no data	no data	26.4	L + V → V	344.8	L + V → V	0.5
AVE	22.37	0.72	0.28	-29.5	-96.3	-57.3	-26.0		8.5	26.5		322.0		0.5

Table A2.7: Microthermometry data for Type 5 fluid inclusions from an Uis pegmatite. All temperature data in °C.

FliNC No.	Size (µm)	D.F. vapour	D.F. liquid	Tf H2O	Tm i	Tm ice	Th H2O	Comments	Bulk ρ (g/cc)	Salinity (wt %)
1	12.61	0.20	0.80	-38.7	-21.1	-2.2	165.3	L + V → L	0.7	3.7
2	10.81	0.15	0.85	-39.3	-21.6	-2.5	101.3	L + V → L	0.7	4.2
3	8.94	0.14	0.86	-40.9	-21.1	-2.7	109.9	L + V → L	0.8	4.5
4	7.92	0.21	0.79	-37.2	-21.4	-1.0	158.6	L + V → L	0.3	1.7
5	6.67	0.19	0.81	-39.4	-20.9	-2.9	146.5	L + V → L	0.9	4.8
6	12.14	0.17	0.83	-39.5	-21.9	-2.1	147.9	L + V → L	0.6	3.5
7	8.91	0.15	0.85	-42.4	-21.0	-2.5	122.6	L + V → L	0.7	4.2
8	6.78	0.21	0.79	-43.6	-22.5	-2.7	125.0	L + V → L	0.8	4.5
9	19.78	0.14	0.86	-36.2	-21.7	-1.6	151.6	L + V → L	0.5	2.7
10	5.30	0.24	0.76	-38.9	-21.3	-1.0	141.1	L + V → L	0.3	1.7
11	9.86	0.14	0.86	-38.8	-21.2	-3.1	157.4	L + V → L	0.9	5.1
12	6.26	0.19	0.81	-38.4	-21.2	-1.0	149.0	L + V → L	0.3	1.7
13	5.98	0.21	0.79	-39.2	-21.7	-3.6	118.1	L + V → L	1.1	5.9
14	8.19	0.17	0.83	-38.5	-21.2	-0.8	141.4	L + V → L	0.2	1.4
15	6.82	0.16	0.84	-37.8	-21.2	-1.2	149.5	L + V → L	0.4	2.1
16	4.02	0.20	0.80	-39.7	-21.2	-1.1	141.9	L + V → L	0.3	1.9
17	4.98	0.27	0.73	-41.2	-21.1	-2.8	191.2	L + V → L	0.8	4.6
18	13.57	0.10	0.90	-35.5	-20.7	0.0	152.2	L + V → L		
19	6.24	0.18	0.82	-32.3	-21.3	-2.9	201.2	L + V → L	0.9	4.8
20	6.43	0.14	0.86	-37.0	-21.3	9.3	22.1	L + V → L		
21	4.18	0.16	0.84	-38.8	-21.6	-0.4	126.3	L + V → L	0.1	0.7
22	13.15	0.14	0.86	-38.0	no data	-0.4	164.9	L + V → L	0.1	0.7
23	12.29	0.13	0.87	-38.4	no data	-4.6	180.3	L + V → L	1.3	7.3
24	6.03	0.19	0.81	-39.1	-21.4	-1.7	143.8	L + V → L	0.5	2.9
25	6.47	0.26	0.74	-41.6	-20.7	-2.2	154.1	L + V → L	0.7	3.7
26	8.71	0.14	0.86	-42.5	-21.1	-1.3	112.9	L + V → L	0.4	2.2
27	7.96	0.20	0.80	-38.5	-21.5	-2.2	160.9	L + V → L	0.7	3.7
28	8.10	0.20	0.80	-40.2	-21.1	-1.4	145.4	L + V → L	0.4	2.4

Floc No.	Size (µm)	D.F. vapour	D.F. liquid	Tf H2O	Tm i	Tm ice	Th H2O	Comments	Bulk ρ (g/cc)	Salinity (wt %)
29	7.56	0.15	0.85	-39.2	-21.5	-1.4	116.2	L + V → L	0.4	2.4
30	7.73	0.20	0.80	-37.4	-20.3	-4.1	144.9	L + V → L	1.2	6.6
AVE	8.48	0.18	0.82	-38.9	-21.3	-1.6	141.5		0.6	3.4

Table A2.8: Microthermometry data for Type 1 fluid inclusions from a Karlowa pegmatite. All temperature data in °C.

FInc No.	Size (µm)	D.F. CO2	D.F. H2O	Tf H2O	Tf CO2	Tm CO2	Tm i	Tm ice	Tm cl	Th CO2	Mode of homogenisation	Th Total	Mode of homogenisation	Salinity (wt %)	Bulk ρ
2	23.92	0.67	0.33	-39.9	-96.4	-57.6	-24.6	no data	9.0	22.7	L + V → L	325.6	L + V → V		0.9
3	30.45	0.72	0.28	no data	-91.4	-57.6	no data	no data	9.0	22.1	L + V → L	315.8	L + V → V		0.9
4	20.14	0.70	0.30	-28.1	-95.8	-57.7	-25.5	no data	9.5	23.4	L + V → L	312.6	L + V → V		0.9
5	8.03	0.70	0.30	-30.4	-94.3	-57.5	no data	no data	9.6	23.8	L + V → L	317.7	L + V → V		0.9
6	19.00	0.70	0.30	-29.8	-96.7	-57.5	no data	no data	9.6	23.6	L + V → L	321.8	L + V → V		0.9
7	16.88	0.69	0.31	-27.8	-96.9	-57.6	no data	no data	9.7	23.4	L + V → L	327.1	L + V → V		0.9
8	20.43	0.63	0.37	-28.6	-97.7	-57.7	-24.6	no data	9.7	24.4	L + V → L	325.8	L + V → V		0.8
9	14.70	0.76	0.24	-28.4	-97.9	-57.7	-24.0	no data	9.7	23.8	L + V → L	312.3	L + V → V		0.8
10	27.15	0.54	0.46	-38.9	-97.8	-57.7	-25.0	no data	7.8	24.4	L + V → L	332.9	L + V → V		0.9
11	19.28	0.69	0.31	-29.4	-97.6	-57.7	-25.1	no data	9.9	23.4	L + V → L	326.1	L + V → V		0.9
12	14.19	0.71	0.29	-28.4	-98.0	-57.7	-25.5	no data	10.0	23.4	L + V → L	311.4	L + V → V		0.9
13	19.10	0.69	0.31	-28.1	-95.4	-57.6	-25.8	no data	9.8	22.2	L + V → L	316.5	L + V → V		0.9
14	11.50	0.71	0.29	-28.4	-96.8	-57.6	-25.2	no data	9.6	22.9	L + V → L	318.1	L + V → V		0.9
15	15.30	0.70	0.30	-29.7	-96.5	-57.3	no data	no data	9.7	24.1	L + V → L	314.6	L + V → V		0.8
16	33.52	0.69	0.31	-25.6	-91.8	-57.6	-24.6	no data	9.3	22.9	L + V → L	317.4	L + V → V		0.9
17	19.04	0.69	0.31	no data	-96.2	-57.4	-24.7	no data	9.8	23.2	L + V → L	317.3	L + V → V		0.9
18	15.40	0.72	0.28	-28.1	-96.0	-57.5	-24.4	no data	9.3	22.4	L + V → L	322.2	L + V → V		0.9
19	12.02	0.72	0.28	-30.2	-96.9	-57.6	no data	no data	8.7	21.7	L + V → L	310.9	L + V → V		0.9
20	11.99	0.62	0.38	-28.8	-96.7	-57.3	-24.5	no data	9.8	23.6	L + V → L	315.9	L + V → V		0.9
21	11.16	0.70	0.30	-29.6	-94.3	-57.4	no data	no data	8.8	21.5	L + V → L	319.4	L + V → V		0.9
22	13.33	0.71	0.29	-28.9	-94.6	-57.6	-24.7	no data	9.3	21.3	L + V → L	282.5	L + V → V		0.9
23	13.74	0.70	0.30	-28.1	-96.9	-57.5	-26.0	no data	9.7	23.4	L + V → L	319.1	L + V → V		0.9
24	10.94	0.71	0.29	no data	-95.0	-57.5	-25.8	no data	9.9	23.4	L + V → L	315.1	L + V → V		0.9
25	10.86	0.70	0.30	-29.3	-100.1	-57.5	-25.2	no data	9.9	23.9	L + V → L	302.3	L + V → V		0.8
AVE	17.23	0.69	0.31	-30.02	-96.08	-57.56	-25.01	-4.10	9.47	23.22		316.68		6.7	0.9

Table A2.9: Microthermometry data for Type 5 fluid inclusions from a Karlowa pegmatite. All temperature data in °C.

FliNC No.	Size (µm)	D.F. v	D.F. l	Tf H2O	Tm i	Tm ice	Th H2O	Mode of homogenisation	Bulk ρ (g/cc)	Salinity (wt %)
1	34.37	0.23	0.77	-34.7	-21.3	-3.1	180.1	L + V → L	0.93	5.11
2	7.87	0.21	0.79	-35.7	-21.7	-3.1	182.7	L + V → L	0.93	5.11
3	5.25	0.24	0.76	-34.0	-21.4	-3.4	206.1	L + V → L	0.90	5.56
4	12.42	0.18	0.82	-34.3	-21.3	-2.8	158.1	L + V → L	0.94	4.65
5	10.69	0.23	0.77	-35.4	-21.2	-2.8	179.3	L + V → L	0.93	4.65
6	8.55	0.28	0.72	-35.6	-21.2	-3.1	189.8	L + V → L	0.92	5.11
7	8.20	0.28	0.72	-34.0	-21.3	-2.8	176.3	L + V → L	0.93	4.65
8	8.14	0.38	0.62	-35.7	-21.1	-3.3	180.8	L + V → L	0.93	5.41
9	6.36	0.34	0.66	-36.3	-21.4	-3.1	191.8	L + V → L	0.92	5.11
10	19.73	0.27	0.73	-34.1	-21.4	-2.8	172.5	L + V → L	0.93	4.65
11	15.04	0.29	0.71	-33.9	-21.4	-2.8	175.0	L + V → L	0.93	4.65
12	18.10	0.26	0.74	-34.4	-21.5	-2.6	176.0	L + V → L	0.93	4.34
13	25.27	0.21	0.79	-35.5	-21.1	-3.0	175.7	L + V → L	0.93	4.96
14	7.81	0.25	0.75	-36.4	-21.6	-3.3	184.3	L + V → L	0.93	5.41
15	7.04	0.36	0.64	-36.1	-21.1	-2.8	189.8	L + V → L	0.91	4.65
16	18.90	0.20	0.80	-35.3	-21.8	-3.0	180.4	L + V → L	0.93	4.96
17	9.04	0.22	0.78	-35.7	-21.3	-3.0	177.2	L + V → L	0.93	4.96
18	7.11	0.23	0.77	-35.5	-21.5	-3.0	162.0	L + V → L	0.94	4.96
19	20.65	0.20	0.80	-33.9	-21.1	-2.7	179.2	L + V → L	0.92	4.49
20	11.39	0.25	0.75	-34.2	-21.4	-2.9	169.9	L + V → L	0.93	4.80
21	10.19	0.30	0.70	-33.9	no data	-2.6	166.6	L + V → L	0.93	4.34
22	14.83	0.20	0.80	-34.6	-21.4	-2.8	170.3	L + V → L	0.93	4.65
23	12.46	0.32	0.68	-36.2	-21.2	-3.1	193.5	L + V → L	0.91	5.11
24	12.67	0.23	0.77	-35.3	-21.1	-2.9	181.5	L + V → L	0.92	4.80
25	9.63	0.35	0.65	-34.4	-21.8	-3.6	223.5	L + V → L	0.89	5.86
26	13.39	0.22	0.78	-35.8	-21.3	-2.7	178.9	L + V → L	0.92	4.49
27	12.84	0.27	0.73	-36.0	-21.2	-2.8	178.4	L + V → L	0.93	4.65
28	14.57	0.32	0.68	-34.9	-21.3	-2.8	189.2	L + V → L	0.92	4.65

Finc No.	Size (μm)	D.F. v	D.F. l	Tf H2O	Tm i	Tm ice	Th H2O	Mode of homogenisation	Bulk ρ (g/cc)	Salinity (wt %)
29	9.65	0.17	0.83	-35.9	-21.3	-3.0	164.9	L + V → L	0.94	4.96
AVE	12.83	0.26	0.74	-35.09	-21.35	-2.96	180.48		0.93	4.89

Table A2.10: Microthermometry data for Type 1 fluid inclusions from the Omapyu pegmatite. All temperature data in °C.

Finc No.	Size (µm)	D.F. CO2	D.F. H2O	Tf H2O	Tf CO2	Tm CO2	Tm i	Tm ice	Tm cl	Th CO2	Mode of homogenisation	Th Total	Mode of homogenisation	Bulk ρ (g/cc)	Salinity (wt %)
1	7.93	0.38	0.62	-39.2	-96.5	-56.8	-25.3	-6.5	8.5	22.4	L + V → L			1.0	10.0
2	8.64	0.52	0.48	-29.9	-96.9	-56.6	-24.8	-5.3	8.6	22.8	L + V → L	326.0	L + V → L	0.9	8.4
3	7.60	0.43	0.57	-28.4	-96.4	-56.6	-25.1	-5.8	8.4	23.7	L + V → L			0.9	9.1
4	7.98	0.45	0.55		-95.6	-56.7	-25.1	-5.8	8.9	23.1	L + V → L	308.0	L + V → L	0.9	9.1
5	7.48	0.42	0.58	-30.7	-98.4	-56.7	-25.4	-5.4	8.5	23.0	L + V → L	307.8	L + V → L	0.9	8.5
6	12.35	0.54	0.46	-29.8	-96.4	-56.6	-24.4	-6.4	8.6	22.2	L + V → L	321.6	L + V → L	0.9	9.9
7	12.49	0.54	0.46	-29.7	-95.6	-56.7	-25.6	-5.5	8.5	22.0	L + V → L	324.1	L + V → L	0.9	8.7
8	10.00	0.48	0.52	-39.7	-95.6	-56.7	-25.4	-5.5	8.6	22.6	L + V → L	306.5	L + V → L	0.9	8.7
9	7.90	0.38	0.62		-95.6	-56.7	-26.2	-5.5	8.8	22.5	L + V → L	311.9	L + V → L	1.0	8.7
10	8.00	0.49	0.51	-36.7	-96.6	-56.7	-25.1	-5.0	8.5	22.7	L + V → L	330.3	L + V → L	0.9	8.0
11	9.85	0.36	0.64	-36.5		-56.6	-25.2	-4.8	8.3	22.4	L + V → L	315.8	L + V → L	1.0	7.7
12	5.74	0.52	0.48	-38.9	-96.1	-56.7	-24.5	-5.4	8.6	22.6	L + V → L	323.2	L + V → L	0.9	8.5
13	6.26	0.39	0.61	-39.7	-96.4	-56.6	-25.1	-5.5	8.2	22.5	L + V → L	306.5	L + V → L	0.9	8.7
14	5.48	0.69	0.31	-29.0	-96.7	-56.6	-25.3	-6.4	8.0	23.1	L + V → L	325.3	L + V → L	0.8	9.9
15	5.16	0.50	0.50	-39.7	-96.5	-56.7	-25.0	-5.5	8.4	23.0	L + V → L	323.7	L + V → L	0.9	8.7
16	7.68	0.41	0.59	-32.6	-94.9		-24.8	-5.2	8.4	22.8	L + V → L	328.3	L + V → L	0.9	8.3
17	5.25	0.44	0.56	-35.5	-98.3	-56.9	-25.6	-4.6	8.1	22.7	L + V → L	329.6	L + V → L	0.9	7.4
18	5.85	0.53	0.47	-29.8	-99.3	-56.6	-25.7	-5.5	8.5	22.5	L + V → L	339.0	L + V → L	0.9	8.7
19	5.28	0.42	0.58	-38.6	-96.5	-56.7	-25.7	-5.4	8.2	22.7	L + V → L	318.9	L + V → L	0.9	8.5
20	8.14	0.44	0.56	-38.6	-96.6	-56.7	-25.5	-5.0	8.7	22.7	L + V → L			0.9	8.0
21	5.08	0.44	0.56	-28.9	-96.9	-56.7	-25.1	-5.4	8.4	22.6	L + V → L	323.5	L + V → L	0.9	8.5
22	7.94	0.52	0.48	-31.3	-95.4	-56.7	-25.2	-5.0	8.5	22.7	L + V → L	325.6	L + V → L	0.9	8.0
23	5.90	0.47	0.53	-30.1	-96.4	-56.7	-25.0	-5.6	8.5	22.5	L + V → L	328.1	L + V → L	0.9	8.8
24	6.85	0.56	0.44	-29.4	-96.3	-56.6	-25.3	-5.1	8.3	22.9	L + V → L	323.3	L + V → L	0.9	8.1

Finc No.	Size (μm)	D.F. CO2	D.F. H2O	Tf H2O	Tf CO2	Tm CO2	Tm i	Tm ice	Tm cl	Th CO2	Mode of homogenisation	Th Total	Mode of homogenisation	Bulk ρ (g/cc)	Salinity (wt %)
25	6.30	0.55	0.45	-29.5	-96.8	-56.7	-25.5	-5.8	8.2	22.6	L + V \rightarrow L	324.3	L + V \rightarrow L	0.9	9.1
26	6.79	0.49	0.51	-37.8	-96.7	-56.7	-25.5	-5.3	8.0	22.5	L + V \rightarrow L	324.9	L + V \rightarrow L	0.9	8.4
27	9.27	0.40	0.60		-96.2	-56.7	-25.1	-6.4	8.6	23.1	L + V \rightarrow L	329.6	L + V \rightarrow L	0.9	9.9
AVE	7.53	0.47	0.53	-33.75	-96.52	-56.68	-25.24	-5.50	8.44	22.70		321.91		0.9	8.7

Table A2.11: Microthermometry data for Type 4 fluid inclusions from the Omapyu pegmatite. All temperature data in °C.

FliNC No.	Size (µm)	D.F. V	D.F. L	Tf CO2	Tm CO2	Th CO2	Mode of homogenisation	ρ CO2 (g/cc)
1	4.10	0.58	0.42	-97.8	-57.4	23.5	L + V → L	0.7
2	4.72	0.51	0.49	-98.3	-57.3	23.4	L + V → L	0.7
3	4.18	0.60	0.40	-97.4	-57.1	23.7	L + V → L	0.7
4	4.12	0.53	0.47	-96.8	-57.2	23.7	L + V → L	0.7
5	5.44	0.55	0.45	-97.3	-57.0	23.8	L + V → L	0.7
6	4.47	0.47	0.53	-98.0	-57.1	23.4	L + V → L	0.7
7	3.81	0.49	0.51	-97.7	-56.9	23.7	L + V → L	0.7
8	5.51	0.64	0.36	-97.7	-56.9	23.6	L + V → L	0.7
9	5.10	0.49	0.51	-96.8	-57.2	23.5	L + V → L	0.7
10	4.62	0.50	0.50	-97.6	-57.5	23.2	L + V → L	0.7
11	4.37	0.54	0.46	-96.6	-57.3	23.6	L + V → L	0.7
12	4.64	0.44	0.56	-98.6	-57.2	23.2	L + V → L	0.7
13	2.83	0.58	0.42	-97.7	-57.3	23.8	L + V → L	0.7
14	2.45	0.44	0.56	-96.9	-57.4	23.5	L + V → L	0.7
15	3.62	0.50	0.50	-97.8	-57.5	23.2	L + V → L	0.7
16	3.79	0.51	0.49	-96.5	-57.2	23.3	L + V → L	0.7
17	4.94	0.58	0.42	-97.7	-57.1	23.3	L + V → L	0.7
18	4.99	0.53	0.47	-98.5	-57.0	23.3	L + V → L	0.7
19	3.59	0.50	0.50	-97.7	-57.0	23.5	L + V → L	0.7
20	3.72	0.56	0.44	-97.8	-57.1	23.1	L + V → L	0.7
AVE	4.25	0.53	0.47	-97.56	-57.19	23.47		0.7

Table A2.12: Microthermometry data for Type 5 fluid inclusions from the Omapyu pegmatite. All temperature data in °C.

FliNC No.	Size (µm)	D.F. V	D.F. L	Tf H2O	Tm i	Tm ice	Th H2O	Mode of homogenisation	Bulk ρ	X H2O	Salinity (wt %)
1	7.57	0.31	0.69	-38.3	-21.0	0.9	103.6	L + V → L	1.0	1.0	
2	4.47	0.28	0.72	-30.4	-20.9	0.1	132.9	L + V → L	0.9	1.0	
3	7.16	0.24	0.76	-28.2	-21.2	-5.2	130.2	L + V → L	1.0	0.9	8.1
4	9.80	0.16	0.84	-31.6	-21.6	0.6	100.3	L + V → L	1.0	1.0	
5	3.01	0.30	0.70		-21.6	0.8	135.3	L + V → L	0.9	1.0	
6	3.59	0.32	0.68	-30.3	-21.4	-1.0	179.9	L + V → L	0.9	1.0	1.7
7	5.55	0.28	0.72	-27.8		-0.1	125.5	L + V → L	0.9	1.0	0.2
8	2.86	0.36	0.64	-31.1	-21.5	-0.2	140.0	L + V → L	0.9	1.0	0.4
9	5.82	0.20	0.80	-38.4	-20.7	-0.1		L + V → L			
10	2.36	0.34	0.66	-37.0		1.8	111.9	L + V → L	0.9	1.0	
11	3.15	0.32	0.68	-38.4		1.8	106.4	L + V → L	1.0	1.0	
12	3.47			-38.3		1.8		L + V → L			
13	12.08	0.23	0.77		-21.4	-0.9	110.7	L + V → L	1.0	1.0	1.6
14	7.41	0.27	0.73		-21.4	1.5	131.0	L + V → L	0.9	1.0	
15	16.84	0.29	0.71	-32.2	-21.2	-2.6	97.3	L + V → L	1.0	1.0	4.3
16	2.64	0.30	0.70	-36.3		-1.8	115.3	L + V → L	1.0	1.0	3.1
17	3.89	0.27	0.73	-38.0		1.7	119.4	L + V → L	0.9	1.0	
18	3.02	0.27	0.73	-46.2		1.4	114.0	L + V → L	0.9	1.0	
19	8.26	0.23	0.77	-46.6	-21.5	-2.2	136.1	L + V → L	1.0	1.0	3.7
20	6.68	0.31	0.69	-46.2	-20.8	-2.1	129.3	L + V → L	1.0	1.0	3.5
AVE	5.98	0.28	0.72	-36.2	-21.2	-0.2	123.3		0.9	1.0	3.0

Table A2.13: Microthermometry data for Type 4 fluid inclusions from a Valencia pegmatite. All temperature data in °C.

FliNC No.	Size (µm)	Tf CO ₂	Tm CO ₂	Th CO ₂	Mode of homogenisation	ρ CO ₂ (g/cc)
1	15.77	-95.0	-56.5	9.4	L + V → L	0.9
2	9.40	-94.5	-56.5	8.4	L + V → L	0.9
3	10.70	-94.2	-56.4	10.5	L + V → L	0.9
4	6.73	-95.8	-56.5	13.1	L + V → L	0.8
5	6.78	-95.0	-56.4	11.9	L + V → L	0.8
6	11.21	-95.2	-56.4	8.5	L + V → L	0.9
7	6.90	-94.4	-56.4	13.0	L + V → L	0.8
8	11.33	-94.5	-56.4	8.5	L + V → L	0.9
9	12.01	-94.9	-56.4	16.1	L + V → L	0.8
10	6.18	-93.8	-56.4	8.4	L + V → L	0.9
11	9.73	-93.9	-56.4	12.3	L + V → L	0.8
12	8.08	-96.4	-56.4	10.5	L + V → L	0.9
13	6.16	-94.7	-56.3	10.5	L + V → L	0.9
14	7.58	-94.5	-56.4	11.2	L + V → L	0.9
15	6.53	-92.1	-56.4	4.8	L + V → L	0.9
16	7.76	-95.5	-56.4	9.3	L + V → L	0.9
17	13.93	-94.4	-56.4	7.4	L + V → L	0.9
18	6.48	-94.8	-56.4	10.8	L + V → L	0.9
19	7.56	-94.7	-56.4	11.1	L + V → L	0.9
20	10.96	-95.0	-56.4	15.1	L + V → L	0.8
21	9.04	-92.7	-56.3	10.1	L + V → L	0.9
22	8.42	-93.7	-56.3	17.2	L + V → L	0.8
23	10.19	-95.3	-56.4	14.6	L + V → L	0.8
24	6.40	-94.8	-56.4	10.8	L + V → L	0.9
25	8.45	-94.4	-56.3	18.0	L + V → L	0.8
26	6.83	-94.9	-56.4	18.8	L + V → L	0.8
27	10.75	-94.1	-56.4	14.9	L + V → L	0.8
28	5.54	-95.5	-56.3	16.3	L + V → L	0.8

Finc No.	Size (µm)	Tf CO2	Tm CO2	Th CO2	Mode of homogenisation	ρ CO2 (g/cc)
29	10.88	-82.2	-56.4	15.0	L + V → L	0.8
30	9.66	-94.8	-56.4	11.9	L + V → L	0.8
AVE	8.93	-94.2	-56.4	11.9		0.8

Table A2.14: Microthermometry data for Type 5 fluid inclusions from a Valencia pegmatite. All temperature data in °C.

FliNC No.	Size (µm)	D.F. V	D.F. L	Tf H2O	Tm i	Tm ice	Th H2O	Mode of homegenisation	Bulk ρ (g/cc)	Salinity (wt %)
1	7.36	0.20	0.80	-32.3	-21.0	-1.1	174.7	L + V → L	0.9	1.9
2	8.17	0.18	0.82	-35.4	-20.9	-1.2	169.1	L + V → L	0.9	2.1
3	8.25	0.18	0.82	-35.2	-21.1	-1.4	172.5	L + V → L	0.9	2.4
4	5.61	0.20	0.80	-40.1	-21.2	-1.2	173.8	L + V → L	0.9	2.1
5	7.48	0.22	0.78	-38.1	-20.9	-1.2	169.5	L + V → L	0.9	2.1
6	5.61	0.18	0.82	-35.3	-20.9	-1.3	171.3	L + V → L	0.9	2.2
7	4.97	0.22	0.78	-42.0	-21.0	-1.1	169.4	L + V → L	0.9	1.9
8	5.72	0.21	0.79	-42.1	-21.0	-1.3	175.9	L + V → L	0.9	2.2
9	9.92	0.18	0.82	-40.1	-21.0	-1.1	171.8	L + V → L	0.9	1.9
10	7.32	0.18	0.82	-41.4	-21.1	-1.3	179.1	L + V → L	0.9	2.2
11	7.28	0.22	0.78	-41.0	-21.4	-1.1	174.6	L + V → L	0.9	1.9
12	5.22	0.21	0.79	-35.2	-21.2	-1.3	179.3	L + V → L	0.9	2.2
13	6.12	0.19	0.81	-40.8	-21.4	-1.2	171.7	L + V → L	0.9	2.1
14	6.36	0.18	0.82	-35.3	-21.1	-1.3	167.8	L + V → L	0.9	2.2
15	7.33	0.18	0.82	-32.5	-21.1	-1.2	161.8	L + V → L	0.9	2.1
16	10.62	0.17	0.83	-32.7	-20.9	-1.4	160.0	L + V → L	0.9	2.4
17	7.15	0.17	0.83	-33.4	-21.3	-1.3	170.9	L + V → L	0.9	2.2
18	11.29	0.16	0.84	-41.6	-21.0	-1.1	174.2	L + V → L	0.9	1.9
19	7.85	0.18	0.82	-36.2	-21.2	-1.2	173.3	L + V → L	0.9	2.1
20	5.68	0.23	0.77	-41.3	-21.0	-1.3	176.4	L + V → L	0.9	2.2
21	12.29	0.18	0.82	-31.7	-21.1	-1.7	159.1	L + V → L	0.9	2.9
22	11.19	0.15	0.85	-42.1	-20.9	-1.5	153.1	L + V → L	0.9	2.6
23	8.48	0.16	0.84	-42.3	-21.1	-1.5	159.5	L + V → L	0.9	2.6
24	9.01	0.19	0.81	-36.6	-21.0	1.5	146.2	L + V → L	0.9	
25	22.69	0.14	0.86	-32.9	-21.0	-1.3	165.9	L + V → L	0.9	2.2
26	15.22	0.15	0.85	-31.9	-21.4	1.3	151.8	L + V → L	0.9	
27	7.78	0.23	0.77	-34.1	-21.1	-1.4	171.2	L + V → L	0.9	2.4
AVE	8.59	0.19	0.81	-37.2	-21.1	-1.1	168.3		0.9	2.2

Appendix 3: Trace Element in Quartz Data

Table A3: Trace elements measured in double-polished quartz wafers.

Element (ppm)	Li	Be	B	Mn	Ge	Rb	Sr	Na	Al	P	K	Ca	Ti	Fe	T (°C)	
Locality	Sample No.															
Rubicon	IIRUB-A	193.00	0.73	20.55	0.00	14.00	0.10	0.09	181.30	1187.38	14.92	6.38	15.22	2.07	0.64	427.46
	IlgRUB-B	168.77	0.37	4.82	0.26	13.33	0.00	0.08	0.00	1190.52	46.69	6.03	18.22	3.39	19.86	456.68
	IlgRUB-C	157.00	0.19	3.72	0.37	11.98	0.00	0.07	0.00	3103.30	1.46	8.69	16.96	0.93	3.62	385.04
	IUB1-1-A	82.04	0.39	2.24	0.40	2.76	0.16	0.14	3397.91	1704.67	9.28	839.04	2852.35	19.77	26.10	583.83
	IIRUB1-1-B	76.68	0.29	7.49	1.07	2.63	1.12	1.22	49202.52	6367.34	14.66	4493.87	28646.76	75.94	78.55	715.31
	IIRUB1-1-C	66.29	0.37	4.07	2.63	2.76	2.57	3.17	59798.44	7042.06	37.08	5405.45	33921.63	102.90	115.26	750.78
Helicon	1HEL1-1-A	116.89	0.42	0.89	0.33	5.56	0.31	0.17	0.00	721.37	13.10	7.23	11.72	1.23	1.78	399.31
	1HEL1-1-B	107.80	0.76	1.46	0.00	3.50	0.45	1.16	368.65	1016.84	23.04	0.00	0.00	0.00	0.60	
	1HEL1-1-C	154.56	0.68	1.33	0.55	4.72	0.37	0.13	0.00	886.85	10.82	4.79	7.71	2.13	0.19	429.10
	1HEL4-1-A	153.01	0.00	2.24	1.11	10.77	0.13	0.16	38.88	1139.00	21.30	27.58	10.74	0.00	17.34	
	1HEL4-1-B	99.99	0.43	2.20	0.96	12.63	0.00	0.13	0.00	557.77	17.34	4.86	47.84	0.00	21.94	
	1HEL4-1-C	94.98	0.55	2.77	1.78	11.61	0.06	0.48	19.40	1653.98	6.37	9.74	0.00	0.00	4.97	
Uis	IUIS2-A	150.92	0.46	7.88	0.42	5.16	0.32	0.08	586.37	1053.64	19.82	20.12	4.01	3.99	6.12	466.89
	IUIS2-B	165.39	1.79	2.91	0.51	5.47	1.03	0.17	115.98	983.41	6.96	6.63	4.11	2.91	1.31	447.37
	IUIS2-C	110.74	0.31	2.86	0.43	4.94	0.07	0.09	265.64	1661.59	13.65	16.91	7.88	2.07	2.26	427.71
	IUIS4-A	40.13	0.13	1.75	0.36	6.80	0.02	0.07	0.00	264.42	27.31	5.95	0.00	1.29	12.18	401.97
	IUIS4-B	44.54	0.30	2.78	0.77	6.81	0.08	0.13	4.53	683.37	61.13	7.45	0.00	2.02	7.28	426.21
	IUIS4-C	56.92	0.29	3.74	0.37	7.76	0.09	0.09	73.72	2298.74	83.02	56.27	31.40	2.10	14.29	428.48
	IUIS2-A	147.38	0.35	15.63	0.00	6.27	0.67	0.04	298.20	585.65	2.70	23.34	5.23	2.14	1.73	429.40
	IUIS2-B	115.83	0.42	6.04	0.00	5.28	0.46	0.10	1018.40	1023.22	8.50	74.85	2.54	2.38	1.91	435.61
	IUIS2-C	97.30	0.14	5.85	1.70	5.67	0.71	0.09	599.48	937.49	0.82	51.03	2.32	2.85	8.10	446.27
Karlowa	IKAR5-A	46.26	0.00	4.62	1.01	6.94	0.31	0.48	0.00	732.82	130.02	11.97	5.24	0.00	30.94	
	IKAR5-B	61.94	0.00	0.00	2.32	4.21	0.00	0.17	0.00	601.85	41.78	2.05	0.00	0.00	6.11	
	IKAR5-C	74.83	0.39	4.76	0.97	6.67	0.00	0.33	0.00	576.70	42.11	8.53	0.00	0.00	6.38	

	IIKAR1-A	63.89	0.37	2.74	0.42	5.81	0.09	0.11	0.00	445.48	4.53	3.00	0.00	5.77	1.24	490.87
	IIKAR1-B	59.52	0.37	1.86	0.43	6.10	0.09	0.12	0.00	370.90	10.86	6.13	4.79	10.91	1.26	536.30
	IIKAR1-C	87.74	1.06	4.61	1.30	5.82	0.13	0.27	14.44	750.27	12.06	19.11	2.02	11.14	3.17	537.85
Usakos	USK8-A	131.26	0.24	1.46	0.28	4.58	0.02	0.04	8.01	517.29	4.32	0.68	0.00	1.67	0.48	415.63
	USK8-B	99.48	0.30	3.01	0.49	5.03	0.05	0.08	174.79	585.10	2.52	4.35	2.18	2.18	3.31	430.41
	USK8-C	131.55	0.28	1.38	0.43	4.89	0.02	0.03	22.41	580.06	5.95	0.79	0.00	1.29	0.46	401.91
Omapyu	OMA4-A	61.32	0.11	12.00	1.15	2.85	0.26	0.11	200.82	915.95	10.06	157.37	93.90	29.71	23.08	619.80
	OMA4-B	62.61	0.00	9.58	0.79	2.29	0.21	0.24	146.84	727.69	7.35	33.49	121.09	20.98	54.26	588.92
	OMA4-C	64.34	0.10	16.87	1.23	2.68	0.55	0.31	227.18	763.46	20.65	47.28	22.38	19.23	16.66	581.51
	OMA6-A	45.04	0.18	3.24	0.67	2.86	0.00	0.11	0.00	352.97	8.09	3.70	13.81	12.84	0.52	548.79
	OMA6-B	59.95	0.00	2.82	0.61	2.88	0.07	0.10	0.00	328.50	47.50	4.54	0.00	9.75	4.44	527.87
	OMA6-C	59.58	0.08	3.91	1.00	2.82	0.16	0.09	0.00	334.69	5.50	3.70	0.00	11.44	0.97	539.88
Valencia	VALG04-A	13.79	1.42	9.12	1.42	2.71	0.31	0.09	0.00	342.71	0.00	2.50	5.01	50.26	9.99	670.89
	VALG04-B	9.25	1.13	8.06	0.71	2.65	0.42	0.08	0.00	166.63	0.12	3.15	0.00	37.06	5.29	640.59
	VALG04-C	10.63	1.39	9.32	1.12	2.58	0.34	0.10	0.00	278.32	1.68	11.25	0.00	35.29	7.51	635.92
	VALG06-A	18.60	0.07	3.71	0.47	1.91	0.26	0.11	0.00	121.44	1.98	19.12	13.88	41.54	1.92	651.70
	VALG06-B	18.03	0.05	5.72	1.32	1.70	1.07	0.13	0.00	122.02	13.36	15.64	1.96	33.46	2.19	630.86
	VALG06-C	12.37	0.16	6.70	1.43	1.74	1.62	0.10	0.00	233.33	17.25	29.81	31.75	35.50	5.37	636.46
	not useable	elevated due to micro inclusions														